AD-A237 063

①

WHOI-90-24

Woods Hole Oceanographic Institution
Massachusetts Institute of Technology

Joint Program
in Oceanography
and
Oceanographic Engineering

DOCTORAL DISSERTATION

Stochastic Modelling of Seafloor Morphology

by

John Anson Goff

June 1990

91 6 14 002

91-02136

WHOI-90-24

Stochastic Modelling of Seafloor Morphology

by

John Anson Goff

Woods Hole Oceanographic Institution
Woods Hole, Massachusetts 02543

and

The Massachusetts Institute of Technology
Cambridge, Massachusetts 02139

June 1990

Accession For
NTIS GRA&I ☑
DTIC TAB ☐
Unannounced ☐
Justification
By
Distribution/
Availability Codes
Avail and/or
Dist Special
A-1

Doctoral Dissertation

Funding was provided by the Office of Naval Research
through the Massachusetts Institute of Technology.

Reproduction in whole or in part is permitted for any purpose of the
United States Government. This thesis should be cited as:
John Anson Goff, 1990. Stochastic Modelling of Seafloor Morphology.
Ph.D. Thesis. MIT/WHOI, WHOI-90-23.

Approved for publication; distribution unlimited.

Approved for Distribution:

David A. Ross

David A. Ross, Chairman
Department of Geology and Geophysics

Craig E. Dorman
Acting Dean of Graduate Studies

STOCHASTIC MODELING OF SEAFLOOR MORPHOLOGY

by

JOHN ANSON GOFF
Sc. B. BROWN UNIVERSITY (1985)

SUBMITTED IN PARTIAL FULFILLMENT OF THE
REQUIREMENTS FOR THE DEGREE OF
DOCTOR OF PHILOSOPHY

at the

MASSACHUSETTS INSTITUTE OF TECHNOLOGY

and the

WOODS HOLE OCEANOGRAPHIC INSTITUTION

April, 1990

© Massachusetts Institute of Technology. All rights reserved.

Signature of Author John A. Goff

Joint Program in Oceanography:
Department of Earth, Atmospheric and Planetary Sciences,
Massachusetts Institute of Technology, and
Department of Geology and Geophysics,
Woods Hole Oceanographic Institution

Certified by Thomas H. Jordan

Thesis Supervisor

Accepted by G. P. Lohmann

Chair, Joint Committee for Geology and Geophysics,
Massachusetts Institute of Technology/
Woods Hole Oceanographic Institution

STOCHASTIC MODELING OF SEAFLOOR MORPHOLOGY

by

JOHN ANSON GOFF

Submitted to the Department of Earth, Atmospheric and Planetary Sciences
Massachusetts Institute of Technology
and
the Department of Geology and Geophysics
Woods Hole Oceanographic Institution
April 5, 1990
in partial fulfillment of the requirements for the degree of Doctor of Philosophy

ABSTRACT

At scale lengths less than 100 km or so, statistical descriptions of seafloor morphology can be usefully employed to characterize processes which form and reshape abyssal hills, including ridge crest volcanism, off-axis tectonics and volcanism, mass wasting, sedimentation, and post-depositional transport. The objectives of this thesis are threefold: (1) to identify stochastic parameterizations of small-scale topography that are geologically useful, (2) to implement procedures for estimating these parameters from multibeam and side-scan sonar surveys that take into account the finite precision, resolution, and sampling of real data sets, and (3) to apply these techniques to the study of marine geological problems.

The seafloor is initially modeled as a stationary, zero-mean, Gaussian random field completely specified by its two-point covariance function. An anisotropic two-point covariance function is introduced that has five free parameters describing the amplitude, orientation, characteristic width and length, and Hausdorff (fractal) dimension of seafloor topography. The general forward problem is then formulated relating this model to the statistics of an ideal multibeam echo sounder, in particular the along-track autocovariance functions of individual beams and the cross-covariance functions between beams of arbitrary separation. Using these second moments as data functionals, we then pose the inverse problem of estimating the seafloor parameters from realistic, noisy data sets with finite sampling and beamwidth, and we solve this inverse problem by an iterative, linearized, least squares method.

Resolution of this algorithm is tested against ship variables such as length of data, the orientation of ship track with respect to topographic grain, and the beamwidth. This analysis is conducted by inverting sets of synthetic data with known statistics. The mean and standard deviation of the inverted parameters can be directly compared with the input parameters and the standard errors output from the inversion. The experiments conducted in this study show that the rms seafloor height can be estimated to within ~15% and anisotropic orientation to within ~5° (for a strong lineation) using very short track lengths (down to 3 characteristic lengths, or ~10 to 100 km), and characteristic lengths of seafloor topography can be estimated to within ~25% using fairly short track lengths (down to 5 or 6 characteristic lengths, or 10's of km to ~200 km). The number of characteristic lengths sampled by a ship track, and hence the accuracy of the estimation, is maximized when the ship track runs perpendicular to abyssal hill lineation.

Using the assumed beamwidth, the measured noise values, and the seafloor parameters recovered from the inversion, Sea Beam "synthetics" are generated whose statistical character can be directly compared with raw Sea Beam data. However, these comparisons are spatially limited in the athwartship direction. A recent SeaMARC II survey along the flanks and crest of the East Pacific Rise between 13° and 15° N included sufficient off-axis topography to permit a comparison of a complete 2-D synthetic topographic field with a region of abyssal-hill terrain that has close to 100% data coverage. Synthetic data is compared to both Sea Beam swaths and SeaMARC II survey data. These comparisons generally indicate that we are successful in characterizing the second order properties of the seafloor. They also indicate the directions we will need to take to improve our modeling, including generalization of the second-order model and characterization of higher moments.

The inversion procedure is applied to a data set of 64 near-ridge Sea Beam swaths to characterize near ridge abyssal hill morphology and its relationship to ridge properties. Much of the data (27 swaths) comes from cruises to the Pacific-Cocos spreading section of the East Pacific Rise between 9° and 15° N. These data provide very good abyssal hill coverage of this well-mapped and studied ridge section and form the basis of a regional analysis of the correlation between ridge morphology and stochastic abyssal hill parameters. This regional analysis suggests a strong relationship between magma supply and the character of abyssal hills. We also have data from near the Rivera (9) and Nazca (7) spreading sections of the East Pacific Rise, the Mid-Atlantic Ridge (18), and the Indian-African Ridge (3). Though spotty, this constitutes a good initial data set for the analysis of correlations among covariance parameters and between parameters and ridge characteristics, especially spreading rate. A working hypothesis is introduced to explain the observations within a geological framework. This hypothesis contends 1) that the maximum size of abyssal hills is related to the lithosphere's ability to elastically support the load, 2) that fissuring and horst and graben formation dominate abyssal hill formation at fast spreading ridges, and 3) that volcanic edifice formation, modified by faulting driven by lithospheric necking, dominates abyssal hill formation at slow spreading ridges.

To quantify abyssal hill characteristics such as vertical and lateral asymmetry and "peakiness" we must appeal to higher statistical moments than order two. A mathematical framework is introduced for the study of higher moments of a topographic field. This framework is built upon the concept that lower-order moment provide the groundwork for studying the higher-order moments. A simple 1-D parameterized model is proposed for moments up to order 4. This model includes two parameters for the third moment, describing vertical and lateral asymmetries, and one for the fourth moment, which describes the peakiness of topography. Initial methods are developed for estimating these parameters from bathymetric profiles. Results from the near ridge data set are presented and interpreted with regard to abyssal hill forming processes.

Thesis Supervisor: Thomas H. Jordan, Professor of Geophysics

TABLE OF CONTENTS

ABSTRACT 3
ACKNOWLEDGEMENTS 8
DEDICATION 10

CHAPTER 1

INTRODUCTION 12
- Organization 14
- Previous Publications 17
FIGURE 18

CHAPTER 2

INVERSION OF SEA BEAM DATA FOR SECOND ORDER STATISTICS 19
- INTRODUCTION 19
- SEAFLOOR TOPOGRAPHY AS A RANDOM FIELD 20
  - The Problem of Statistical Heterogeneity 21
  - Second-Order Statistics 24
  - A Gaussian Model for Seafloor Topography 25
- INVERSION OF SEA BEAM DATA FOR SECOND-ORDER MODELS 30
  - Sea Beam System Response and Noise Characteristics 31
  - Estimates of Cross Covariances and their Uncertainties 37
  - Inversion of the Cross-Covariance Functions for Model Parameters 40
- IMAGES OF THE SEAFLOOR SYNTHESIZED FROM THE STOCHASTIC MODEL .. 43
  - Synthetic Seafloor Topography 44
  - Comparison of Sea Beam Synthetics with Real Data 44
- CONCLUSIONS 47
- TABLE 2.1. Sea Beam Data Used in Second-Order Analysis 50
- TABLE 2.2. Statistical Parameters Derived From Inversion 51
- FIGURES 52

CHAPTER 3

RESOLUTION OF TOPOGRAPHIC PARAMETERS BY SEA BEAM DATA 69
- INTRODUCTION 69
- COVARIANCE OF THE ESTIMATES 71
- NUMERICAL EXPERIMENTS 75
  - Estimation of Scale and Orientation Parameters 76
  - Estimation of Hausdorff Dimension 79
- RESOLVABILITY OF NON-STATIONARY BEHAVIOR 82
- DISCUSSION 84
- TABLE 3.1. Statistical Parameters Derived From Inversion of Data Shown in Figure 3.1 87
- FIGURES 88

CHAPTER 4

COMPARISON OF A STOCHASTIC SEAFLOOR MODEL WITH SEA MARC II BATHYMETRY AND SEA BEAM DATA NEAR THE EAST PACIFIC RISE 13° - 15° N 103
- INTRODUCTION 103
- DESCRIPTIVE MORPHOLOGY OF SEAFLOOR FROM SEAMARC II AND SEA BEAM DATA 104
- SEA BEAM RESULTS AND DATA-SYNTHETIC COMPARISONS 107
- SEAMARC II DATA-SYNTHETIC COMPARISON 109
  - The Southern Section 112
  - Central and Northern Sections 114
- GEOLOGIC CORRELATIONS WITH STOCHASTIC PARAMETERS 115
- CONCLUSIONS AND DISCUSSION 118
- TABLE 4.1. Sea Beam Data Used for Parameter Estimation 123
- TABLE 4.2. Stochastic Parameters Derived from Inversion 124
- FIGURES 125

CHAPTER 5

A GLOBAL AND REGIONAL ANALYSIS OF NEAR-RIDGE ABYSSAL HILL MORPHOLOGY 139
- INTRODUCTION 139
- THE FORMATION OF ABYSSAL HILLS 140
- GLOBAL ANALYSIS 144
  - Inter-Parameter Correlations 145
  - Spreading Rate Correlations 146
  - Interpretation 147
- REGIONAL ANALYSIS 149
  - Ridge Morphology and Magma Supply 150
  - H and λ_n 151
  - a and $\Delta\zeta_s$ 152
- CONCLUSIONS 154
- TABLE 5.1. Sea Beam Data Used for Parameter Estimation 157
- TABLE 5.2. Stochastic Parameters Derived From Inversion 159
- FIGURES 161

CHAPTER 6

NON-GAUSSIAN STOCHASTIC ANALYSIS OF THE SEAFLOOR 179
- INTRODUCTION 179
- FRAMEWORK FOR THE STUDY OF HIGHER-ORDER MOMENTS 180
  - Decomposition of the N-Point Moment 181
  - Mapping Models and the Calculation of $f_j(h_i)$ 183
- A SIMPLE THIRD AND FOURTH MOMENT MODEL 185
  - Vertical Asymmetry and Peakiness 185
  - Lateral Asymmetry 188
- INITIAL ATTEMPTS AT ESTIMATION OF HIGHER MOMENT PARAMETERS 191
  - Vertical Asymmetry and Peakiness 192

Lateral Asymmetry.......... 194
RESULTS AND DISCUSSION.......... 198
CONCLUSIONS.......... 202
FIGURES.......... 204

APPENDIX A

A COVARIANCE FUNCTION FOR SEAFLOOR TOPOGRAPHY.......... 223
The Power Spectrum.......... 224
Calculation of the Hausdorff Dimension.......... 225
Self-Affine Scaling at Small Scales.......... 226
Asymptotic Equation.......... 228
Calculation of Characteristic Length.......... 228
Slope Statistics.......... 230

APPENDIX B

NESTED STOCHASTIC SEAFLOOR REALIZATIONS.......... 233
Deterministic and Stochastic Components of Seafloor Topography...... 233
The Nesting Algorithm.......... 234
Stochastic Interpolation of Gridded Bathymetric Data.......... 236
Aliasing.......... 237
FIGURES.......... 239

APPENDIX C

STATISTICAL ANALYSIS OF SEAMARC II NOISE.......... 243
FIGURES.......... 248
REFERENCES.......... 257

ACKNOWLEDGEMENTS

Of all the many people to whom I owe thanks, there are a special few who, by the strength of their personalities, had particular influence in leading me down my chosen path. Judy Belsky showed me that science can be fun (even if its chemistry). Joe Harris showed me that math can be fun (and, perhaps, even transcendental). Don Forsyth showed me that research can be fun (or at least that it was better than classes), thereby keeping me out of the real world. And Tom Jordan showed me that not only can geophysics be fun, but that life can be fun even when doing geophysics.

I owe a great deal of gratitude to all those who have listened, commented, argued and discussed with me various aspects of seafloor morphology. Foremost among these contributors are Debbie Smith, Peter Shaw, Alberto Malinverno, and Clyde Nishimura. I am also deeply indebted to my coauthors at Lamont, Margo Edwards and Dan Fornari, for their generous collaboration. Others whom I thank for stimulating and helpful conversation include Sandy Shor, Chris Fox, Dan Rothman, Tom Reed, Marty Kleinrock, Hans Shouten, John Delaney, Rob Pockalny, and Steve Miller. Without all these people this thesis would be considerably less than it is.

In the course of my research I have been able to compile a fairly large and diverse Sea Beam data set. This amazing feat could not have been accomplished without the kind help of several people, including Geoff Abers, Kurt Feigl, Debbie Smith, Joyce Miller, Uta Albright, Stacey Tighe, Lewis Gilbert, and Rob Pockalny.

Much of my work has involved the use of the Apollo/Alliant computing facilities at MIT, which would surely be a chaotic mess if not for the valiant an tireless work of Dave Krowitz. Dave's patience with questions, skills at trouble shooting, and expertise in plotting software have probably shaved a good year off my tenure as a grad student.

The support staff at MIT has helped to keep my sanity by guiding me through the murky waters of MIT bureaucracy. I especially thank Jan Sahlstrom, Laura Doughty, Katherine Ware, and Marie Senát for their effort, kindness, and patience.

Life in grad school is hard, but, because of the people one runs into around here, is on balance quite enjoyable. Several of those people deserve special mention. Anne Sheehan and Jeanie Sauber, long time office mates, have always been willing distractions from the monotony of work. Robin Jordan was a consummate hostess at innumerable parties and happily took on the job of mom-away-from-home. Greg Beroza, Peter Puster, Mark Murray, Bob Grimm, and Justin Revenaugh were all good golf/drinking buddies. And while Lind Gee didn't golf, she did occasionally drink, and often kept us sugared up with care packages from home. Kurt Feigl also didn't golf, but did drink, ski, and was kind enough to send me to a hilltop in California overlooking a golf course. Mike Bergman gave me my big break at third base, and Steve Shapiro was always willing to "have a catch". Marcia McNutt also deserves thanks for taking me along on one of her fun-in-the-sun cruise to the South Pacific with Cecily Wolfe.

Gail Christeson has been my friend and companion for more than a year. Her love, patience, and support have turned what is supposed to be the most difficult year of a grad students life into one of the most enjoyable.

I also thank Mom, Dad, Barbi, Ellie, Robbie, Dick and Jean, Trudy and Will, Grandma and Grandpa Bergstresser, Grandma and Grandpa Goff, and the extended family for their generous moral and financial support (and occasional vacation retreats) during my long career as a student.

This research was supported by Office of Naval Research under grants N00014-86-k-0325 and N00014-90-J-1584.

DEDICATION

This thesis is dedicated to the memory of my grandfather, Dr. Willard Goff. His ability to communicate the wonder of a tide pool, a robin's nest, or a beach agate has inspired me to look beyond what my eyes can see.

"In contrast to chess, the axioms of geometry and of mechanics have an intuitive background. In fact, geometrical intuition is so strong that it is prone to run ahead of logical reasoning. ... It is certain that intuition can be trained and developed. The bewildered novice in chess moves cautiously, recalling individual rules, whereas the experienced player absorbs a complicated situation at a glance and is unable to account rationally for his intuition. In like manner mathematical intuition grows with experience, and it is possible to develop a natural feeling for concepts such as four-dimensional space."

William Feller (1906-1970)
An Introduction to Probability Theory and Its Applications, vol. 1, 1968

"And I tell you, if you have the desire for knowledge and the power to give it physical expression, go out and explore. If you are a brave man you will do nothing: if you are fearful you may do much, for none but cowards have need to prove their bravery. Some will tell you that you are mad, and nearly all will say, 'What is the use?' For we are a nation of shopkeepers, and no shopkeeper will look at research which does not promise him a financial return within a year. And so you will sledge nearly alone, but those with whom you sledge will not be shopkeepers: that is worth a good deal. If you march your Winters Journeys you will have your reward, so long as all you want is a penguin's egg."

Capt. Robert Falcon Scott (1868-1912)

CHAPTER 1

INTRODUCTION

> "A first order model of spreading centers as idealized linear boundaries of crustal and lithospheric generation provides only a gross understanding of the global plate kinematics. As we attempt to understand the complexity of crustal and lithospheric structure of two thirds of the earth's surface, it is becoming increasingly necessary to study the tectonic, volcanic, and hydrothermal processes within the spreading center plate boundary zone. All oceanic crust bears the imprint of these processes."
>
> *Ken Macdonald* [1982]

> "... phenomena are not in and of themselves inherently stochastic or deterministic. Rather, to model phenomena as stochastic or deterministic is the choice of the observer."
>
> *Howard Taylor and Samuel Karlin*
> *An Introduction to Stochastic Modeling* [1984]

The geological history of the ocean basins is recorded in the shape and form of the deep seafloor. Features of interest to the marine morphologist are characterized by horizontal dimensions spanning 7 orders of magnitude, from the size of typical lava pillows ($\sim 10^{-3}$ km) to the width of the ocean basins themselves ($\sim 10^{4}$ km). For scale lengths in the upper part of this size spectrum, say, above 100 km or so, the most common and useful representation of seafloor morphology is a deterministic one, the standard bathymetric map. Much of our knowledge about plate tectonic processes has been derived from the morphological relationships made evident by bathymetric maps. The development of the plate tectonic model has advanced our understanding of major physiographic features such as ridges, transform faults, trenches, and linear island chains to the point that many of the interesting questions of marine geology now concern the processes which have shaped the details of the seafloor on a horizontal scale of a few tens of kilometers or less, including ridge-crest processes, off-ridge tectonics and vulcanism, sedimentation, and post-depositional transport. In principle, maps of sufficient scale can be used to represent features of arbitrarily small size. In practice, the number and variability of small-scale features are so large that recovering significant information from high-resolution bathymetric surveys requires that the morphological characteristics be averaged over families or ensembles, which leads to a stochastic, or statistical, representation. Figure 1.1 illustrates the range of scales over which stochastic and deterministic descriptions of morphological features of the seafloor are useful.

Stochastic descriptions underlie many qualitative statements about seafloor morphology: "abyssal hills tend to be parallel to ridges," "slower spreading ridges produce more severely faulted topography than faster spreading ridges," and "sedimentation smooths rough topography," to state a few. Moreover, the parameterization of topography in terms of its statistical properties is the most useful representation for describing acoustic scattering from a rough seafloor [e.g., *Clay and Medwin*, 1977; *Stanton*, 1985], as well as bottom interactions with abyssal currents [*Carrier*, 1970; *Elter and Molyneux*, 1972; *Bell*, 1975*a*]. The basis for any stochastic treatment is to consider the small-scale bathymetry to be a sample of a two-dimensional random process described by a set of observable statistics. We can distinguish between two types of statistical models, processes involving the distribution of discrete landforms (e.g., volcanoes or fault scarps) and processes represented as random fields defined over a continuous set of geographic coordinates. The former provide the mathematical basis for the investigation of seamount populations [*Jordan et al.*, 1983; *Smith and Jordan*, 1987], whereas the latter are more useful in describing the undulations and roughness expressed, for example, in power spectra of seafloor topography [*Bell*, 1975*b*].

The primary subjects of random field models are abyssal hills, intermediate to small-scale bathymetric features (5-50 km long, 1-20 km wide) that generally flank and are adjacent to mid-ocean ridge axes, and dominate the fabric of deep ocean basins. They are thought to form by a combination of tectonic and constructional volcanic processes related in a complex way to the spreading rate, magmatic budget and tectonic forces along a mid-ocean ridge segment. Through time they are modified by mass wasting, sedimentation, and off-axis volcanism. The abyssal hill fabric, described quantitatively by stochastic parameterization, represents a potential source of information regarding spatial and temporal variation of these processes.

Although power spectra [*Neidell*, 1966; *Bell*, 1975*b*, 1978; *Fox and Hayes*, 1985] and spatial covariance functions [*Krause and Menard*, 1965; *McDonald and Katz*, 1969; *Yesyunin*, 1975] have been computed from bathymetric data, systematic methodologies have not yet been developed for recovering random field parameters from nonidealized surveys. Consequently, with a few notable exceptions [e.g., *Bell*, 1978, Figure 3], little work has been done to quantify the dependence of physiographic characteristics such as abyssal hill lineation and roughness on the controlling geological variables such as spreading rate and sediment thickness. The objectives of this thesis are threefold: (1) to identify stochastic parameterizations of small-scale topography that are geologically useful, (2) to implement procedures for estimating these parameters from multibeam and side-scan sonar surveys that take into account the finite precision, resolution, and sampling of real data sets, and (3) to apply these techniques to the study of marine geological problems.

Organization

The bulk of the work in this thesis is concerned with estimating second-order statistical parameters from multi-beam bathymetric data. We regard the second-order analysis as the building block upon which higher-order analysis is based. In one sense we have organized this work as a perturbation problem. To lowest order we assume that the stochastic component of seafloor depth has a Gaussian probability distribution, completely described by its first and second moments (the mean and covariance function). After the second-order analysis, higher moments are then considered as perturbations to the Gaussian form.

Chapter 2 and Appendix A constitute the theoretical foundation of the second-order characterization of the seafloor and the procedure for estimating statistical parameters from bathymetric data. In it we introduce a five-parameter, second-order stochastic which provides quantitative physical information regarding abyssal hills, including the rms height, characteristic width and length, azimuth of lineation, and Hausdorff (fractal) dimension. The forward and inverse problems of estimating model parameters from realistic, noisy multibeam data are then developed. Five Sea Beam swaths are chosen to illustrate the procedure. Synthetic data sets are generated from the inverted parameter for comparison with actual data, providing a means of subjectively evaluating the model through data-synthetic comparisons.

Chapter 3 explores in detail the resolving powers of the inversion procedure. The primary goal of this work is to assess the performance of the inversion and to determine the scale at which changes in stochastic behavior can be detected. The resolving power is evaluated as a function of the swath length, orientation of ship track with respect to topographic grain, and the response width of the sounding system. The analysis is conducted by inverting sets of synthetic data with known statistics. The mean and standard deviation of the inverted parameters are directly compared with the input parameters and the standard errors output from the inversion.

Chapter 4 is a case study of abyssal hill morphology near the East Pacific Rise 13° - 15° N. The primary motivation for this study was provided by a recent Sea MARC II survey of this region which included sufficient off-axis topography to permit a comparison of a complete 2-D synthetic topographic field with a region of abyssal-hill terrain that has close to 100% data coverage. The parameters used to generate the synthetic fields were estimated from Sea Beam swaths which pass through the region. These comparisons provide a detailed accounting of the extent to which the model and inversion procedure succeed in characterizing the seafloor, and the directions that will be needed to improve the modeling. The extensive Sea MARC II coverage of nearby ridge morphology also provides an opportunity to correlate regional variations in abyssal hill characteristics with variations in ridge characteristics. This analysis suggests that such variations may be tied to the relative abundance of magma supply feeding the ridge.

Chapter 5 presents the results of a global and regional analysis of near-ridge abyssal hill morphology. It represents the culmination of the second-order analysis in this thesis. The global data set consists of 64 Sea Beam swaths near the Rivera, Cocos, and Nazca spreading sections of the East Pacific Rise, the Mid-Atlantic Ridge, and the SW Indian Ridge. These provide a good initial data set for the analysis of general correlations among covariance parameters and between parameters and ridge characteristics, especially spreading rate. We interpret these results in light of previous work concerning the formation of abyssal hills in different regions. The regional data set (a sub set of the global data set) consists of 27 swaths along the Cocos spreading section of the East Pacific Rise, concentrated between the Siquieros and Orozco fracture zones. These data provide very good abyssal hill coverage of this well-mapped and studied region and form the basis of a regional analysis of the correlation between ridge morphology and stochastic abyssal hill parameters. This study strengthens the correlation between these parameters and magma supply made in the previous chapter.

Chapter 6 is a general analysis of higher order statistical moments. Higher moments provide a means of quantifying important abyssal hill characteristics, such as vertical and lateral asymmetry, and "peakiness", which cannot be characterized by second-order moments. We begin by introducing a mathematical framework for the study of higher order moments of a topographic field. Following this general discussion we propose a very simple 1-D 3-parameter model for moments up to order 4. The two third-order parameters describe the vertical and lateral asymmetry of the profile, and the fourth-order parameter describes the peakiness. We then describe initial methods for estimating these parameters from bathymetric profiles. And finally, we present a general comparison of results at different spreading rates.

Previous publications

Most of the work presented in this thesis has been published or submitted for publication. Most of Chapter 2 and Appendix A are contained in *Goff and Jordan* [1988, 1989*a*]. Chapter 3 is contained within *Goff and Jordan* [1989*b*]. Chapter 4 and Appendix C were submitted as *Goff et al.* [1990*a*], and Appendix B was printed as *Goff and Jordan* [1990*b*].

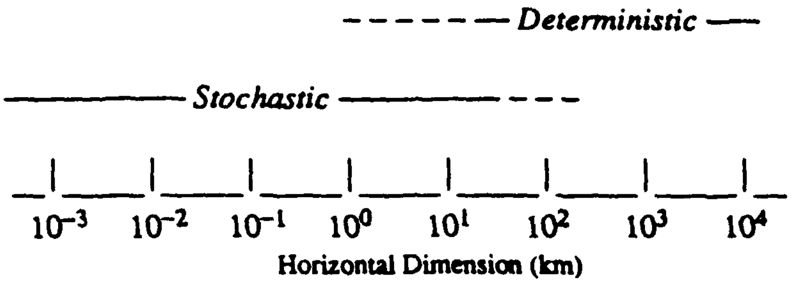
Deterministic
Stochastic
10^{-3}
10^{-2}
10^{-1}
10^{0}
10^{1}
10^{2}
10^{3}
10^{4}
Horizontal Dimension (km)

Figure 1.1. Range of horizontal spatial scales usefully described by deterministic and stochastic representations of seafloor morphology.

CHAPTER 2

INVERSION OF SEA BEAM DATA FOR SECOND ORDER STATISTICS

INTRODUCTION

> "In applications, the abstract mathematical models serve as tools, and different models can describe the same empirical situation. The manner in which mathematical theories are applied does not depend on preconceived ideas; it is a purposeful technique depending on, and changing with experience."
>
> *William Feller* (1906-1970)
> *An Introduction to Probability Theory and Its Applications*, vol. 1, 1968

In this chapter we propose a method for modeling the second-order statistics of seafloor morphology - a tool, in Feller's words, for quantitatively describing our empirical observations. This methodology is a first step, and as we gain experience in stochastically modeling the seafloor we expect to modify the model and its applications. This work is, to a large extent, exploratory, as we seek to understand the abilities and limitations of a new tool of our own fashioning.

The methodology presented here is tailored to the use of data collected by multibeam bathymetric devices such as Sea Beam. A recurring theme within this thesis is that if we are to understand seafloor morphology, statistical or otherwise, we must understand the way in which our bathymetric measuring device responds to or processes the seafloor; bathymetric data does not equal seafloor. The discussion is general enough, however, that other bathymetric devices can be used as long as their response to the seafloor is understood.

This chapter begins by introducing a homogeneous Gaussian model specified by an anisotropic two-point moment (covariance) function. The model has five parameters describing the topographic amplitude, orientation and characteristic scale lengths of topographic elongations (abyssal hills), and Hausdorff (fractal) dimension of seafloor roughness. We next formulate the forward problem of calculating the cross-covariance functions between the data recorded on two channels of a swath-mapping device from the covariance function of the seafloor, the system response, and the system noise characteristics. We then pose and solve the inverse problem of estimating the parameters of the seafloor covariance function given cross-correlation estimates derived from the multibeam data.

As an initial test of this methodology, we apply this procedure to five examples of Sea Beam transit data from the Pacific and Atlantic oceans. To assess how well the parameterization characterizes the statistical properties of the seafloor and the Sea Beam system, we generate synthetic Sea Beam data by a Fourier method from the Gaussian models and description of system noise and response, and compare the results with actual profiles.

SEAFLOOR TOPOGRAPHY AS A RANDOM FIELD

We begin by introducing the bathymetry function $b(\mathbf{x})$, defined to be the depth of the seafloor as a function of the coordinate vector $\mathbf{x}$, which ranges over a two-dimensional domain M. Represented on the map $\{b(\mathbf{x}) : \mathbf{x} \in \mathrm{M}\}$ will be the large-scale bathymetric signals associated with plate subsidence, major volcanoes, aseismic ridges, oceanic plateaus, abyssal plains, the larger fracture zones, etc., as well as small-scale features such as abyssal hills, small volcanic cones, lava flows, and sediment ponds. The former are few enough to be dealt with from a deterministic point of view, i.e., plate subsidence can be modeled by conductive cooling, and specific features can be individually described (and named), whereas the latter are numerous enough to be represented by their average, or ensemble, properties. The bathymetry function is thus partitioned into a deterministic part $b_0(\mathbf{x})$ and a stochastic part $h(\mathbf{x})$:

$$b(\mathbf{x}) = b_0(\mathbf{x}) + h(\mathbf{x}) \tag{2.2}$$

The small-scale seafloor topography is considered here to be a random field, generalizing $h(\mathbf{x})$ from a particular function to a two-dimensional stochastic process specified by a joint probability density function $p(h(\mathbf{x}_1),h(\mathbf{x}_2),\ldots : \mathbf{x}_1,\mathbf{x}_2,\ldots \in \mathrm{M})$.

The Problem of Statistical Heterogeneity

Stochastic modeling is a standard tool for describing deterministic complexity in the physical sciences, and it has a long history in geomorphology. In his discussion of coastlines, *Mandelbrot* [1983, p. 201] argues eloquently for a statistical approach:

> The goal of achieving a full description is hopeless, and should not even be entertained. In physics, for example the theory of Brownian motion, the key out of this difficulty lies in statistics. In geomorphology, statistics is even harder to avoid. Indeed, while the laws of mechanics affect molecular motion directly, they affect geomorphological patterns through many ill-explored intermediaries. Hence, even more than the physicist, the geomorphologist is compelled to forsake a precise description of reality and to use statistics.

Nevertheless, the notion of invoking a probabilistic model to describe a single well-defined, deterministic function, the actual topography of the seafloor, raises a certain level of metaphysical anxiety among some marine geologists. Some of the philosophical concern stems from an unfamiliarity with statistical methods, but at least part of it is rooted in the recognition of a fundamental difficulty that is often glossed over in statistical treatments of bathymetric data: For stochastic modeling to be practicable, the statistics of $h(\mathbf{x})$ must be approximated as being spatially homogeneous or stationary. This assumption is dubious to anyone familiar with the bathymetry of the deep-ocean basins, yet it is essential to workable algorithms for parameter estimation, including the one presented here.

Of course, a statistically homogeneous seafloor would be very dull indeed; spatial heterogeneity and the processes controlling it are precisely what we seek to study and understand. To employ idealized stochastic models in this context requires careful mathematical formulation and judicious data analysis.

The properties of $h(\mathbf{x})$ most easily recovered from observations are those specified by its low-order statistical moments. The expected value of the bathymetry is taken to be the reference surface $b_0(\mathbf{x})$, so that the topography $h(\mathbf{x})$ is defined to be a zero-mean process:

$$\langle h(\mathbf{x})\rangle = \int_{-\infty}^{\infty} h(\mathbf{x})\, p(h(\mathbf{x}))\, dh = 0 \tag{2.2}$$

Its higher-order properties are contained in the N-point moment functions

$$\begin{aligned} C_N(\mathbf{x}_1, \dots, \mathbf{x}_N) &= \langle h(\mathbf{x}_1) \dots h(\mathbf{x}_N)\rangle \\ &= \int_{-\infty}^{\infty}\!\!\dots\int_{-\infty}^{\infty} h_1 \dots h_N\, p(h_1, \dots, h_N)\, dh_1 \dots dh_N \end{aligned} \tag{2.3}$$

where $h_n = h(\mathbf{x}_n)$. When all of the coordinate indices are equal, the first through fourth moments are associated with the familiar names of mean, variance, skewness, and kurtosis, respectively.

The assumption of spatial homogeneity is equivalent to the statement that the N-point moments of seafloor topography are invariant with respect to spatial translation; that is,

$$C_N(\xi+\mathbf{x}_1, \dots, \xi+\mathbf{x}_N) = C_N(\mathbf{x}_1, \dots, \mathbf{x}_N) \tag{2.4}$$

Because of this translational symmetry we can invoke an ergodic hypothesis to identify spatial averages with ensemble averages [*Beran*, 1968]. In particular, for any fixed set $\{\mathbf{x}_n\}$ we can construct an unbiased estimator of the form

$$\tilde{C}_N(\mathbf{x}_1, \ldots, \mathbf{x}_N) = \frac{1}{A} \int_M h(\xi+\mathbf{x}_1) \ldots h(\xi+\mathbf{x}_N)\, dA(\xi) \qquad (2.5)$$

where the domain of integration M has an area A and is chosen so that $\xi+\mathbf{x}_n \in \mathrm{M}$ for all n.

The approach adopted in this chapter is to use (2.5) to retrieve the parameters of a spatially homogeneous statistical model. On the one hand, it is clearly advantageous for M to be as large as possible; as the area A gets larger, the uncertainties associated with the parameter estimates decrease, and the estimator in this equation converges to the true value of $C_N(\mathbf{x}_1, \ldots, \mathbf{x}_N)$. On the other hand, the domain M over which the empirical moments are computed must be consistent with the assumption of statistical homogeneity. Although this region can be chosen to exclude major topographic features such as fracture zones and large volcanoes, and it is possible to incorporate other nonstationary aspects of seafloor topography into the reference surface $b_0(\mathbf{x})$, the averaging area A is ultimately limited by the scale of statistical heterogeneity.

Hence, from a practical point of view, the type of stochastic modeling described here will be useful if we can identify a set of topographic domains $\{\mathrm{M}_k\}$ which satisfy two competing criteria:

1. To some order N_{max} the estimators $\{C_N\}$ computed from any set of subdomains in M_k (k fixed) are consistent with the same stochastic parameterization.

2. The sizes of the averaging areas A_k are sufficiently large that the stochastic parameters are determined with small enough uncertainties to be morphologically interesting.

In Chapter 3 we discuss the trade-off between spatial resolution of non-stationarity and resolution of the change in stochastic parameters from one averaging area to the next.

Second-Order Statistics

The stringency of these criteria increases rapidly with the maximum order of the statistical moments used in the parameter estimation, N_{max}. For most of this thesis we shall be content to explore the case where $N_{max} = 2$, the estimation problem for second-order statistics. Since the process $h(\mathbf{x})$ is defined to have zero mean, we are only concerned with its two-point moment, or covariance function. Translation symmetry allows us to write

$$C_{hh}(\mathbf{x}) \equiv C_2(\xi, \xi + \mathbf{x}) = \langle h(\xi)\, h(\xi + \mathbf{x}) \rangle \qquad (2.6)$$

Hence, for a stationary process, the covariance function depends only on the the spatial lag vector **x**, and its two-dimensional Fourier transform is the power spectrum [*Bracewell*, 1978]:

$$P_h(\mathbf{k}) = \int_{-\infty}^{\infty}\int_{-\infty}^{\infty} C_{hh}(\mathbf{x})\, e^{-i\,\mathbf{k}\cdot\mathbf{x}}\, d^2\mathbf{x} \qquad (2.7)$$

Both the covariance and the power spectrum are real-valued functions symmetric about the origin; e.g., $C_{hh}(-\mathbf{x}) = C_{hh}(\mathbf{x})$.

A Gaussian process is one completely specified by its first and second moments. If $h(\mathbf{x})$ is stationary and Gaussian with total topographic variance $H^2 \equiv C_{hh}(\mathbf{0})$, then the joint probability density function for $h_1 = h(\mathbf{x}_1)$ and $h_2 = h(\mathbf{x}_2)$ has the familiar form

$$p(h_1,h_2) = \frac{1}{2\pi H^2\sqrt{1-\rho_{hh}^2}} \exp -\left[\frac{h_1^2 - 2\rho_{hh}h_1h_2 + h_2^2}{2H^2(1-\rho_{hh}^2)}\right] \tag{2.8}$$

where $\rho_{hh} \equiv H^{-2}\,C_{hh}(\mathbf{x}_1-\mathbf{x}_2)$ is the correlation coefficient. In this case, the three-point moment vanishes, and the four-point moment is given by [*Beran,* 1968]

$$\begin{aligned} C_4(\mathbf{x}_1,\mathbf{x}_2,\mathbf{x}_3,\mathbf{x}_4) &= C_{hh}(\mathbf{x}_1-\mathbf{x}_2)\,C_{hh}(\mathbf{x}_3-\mathbf{x}_4) \\ &+ C_{hh}(\mathbf{x}_1-\mathbf{x}_3)\,C_{hh}(\mathbf{x}_2-\mathbf{x}_4) + C_{hh}(\mathbf{x}_1-\mathbf{x}_4)\,C_{hh}(\mathbf{x}_2-\mathbf{x}_3) \end{aligned} \tag{2.9}$$

It is worthwhile to stress at this point that the second-order statistics contained in the covariance function or power spectrum are insufficient to characterize many salient features of seafloor topography. Because the Gaussian density function given by (2.8) is unaffected by a change in the sign of h_1-h_2 or $\mathbf{x}_1-\mathbf{x}_2$, it cannot represent asymmetry about either a vertical or horizontal axis. To describe the slope asymmetry commonly associated with the tilting and rotation of fault blocks near the ridge crest [*Macdonald and Luyendyk,* 1977; *Schouten and Denham,* 1983], or vertical asymmetries due to sediment ponding requires moments out to at least third order, for example, whereas four-point moments are needed to represent a "boxy" or "peaky" appearance.

A Gaussian Model for Seafloor Topography

To formulate the forward and inverse problems for a multibeam echosounder, it is desired to have a covariance function $C_{hh}(\mathbf{x})$ specified by a small set of well-chosen geomorphic parameters. The second-order statistics of seafloor topography have been investigated by a number of authors using a variety of space domain [*Krause and Menard,* 1965; *McDonald and Katz,* 1969; *Yesyunin,* 1975] and spectral domain [*Neidell,* 1966;

Bell, 1975*b*, 1978; *Fox and Hayes,* 1985] techniques, but only a few have explored parameterized models. *Bell* [1975*b*] considered a power spectrum with the functional form

$$P_h(k) = \frac{F_0}{k^2 + k_0^2} \tag{2.10}$$

At large wave number ($k >> k_0$), this spectrum rolls off at the rate k^{-2}. *Fox and Hayes* [1985] argued that spectral slopes other than -2 are observed on bathymetric profiles; they fit their one-dimensional spectra to a two-parameter power law

$$P_h(k) = a^2 k^{-2b} \tag{2.11}$$

Although (2.11) generalizes (2.10) to an arbitrary asymptotic roll-off rate, it is clearly inadequate at low wave number, since extrapolating a power law too far in this direction leads to large values of topographic variance, in conflict with the overall flatness of the ocean bottom at long wavelength. Bell's parameterization (2.10) avoids this problem by having a corner k_0 that separates a "white" spectrum at low wave number from a "brown" spectrum at high wave number. On the bathymetric profiles examined by *Bell* [1978] the length scale k_0^{-1} corresponding to this transition is the characteristic dimension of the abyssal hills, whose amplitude tends to decrease with spreading rate.

Abyssal hills are topographic features created by vulcanism and block faulting at the ridge crests, and they tend to be elongated perpendicular to the direction of spreading. Any stochastic model describing such topography must therefore be anisotropic; i.e., the statistics along profiles must be allowed to vary with azimuth. Both *Bell* [1978] and *Fox and Hayes* [1985] investigated anisotropy by letting their one-dimensional spectral parameterizations vary with the orientation of the profile, but neither suggested an adequate two-dimensional model.

Before proceeding to generalize their parameterizations to two dimensions, it is instructive to examine the space domain properties of a one-dimensional random process whose spectrum is given by (2.10). Taking the inverse Fourier transform yields the exponential covariance function

$$C_{hh}(x) = H^2 e^{-k_0 |x|} \tag{2.12}$$

where $H^2 = F_0/2k_0$. The discontinuity in the derivative of C_{hh} at $x = 0$ implies that the variance of the random process, $dh(x)/dx$, is unbounded; $h(x)$ is continuous but not differentiable. In the terminology of *Mandelbrot* [1983], $h(x)$ is a random fractal of Hausdorff-Besicovitch dimension 3/2. (*Mandelbrot* [1983] equates the Hausdorff-Besicovitch dimension with the "fractal dimension," a term which has gained wide use. In this paper we refer to it by the more traditional "Hausdorff dimension") It is also a Markov process; in fact, it is the only one-dimensional Markov process that has stationary, Gaussian transition probabilities (the Ornstein-Uhlenbeck process) [*Feller,* 1971].

In two dimensions any dependence of the covariance function $C_{hh}(\mathbf{x})$ on azimuth gives rise to spatial anisotropy. We shall assume that the only azimuthal variation is through the dimensionless ellipsoidal (Riemannian) norm

$$r(\mathbf{x}) = \left[\mathbf{x}^{\mathrm{T}} \mathbf{Q}\, \mathbf{x}\right]^{1/2} = \sqrt{q_{11}x_1^2 + 2q_{12}x_1x_2 + q_{22}x_2^2} \tag{2.13}$$

where $\mathbf{Q}$ is a positive-definite, symmetric matrix whose Cartesian elements q_{ij} have dimensions of (length)$^{-2}$. $\mathbf{Q}$ can be expressed in terms of its ordered eigenvalues $k_n^2 \geq k_s^2$ and its normalized eigenvectors $\hat{\mathbf{e}}_n$ and $\hat{\mathbf{e}}_s$,

$$\mathbf{Q} = k_n^2\, \hat{\mathbf{e}}_n \hat{\mathbf{e}}_n^{\mathrm{T}} + k_s^2\, \hat{\mathbf{e}}_s \hat{\mathbf{e}}_s^{\mathrm{T}} \tag{2.14}$$

Since the eigenvectors are orthogonal ($\hat{\mathbf{e}}_n^{\mathrm{T}}\,\hat{\mathbf{e}}_s = 0$), they depend on only one orientation parameter, which is chosen to be the azimuth ζ_s of $\hat{\mathbf{e}}_s$, measured clockwise from north. This direction corresponds to the smaller characteristic wavenumber k_s. The characteristic values define an aspect ratio

$$a = k_n / k_s \tag{2.15}$$

which is unity in the case of an isotropic random field. In regions where $h(\mathbf{x})$ is dominated by abyssal hills, the angle ζ_s will generally be their average local strike, and a will be their average length-to-width ratio.

The most straightforward generalization of (2.12) to a two-dimensional field is

$$C_{hh}(\mathbf{x}) = H^2 e^{-r(\mathbf{x})} \tag{2.16}$$

The power spectrum obtained from this covariance function is

$$P_h(\mathbf{k}) = 2\pi H^2 \,|\mathbf{Q}|^{-1/2} \left[u^2(\mathbf{k}) + 1\right]^{-3/2} \tag{2.17}$$

where u is the dimensionless norm of $\mathbf{k}$ defined in terms of its modulus k and azimuth ζ by

$$u(\mathbf{k}) = \left[\mathbf{k}^{\mathrm{T}} \mathbf{Q}^{-1} \mathbf{k}\right]^{1/2} = \sqrt{(k/k_s)^2 \cos^2(\zeta - \zeta_s) + (k/k_n)^2 \sin^2(\zeta - \zeta_s)} \tag{2.18}$$

The covariance function for a profile with arbitrary orientation $\hat{\mathbf{e}}_p$ across a homogeneous, two-dimensional Gaussian field conforming to (2.16) is clearly an exponential of the form

(2.12) with $k_0^2 = \hat{e}_p^T Q\, \hat{e}_p$, and (2.17) is related to Bell's one-dimensional spectrum (2.10) by the integral [*Longuet-Higgins*, 1957]:

$$P_h(k') = \int_{-\infty}^{\infty} P_h(\mathbf{k})\, dl \qquad l \equiv (\,|\mathbf{k}|^2 - k'^2) \tag{2.19}$$

In the isotropic case where $k_n = k_s = k_0$, (2.19) reduces to an Abel transform [*Bracewell*, 1978]. Hence, an asymptotic roll-off rate of k'^{-2} in one dimension corresponds to a roll-off rate of k^{-3} in two. (In an appendix to his paper, *Bell* [1975*b*] discussed the extrapolation of (2.10) to a two-dimensional isotropic field, but his results contain a normalization error leading to an incorrect roll-off rate.)

Fox and Hayes's [1985] observation that seafloor spectra decay at different asymptotic rates provides motivation to generalize the covariance model (2.16) in the following way. We define the set of functions

$$G_\nu(r) = r^\nu K_\nu(r) \qquad 0 \le r < \infty \qquad \nu \in [0,1] \tag{2.20}$$

where K_ν is the modified Bessel function of order ν, and we let

$$C_{hh}(\mathbf{x}) = H^2\, G_\nu(r(\mathbf{x})) \,/\, G_\nu(0) \tag{2.21}$$

The mathematical properties of this covariance function and the two-dimensional Gaussian process it describes are discussed in Appendix A. The power spectrum of the process is

$$P_h(\mathbf{k}) = 4\pi \nu H^2\, |\mathbf{Q}|^{-1/2} [u^2(\mathbf{k}) + 1]^{-(\nu+1)} \tag{2.22}$$

The generalized model is thus one having a spectrum with an asymptotic roll-off rate equal to $-2(\nu + 1)$, and in the special case $\nu = 1/2$ its covariance reduces to the exponential form (2.16). Figure 2.1 shows the covariance functions and power spectra for several values of ν. It is demonstrated in Appendix A that the Hausdorff dimension of such a stochastic process is

$$\mathrm{D} = 3 - \nu \tag{2.23}$$

Hence, decreasing the parameter ν increases the roughness, with the limiting cases of unity and zero corresponding to a random field with continuous derivative (Euclidean surface, D = 2) and one which is "space-filling" (Peano surface, D = 3), respectively. All realizations of this covariance model are bounded self-affine fractal surfaces (see Appendix A), with the special case D = 2 corresponding to a bounded self-similar surface. Profiles across sample surfaces of various Hausdorff dimensions are illustrated in Figure 2.2.

It is also shown in Appendix A that a characteristic length λ_θ along a profile in the $\hat{\mathbf{e}}_\theta$ direction can be defined in terms of the second moment, or width of the covariance function in the same direction, which yields

$$\lambda_\theta = \frac{2\sqrt{2(\nu + 1/2)}}{k_\theta}, \quad k_\theta = \left[\hat{\mathbf{e}}_\theta^{\mathrm{T}}\, \mathbf{Q}\, \hat{\mathbf{e}}_\theta^{\mathrm{T}}\right]^{1/2} \tag{2.24}$$

where k_θ is the scale parameter in the $\hat{\mathbf{e}}_\theta$ direction. λ_n may be interpreted as being the characteristic abyssal hill width, and λ_s as the characteristic abyssal hill length.

INVERSION OF SEA BEAM DATA FOR SECOND-ORDER MODELS

The Gaussian model of seafloor topography formulated in the last section is specified by five parameters, the root-mean-square (rms) amplitude H, the lineation direction ζ_s, two characteristic scale parameters k_n and k_s, and the Hausdorff dimension D. We pose the following inverse problem: What values of these statistical parameters best describe an area of seafloor sampled by a swath of multibeam echo sounding data?

The particular echo sounding device that we shall consider is the Sea Beam system now installed on a number of research vessels [*Renard and Allenou,* 1979; *Farr,* 1980]. In the standard mode of Sea Beam operation, 12-kHz signals are generated by a transducer array mounted along the ship's keel, received by a hull-mounted array of hydrophones, and stacked into 16 athwartship beams, each with a half-power width of approximately 2.7°. At a ship speed of 18.5 km/h (10 knots) in deep water (~4 km), soundings are typically made once every 10 s, so that the along-track sampling interval (~50 m) is about 4 times smaller than the beam resolution and cross-track spacing (~190 m).

The inversion technique developed in this paper takes advantage of the dense along-track sampling to separate the seafloor signal from Sea Beam system noise. We illustrate the technique by applying it to five short profiles of Sea Beam transit data, four in the North Pacific and one in the North Atlantic (Figure 2.3). The profiles range from 145 to 210 km in length, and the average water depths from 3500 to 5600 m (Table 2.1).

Sea Beam System Response and Noise Characteristics

Most of the published work on the Sea Beam system response has concerned the recognition of artifacts that might distort bathymetric maps or be misinterpreted in terms of bathymetric features [e.g., *de Moustier and Kleinrock,* 1986]. To do statistical modeling, we need a more quantitative understanding of how Sea Beam data are affected by sampling density, finite beamwidth, and errors in echo detection and processing. The problem is intrinsically nonlinear in the sense that the response operator and noise levels of any echo sounding system depend on the amplitude and character of the bottom topography reflecting the acoustic signals. It is beyond the scope of this thesis to undertake a detailed treatment of the Sea Beam system response, which would require information from carefully designed experiments conducted at sea. Instead, we resort to a simplified, linear analysis.

Figure 2.4 shows a 22-km segment of swath 1 taken on the Papatua 11 cruise of the R/V *Thomas Washington* about 300 km south of the Aleutian Trench. In the upper panel, the "raw" (single-ping) soundings are plotted as 16 individual traces with a vertical exaggeration of about 8:1; time increases along the ship's track from left to right, and the beam numbers increase from port to starboard, with zero corresponding to the center beam. The long-wavelength variations lineated at an angle of about 35° to the profile are the abyssal hills (in this region the lineations run nearly east-west with north-south wavelengths of ~10 km), whereas the spiky ping-to-ping variations represent system noise. A standard display procedure is to smooth the data by a five-point running mean, decimate to an along-track interval approximately equal to the beam spacing (middle panel), and then contour these values to obtain a swath map (lower panel). The along-track averaging removes signals and noise with wavelengths less than the beam spacing and allows the interpolation across some of the smaller data gaps common on the outer beams.

Our approach is to avoid the smoothing, interpolation, and regridding of the bathymetric data employed by the contouring algorithms (as well as by most image-processing and spectral analysis procedures); instead, we deal directly with the raw soundings displayed in Figure 2.4*a*. From a signal-processing point of view, these are the discretized output of a noisy, band-limited, 16-channel "black box" whose input is $h(\mathbf{x})$. In this paper we assume that the response of the system is linear and the noise is additive. We represent the apparent topography on track p at time t by an equation of the form

$$s_p(t) = \int_{A_p} B_p(\mathbf{x},t)\, h(\mathbf{x})\, dA(\mathbf{x}) + n_p(t) \tag{2.25}$$

$B_p(\mathbf{x},t)$ is the effective response of the pth beam subtending an area $A_p(t)$, and $n_p(t)$ is the system noise.

We assume that the noise samples a stationary Gaussian process with zero mean, and that the beam pattern is independent of time; i.e., $B_p(\mathbf{x},t) = B_p(\mathbf{x} - \xi_p(t))$, where $\xi_p(t)$ is the center position of the beam. If the ship maintains a constant velocity $\mathbf{v}$, $s_p(t)$ will then be a zero-mean, stationary Gaussian process, and the statistical properties of the multichannel response $\{s_p(t)\}$ will be completely described by the auto- and cross-covariance functions

$$C_{pq}(t) \equiv \langle s_p(\tau)\, s_q(\tau + t)\rangle \tag{2.26}$$

The inverse problem thus reduces to determining the parameters of $C_{hh}(\mathbf{x})$ from estimates of $C_{pq}(t)$. (For notational simplicity, we will restrict our attention to the special case of constant ship velocity; generalizing to an arbitrary ship track is straightforward.)

To fix ideas, let us first consider an ideal multibeam echo sounder with no noise and infinite resolution: $n_p(t) = 0$, $B_p(\mathbf{x},t) = \delta(\mathbf{x} - \xi_p(t))$, where $\delta(\mathbf{x})$ is the Dirac delta function. We choose a coordinate system $\mathbf{x} = [x_1, x_2]$ such that the center beam along the (straight) ship track corresponds to the locus $\xi_0(t) = [vt, 0]$, where v is the (constant) ship speed. In general, the center position of the pth beam, ξ_p, is displaced perpendicular to the ship track by an amount $\Delta\xi_{p0} = -D \tan\phi_p$, where D is the water depth and ϕ_p is the beam angle relative to the vertical, measured positive to starboard (a convention that introduces the minus sign). It is then a simple matter to show that

$$C_{pq}(t) = C_{hh}(vt, \Delta\xi_{pq}) \tag{2.27}$$

where $\Delta\xi_{pq} = \Delta\xi_{p0} - \Delta\xi_{q0}$ (cf. (2.31)). Equation (2.27) says that the cross-covariance function between two beams is given by the intersection of the two-dimensional covariance function $C_{hh}(x_1, x_2)$ with a vertical plane parallel to the x_1 axis, a geometrical interpretation illustrated in Figure 2.5. If $p = q$, the vertical plane goes through the origin, yielding the symmetric autocovariance function C_{pp}. The amplitude of C_{pp} is proportional to H^2, and its properties near $t = 0$ determine the fractal dimension D. The decay rate of C_{pp} for large t fixes q_{11} in (2.13) but is independent of q_{12} and q_{22}. However, if $p \neq q$, the vertical plane is displaced by $\Delta\xi_{pq}$ in the x_2 direction, yielding a cross-covariance function whose shape depends on the entire **Q** matrix.

Generalizing these arguments, we see that in the idealized situation of perfect resolution and accuracy a combination of measurements made from the autocovariance function for one beam and the cross-covariance function between any two beams completely determines the five-parameter model.

What complicates this picture, of course, is the smoothing and noise introduced by any real echo sounding system, which modifies the relationship between C_{pq} and C_{hh}, as well as the fact that C_{pq} cannot be exactly determined from any finite sample of data. Any practicable algorithm for the inversion of estimates of C_{pq} to obtain the parameters of C_{hh} must take these effects into account. The net response of the Sea Beam system depends in a complicated way on the transducer array geometry, the pulse-shaping filters, and the algorithms for detecting signal returns and correcting for pitch, roll, and other environmental factors. Our simplistic model considers none of these complications explicitly, but parameterizes finite resolution of the Sea Beam system by a single number, $\delta\phi_{1/2}$, the half angle of a beam at its half-power point, which we assume to be independent of the beam number p as well as the azimuth about the beam axis.

If the width of this circular beam is small, its projection onto a flat seafloor is an ellipse centered at ξ_p with a (half-power) semiminor axis of length $\delta\phi_{1/2}D/\cos\phi_p$ in the fore-aft direction and a semimajor axis of length $\delta\phi_{1/2}D/\cos^2\phi_p$ athwartships. The response functions plotted by *de Moustier and Kleinrock* [1986, Figure 2] indicate that the main lobe of the beam pattern is well represented by a cosine-squared function with $\delta\phi_{1/2} = 1.33° = 0.023$ rad. We therefore approximate the response kernel by a Hanning taper of the form

$$\begin{aligned} B_p(x_1,x_2) &= \beta_p \cos^2 (\pi/2\, \psi_p(x_1,x_2)) \qquad & \psi_p \le 1 \\ B_p(x_1,x_2) &= 0 & \psi_p > 1 \end{aligned} \tag{2.28}$$

where

$$\psi_p(x_1,x_2) = \frac{2\Psi \cos \phi_p}{\pi\, \delta\phi_{1/2} D} \sqrt{x_1^2 + x_2^2 \cos^2 \phi_p} \tag{2.29}$$

$\Psi \equiv \arccos (1/2^{1/4}) = 0.5718...$, and β_p is a normalization constant chosen to make the kernel unimodular.

The signals put out by the beam-forming operations have a complex, highly variable structure consisting of the many individual arrivals (see *de Moustier and Kleinrock* [1986] for examples). Because of these variations the arrival times picked by the Sea Beam system exhibit fluctuations with rms amplitudes of 10–30 ms that are the chief source of the noise evident in the unsmoothed data of Figure 2.4*a*. The high-frequency character of this noise indicates that its autocorrelation falls off rapidly with lag time, consistent with it being generated by scattering from fine-scale features of the rough topography. Therefore, the cross correlation between the noise on different beams is expected to be small, and the covariance functions for the noise can be approximated by

$$\langle n_p(\tau)\, n_q(\tau + t)\rangle = N_p^2 \rho_{nn}(t)\, \delta_{pq} \tag{2.30}$$

where N_p is an rms amplitude, which may vary from beam to beam, and ρ_{nn} is a correlation function that decays rapidly from a value of unity at zero lag. Analysis of Sea Beam swaths supports these assumptions (see below).

To complete our model, we assume the cross correlation between the two terms on the right-hand side of (2.25) is small. Then, squaring this equation and averaging over the ensemble yields

$$C_{pq}(t) = \iint R_{pq}(x_1 - vt, x_2 - \Delta\xi_{pq})\, C_{hh}(x_1, x_2)\, dx_1\, dx_2 + N_p^2\, \rho_{nn}(t)\, \delta_{pq} \tag{2.31}$$

The integral kernel in (2.31) is defined by

$$R_{pq}(x_1, x_2) = \iint B_p(x_1', x_2')\, B_q(x_1' + x_1, x_2' + x_2)\, dx_1'\, dx_2' \tag{2.32}$$

The beam function given by (2.28) is nonzero only within a finite domain, which sets the limits of integration in (2.31) and (2.32). R_{pq} is non-negative, strongly peaked at the origin, and approaches the Dirac delta as $\delta\phi_{1/2} \rightarrow 0$.

The effects of system response and noise on an autocovariance function C_{pp} and its spectrum are schematically illustrated in Figure 2.6. Finite beam resolution smooths out the high-wave-number features of the bathymetry; it therefore rounds off the peak of the autocovariance at zero lag and rolls off the power spectrum at high frequencies. The noise adds a spike at the origin and a nearly constant level to the power spectrum, which dominates at high frequencies. If the characteristic wavelengths of the bathymetry are large compared to $\delta\phi_{1/2}D$ and we avoid using estimates of C_{pq} at small lag values, then we expect the impact of these effects on the estimation of H, ζ_s, k_n, and k_s to be relatively small. It is clear, however, that if they are ignored, any estimates of the fractal dimension D can be severely corrupted.

Estimates of Cross Covariances and their Uncertainties

Equation (2.31) represents the solution to the forward problem of computing the cross-covariance functions $\{C_{pq}\}$ for a multibeam echo sounder from the autocovariance function C_{hh} of statistically homogeneous seafloor. Of course, the cross-covariance functions $\{C_{pq}\}$ are not known; only estimates constructed from finite samples of data are available. In setting up the inverse problem we must account for the statistical variations imposed by the limited sampling.

It is presumed that the data are collected at a set of M equally spaced points $\{t_i = i\Delta t = i\Delta x/v$: $i = 1, 2, \ldots, M\}$. At the lag point j we shall employ the unbiased estimator

$$\tilde{C}_{pq}(j) = \frac{1}{M_j} \sum_{i=1}^{M_j} s_p(t_i)\, s_q(t_i + t_j) \qquad M_j = M - j \tag{2.33}$$

This estimator assumes that water depth and ship speed do not vary much about their mean values.

A typical example of an autocovariance estimate, in this case computed from beam -3 of swath 3, is displayed with its spectrum in Figure 2.7. As will be discussed in more detail later, the character of the seafloor topography along swath 3 is reasonably well matched by a Gaussian model with an approximately exponential correlation function (D ≈ 5/2). We have therefore superposed on the figure the theoretical autocovariance function (2.31) computed from the model (2.21) with an appropriate choice of parameters (Table 2.2). For reference we also display the theoretical values derived from (2.27), corresponding to an ideal echo sounder unmodified for Sea Beam system response and noise. Near zero lag, the comparison between theory and data is very good, both the theoretical and actual autocovariances showing the basic features sketched in Figure 2.6. The peak at zero lag is rounded by an amount consistent with a beam width expected in water of this depth (~5400 m), and a sharp noise spike is clearly evident. Near 0.6 cycle/km, the increased roll-off of the spectrum due to finite-beam smoothing becomes appreciable, and above 2 cycles/km, the spectrum flattens owing to system noise.

In this example and most others that we have observed, the noise spike comprises only the single, zero-lag sample point of the autocovariance estimate, and it is not observed at all on the cross-covariance estimates. These observations imply that the characteristic width of the correlation function $\rho_{nn}(t)$ is considerably less than the 10-s (~50 m) sample spacing. The large separation between the characteristic scales of the noise and seafloor topography allows us to estimate the noise power N_p^2 by the simple procedure of measuring the amplitude of the noise spike off the autocovariance plots. Figure 2.8 shows the results as a function of beam number for each of the five swaths listed in Table 2.1. In most cases the rms amplitude N_p is smallest for the center beam and increases with beam angle, as expected.

Away from zero lag, the estimated autocovariance initially decays like the model, but after a few kilometers it begins to deviate significantly, and at large lag (> 10 km) it begins to oscillate about zero with a wavelength $\sim 2k_0^{-1}$. This behavior is a manifestation of the estimation variance due to the finite length of profile, expressions for which we will now derive. The estimator is unbiased, since its expected value is

$$\langle \tilde{C}_{pq}(j) \rangle = \frac{1}{M_j} \sum_{i=1}^{M_j} \langle s_p(t_i)\, s_q(t_i + t_j) \rangle = \frac{1}{M_j} \sum_{i=1}^{M_j} C_{pq}(t_j) = C_{pq}(t_j) \qquad (2.34)$$

The variation of (2.33) about this mean is measured by the cross covariances

$$V_{pqrs}(j,l) \equiv \mathrm{Cov}\left[\tilde{C}_{pq}(j), \tilde{C}_{rs}(l)\right] = \langle \tilde{C}_{pq}(j)\, \tilde{C}_{rs}(l) \rangle - C_{pq}(t_j)\, C_{rs}(t_l) \qquad (2.35)$$

The expected value on the right-hand side of (2.35) involves the fourth moment of (2.25):

$$\langle \tilde{C}_{pq}(j)\, \tilde{C}_{rs}(l) \rangle \;=\; \frac{1}{M_j\, M_l} \sum_{i=1}^{M_j} \sum_{k=1}^{M_l} \langle s_p(t_i)\, s_q(t_i + t_j)\, s_r(t_k)\, s_s(t_k + t_l) \rangle \qquad (2.36)$$

Because $s_p(t)$ is Gaussian, the fourth moments can be related to products of second moments:

$$\langle s_p s_q s_r s_s \rangle \;=\; \langle s_p s_q \rangle \langle s_r s_s \rangle \;+\; \langle s_p s_r \rangle \langle s_q s_s \rangle \;+\; \langle s_p s_s \rangle \langle s_q s_r \rangle \qquad (2.37)$$

Substituting (2.37) into (2.36) and summing over the first term yield $C_{pq}(t_j)\, C_{rs}(t_l)$, which cancels the last term in (2.35). The remaining two terms give

$$V_{pqrs}(j,l) \;=\; \frac{1}{M_j\, M_l} \sum_{i=1}^{M_j} \sum_{k=1}^{M_l} \left[C_{pr}(t_{k-i})\, C_{qs}(t_{k-i+l-j}) + C_{ps}(t_{k-i+l})\, C_{qr}(t_{k-i-j}) \right] \qquad (2.38)$$

For fixed values of the lag indices j and l, the covariance between the estimates of C_{pq} and C_{rs} decreases as the square of the sample length M.

Because of the Fourier relationship (2.7) we could formulate the problem in the spectral domain, say by fast Fourier transforming segments of individual beams and stacking their products to obtain estimates of the power and cross spectra and then retransforming to get the autocovariance and cross-covariance functions. However, there are considerable practical advantages to computing these functions directly in the physical (space or time) domain. In particular, the data for the outer beams typically show a number of dropouts, which occur when noise bursts swamp the bottom returns (e.g., Figure 2.4), and these must be filled by some sort of interpolation algorithm before the Fast Fourier Transform

(FFT) can be applied. This operation requires a priori assumptions to be made regarding the statistical character of the seafloor, and it becomes difficult to assess the estimation uncertainties. On the other hand, the physical domain estimator (2.33) can be computed from the raw data simply by summing over the available points. As long as M_j is redefined to be the total number of points used for each lag, the covariance of the estimates given by (2.38) remains valid.

Inversion of the Cross-Covariance Functions for Model Parameters

We are now in a position to estimate the second-order statistics of the seafloor topography from a finite sample of multibeam echo sounding data. Since (2.31) specifies a linear relationship between the autocovariance function C_{hh} and the cross-covariance functions $\{C_{pq}\}$, it can be inverted by the Hilbert space methods of *Backus and Gilbert* [1970] and *Franklin* [1970]. At this early stage of investigation we avoid this functional analysis approach. Despite the considerable mathematical formalisms developed around such treatments, the results are difficult to assess: After deconvolving the Sea Beam response to get an estimate of the two-dimensional function C_{hh}, we are still stuck with the task of interpreting it in terms of quantities having more geological significance, yet another inverse problem.

Instead, we adopt a model of C_{hh} specified by the covariance (2.21), whose five parameters are well-defined morphological quantities. Our intent is to begin to test how well this model can represent the fine-scale topography of the deep oceans. Although not much Sea Beam data has yet been analyzed, even the limited sample examined here indicates that more elaborate parameterizations will prove useful. Some comments on how this might be accomplished are made in a later section.

The observables $\{C_{pq}\}$ are linear in the squared amplitude H^2, but they are nonlinear functions of the azimuth ζ_s, the two characteristic scale parameters k_n and k_s, and the Hausdorff dimension D. Therefore we solve the parameter estimation problem by the standard methodology of iterative, linearized, least squares minimization [e.g., *Bard*, 1974; *Menke*, 1984]. Our algorithm proceeds by the following steps:

1. $\{C_{pq}(j)\}$ are computed from (2.33) for all available points for all 16 beams up to lag values $j\Delta x \approx 20$ km. (Because $C_{pq} = C_{qp}$, only estimates for $p \geq q$ are made.)

2. Starting values for H, D, and the along-track scale parameter q_{11} are estimated by an eyeball fit to the autocovariance functions for the center beam. Noise spikes are measured from the zero-lag values of the autocovariances for all beams. Starting values for the orientation parameter ζ_s and the cross-track scale parameter q_{22} are obtained from the skewness and decay of the cross-correlation estimates.

3. The **Q** matrix is constructed and diagonalized to yield estimates of k_n and k_s. The estimation covariance matrix $V_{pqrs}(j,l)$ is computed.

4. Refined values H, ζ_s, k_n, k_s, and D are obtained by an iterative, weighted, least squares fit to $\{C_{pq}(j)\}$. The calculation requires the partial derivatives of $C_{pq}(j)$ with respect to the model parameters, which can be obtained analytically for all parameters. $V_{pqrs}(j,l)$ is recomputed at each iteration, and its inverse is used as a weighting matrix for the inversion.

5. Standard errors are obtained as the square roots of the diagonal elements of the parameter covariance matrix computed from the partial derivative matrix and $V_{pqrs}(j,l)$. We also calculate the off-diagonal elements, which specify the covariances between parameters.

Numerical experiments show that while the estimates of H and the parameters of the scale matrix **Q** are generally quite robust with respect to this procedure, the retrieval of the Hausdorff dimension D is often not. Specifically, estimation of D is corrupted by deviations from the idealized cross-track covariance model (2.38). The robustness of the algorithm can be strengthened and its convergence properties improved by sequencing step 4 in two parts.

4*a*. The preliminary values of H, q_{11}, and D are first refined using several dozen closely spaced points of each several autocovariance estimates $\{C_{pp}\}$.

4b. D is then fixed and the estimates of H, ζ_s, k_n, and k_s are revised by the inversion of a more widely spaced sampling of the autocovariance and cross-covariance estimates $\{C_{pq}\}$.

If necessary, the sequence is repeated.

The results for swath 1 are tabulated in Table 2.2 and illustrated in Figures 2.9 and 2.10. Figure 2.9 compares the autocovariance estimates from five beams with the model autocovariance function from (2.31). The average amplitude and shape of the sample curves are in good agreement with the model curve, especially near the origin where the estimation points are concentrated. In this case, the inversion of step *4a* yielded a reasonably well constrained value of the Hausdorff dimension: $D = 2.47 \pm 0.08$.

Figure 2.10 compares the autocovariance and cross-covariance estimates from five beams with model curves corresponding to the values of H, ζ_s, k_n, and k_s determined in step *4b*. The four average characteristics of the empirical curves that control the estimates of these quantities are (1) the mean height, (2) the move-out of the maxima with increasing beam separation, (3) the decay from the maxima with increasing lag, and (4) the decay of the maxima with increasing beam separation. The first constrains the rms amplitude H, and the remaining three jointly constrain the azimuth of elongation ζ_s and the scale parameters k_n and k_s. In the case of swath 1, which is the shortest profile among the five used in this study (only 146 km), H is determined to a 1-sigma precision of ± 15% and ζ_s to ± 3°, whereas the uncertainties in the estimates of k_n and k_s are proportionately much larger, ± 33% and ± 62%, respectively. The variations of the estimates about the model curves observed in Figures 2.9 and 2.10 are in good quantitative agreement with the fluctuations due to the finite length of the profile described by (2.38), giving us some confidence in the stochastic model.

The covariance of the errors can be readily calculated for any pair of parameter estimates not including D. The covariance between D and H or ζ_s is fairly small and can usually be ignored. Its coupling to the along-track scale parameter q_{11} can be significant, however. A larger value of D causes a greater rate of decay in the covariance (see Figure 2.1). The along-track data constrain the characteristic length (2.24) to be within a fairly narrow range, so that an overestimate of D will force an underestimate of the along-track wave number ${q_{11}}^{-1/2}$, and vice versa.

Another potential source of bias in estimating the Hausdorff dimension is the trade-off between D and the half beamwidth $\delta\phi_{1/2}$: The zero-lag peak of the autocovariance function can be made smoother either by decreasing the former or increasing the latter. In lieu of a more direct calibration of the Sea Beam system, we have adopted a linearized, time-invariant response function conforming to the nominal parameters of *de Moustier and Kleinrock* [1986]. An experimental program to collect such data would clearly enhance the accuracy of the inversion results.

The parameters obtained by inverting the five swaths of Table 2.1 are listed with their standard errors in Table 2.2. They represent a substantial range in stochastic character. The rms height H and the characteristic length λ_n vary by a factor of 4. Aspect ratios vary by a factor of almost 3, and Hausdorff dimension ranges from as low as 2.1 (swath 4) to as high as 2.6 (swath 3). Given such a range in stochastic character, the prospects for learning about geological processes from the mapping of these morphological parameters appear to be promising.

IMAGES OF THE SEAFLOOR SYNTHESIZED FROM THE STOCHASTIC MODEL

The zero-mean Gaussian model completely specifies the two-dimensional stochastic process representing fine-scale seafloor topography in terms of its autocovariance function $C_{hh}(\mathbf{x})$. Our model assumes that this function is adequately approximated by (2.21). Numerical realizations of the process can thus be computed from the parameters listed in Table 2.2; in other words, the data in Table 2.2 allow us to create "synthetic images" of the seafloor to arbitrary resolution and scale. Such images render the statistical character of the model to all orders, not just the two-point averages employed in the inversion. In particular, we can feed these images through the linearized response of the multichannel system and generate "Sea Beam synthetics" for comparison with the actual data, thereby providing a powerful method for the subjective assessment of all modeling assumptions.

Synthetic Seafloor Topography

To generate synthetic topography, we compute a Fourier spectrum on a regularly spaced wave number grid by multiplying the square root of the power spectrum (2.22) by a phase factor exp $(i\phi)$, where ϕ is a random number uniformly distributed on the interval $[0, 2\pi)$ [*Priestly*, 1981]. The space domain image is then obtained from a two-dimensional, fast Fourier transform. (The algorithm is complicated somewhat by the care that must be taken to avoid aliasing and other numerical sampling effects, given finite computing resources.) Appendix B provides some examples of this algorithm and a discussion of aliasing. Appendix B also describes a nesting algorithm, which allows us to stochastically interpolate a section of topography. By nesting we can display a synthetic realizations to arbitrary resolution.

Comparison of Sea Beam Synthetics with Real Data

The procedure we use to calculate Sea Beam synthetics is illustrated in Figure 2.11: (*a*) synthetic topography is generated from the estimated model parameters by the Fourier method, (*b*) the response function (2.28) is convolved with the topography to obtain the beam values on a rectangular grid approximating the Sea Beam sample points, (*c*) Gaussian white noise is added with an rms value appropriate to the system noise observed on each beam, and (*d*) data are dropped at random to match the observed dropout rate.

Figure 2.12 compares 5 hours of data from swath 1 with 5 hours of synthetically generated data. System noise has been suppressed by smoothing both the actual data and the synthetic with a five-ping running average. A seamount has been edited from the former, causing the data gap between 0230 and 0300, whereas the synthetic does not include any data drops. The overall comparison is quite favorable; the rms height, the topographic orientation, and the scale length in the $\hat{\mathbf{e}}_n$ direction appear to be matched within the estimation uncertainties. The agreement in scale length in the $\hat{\mathbf{e}}_s$ is difficult to gauge, although it does appear to be slightly underestimated in the synthetics. This difficulty is not surprising considering the large formal uncertainty (± 60%) on the estimate of λ_s. These large uncertainties are predominantly a result of the generally poor sampling of the longer-wavelength properties of the seafloor in the $\hat{\mathbf{e}}_s$ direction. The agreement in Hausdorff dimension is also difficult to gauge, but it does appear that the high-wave-number characteristics on both synthetic and data are very similar.

Figure 2.13 is a more detailed comparison between actual and synthetic data for swath 1. The upper panels of each set are 1-hour samples, whereas the lower panels show the results of subtracting a five-ping running mean from each beam. This stripping operation is a high-pass filter that brings out some features of the noise not accounted for by the model. In particular, the noise is neither stationary nor uncorrelated between beams, as the model assumes. High-amplitude, high-wave-number energy appears in the form of noise spikes appearing across the swath at discrete times or as noise bursts associated with scattering from topographic scarps. Clearly, a more sophisticated model for noise is needed to match these observations.

Swath 2, located in the North Pacific between the Mendicino and Pioneer fracture zones, is the most lineated in our data set ($a = 6.1$), and it has the smallest characteristic length ($\lambda_n = 4$ km). Because of the very short width of the autocovariance functions computed for individual beams the trade-off between the Sea Beam response function and the Hausdorff dimension is exceptionally strong. Hence, we chose to fix D at a nominal value of 2.5 in step 4*b* of the inversion procedure. The overall comparison between real and synthetic data, shown in Figure 2.14, is as good as for any of the other swaths. However, the valleys in the real data tend to be flattened relative to the peaks, which is presumably an effect of sediment ponding. This behavior cannot be replicated by a Gaussian model.

Swath 3 is located south and east of swath 2 across the Pioneer fracture zone (see Figure 2.3). Despite their proximity, there are resolvable differences in the statistical character of the seafloor sampled by the two swaths, primarily in their aspect ratio, which decreases by almost a factor of 2. Although a visual comparison confirms the existence of systematic differences, the 5-hour sample of swath 3 in Figure 2.15 displays some apparent nonstationarity. The regions centered near 1130 and 1300 appear to be smoother than adjacent areas, and this character is not matched by the synthetic. We suspect that the net effect of the nonstationarity might to bias the scale lengths to smaller values, which could account for some of the differences in the cross-track scale estimates for swaths 2 and 3.

Swath 4 is located in the Cretaceous quite zone on crust approximately twice as old as that imaged by swaths 2 and 3, and the sediment cover is nearly twice as thick (~200 m), which acts to smooth the topographic profiles. Because sedimentation preferentially fills in the high-wave-number features, the value of Hausdorff dimension recovered by the inversion is the lowest of the Pacific regions sampled in this study. Although the data-synthetic comparison in Figure 2.16 appears to be fairly good, the amplitudes are low, and subtle differences are harder to spot. Again, one difference is the existence of "flat spots" in the data not contained in the synthetics.

On the balance, however, we are impressed by the general success of the second-order model in matching the statistical character of the Pacific data we have examined thus far. The agreement suggests that the parameters in our Gaussian model are capable of representing the first-order features of Pacific seafloor morphology at scale lengths less than a few tens of kilometers.

The same cannot be said for swath 5, collected in the North Atlantic. The comparison between real and synthetic data (Figure 2.17) is obviously poor. Although the rms height, orientation, and aspect ratio of the small-scale topography are reasonably well fit, the overall statistical character of the seafloor is quite different from that given by the second-order model. First, the data exhibit a strong periodic behavior, which would require the power spectrum to be peaked and the covariance function to oscillate between positive and negative values. Generalizing the form of C_{hh} to allow for a stronger periodicity would improve the agreement. It is also clear that the jaggedness and asymmetry of the peaks caused by faulting, as well as the flatness of the valleys caused by differential sedimentation, will require the use of non-Gaussian statistics. Extending the space-domain forward modeling and inversion procedures developed in this study to the analysis of higher-order correlation functions is one approach to the problem.

CONCLUSIONS

In this chapter we have developed a method for estimating stochastic parameters of the seafloor from Sea Beam transit data that accounts for the finite precision, resolution and sampling of the multibeam echo sounding system. In this initial work we have restricted our attention to the recovery of second-order statistics, although the space domain methods developed here can be generalized to higher-order analysis. The seafloor is modeled as a stationary, zero-mean, Gaussian random field completely specified by its covariance function. The parameterized form of the covariance function given by (2.21) is employed which generalizes expressions used by previous authors. The five independent parameters of this second-order model specify the rms height and characteristic scale of the topography, the orientation and aspect ratio of its anisotropy, and its decay with increasing wave number. Using a linear approximation to the echo sounder response, we have solved the forward problem relating the second-order model to the along-track autocovariance functions of individual beams and cross-covariance functions between beams of arbitrary separation. The finite beam width, precision and sampling of the multibeam echosounder is explicitly included in our space-domain formulation. Proceeding from this forward problem, we have obtained estimates of model parameters from a linearized, least squares inversion of the Sea Beam autocovariance and cross-covariance data.

We have developed a Fourier method for generating numerical realizations of the stochastic topography, allowing the creation images of arbitrary resolution and scale using the parameters derived from inversion of Sea Beam data. Such images render the statistical character of the model to all orders, not just the two-point averages employed in the inversion. By feeding these images through the linearized response of the multichannel system, we have been able to generate "Sea Beam synthetics" for comparison with the actual data. Such synthetics provide a powerful method for assessing all of the modeling assumptions.

The synthetic-data comparisons show that the procedures described above generally yield good first-order stochastic descriptions of seafloor morphology. We are therefore confident that they can be used to map important geomorphic characteristics and study the geological processes that shape the seafloor. However, the comparisons also show that more complex analysis will be necessary to map other geologically significant characteristics. First, the periodicity exhibited by swath 5 indicates that the covariance function used in this case does not provide a very good approximation and generalizing its form may be necessary. This could be done by a more complex parameterization or by a direct inversion for C_{hh} as a function of spatial lag. Second, characteristics such as sediment ponding and abyssal-hill tilting will require the use of non-Gaussian statistical descriptions. One possibility is to extend this analysis to the recovery of higher-order correlation functions. Finally, nonstationarity appears to exist in some cases with scale lengths less than the length of record needed for resolving statistical parameters. In such cases the parameter estimation tends to be biased toward smaller scale lengths. Incorporating nonstationary behavior into the stochastic description is an important problem for future consideration.

The stochastic model allows us to go beyond the constraints of the echo sounding system. Generating synthetic topography to fine scales from estimated stochastic parameters thus represent extrapolations of the observed lower-wave-number power-law behavior into the high-wave-number domain. This is a simple procedure mathematically, but whether or not such extrapolations are physically valid is still an unanswered question. It is likely, for example, that the large-scale behavior of surface faulting cannot be extrapolated to small-scale faulting; i.e., there may exist a minimum scale below which surface faulting does not occur. On the other hand, it is easy to envisage volcanic extrusives producing features down to the smallest measurable scales. This question is important to the field of acoustic seafloor scattering (as well as marine geology), which requires a knowledge of seafloor roughness characteristics at scales much smaller than Sea Beam resolution. Answering this question will require the coordinated measurement of seafloor bathymetry using instruments of differing resolution.

Fine-tuning our stochastic description of the seafloor will require improvements in the statistical model of Sea Beam response and noise. Both represent very interesting problems in seafloor acoustics. To refine our analysis of Sea Beam response, we must be able to model the nonlinear relationship between a stochastic seafloor and a narrow-beam echo sounding. To obtain a more adequate description of the noise, we need to model its correlation with topography.

TABLE 2.1. Sea Beam Data Used in Second-Order Analysis

Data Set	Cruise	Ship	Starting Date	Starting Time	Starting Latitude, deg N	Starting Longitude, deg E	Length of data, hours	Length of data, km	Number of Data Points	Average Water Depth, m	Sediment Cover, km	Reference
1	Papatua 11	*Thomas Washington*	Aug. 10, 1986	0000	47.63	−177.26	6.5[b]	146[b]	2293	5645	0.1[a]	P. Londsdale
2	Papatua 11	*Thomas Washington*	Aug. 15, 1986	1000	39.11	−143.98	8.75[b]	169[b]	2830	5317	0.1[a]	P. Londsdale
3	Papatua 11	*Thomas Washington*	Aug. 16, 1986	1000	37.30	−138.75	8.5[b]	173[b]	3238	5359	0.1[a]	P. Londsdale
4	2610	*Robert Conrad*	Sep. 4, 1985	0400	22.87	−174.00	11.25[b]	210[b]	5379	5194	0.2[a]	S. Shore
5	2509	*Robert Conrad*	July 30, 1984	0300	46.41	−30.15	10.0	199	5347	3544	0.1-0.5	J. E. Miller

[a] Sediment thicknesses taken from *Ludwig and Houtz* [1979].

[b] Excluding data which was omitted from use in cross-covariance estimation.

TABLE 2.2. Statistical Parameters Derived From Inversion

Data	H, m	ζ_s, deg	k_n, km^{-1}	λ_n, km	k_s, km^{-1}	λ_s, km	a	D
1	54 ± 8	93 ± 3	0.36 ± 0.12	8	0.08 ± 0.05	36	4.5	2.47 ± 0.08
2	82 ± 5	349 ± 2	0.67 ± 0.16	4	0.11 ± 0.03	26	6.1	2.5[a]
3	66 ± 4	356 ± 4	0.41 ± 0.10	7	0.12 ± 0.04	23	3.4	2.55 ± 0.10
4	31 ± 4	160 ± 7	0.22 ± 0.05	15	0.08 ± 0.03	41	2.8	2.13 ± 0.07
5	126 ± 14	174 ± 4	0.28 ± 0.07	11	0.12 ± 0.03	27	2.3	2.22 ± 0.07

[a] Hausdorff dimension fixed in inversion.

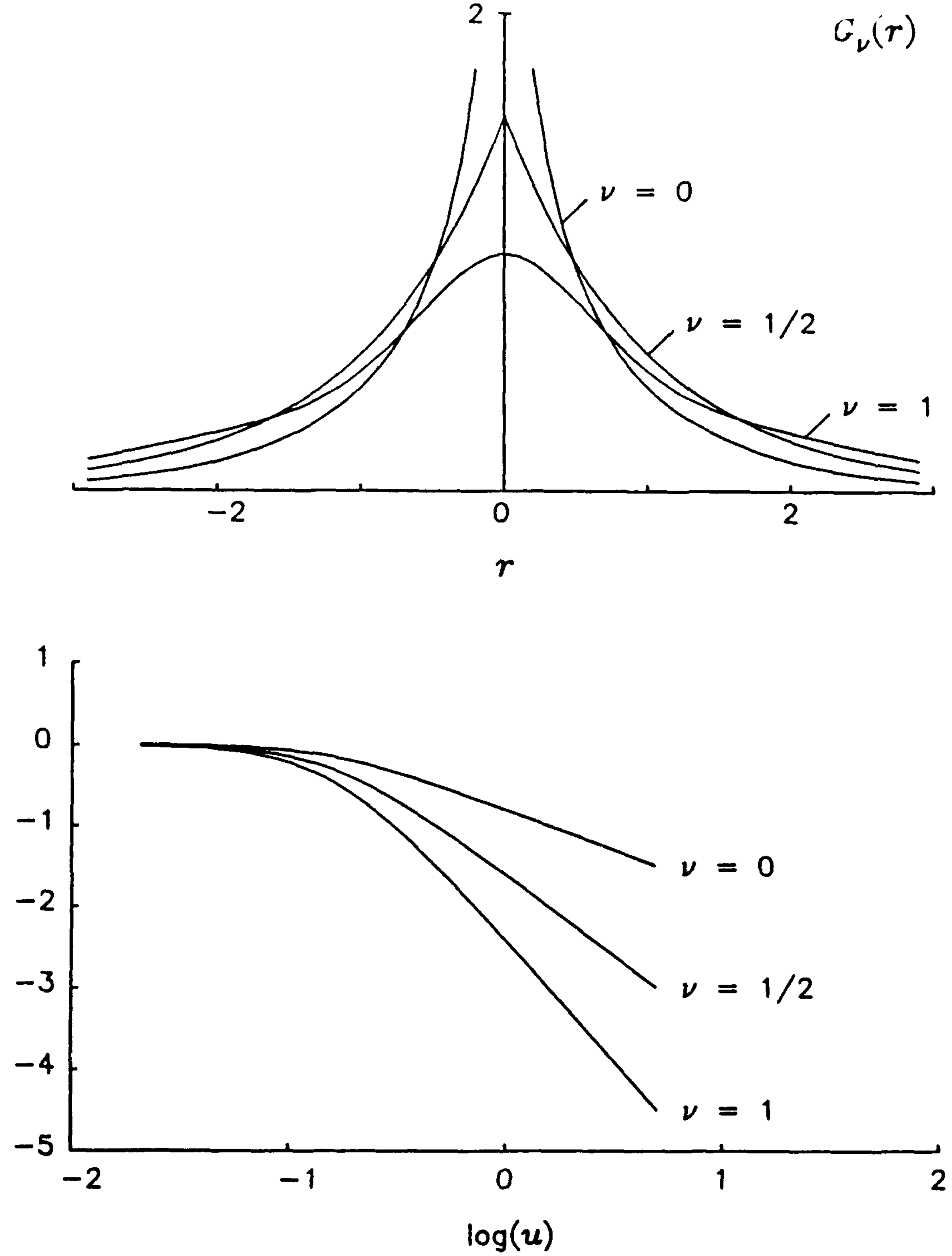

Figure 2.1. Functional form of the model covariance function, $G_\nu(r)$, plotted for values of $\nu = 0$, 1/2, and 1 (top panel), and their normalized Fourier transforms plotted in log-log space.

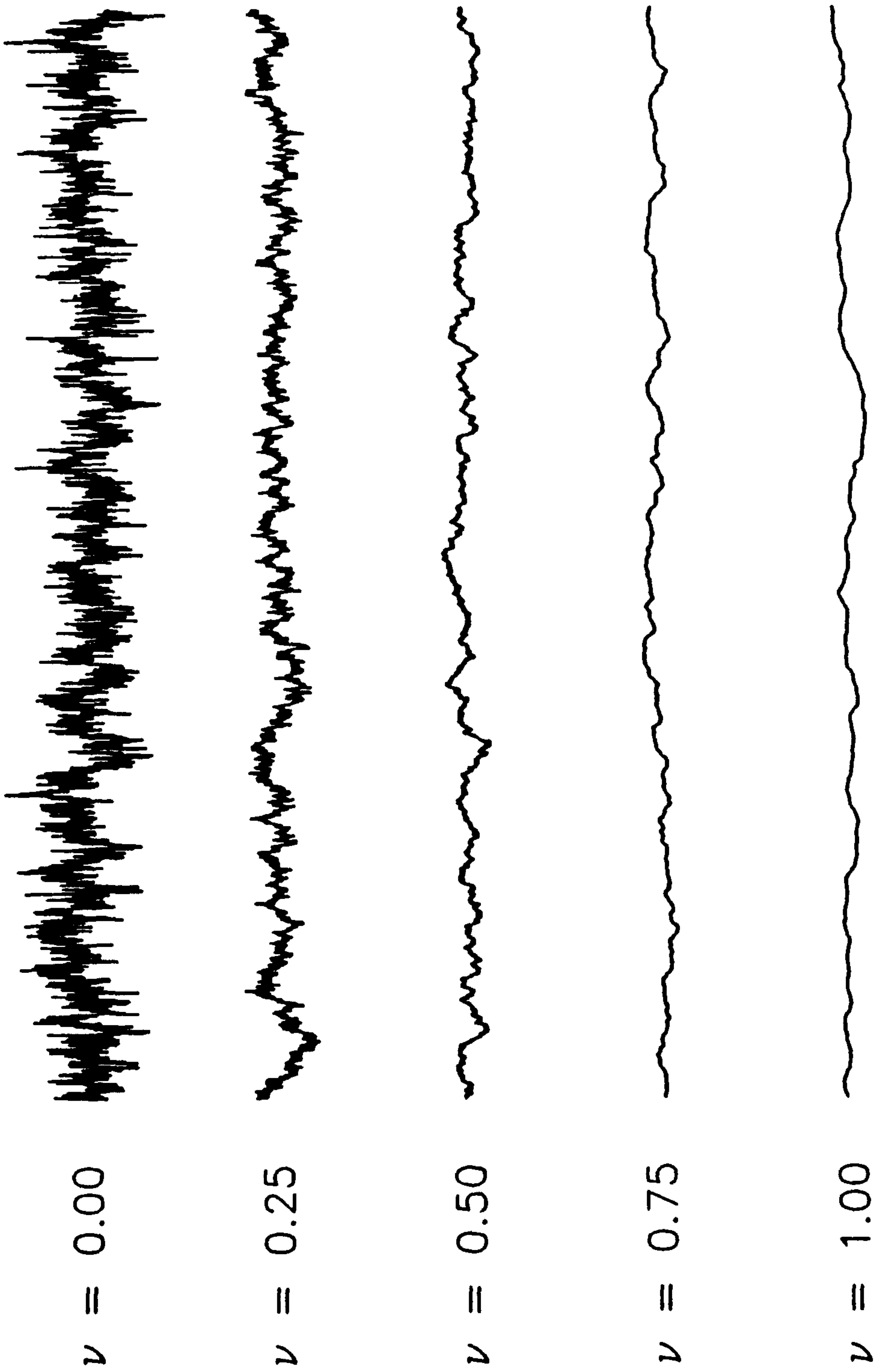

Figure 2.2. Profiles of sample surfaces generated from the model covariance function (1.21) for five values of ν. The Hausdorff dimension of each surface is $D = 3 - \nu$, and for each profile $D = 2 - \nu$. Each profile is drawn from 5000 sampled points.

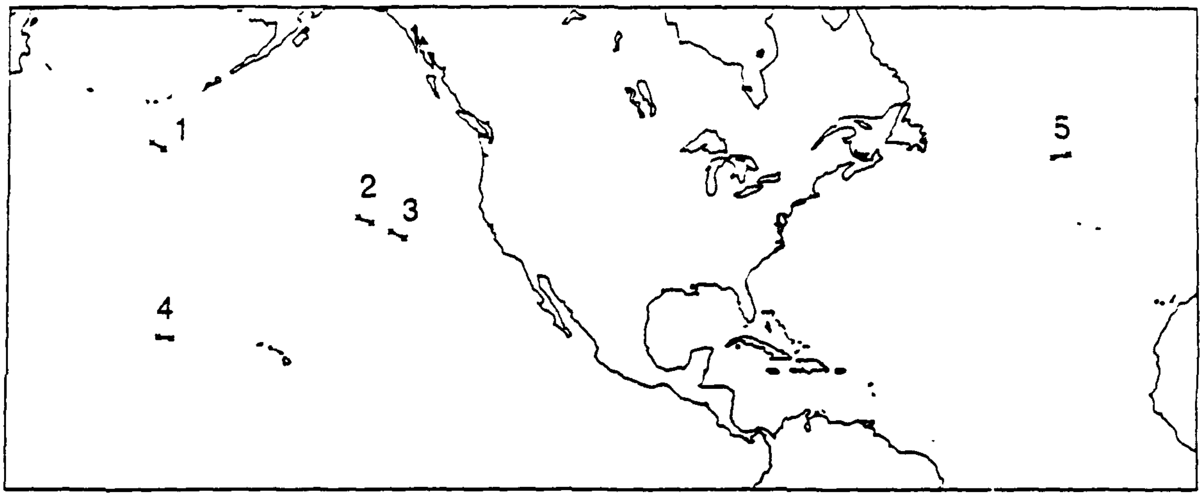

Figure 2.3. Geographic positions of the five swaths listed in Table 2.1. Crosses mark starting and stopping points for each data set.

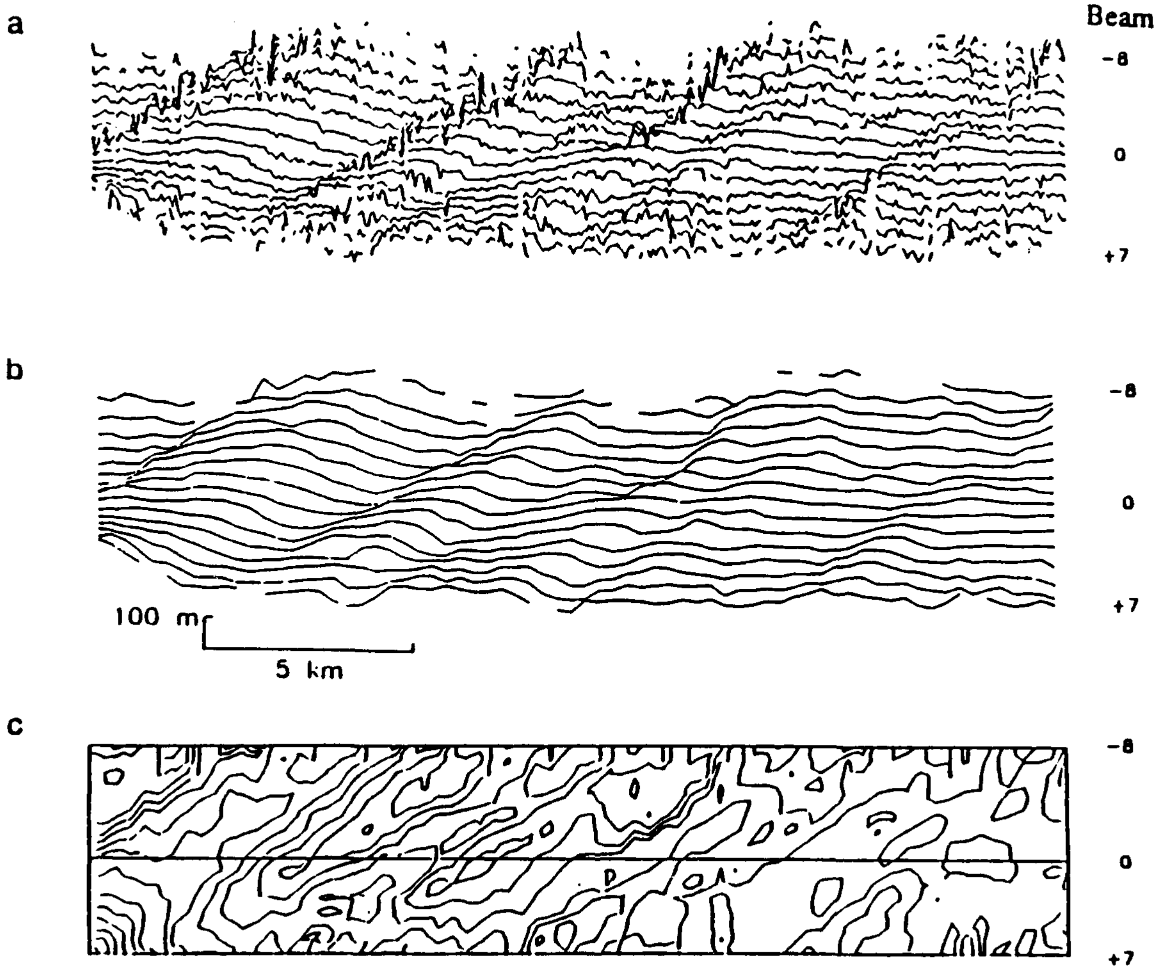

Figure 2.4. One hour record of Sea Beam data from swath 1 plotted (*a*) in raw form, with depth recorded by each beam plotted continuously as a function of track distance, (*b*) as a 5-ping averaging of the raw data, and (*c*) as a 20 m contour plot of the 5-ping averaged data. Forward ship direction is left-to-right. Gaps in Figure 5*a* indicate dropped data.

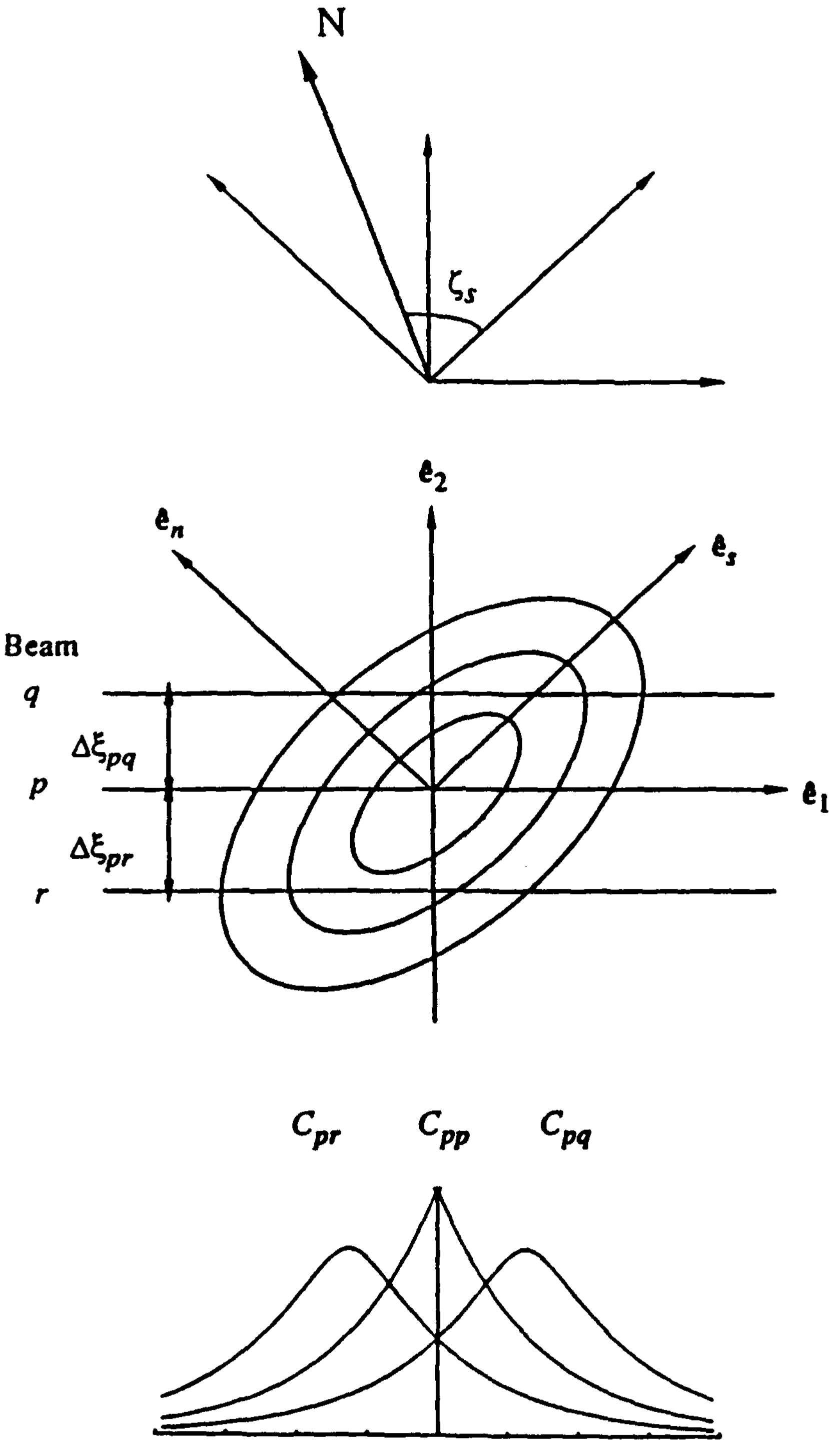
N
ζ_s
$\hat{\mathbf{e}}_2$
$\hat{\mathbf{e}}_n$
$\hat{\mathbf{e}}_s$
Beam
q
$\Delta\xi_{pq}$
p
$\Delta\xi_{pr}$
r
$\hat{\mathbf{e}}_1$
C_{pr}
C_{pp}
C_{pq}

Figure 2.5. Geometric illustration of (2.27) and the coordinate representation. Concentric ellipses (center figure) represent contours of the covariance function $C_{hh}(\mathbf{x})$, with principle axes $\hat{\mathbf{e}}_n$ and $\hat{\mathbf{e}}_s$ as shown. ζ_s is the angle between North and $\hat{\mathbf{e}}_s$, measured clockwise (top figure). Ship coordinates $\hat{\mathbf{e}}_1$ and $\hat{\mathbf{e}}_2$ are the along- and across-track directions, respectively. With the autocovariance function centered on the p beam, the parallel beams q, p, and r, separated by distances of $\Delta\xi_{qp}$ and $\Delta\xi_{pr}$ as shown, trace cross sections of the covariance function which form the cross-covariance functions C_{pq}, C_{pp}, and C_{pr} respectively (bottom figure).

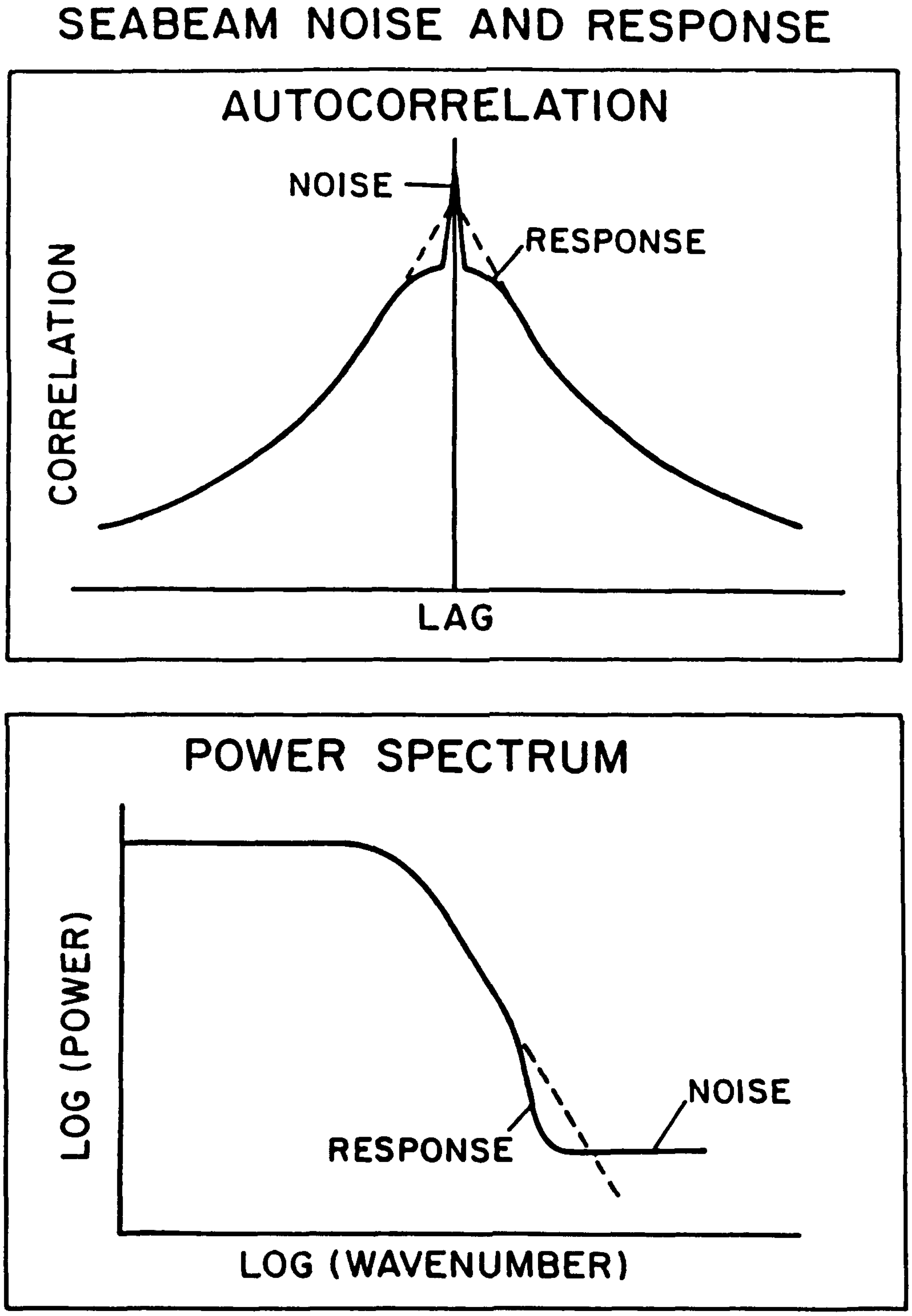
SEABEAM NOISE AND RESPONSE
AUTOCORRELATION
NOISE
RESPONSE
CORRELATION
LAG
POWER SPECTRUM
LOG (POWER)
NOISE
RESPONSE
LOG (WAVENUMBER)

Figure 2.6. Illustration of the effects of a linear response and white noise on the autocovariance function and the power spectrum of a single beam of Sea Beam data. Unaffected curves, representing the perfect echo sounder assumption, are shown in dashed lines for comparison.

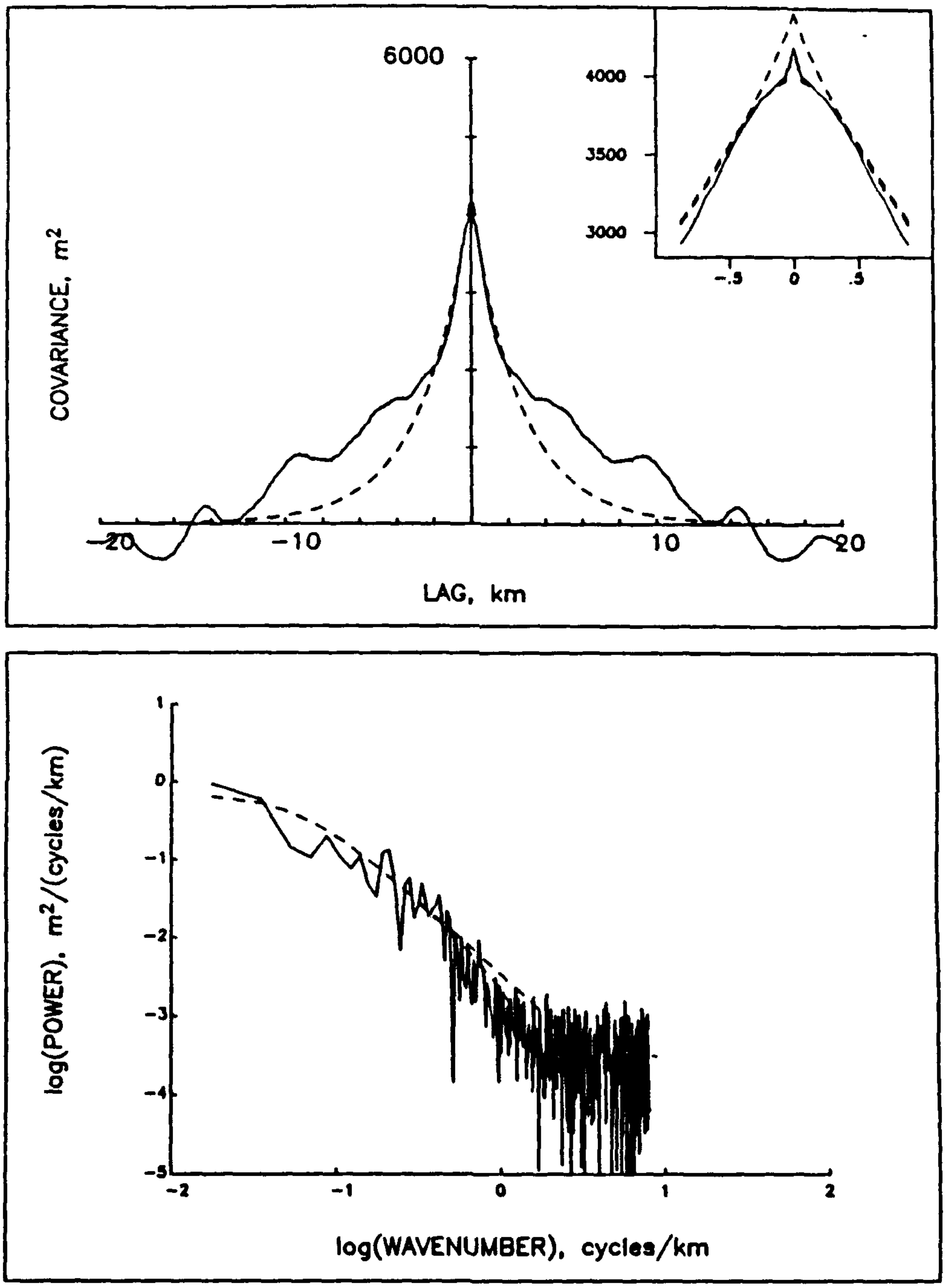

Figure 2.7. Comparison of autocovariance (with insert showing enlargement of origin) and power spectrum estimates calculated from beam -3 of swath 3 (solid curves) with model curves (dashed) generated from (2.31) and its Fourier transform respectively. Two model curves are plotted, using (top) the perfect echosounder assumption, and (bottom) Sea Beam response and noise parameters appropriate to this beam (compare Figure 7). The parameters used to generate model curves are listed in Table 2.3 for swath 3.

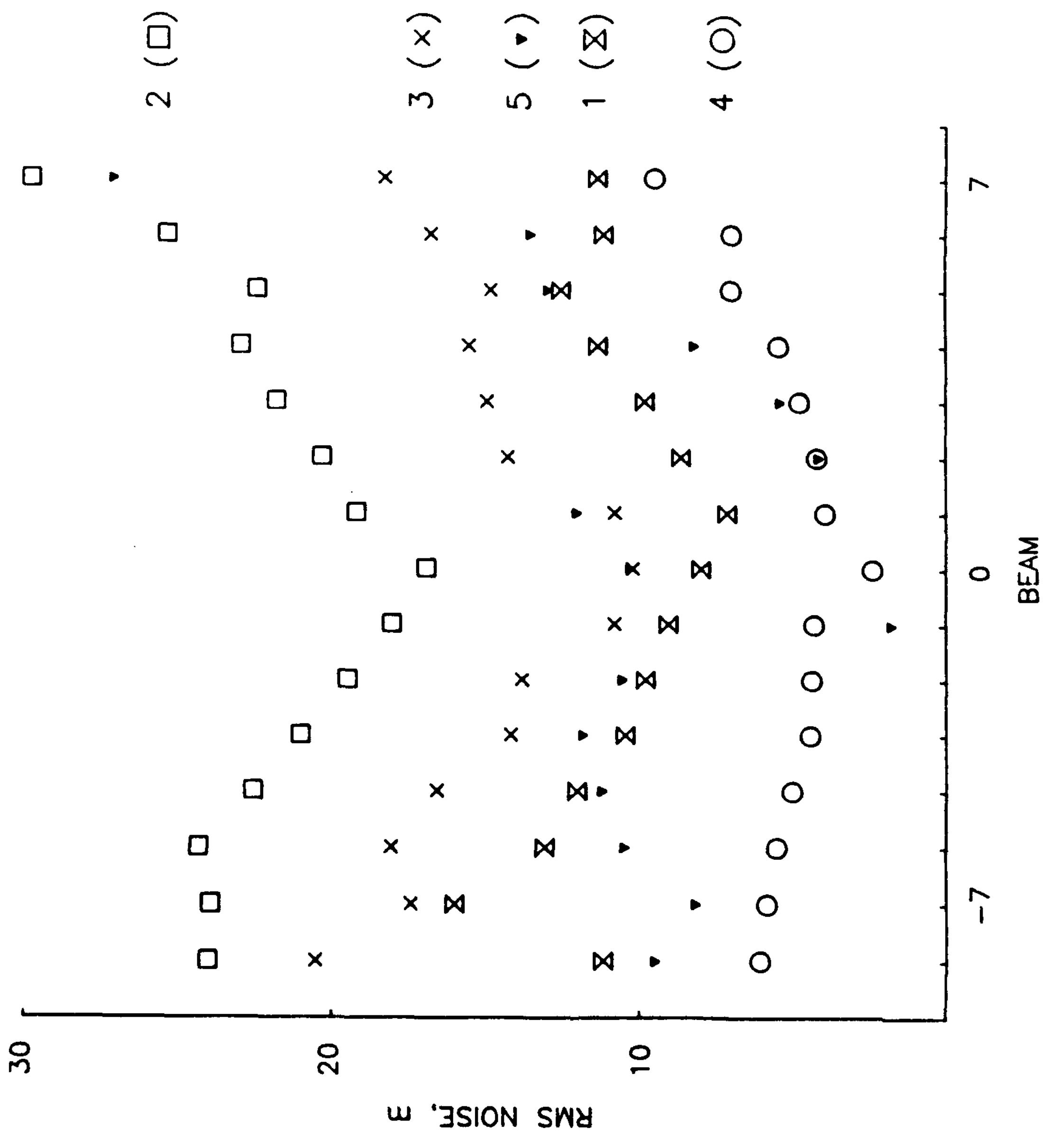

Figure 2.8. Rms noise versus beam number for each of the five Sea Beam swaths listed in Table 2.1. Rms noise for each beam is assumed to be the square root of the difference between the zeroth and first lag of the autocovariance estimation.

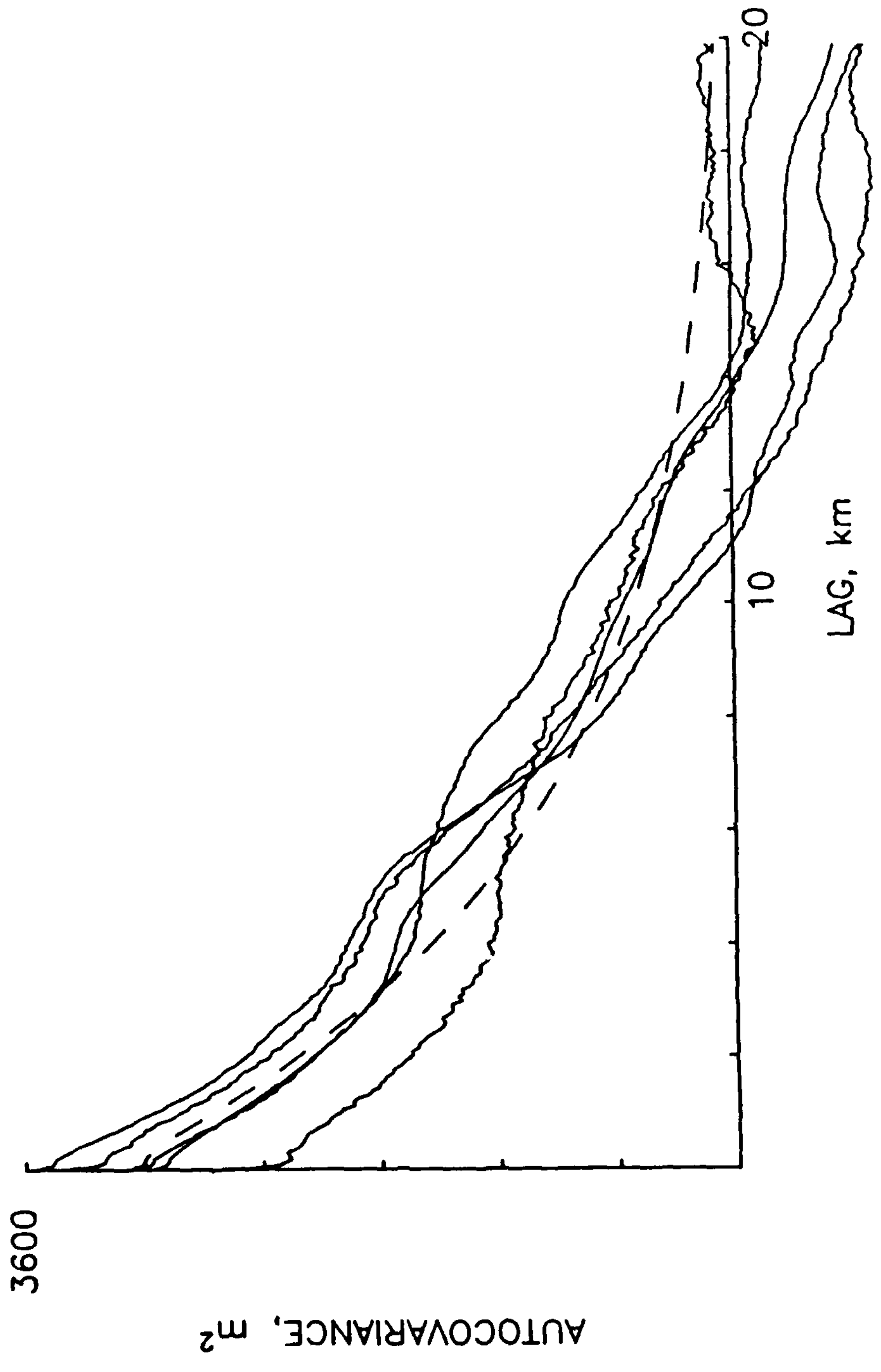

Figure 2.9. Comparison of autocovariance estimates for beams -6, -3, 0, 2, and 5 (solid curves, positive lag only) from swath 1 with the autocovariance model (dashed curve) generated from parameters obtained using step *4a* of the inversion procedure. The rms value of the noise spike added to the origin of the model curve was measured from the autocovariance estimate for the center beam.

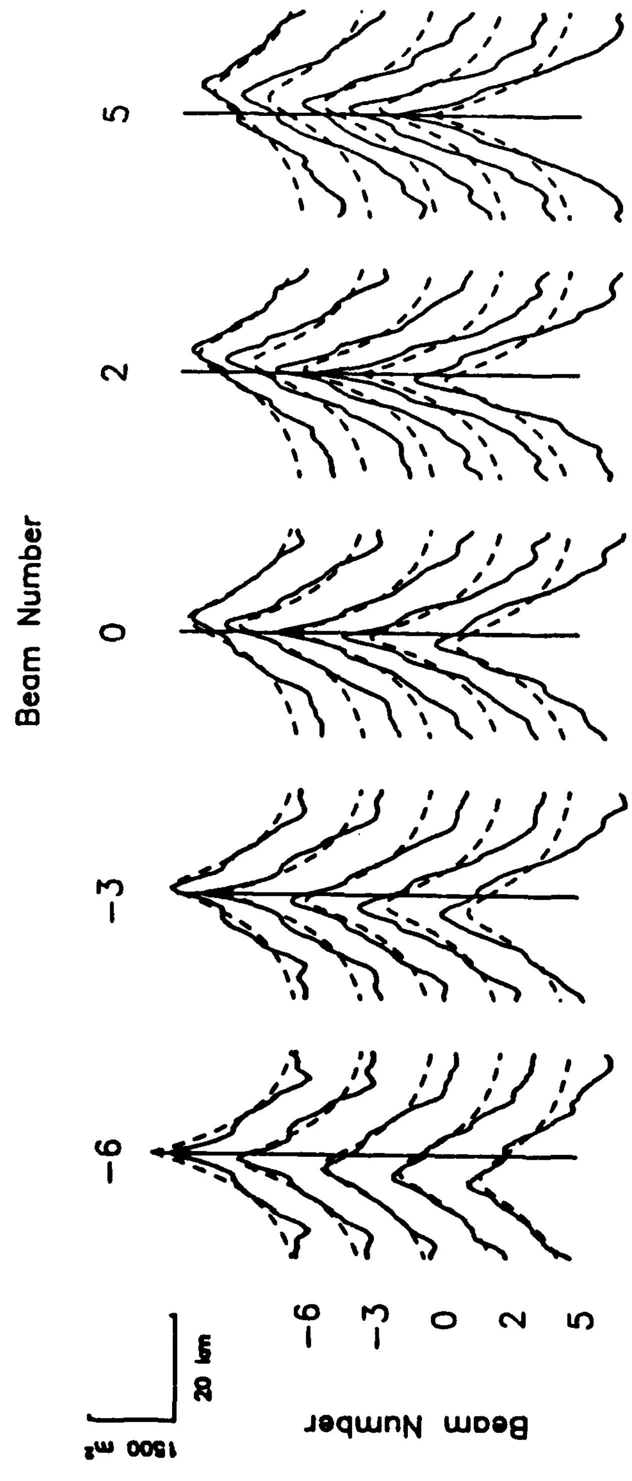

Figure 2.10. Comparison of cross-covariance estimates for swath 1 (solid curves), for beams numbered above and to the left, with cross-covariance model curves (dashed) generated from parameters (Table 2.2) obtained using step 4*b* of the inversion procedure. Vertical lines mark zero lag.

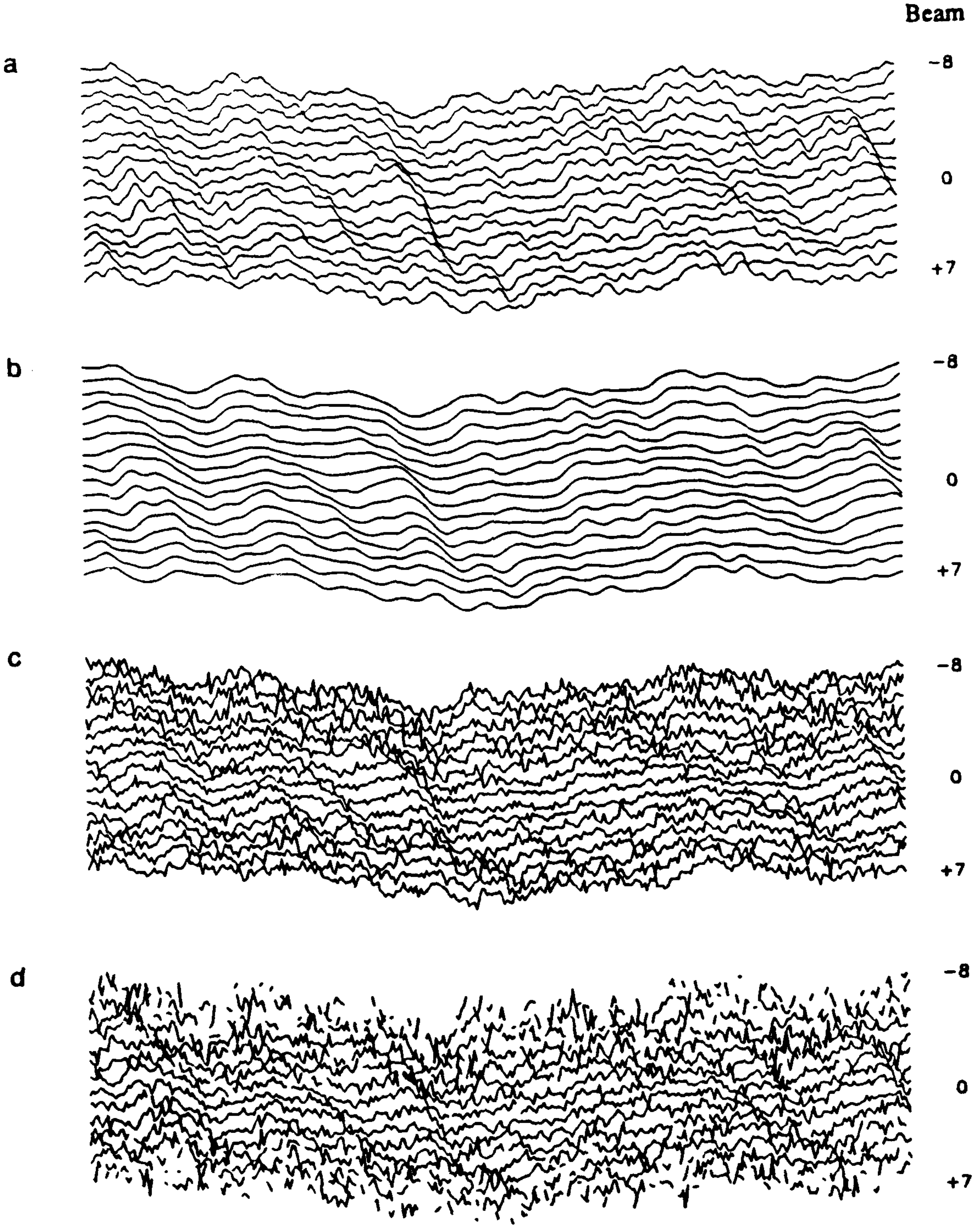

Figure 2.11. Steps involved in generating synthetic Sea Beam data: (*a*) a synthetic topographic surface is generated from the estimated model parameters by the Fourier method, (*b*) the response function is convolved with the topography to obtain the beam values on a rectangular grid approximating Sea Beam points, (*c*) a Gaussian white noise is added with an rms value appropriate to the system noise observed on each beam, and (*d*) data are dropped at random to match the observed dropout rate.

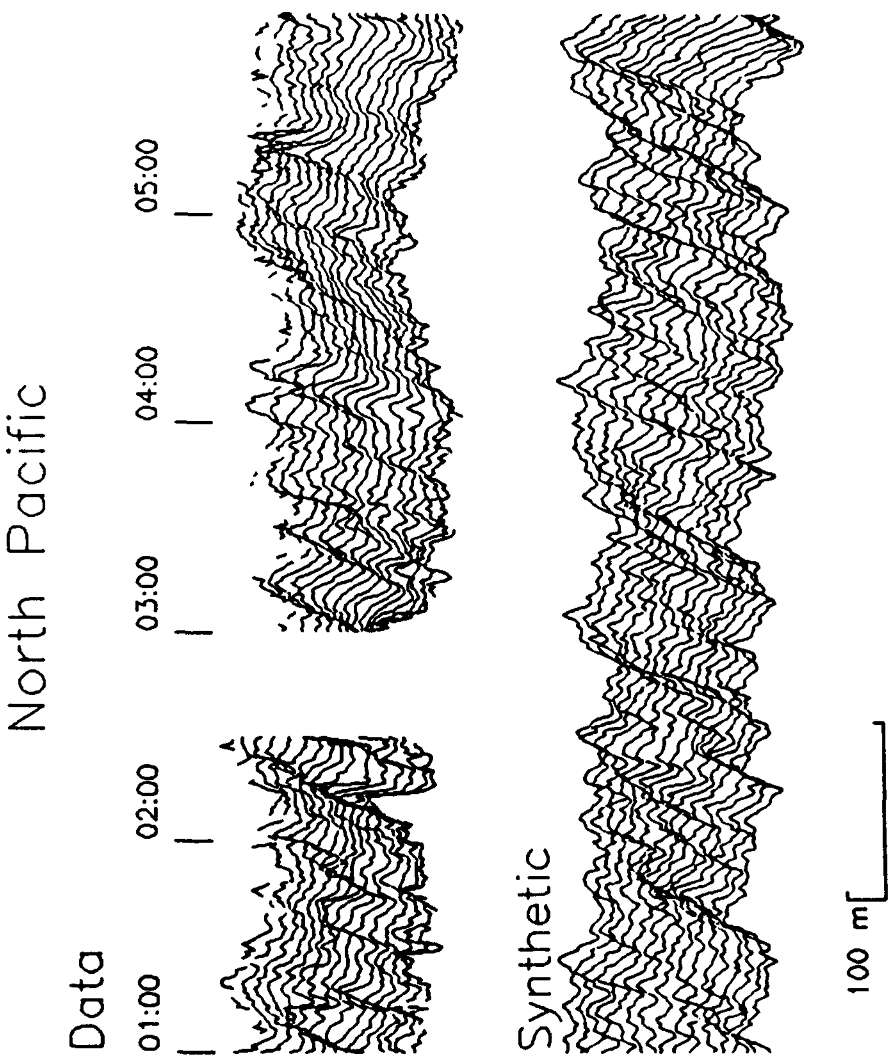

Figure 2.12. Comparison of 5 hours of 5-ping averaged data from swath 1 to 5 hours of 5-ping averaged synthetic data. The synthetic data were generated using the covariance model and rms noise values obtained from swath 1. Data drops were not included. The large gap in the real data between 0230 and 0300 hours is the location of a seamount that was deleted from consideration in the calculation of the cross-covariance estimates.

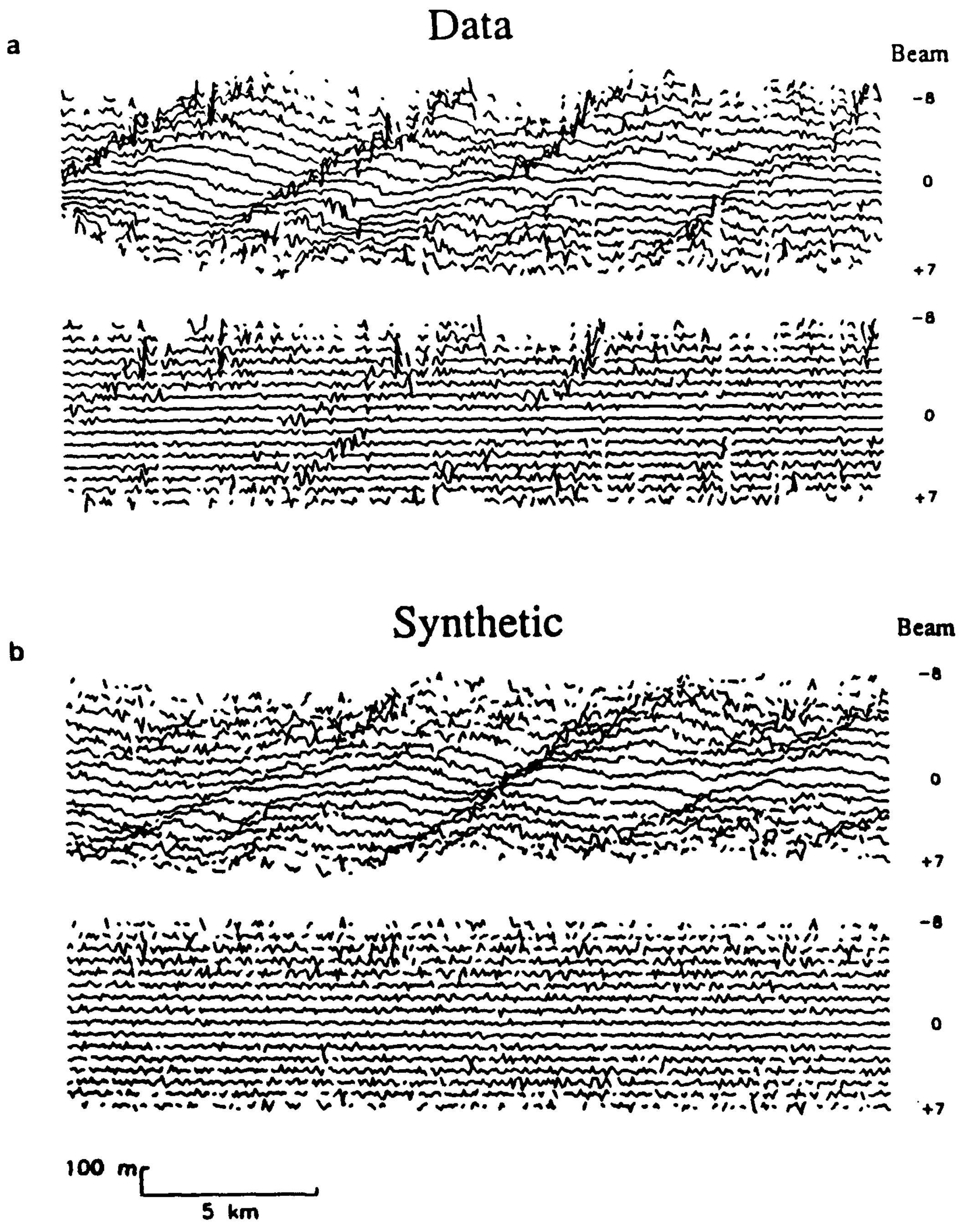

Figure 2.13. Comparison of 1 hour of raw data from swath 1 to 1 hour of synthetic data. The synthetic data were generated using the covariance model, rms noise, and drop values obtained from swath 1. Lower panels of each set show the result of subtracting a 5-point running mean from the data.

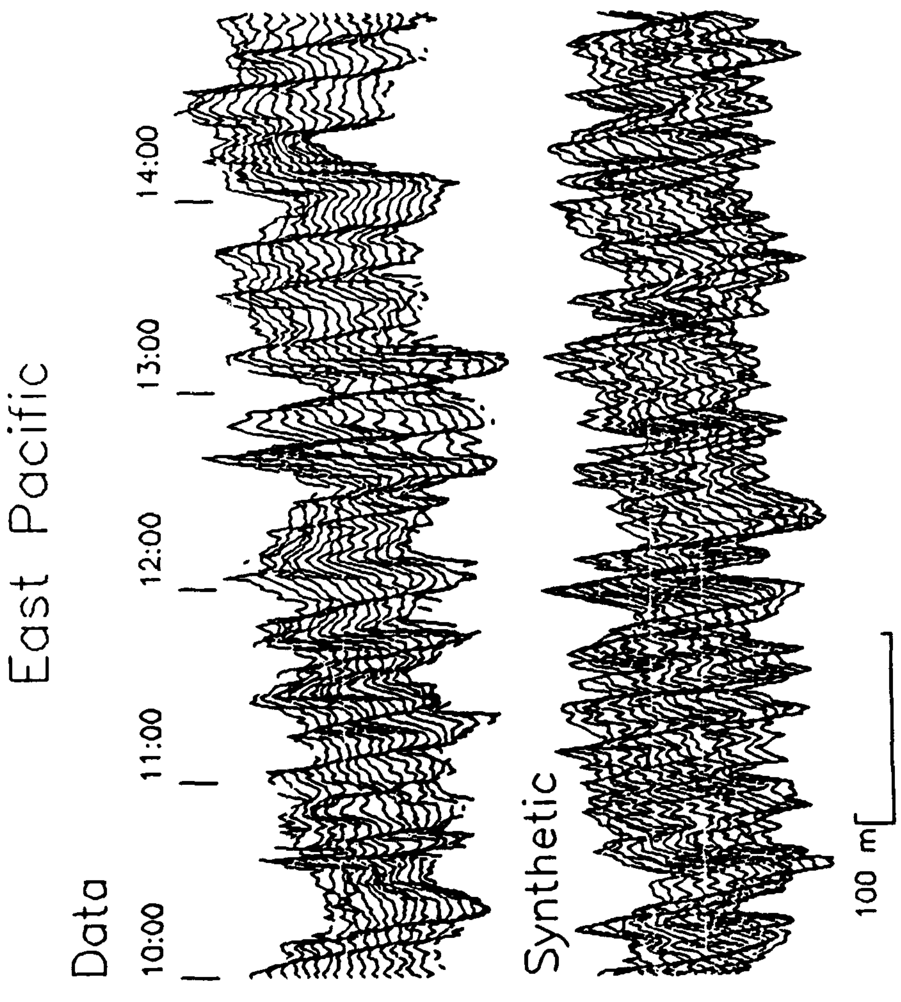

Figure 2.14. Same as Figure 2.12 for swath 2.

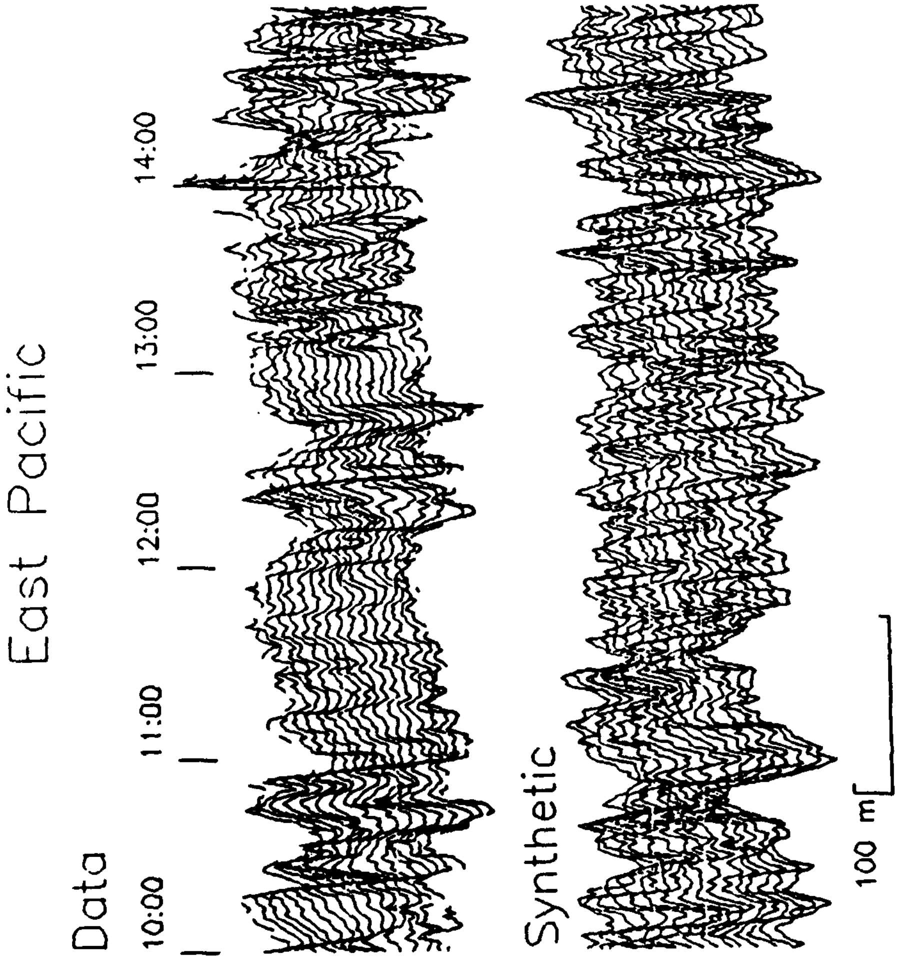

Figure 2.15. Same as Figure 2.12 for swath 3.

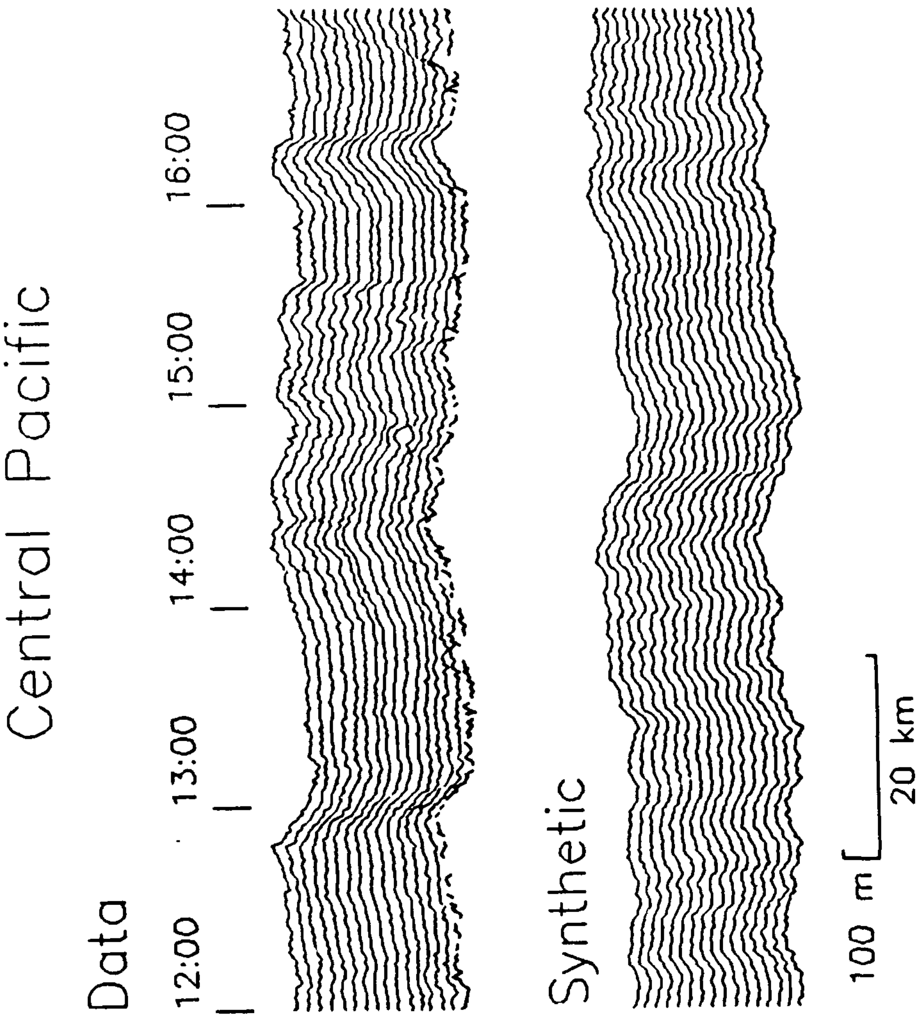

Figure 2.16. Same as Figure 2.12 for swath 4.

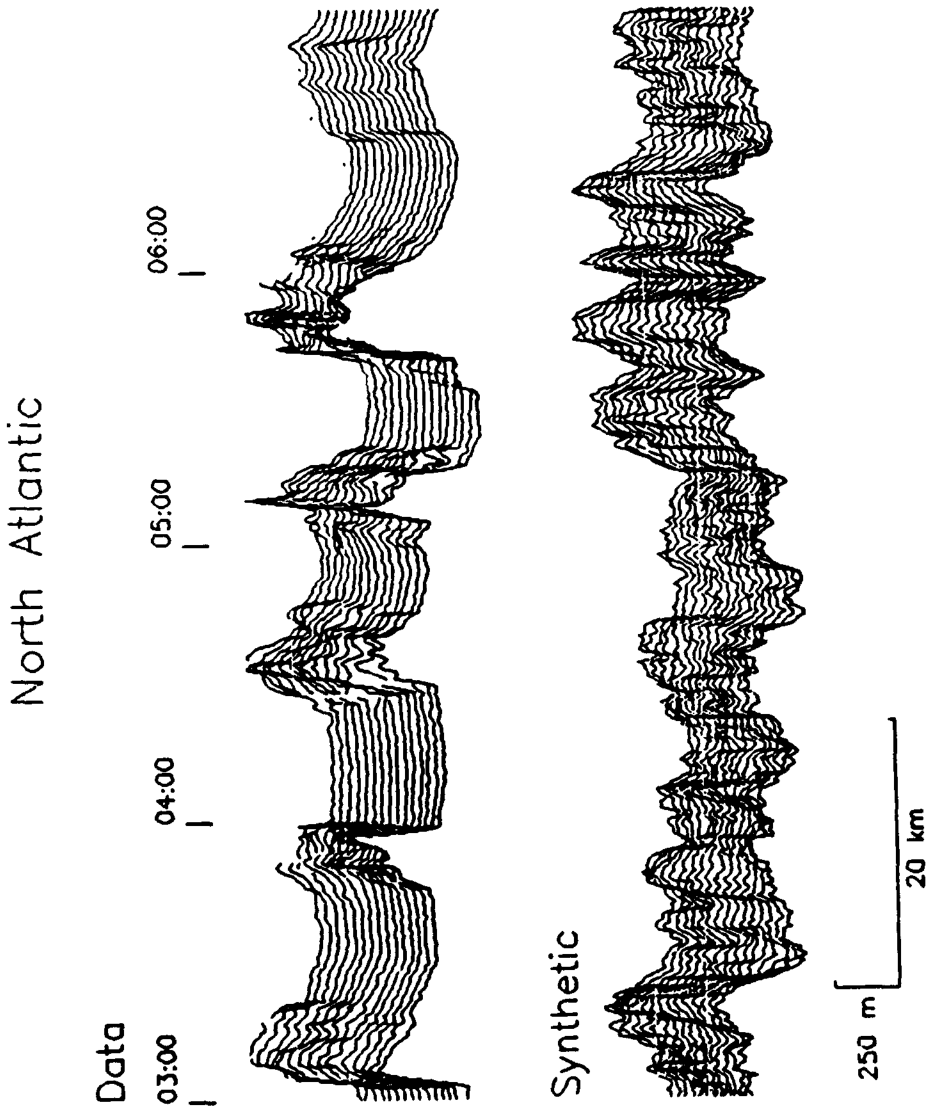

Figure 2.17. Same as Figure 2.12 for 4 hours of swath 5.

CHAPTER 3

RESOLUTION OF TOPOGRAPHIC PARAMETERS BY SEA BEAM DATA

INTRODUCTION

An inherent difficulty lies in any attempt to quantify stochastic observations: an estimate of a random parameter requires the averaging of many observations, and we can never be sure that our sample observations all have the same stochastic characteristics (stationary statistics). The stochastic character of the seafloor does change considerably (non-stationary statistics), and it is precisely the nature of this change that we wish to quantify; i.e. we would like to delineate stochastic provinces of the seafloor in order to identify acoustic domains and to relate the provinces to geologic variables such as spreading rate and age. It is therefore critical to address the question of how many data are needed to make a well-resolved stochastic characterization; i.e. when are the errors in the characterization sufficiently small to distinguish one terrain from another? This will tell us what the minimum scale is over which we can detect changes in stochastic behavior. We also must be content with our inability to detect changes at smaller scales.

Figure 3.1, showing 9 hours of Sea Beam data from the South Atlantic, is a clear example of a change in stochastic behavior: the topography before ~1700 hours is visually very different from the topography following that time. The clearest difference is that the amplitude of topographic variation is much greater after than it is before 1700 hours. What is the quantitative expression of this difference? We should expect that something so easily seen by the eye will be easily resolved by stochastic modeling. Are there other differences which are not obvious to the eye? How well resolved might these differences be given the quantity of data that we have? These are questions which must be addressed if we are to attempt to characterize seafloor terrains by stochastic methods.

In the last chapter we proposed a parameterized model for the stochastic description of the seafloor and developed a method for estimating these parameters from multibeam echosounding data such as derived from a Sea Beam system. In this chapter we explore in detail the resolution capabilities of this inversion as a function of ship variables such as track length, the orientation of the ship track with respect to the topographic grain, and finite beam-width response of the echosounder. The primary purpose of this study will be to assess the performance of the inversion and to determine the scale at which changes in the stochastic behavior of the seafloor can be detected. The information we obtain should also prove invaluable in efforts to design sea-going experiments.

This study employs space-domain techniques to characterize the stochastic behavior of the seafloor. Changes in stochastic behavior are determined by resolvable changes in parameters describing the 2-point moment, or covariance function. Other workers have attempted to locate changes in stochastic behavior using parametric methods in the Fourier domain [*Fox and Hayes*, 1985; *Malinverno*, 1989]. The primary advantage of space-domain methods is that we can invert the data directly without having to regrid or interpolate them.

This analysis is made possible by the procedure, described in Chapter 1 and Appendix B, to synthesize realistic multibeam data sets from a stochastic description of the seafloor and a simple mathematical description of the Sea Beam system effects (Figure 3.2). This allows us to generate many independent data sets with identical statistics which can be inverted in the same manner as real data. The mean and standard deviation of the inverted parameters can then be computed from these Monte Carlo realizations and directly compared with the input parameters and the standard errors estimated from individual inversions.

To generate synthetic topography and perform an error analysis, it is assumed that the joint probability distribution of depth is Gaussian. In this case, all higher moments of the distribution can be expressed in terms of the covariance function. Although the seafloor tends to fail the Kolmogorov-Smirnov test for acceptance of the Gaussian hypothesis [*Gilbert and Malinverno*, 1988], the distribution of seafloor depths is nevertheless nearly Gaussian [*Bell*, 1975*b*]; i.e. the probability density function is peaked near the mean depth and decays to zero similarly in both positive and negative directions. Since we are only characterizing the distribution to second order, the Gaussian assumption is sufficient; the properties of any distribution to second order can be described by a Gaussian form with the same first and second order properties. The study of higher-order moments of the seafloor depth distribution will be an analysis of perturbations from the Gaussian form.

COVARIANCE OF THE ESTIMATES

To understand the resolution of the estimated parameters, we must have knowledge concerning the uncertainty structure (i.e. covariance) of our data functionals (the estimated auto- and cross-covariance functions of the beams). The function $V_{pqrs}(j,l)$ expresses the covariance of the estimated seafloor covariance function, or, more simply stated, the covariance of the estimates. It contains information regarding the *variability*, or variance of the covariance estimate about the expected (model) value and the *correlation* between two covariance estimates of different lag coordinates. Variability tells us how far off the estimation may reasonably be from the expected value. The correlation between estimates tells us to what degree of accuracy we can predict the value of one covariance estimation given another. In order to understand the behavior of the estimates and the way in which this behavior factors as a weighting function in the inversion, we must understand the functional form of $V_{pqrs}(j,l)$.

Although in general $V_{pqrs}(j,l)$ is computed by numerical integration, a simplifying case that can be approximated analytically is sufficient to demonstrate its structure. Setting $\nu = 1/2$ and $B(\mathbf{x},t) = \delta(\xi(t))$, we compute $V_{pppp}(j,l)$, the covariance of an estimated single-beam autocovariance function, by approximating the summations in (2.38) by integrals. We define beam lag distance by $x_j = vt_j$, and beam data length by $X_j = M_j v\Delta t_j$, which expresses the amount of data used in the autocovariance estimation at lag j. k_1 is the scale parameter in the ship track ($\hat{e}_1$) direction. For $\nu = 1/2$ (a fair approximation to rough, unsedimented seafloor), $G_\nu(r)/G_\nu(0) = \exp(-|r|)$, which greatly simplifies integration and yields

$$
\begin{aligned}
V_{pppp}(j,l) = \frac{H^4}{k_1\sqrt{X_j X_l}} & \left\{ \left[1 + k_1(x_j - x_l) + 2\frac{N_p^2}{H^2} \right] \exp -[k_1(x_j - x_l)] \right. + \\
& \left. \left[1 + k_1(x_j + x_l) + 2\frac{N_p^2}{H^2} \right] \exp -[k_1(x_j + x_l)] \right\} + \\
& \frac{N_p^2}{\sqrt{X_j X_l}} \delta_{jl} + O\left[\frac{H^4}{(k_1\sqrt{X_j X_l})^2} \right]
\end{aligned}
\qquad (3.1)
$$

Equation (3.1) assumes x_j is greater than or equal to x_l. Typical values of H^2 and N_p^2 range from 1000–50000 m^2 and 25–500 m^2 respectively and tend to be positively correlated (see Chapter 2). In general then, $H^2 \gg N_p^2$ and we can disregard the contribution of system noise to the variation of the estimates. The dimensionless factor $k_1 X$ is typically greater than 10, so that the terms in (3.1) of order $(k_1 X)^{-2}$ may also be disregarded. These approximations simplify (3.1) to the following form:

$$V_{pppp}(j,l) \cong \frac{H^4}{k_1\sqrt{X_j X_l}} \{[1 + k_1(x_j - x_l)] \exp -[k_1(x_j - x_l)] +$$

$$[1 + k_1(x_j + x_l)] \exp -[k_1(x_j + x_l)] \qquad (3.2)$$

The dependence of the estimation covariance on some of the important model and data parameters is made clear in equation (3.2): $V_{pppp}(j,l)$ increases with the rms topographic height H, decreases linearly with the inverse of length of data used in the estimation X, and decreases with increasing along-track scale parameter k_1. We can physically interpret these relationships in the following ways: The variability of the estimates (determined by the case $j = l$) will increase with variation of topography. Variability will decrease with increased data length because more data will better constrain the estimate. However, H and X do not affect the correlation among estimates (correlation = covariance/variance) since they multiply all lags equally. k_1, on the other hand, affects both the variability and the correlation of the estimates. Given two scale parameters where k_1' is larger than k_1, λ_1' will be less than λ_1. Thus, for a given data length, the characteristic length λ_1' will be sampled more often than λ_1. This will increase the amount of independent information, and thus better constrain the estimates and decrease their variability. Topography with the shorter scale length λ_1' will also vary more rapidly and erratically than topography with the longer scale length λ_1. Hence the correlation among estimates will be decreased for the shorter scale length (larger scale parameter). These effects are easily seen in Figure 3.3, where two sets of autocovariance estimates from 20 independently generated synthetic profiles are plotted. The parameters used to generate the profiles were $H = 55$ m, $\nu = 0.5$, and $k_1 = 1.0$ km^{-1} (top panel) and 0.5 km^{-1} (bottom panel). Clearly the variance of the estimates is greater for the smaller scale parameter $k_1 = 0.5$ km^{-1}. Also, the estimates tend to vary about the expected value more rapidly with lag for the larger scale parameter $k_1 = 1.0$ km^{-1}, indicating that the correlation among estimates is less than where $k_1 = 0.5$ km^{-1}.

The form of $V_{pppp}(j,l)$ is dependent on a lag separation $(x_j - x_l)$ and a lag distance $(x_j + x_l)/2$. Figure 3.4 shows $V_{pppp}(j,l)$ as a function of lag distance for four different lag separations. k_1 is set to 1, H is set to 55 m, X_0 is set to 200 km, and X_j and X_l decrease linearly with x_j and x_l. Each of the curves in Figure 3.4 initially decrease with lag distance, and eventually increase gradually at large lag distances as X_j and X_l decrease linearly. The lag distance at which these curves flatten out is dependent on the scale parameter. The case where lag separation is zero represents the variance of the estimates. Thus the estimates should exhibit their greatest variability at smallest lag. We might expect then that the weighting of the inversion will de-emphasize the importance of small-lag estimations. However, the correlation among estimates is also greatest at small lags. Thus, while the variability of the estimates at small lag may be large, the shape of the estimated function is best-constrained in this region. This phenomenon results from the fact that although we are sampling smaller lags more often than larger lags, and thus better constraining the shape of the autocovariance at small lags, the smaller features are superimposed on the larger ones so that the variance of the larger scales contributes to the total variance at smaller scales.

These effects can also be seen in Figure 3.3. The dashed lines represent 95% confidence limits (1.96 times the square root of $V_{pppp}(j,j)$) on the variance of the estimates about the expected value. Thus we expect one estimate out of 20 to be outside of these limits at any lag. This is generally true in both cases shown in Figure 3.3. The variance does decrease with lag, but this effect is not clearly visible since the decrease is only ~25%, and the curvature near zero lag gives the illusory appearance of better vertical constraint. More easily seen is the stronger correlation near zero lag. The estimates more consistently follow the shape of the expected autocovariance form in this region. Since we are primarily interested in inverting for the form of the covariance function the shape of estimates at the smallest lags should receive the most weight, and this is indeed the case.

The full form of $V_{pqrs}(j,l)$ is obviously more complicated than equation (3.2), but the principal points stated above are still valid. In the general case we can identify scale parameters, lag distances, and lag separations that are directionally dependent and have the same effect on the behavior of the covariance of the estimates as in the one-dimensional case. The order parameter ν, which is inversely proportional to roughness, also affects $V_{pqrs}(j,l)$ in an important way: the correlation of estimates near zero lag increases with ν, as larger values of ν mean smoother topography and hence greater correlation of the estimates.

NUMERICAL EXPERIMENTS

The inversion algorithm provides as output estimates of the covariance parameters and their formal uncertainties, both of which we assume are accurate and unbiased. However, complexities in the inversion, principally the nonlinearity of the problem, force us to question this assumption. In a linear inverse problem, a Gaussian distribution of data results in a Gaussian distribution of inverted parameters. In this case the diagonals of the parameter covariance matrix are easily interpreted as the variances of the parameters. In the non-linear problem, the error distribution of inverted parameters is non-Gaussian. However, since the solution is derived by an iterative, linearized process, the parameter covariance matrix assumes a Gaussian form for the distribution of parameters, and thus does not express the true resolution of the problem. We therefore explore how well the linearized standard errors match the variations calculated in numerical experiments.

In this procedure, we generate several synthetic multibeam data sets with identical known statistics. This is accomplished using the algorithm described in the previous chapter. The synthetic data produced by this algorithm are Gaussian distributed. Each synthetic data set is then inverted as if their statistics were unknown. The mean and standard deviation of the parameters output from the inversion can be directly compared with the input parameters and the average linearized standard errors respectively. In this section we present the results of several such experiments conducted under a variety of circumstances. There are two goals in this study: (1) to determine how accurate the estimated parameters and their standard errors are, and (2) to investigate the resolution of parameters with respect to ship variables such as length of data, angle with respect to the topographic grain, and response width.

The split algorithm for estimating the Hausdorff dimension prior to estimating th: remaining parameters was described in the previous chapter. The two steps are considered here separately.

Estimation of Scale and Orientation Parameters

We begin with numerical tests of step 2 of the inversion algorithm. For the following experiments we set $\nu = 1/2$ ($D = 5/2$) for both the synthesis of data and the inversion of the remaining parameters. This value of the fractal dimension is appropriate for rough, unsedimented seafloor terrain. (Although variations in ν can compensate variations in the scale parameters k_n and k_s, this trade-off is largely described by (2.24) so that the characteristic lengths λ_n and λ_s are not strongly correlated with ν.)

Figures 3.5 and 3.6 show the results of numerical experiments conducted on synthetic Sea Beam data generated from surfaces with covariance parameters $H = 65$ m, $k_n = 0.48$ km^{-1} ($\lambda_n = 5.9$ km), and $k_s = 0.12$ km^{-1} ($\lambda_s = 23.6$ km), using a response width of 0.63 km, and values for the rms noise ranging from 5 m at the center beam to 15 m on the outer beams. All subsequent experiments also use these noise values. θ is defined as the angle between the ship track and the $\hat{\mathbf{e}}_n$ (spreading) direction (Figure 3.2). These parameters, which were used to generate the topography shown in Figure 3.2, are typical of seafloor in the northeast Pacific ocean. Each data point plotted represents the average result of the inversion of 20 independent synthetic data sets. The solid bars represent their standard deviation, and the dashed bars the average of the 20 linearized standard errors from the inversion. Figure 3.5 shows such results for four different track lengths, ranging from 300 km to 75 km, with $\theta = 0°$. In general it is clear that we have succeeded in recovering the covariance parameters that were used to generate the synthetic surface; in all cases the averages of the parameters estimated from the 20 inversions are within a small fraction of the observed deviation from the input parameters. The average linearized standard errors from the inversions are generally within ~10–20% of the observed deviation of the inversion results. The principle exception is for the parameter θ, where the average linearized standard errors tend to overestimate the observed deviation by up to a factor of two, and effect probably ascribable to the linearization. The errors tend to increase with decreasing track length, as expected. We note that the relative errors for k_n and k_s are nearly identical.

Figure 3.6 shows the results for tracks of constant length (150 km) trending at five different values of θ. The errors for all parameters increase with angle to the $\hat{\mathbf{e}}_n$ axis. It may at first be surprising that our best resolution of the parameter k_s comes when the ship track runs perpendicular to the $\hat{\mathbf{e}}_s$ axis. The maximum lag distance in this direction when $\theta = 0°$ is only the width of the Sea Beam swath (~4 km), whereas when $\theta = 90°$, it is the track length. The reasons that resolution of k_s is better in the former case are (1) that the shape of the covariance function is best-constrained near zero lag and (2) we are *independently* sampling that region more often because the characteristic length in the $\hat{\mathbf{e}}_n$ direction is shorter. Thus, the primary determinant of the resolution of all the covariance parameters is the number of characteristic lengths in the along-track profile.

Figures 3.7 and 3.8 show results equivalent to Figures 3.5 and 3.6, respectively, for numerical experiments conducted on synthetic Sea Beam data generated from surfaces with covariance parameters $H = 63.2$ m, $k_n = 1.7$ km^{-1} ($\lambda_n = 1.7$ km), and $k_s = 0.2$ km^{-1} ($\lambda_s = 14.1$ km), and using a response width of 0.39 km. These parameters, which indicate shorter scale lengths and a greater aspect ratio (~twice as large) than the previous examples, are fairly typical of seafloor near the East Pacific Rise. The results are similar to the previous experiments. However, since characteristic lengths are smaller, shorter sections of data are adequate to make good estimations. Where track lengths in Figures 3.5 and 3.7 are similar in terms of number of characteristic lengths sampled along track, the relative errors in the scale parameters are nearly identical. The greater aspect ratio in the latter case improves the resolution of θ. However, it also causes the estimation errors to be a stronger function of ship direction.

The preceding experiments help us to determine what is well-resolved in an absolute sense. The resolution of all parameters is strongly dependent on the number of characteristic lengths sampled by a Sea Beam track, so it is natural to ask: how many characteristic lengths do we need? The resolution of H appears to be very good in all cases. The worst case is shown in Figure 3.8, $\theta = 90°$, where the error is less than 15% of the value of H and the number of characteristic lengths sampled is only 3.5. Thus we can obtain very good estimates of H with quite short track lengths, especially if the ship track runs across the topographic grain. θ is also well estimated for all cases, with a maximum error of ~5° (Figure 3.6). However, θ is dependent on the aspect ratio a. Aspect ratios as low as 2 have been observed (see chapter 5), and in these cases the errors in θ can be 10° or larger. The scale parameter estimates have larger relative errors: ~12% where the track lengths exceed 50 characteristic lengths (Figures 3.5 and 3.7) and up to ~50% at 3.5 characteristic lengths (Figure 3.8). 50% errors are too large to make quantitative statements about abyssal hill morphology that are geologically interesting. The errors are generally well behaved, remaining below ~25%, until about 5 (Figure 3.8) or 6 (Figure 3.6) characteristic lengths, where the errors rise to ~30% . Thus, as a general rule of thumb, we consider 5 or 6 characteristic lengths to be a minimum track length necessary to resolve the scale parameters.

In evaluating the resolving power of a data set, important quantities to consider are the correlations between parameter estimation errors. The correlation coefficient between two parameters 1 and 2 is defined by the ratio of the covariance between parameters C_{12} to the product of their standard deviations σ_1 and σ_2: $\rho_{12} = C_{12}/\sigma_1\sigma_2\,(-1 \leq \rho_{12} \leq 1)$. The parameter covariance matrix is readily obtained from the inversion and thus the correlation coefficients can be calculated. In the numerical experiments shown in Figures 3.5 and 3.6,

H was found to be negatively correlated with k_n and k_s ($\rho \cong -0.75$), k_n and k_s where highly correlated with each other ($\rho \cong +0.85$), and θ was poorly correlated with all the other parameters ($|\rho| < 0.03$). Figure 3.9 illustrates three of these correlations by plotting parameters derived from individual inversions for the case $\theta = 0$ and track length = 75 km. Where the correlation is positive (k_n vs. k_s), these points cluster about a line with positive slope, where the correlation is negative (H vs. k_n), they cluster about a line with negative slope, and where the correlation is near zero (H vs. θ), there is no discernible pattern. In each case the spread of these points matches the shape of the 1-σ error ellipses (39% confidence) very well. The correlation coefficients are nearly identical for the numerical experiments shown in Figures 3.7 and 3.8, with the only appreciable difference being in the correlation between k_n and k_s ($\rho \cong .75$).

Estimation of Hausdorff Dimension

Experimentation has shown that no more than about two dozen covariance estimations at well-spaced lags from all the cross-covariances of 3-4 beams (as widely spaced as possible), spread out over the length of ~3-4 characteristic widths centered about the maximum cross-covariance, are needed for step 2 of the inversion. Beyond this quantity of data, the errors in the estimated parameters do not appreciably decrease with increased data. This is a result of the strong covariance among estimates which limits the amount of independent information available.

A different strategy is needed for optimizing step 1 of the inversion. The Hausdorff dimension is primarily dependent on the shape and curvature of the covariance function near zero lag. The information constraining the Hausdorff dimension is not several single estimations at various lags, as in step 2, but rather the shapes produced by sets of estimations with closely spaced lag coordinates. In this case, it is necessary to take into account the strong correlation among nearby estimates for the inversion to work. Single-beam autocovariances are the only Sea Beam cross-covariances which adequately constrain the shape of the 2-D covariance near zero lag (e.g. equation (2.27)). Thus, step 1 of the inversion must include many closely space points near the origin of these autocovariance functions.

Using estimation points which are closely spaced and highly correlated makes the inversion susceptible to small deviations from the expected form. This is particularly true for higher values of ν and larger response functions since in these cases the correlation among estimates near zero lag is greater. Small-scale variations in the covariance due to noise, which are negligible in step 2, can be significant in step 1. We might expect to be able to solve this problem by including the contribution of noise in the covariance of the estimates. Unfortunately this contributes to destabilization by reducing the correlation among estimates necessary for the inversion to work, and also biases the estimation of ν.

We find that the convergence properties of step 1 are best stabilized when the covariances between single-beam autocovariance estimations are ignored; i.e. each beam is treated as independent from all other beams. Because beams are widely separated from each other compared with the along-track sample spacing, the beams should be fairly independent of each other with respect to the Hausdorff dimension. We would expect the standard errors to be underestimated in such an inversion since we are claiming more independent information than we actually have. However, in general we find that the theoretical standard errors on ν tend to overestimate the observed variation (probably because of the non-linearity of the estimation problem) so that the inversion of 2 or 3 autocovariances treated independently yields theoretical standard errors on ν which are close to the observed variation.

Figure 3.10 shows numerical tests of step 1 conducted on synthetic Sea Beam data generated from surfaces with covariance parameters $H = 65$ m and $k_n = k_s = 0.5$ km^{-1}, and using a response width of 0.5 km. Two different Hausdorff dimensions and four track lengths were used. Data points from two autocovariance estimations were used in these inversions. The results in this case are quite favorable; the averages of the 20 estimated values of ν are well within the observed deviation of the input parameters, and the linearized standard errors are within ~10-20% of the observed deviations. As expected, the errors increase with decreasing track length, and tend to be slightly larger in the case of the lower Hausdorff dimension. There is also some evidence that at low Hausdorff dimension, the estimation of the Hausdorff dimension becomes slightly biased high at shorter track lengths. This may result from fact that ν is constrained to be less than 1 and greater than 0; i.e. as the errors increase for estimation of ν close to 1, there is a greater likelihood of larger errors toward smaller values of ν than toward larger values of ν.

Resolution of the Hausdorff dimension is also heavily dependent on the width of the response function in relation to the characteristic length. Figure 3.11 shows numerical tests of step 1 conducted on synthetic Sea Beam data generated from surfaces with covariance parameters H = 65 m, $k_n = k_s$ = 1.5 km^{-1} and D = 2.5, a track length of 200 km, and echosounder response widths ranging from 0.0 (δ response) to 0.5 km. The characteristic length in this case (1.9 km) is three times shorter than for the D = 2.5 tests in Figure 3.10. The observed deviation is well-constrained (< ± 0.1) at short response widths, but becomes quite large (± 0.17) when the response function reaches 0.5 km. The linearized standard errors, which increase only modestly with increasing response width, do not match this behavior well. Failure to include the effects of noise into the error calculations is a probable cause for this discrepancy.

Assuming an incorrect response width can have a drastic effect on the estimation of the Hausdorff dimension. Figure 3.12 shows numerical tests of step 1 conducted on synthetic Sea Beam data generated from surfaces with covariance parameters H = 65 m, $k_n = k_s$ = 1.5 km^{-1} and D = 2.5, a track length of 200 km, and echosounder response width 0.3 km. The inversions were conducted assuming response widths ranging from 0.0 to 0.5 km. 100 m errors in the assumed response width result in errors in the estimation of D of between 0.1 and 0.2. Failure to consider the echosounder response at all results in errors greater than 0.2. This experiment clearly demonstrates the need for accurate calibration of the echosounding system.

RESOLVABILITY OF NON-STATIONARY BEHAVIOR

It is impossible to address the problem of what is well-resolved with respect to non-stationarity without first identifying limitations on the detectability of stochastic changes. For example, we may wish to identify changes in stochastic character which occur over preset horizontal scales. This would require us to use data sets of a limited track length, which in turn limits the resolution of our parameters. Changes in stochastic character which are within this resolution will not be detected. On the other hand, we may wish to identify changes in stochastic character with a preset resolution. This would require us to use long enough track lengths of data to obtain this resolution. Changes in stochastic character on horizontal scale lengths shorter than such track lengths will also not be detected.

The Sea Beam data shown in Figure 3.1 provides us with an interesting test case for investigating the resolution of non-stationary behavior. Table 3.1 shows the inversion results for the entire data set, for the data prior to 1700 hours, and for the data after 1700 hours. In this case we are interested in determining what parameter changes can be detected given these constraints on data lengths. As is visually obvious, there exists a clearly resolvable difference between the rms heights of the two sections. The data after 1700 hours exhibits nearly a factor of three times the variation in the data prior to 1700 hours. Less visually obvious, and perhaps more interesting, is the fact that there is also a difference in azimuths of the abyssal hill lineation. The data prior to 1700, trending at −13° ± 5°, is consistent with the trend of the mid-Atlantic ridge at this latitude (3.5°S), whereas the data after 1700 hours, trending at 3° ± 9°, is not. The lineation difference is resolved at 80% confidence in this case since the difference $\Delta\theta = 16°$ is greater than the standard deviation $\sigma_{\Delta\theta} = \sqrt{(\sigma_1^2 + \sigma_2^2)} = 10°$. This difference should have important implications for understanding the processes which shaped this terrain. Neither the scale parameters nor the aspect ratios are resolvably different for this comparison. If there is a difference in these parameters, then it is clear that longer data lengths will be needed to resolve it. We were also not able to distinguish the two data sets by a difference in Hausdorff dimension. The inversion of the data before 1700 hours for the Hausdorff dimension was very poorly constrained, tending to settle on a value of $D \cong 2.1 \pm 0.3$. Inverting the data after 1700 hours produced an estimate of $D = 2.30 \pm 0.14$. For inverting the scale and orientation parameters of the data prior to 1700 hours, we fixed D at 2.25 for better comparison with the other data sets. The inversion for the full data set, while tending to split the difference between the two sub-data sets, is more consistent with the data set after 1700 hours. This is to be expected since the much larger amplitude characteristics will tend to dominate the covariance.

As demonstrated in the previous chapter, an important means of subjectively assessing how well we are modeling the stochastic character of the data is to visually compare the data with a synthetic data set generated from the estimated model parameters. Figures 3.13 and 3.14 are data-synthetic comparisons for the data shown in Figure 3.1 prior to and after 1700 hours respectively. The comparison for the data prior to 1700 hours (Figure 3.13) is quite good: the along- and across-track characteristic scales, the rms height, the direction of lineation and the small-scale roughness are all favorably comparable. The primary difference is that the "valleys" of the real data set are rounded compared with the peaks, whereas no such difference exists in the synthetic data. This phenomenon is likely a result of sediment ponding, and causes an asymmetric distribution of depth which cannot be characterized by the Gaussian model. Future analysis will require the use of non-Gaussian random fields. It is also likely that the Hausdorff dimension differs between the valleys and peaks. If so, we will not be able to detect such differences because we must average over at least several characteristic lengths. The comparison for the data after 1700 hours is less favorable; primarily the cross-track characteristic lengths appear too short in the synthetic. A value of k_s more consistent with the earlier data set would be more appropriate, suggesting that a longer data set would not resolve any difference in this parameter for this particular comparison. This data set also displays some fairly exotic terrain, such as the big flat spot at 1900 hours and the very laterally asymmetric, or tilted, abyssal hills between 2000 hours and 2200 hours. As in the case of sediment ponding, abyssal hill tilting will require higher-order (i.e. non-Gaussian) stochastic analysis.

DISCUSSION

The inversion of Sea Beam cross-covariance estimates for the parameters of the seafloor covariance function provides an excellent means of quantitatively characterizing the small-scale (100's of m to 100's of km) stochastic behavior of the seafloor. The experiments performed in this chapter show that resolution of the covariance parameters is strongly dependent on the number of characteristic lengths which are sampled. Rms seafloor height can be estimated to within ~15% and anisotropic orientation to within ~5° (for a strong lineation) using track lengths as short 3 characteristic lengths, or ~10-100 km, and characteristic lengths of seafloor topography can be estimated to within ~25% using track lengths as short 5 or 6 characteristic lengths, or ~20-200 km. The number of characteristic lengths sampled by a ship track, and hence the accuracy of the estimation, is maximized when the ship track runs perpendicular to abyssal hill lineation. Ship surveys of abyssal hill terrain should therefore include many track lines running parallel to flow lines. The estimation of the Hausdorff dimension is more difficult with this method. The most stable and accurate estimation of D is obtained when only autocovariance estimations closely spaced near zero lag are used in the inversion. This inversion becomes increasingly unstable and inaccurate as the characteristic length is shortened with respect to either the response width or the data spacing, as the rms noise is increased, and as the order parameter ν is increased.

The numerical experiments in this chapter do not constitute a completely thorough test of real conditions; in the real world we are not guaranteed that the topography of the ocean floor is Gaussian distributed, or that its covariance function necessarily conforms to the parameterized model. If the seafloor is significantly non-Gaussian, our description of the correlation between estimates will be in error. This will obviously affect the way estimates are weighted. If the covariance deviates significantly from the form of the parameterized model, the inversion will predominantly fit the form of the covariance near zero lag since the form of the estimates in that region receives the most weight. This covariance model does appear to be a good description of the seafloor in many regions of the seafloor from scales between hundreds of kilometers down to Sea Beam resolution (~300 m). However, we have no reason to believe at this point that this covariance model can be extended to smaller scales. It is unlikely, for example, that pillow basalts bear much resemblance to faulted abyssal hills. Extending this stochastic model to smaller scales may be possible if we allow for changes in fractal dimension [*Fox and Hayes*, 1985] and azimuthal dependence with scale. These are all problems of significant interest, and the analysis included here provides a basis for studying them.

Uncertainties in the sonar characteristics also affect the results in this chapter. If the response characteristics are in error, the estimation of the Hausdorff dimension will be incorrect. For example, underestimation of the width of the response function will result in an underestimation of the Hausdorff dimension. Also, if system noise is not white, as we have assumed, the Hausdorff dimension can be overestimated. These uncertainties underscore the need for calibration experiments to accurately determine the Sea Beam response to a rough ocean floor and to properly model the system noise process, including the correlation between noise and seafloor characteristics. If response and noise are properly calibrated, the Sea Beam system may prove useful for obtaining stochastic seafloor information at scales smaller than the deterministic resolution capabilities.

TABLE 3.1. Statistical Parameters Derived From Inversion of Data Shown in Figure 3.1

Data, hrs	H, m	ζ_S, deg	λ_n, km	λ_S, km	a	D
1300-2200	164 ± 15	-2 ± 7	7.9 ± 1.8	15.8 ± 4.7	2.0 ± 0.6	2.26 ± 0.10
1300-1700	75 ± 11	-13 ± 5	7.0 ± 1.9	21.1 ± 8.4	3.0 ± 1.1	2.1 ± 0.3[a]
1700-2200	205 ± 33	3 ± 9	8.2 ± 2.4	15.5 ± 5.4	1.9 ± 0.7	2.30 ± 0.14

[a] Hausdorff dimension fixed at 2.25 for inversion of scale and orientation parameters

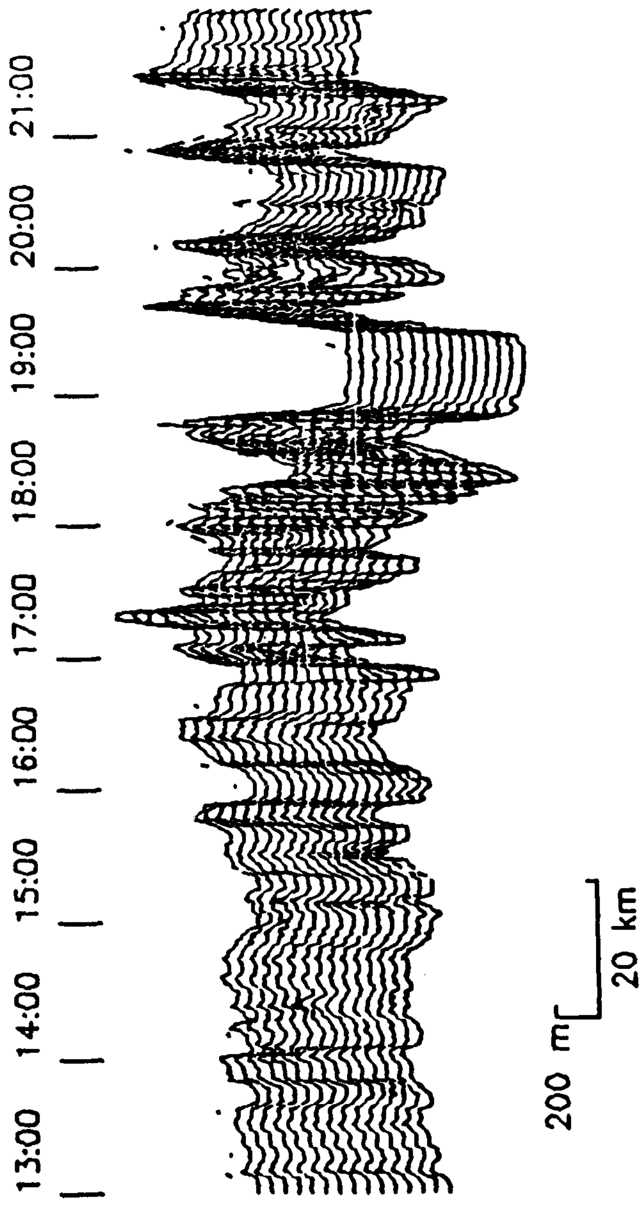

Figure 3.1. 9 hours of 5-ping averaged Sea Beam data from the Robert Conrad cruise 2806. Depth recorded by each beam is plotted continuously as a function of track distance. Forward ship direction is left-to-right. The data was recorded on June 12, 1986, with starting coordinates −3.83°N, −15.92°E and ending coordinates −3.30°N, −13.80°E. The average water depth is 3644 m and the number of data points is 4271.

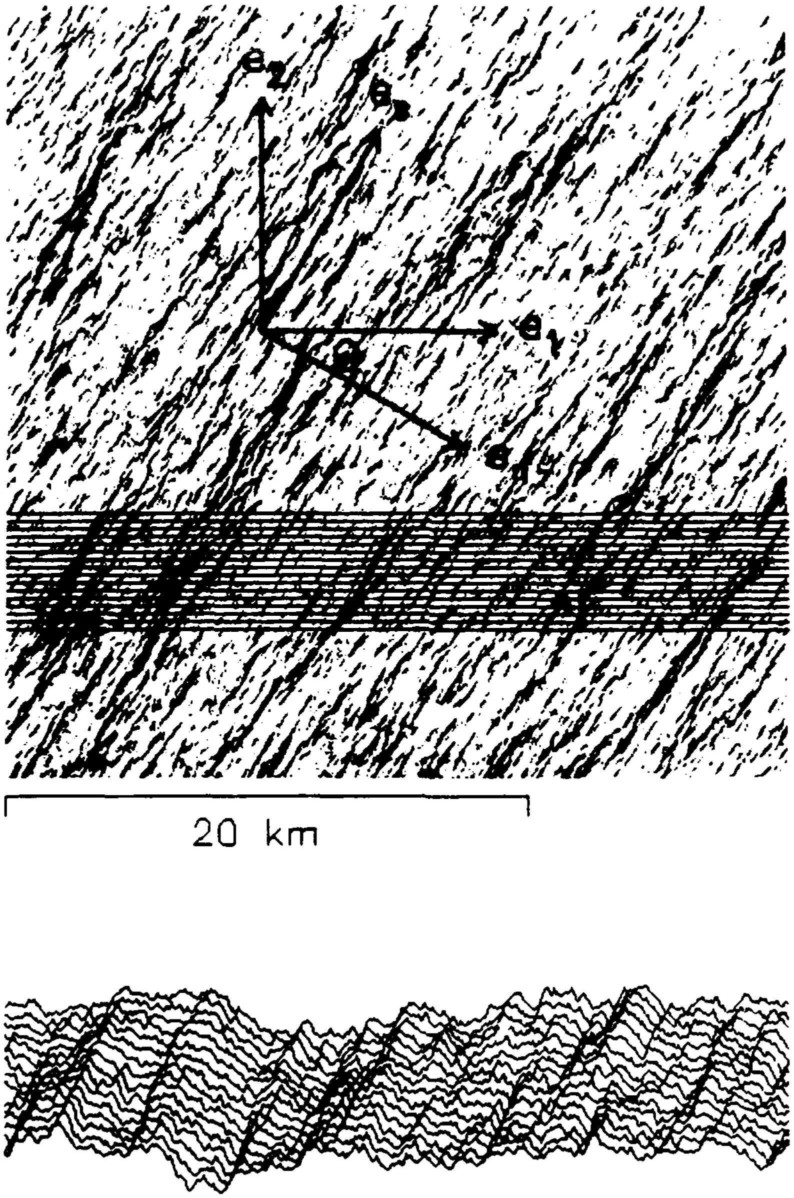

Figure 3.2. Coordinate representation and simulation of Sea Beam recording system. Top panel is a grey-shaded relief image of an anisotropic topographic surface with covariance parameters $H = 55$ m, $k_n = 0.48$ km^{-1} ($\lambda_n = 5.9$ km), $k_s = 0.12$ km^{-1} ($\lambda_s = 23.6$ km), and $\nu = 0.5$. Coordinate axes for both seafloor geometry and ship track geometry ($\hat{e}_1$ is the ship track and $\hat{e}_2$ the cross-track direction) with reference angle θ are overlain on this plot. Parallel lines running in the $\hat{e}_1$ direction represent beam geometry that was used to extract synthetic Sea Beam data, shown in the bottom panel, from the topographic surface.

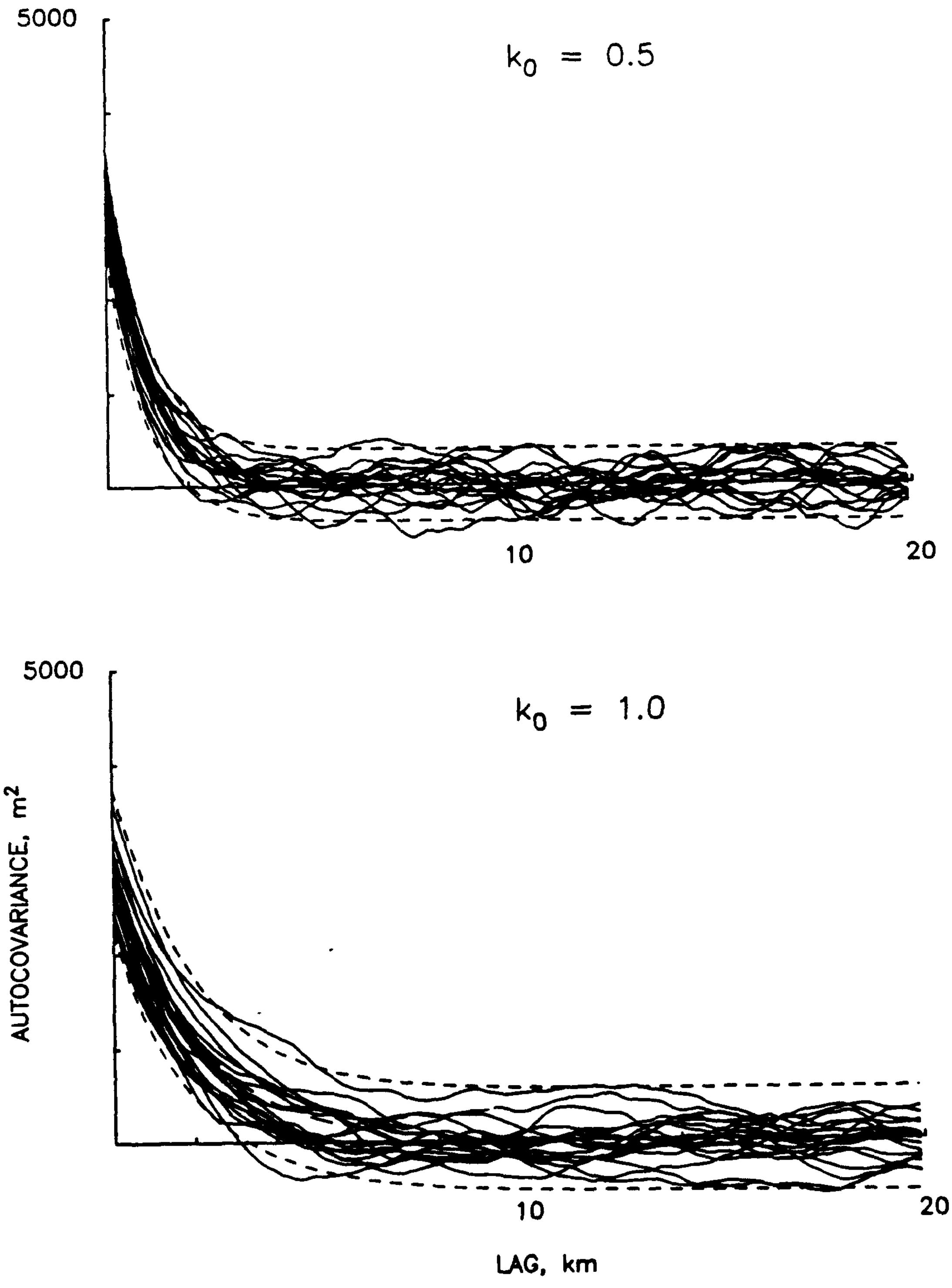

Figure 3.3. Autovariance estimates from 2 sets of 20 independently generated synthetic topographic profiles. The covariance parameters used to generate the profiles were $H = 55$ m, $\nu = 0.5$, and $k_1 = 1.0$ km^{-1} (top panel) and 0.5 km^{-1} (bottom panel). Dashed lines represent 95% confidence limits on the variance of the estimates.

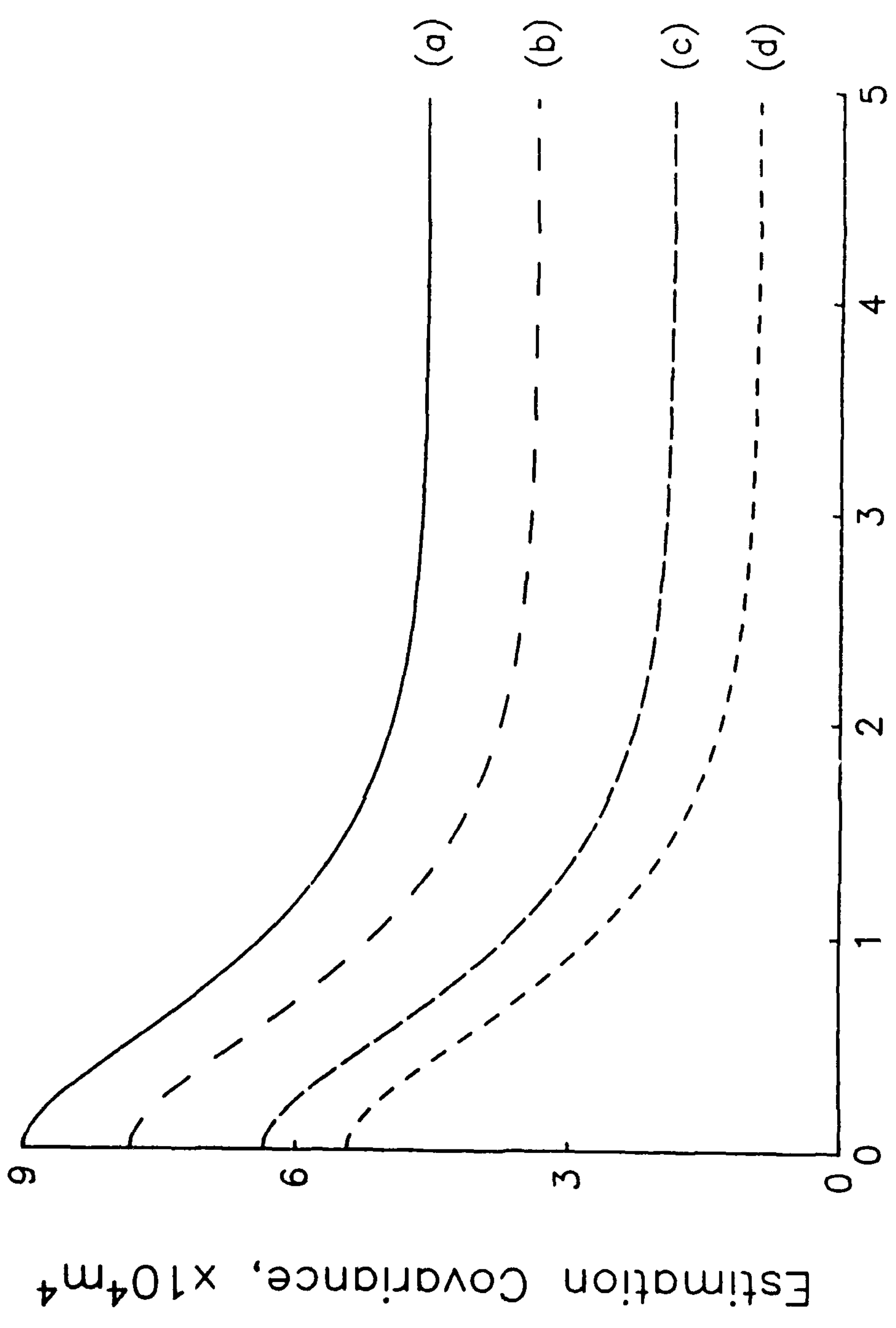

Figure 3.4. Equation (3.2) plotted as a function of lag distance $(x_j + x_l)/2$ for four constant values of lag separation $(x_j - x_l)$: a) 0.0 km, b) 0.8 km, c) 1.6 km, and d) 2.4 km. k_1 is set to 1, H is set to 55 m, X_0 is set to 200 km, and X_j and X_l decrease linearly with x_j and x_l.

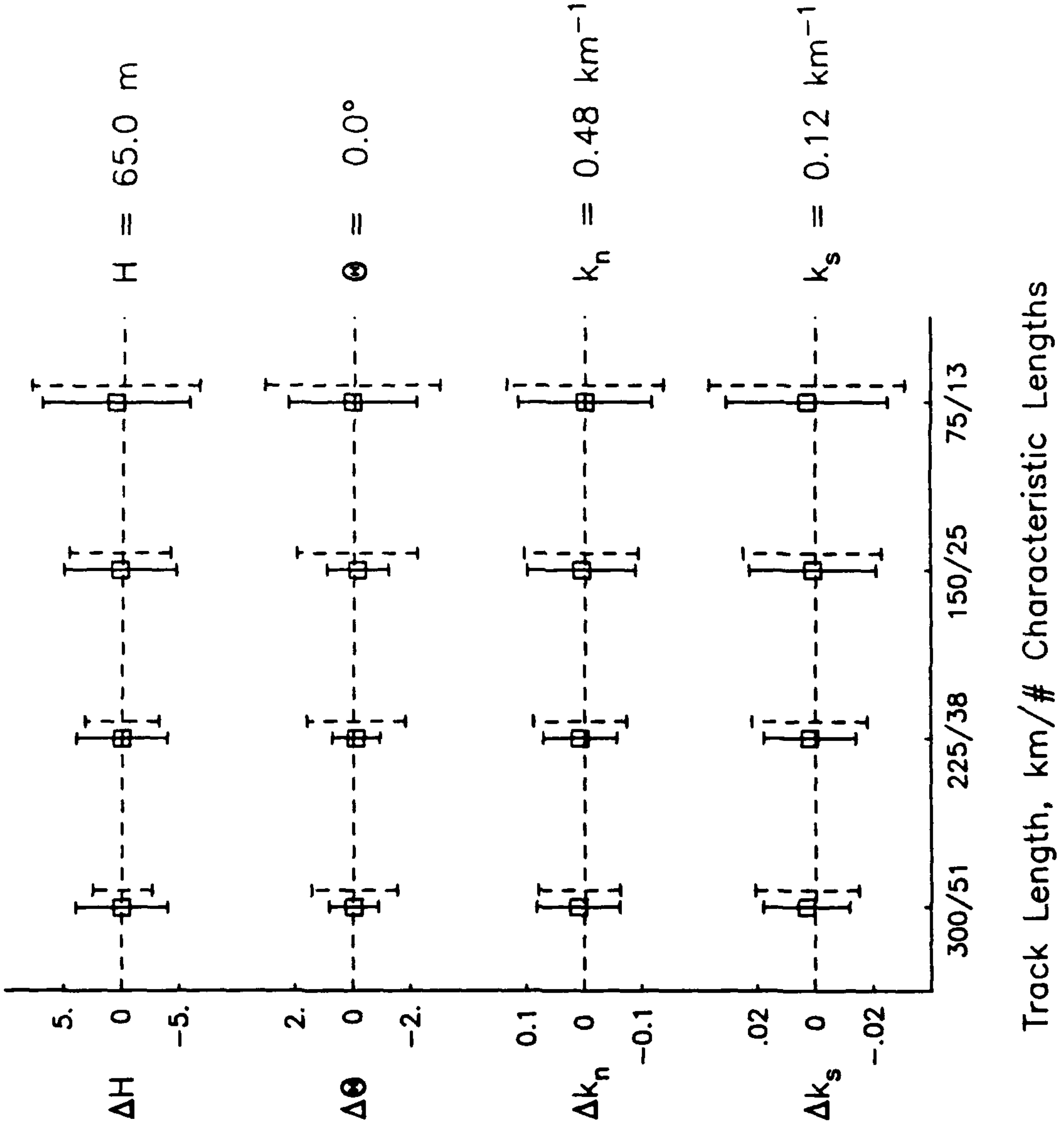

Figure 3.5. Results of numerical experiments of step 2 of the inversion conducted on synthetic Sea Beam data generated from surfaces with covariance parameters $H = 65$ m, $k_n = 0.48$ km^{-1} ($\lambda_n = 5.9$ km), $k_s = 0.12$ km^{-1} ($\lambda_s = 23.6$ km), $\nu = 0.5$, and $\theta = 0°$, using a response width of .63 km, and values for the rms noise ranging from 5 m at the center beam to 15 m on the outer beams. Four different track lengths were used ranging from 300 to 75 km. The number of characteristic lengths spanned by each track length is also shown. Each data point, plotted as a function of the difference with the input parameters, represents the average result of the inversion of 20 independent synthetic data sets. The solid bars represent their standard deviation, and the dashed bars the average of the 20 linearized standard errors from the inversion.

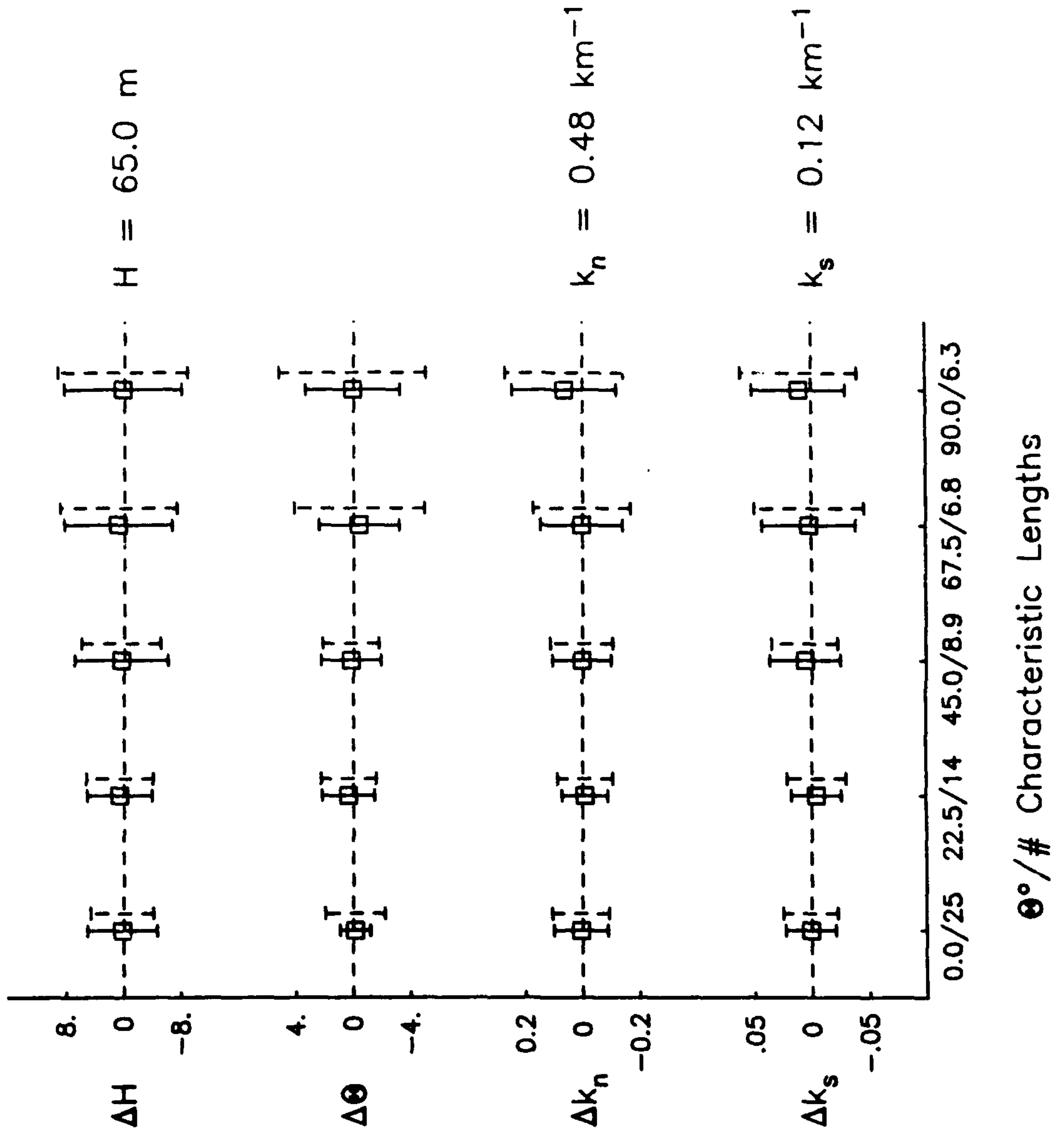

Figure 3.6. Results of numerical experiments of step 2 of the inversion conducted on synthetic Sea Beam data generated from surfaces with covariance parameters $H = 65$ m, $k_n = 0.48$ km^{-1} ($\lambda_n = 5.9$ km), $k_s = 0.12$ km^{-1} ($\lambda_s = 23.6$ km), and $\nu = 0.5$, using a track length of 150 km, a response width of .63 km, and values for the rms noise ranging from 5 m at the center beam to 15 m on the outer beams. Five different values of θ were used ranging from 0 to 90°. See Figure 3.5 for further details.

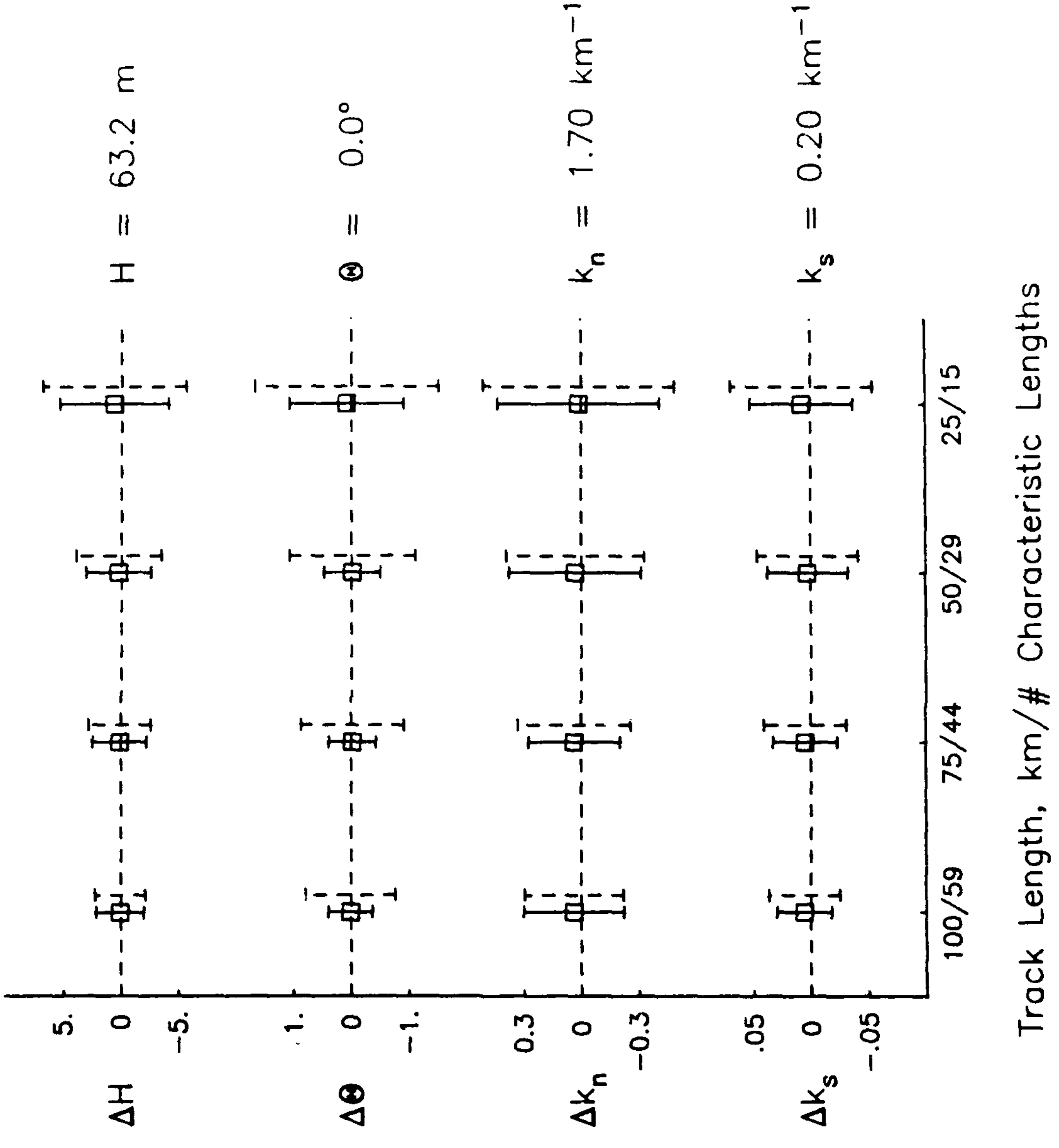

Figure 3.7. Results of numerical experiments of step 2 of the inversion conducted on synthetic Sea Beam data generated from surfaces with covariance parameters $H = 63.2$ m, $k_n = 1.7$ km^{-1} ($\lambda_n = 1.7$ km), $k_s = 0.2$ km^{-1} ($\lambda_s = 14.1$ km), $\nu = 0.5$, and $\theta = 0°$, using a response width of .39 km, and values for the rms noise ranging from 5 m at the center beam to 15 m on the outer beams. Four different track lengths were used ranging from 100 to 25 km. See Figure 3.5 for further details.

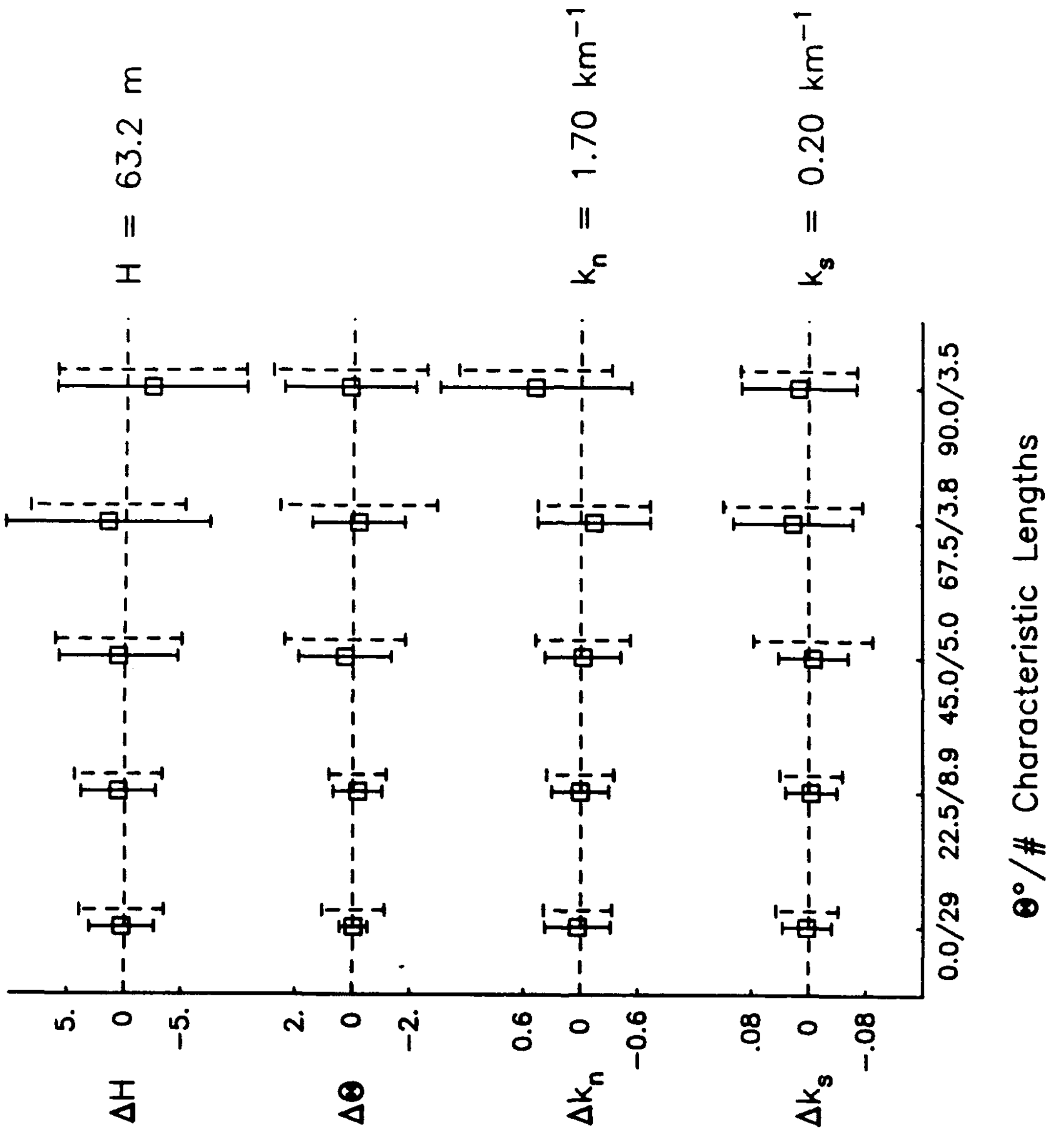

Figure 3.8. Results of numerical experiments of step 2 of the inversion conducted on synthetic Sea Beam data generated from surfaces with covariance parameters $H = 63.2$ m, $k_n = 1.7$ km^{-1} ($\lambda_n = 1.7$km), $k_s = 0.2$ km^{-1} ($\lambda_s = 14.1$ km), and $\nu = 0.5$, using a track length of 50 km, a response width of .39 km, and values for the rms noise ranging from 5 m at the center beam to 15 m on the outer beams. Five different values of θ were used ranging from 0 to 90°. See Figure 3.5 for further details.

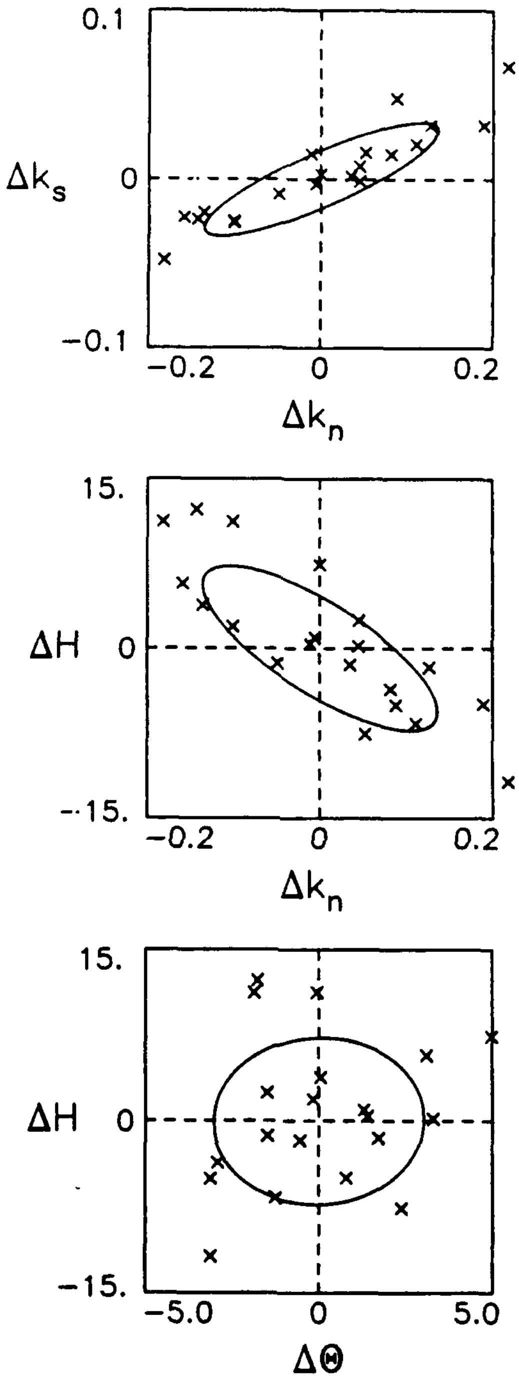

Figure 3.9. Inversion results for three different parameter pairs, plotted as a function of difference with the input parameters, for the 20 synthetic data sets of the $\theta = 0°$ and track length = 75 km numerical experiment (see text and Figure 3.2). 1-σ error ellipses, calculated from the parameter covariance matrix output by the inversion, are also plotted.

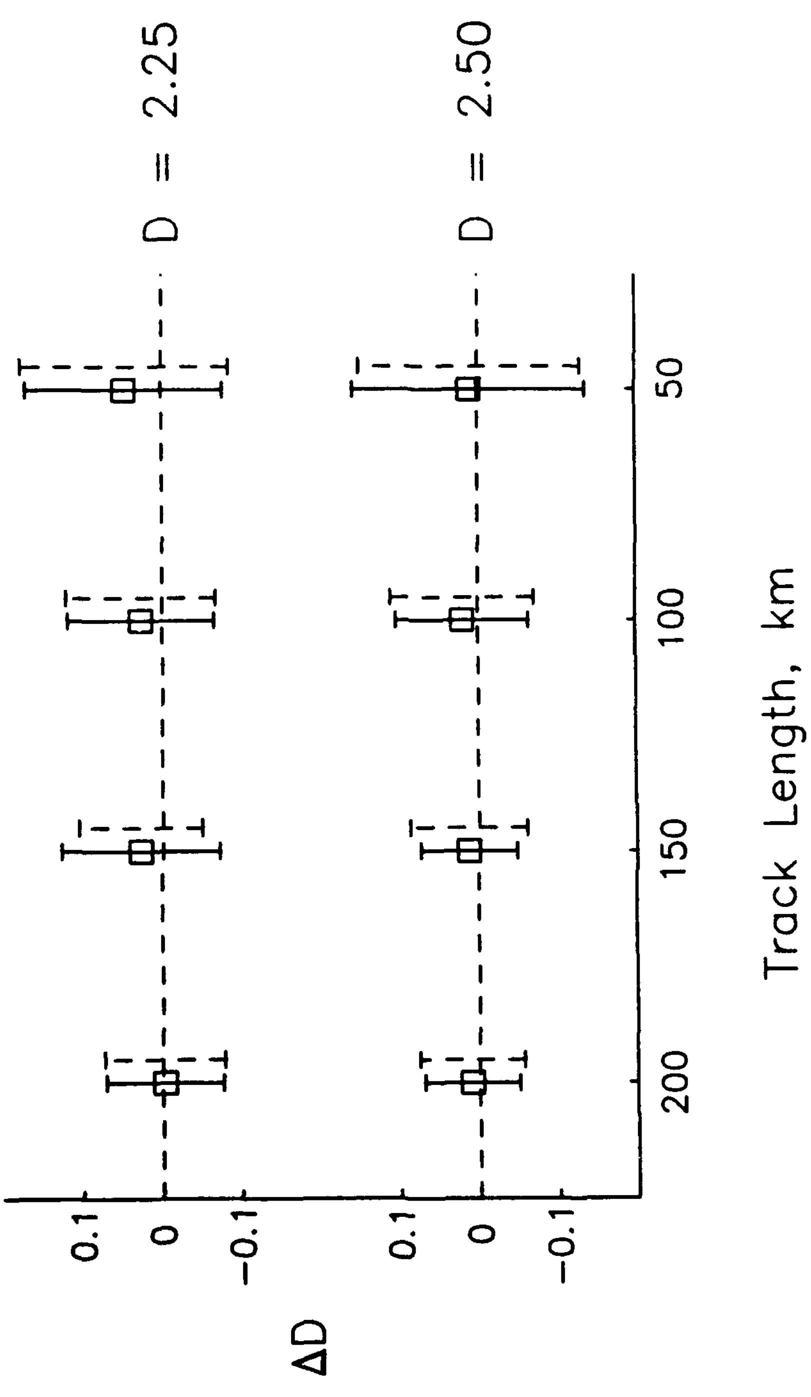

Figure 3.10. Results of numerical experiments of step 1 of the inversion conducted on synthetic Sea Beam data generated from surfaces with covariance parameters $H = 65$m, $k_n = k_s = 0.5$ km^{-1} ($\lambda_n = 5.7$ km), $\nu = 0.75$ (top) and $\nu = 0.5$ (bottom), using a response width of .5 km, and values for the rms noise ranging from 5 m at the center beam to 15 m on the outer beams. Four different track lengths were used ranging from 200 to 50 km. See Figure 3.5 for further details.

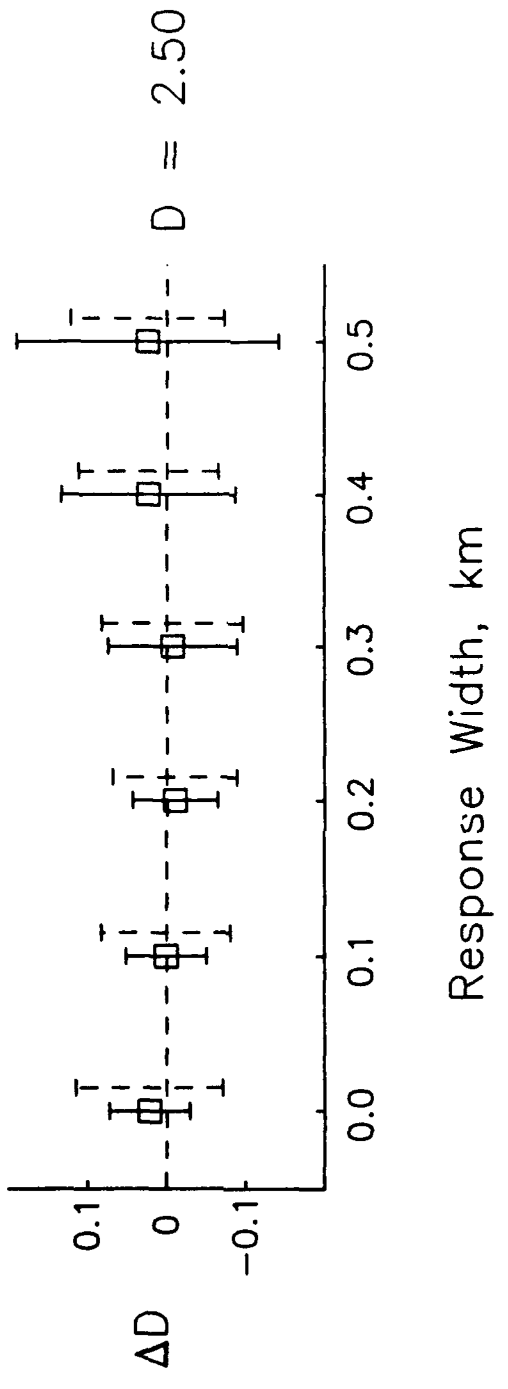

Figure 3.11. Results of numerical experiments of step 1 of the inversion conducted on synthetic Sea Beam data generated from surfaces with covariance parameters H = 65m, k_n = k_s = 1.5 km^{-1} (λ_n = 1.9 km), ν = 0.5, using a track length of 200 km, and values for the rms noise ranging from 5 m at the center beam to 15 m on the outer beams. Six different response widths were used ranging from 0.0 to 0.5 km. See Figure 3.5 for further details.

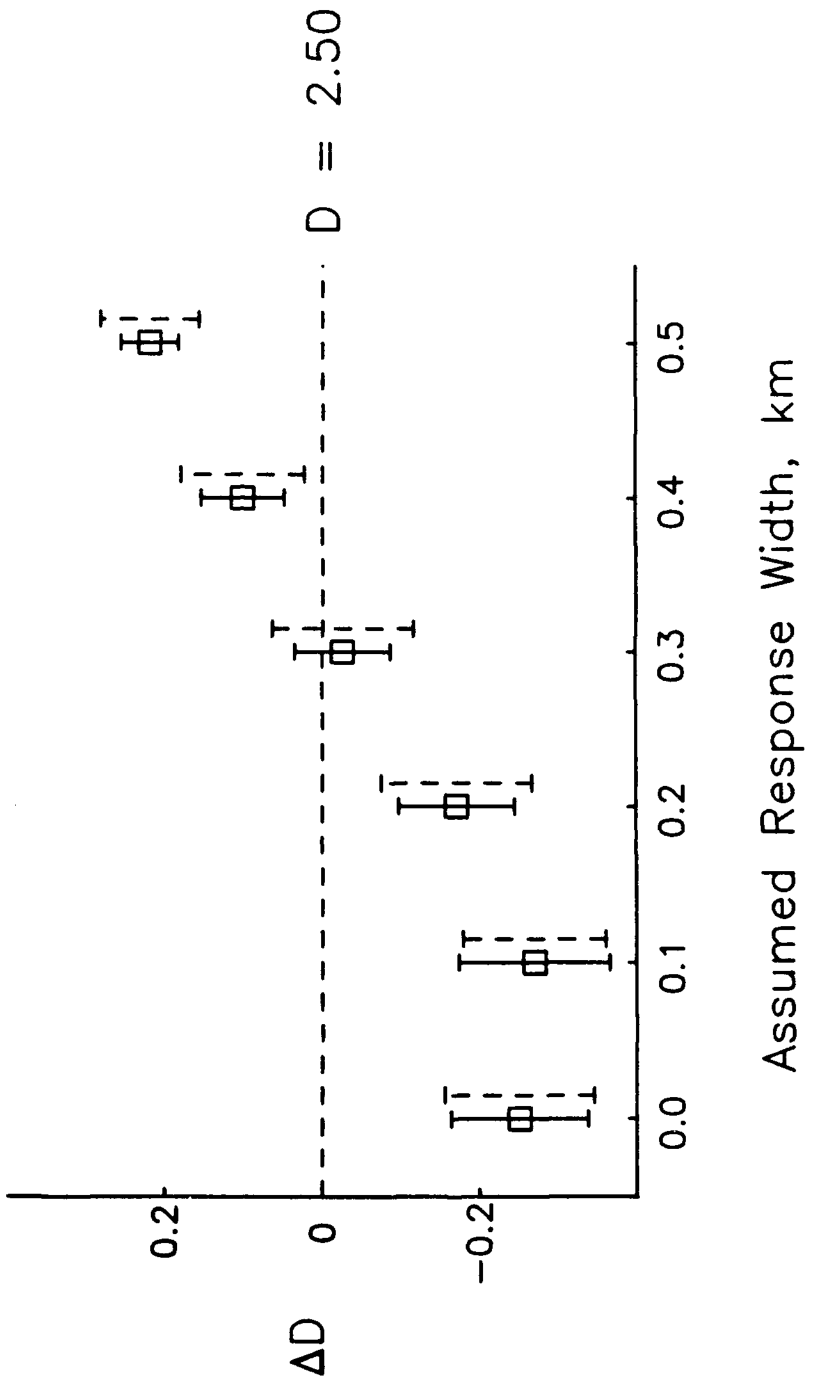

Figure 3.12. Results of numerical experiments of step 1 of the inversion conducted on synthetic Sea Beam data generated from surfaces with covariance parameters $H = 65$m, $k_n = k_s = 1.5$ km^{-1} ($\lambda_n = 1.9$ km), $\nu = 0.5$, using a track length of 200 km, a response width of 0.3 km, and values for the rms noise ranging from 5 m at the center beam to 15 m on the outer beams. Six different response widths were assumed in the inversion ranging from 0.0 to 0.5 km. See Figure 3.5 for further details.

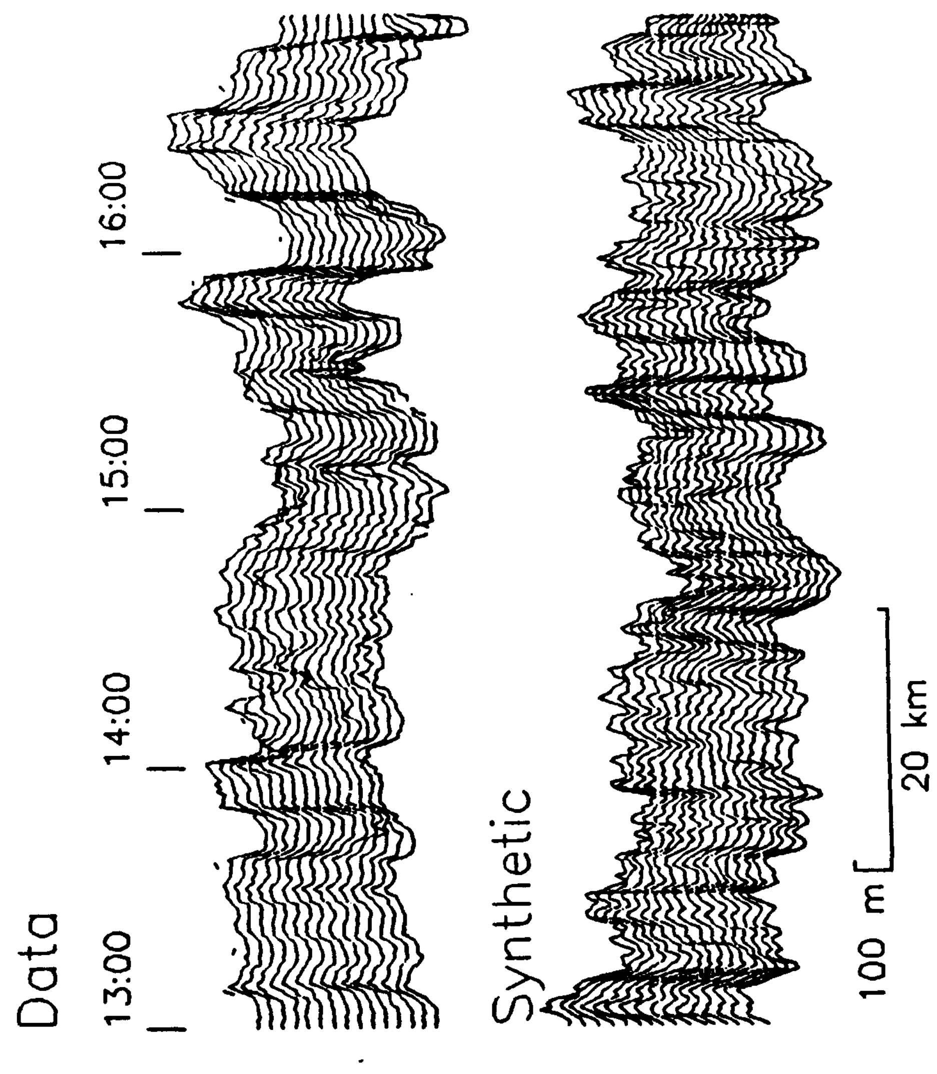

Figure 3.13. Comparison of 4 hours of data shown in Figure 3.1 prior to 1700 hours with 4 hours of synthetic data. The synthetic data was generated using the covariance model parameters (Table 3.1) estimated from inverting this portion of the data, and using appropriate rms noise values and response function.

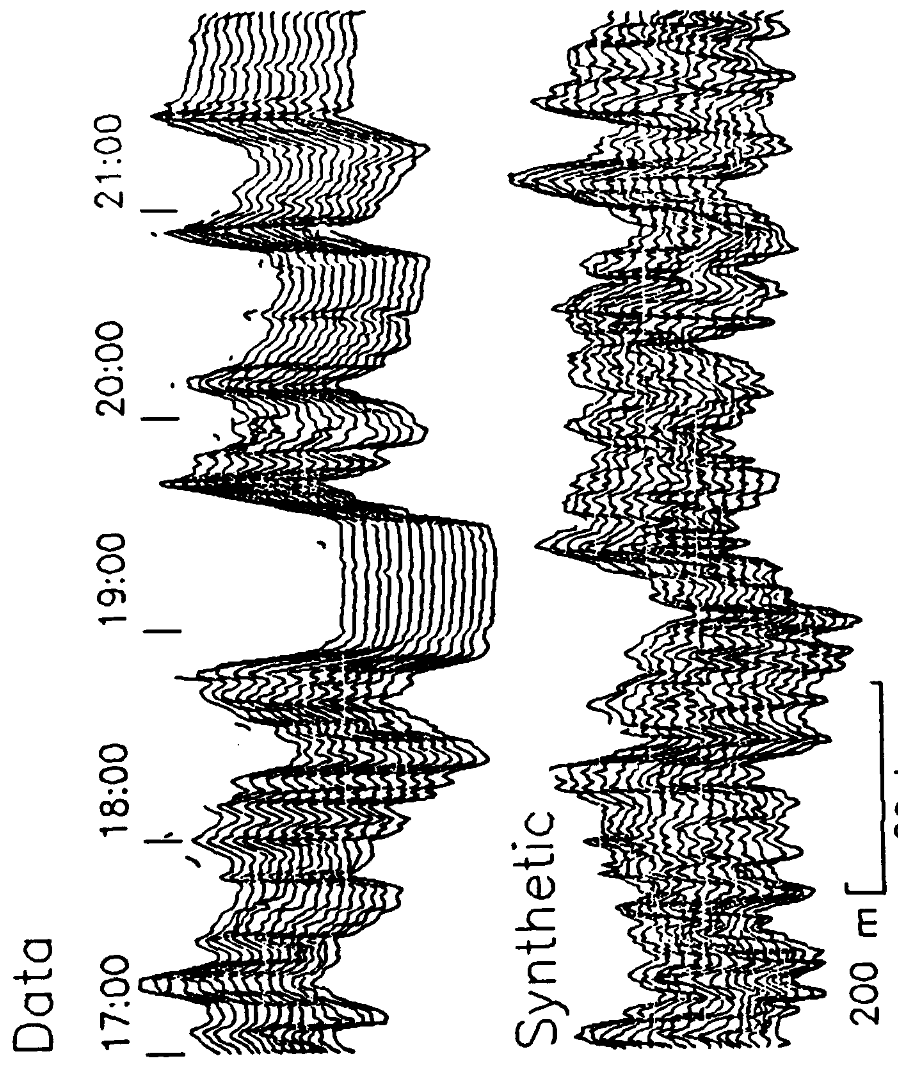

Figure 3.14. Comparison of 5 hours of data shown in Figure 3.1 after 1700 hours with 5 hours of synthetic data. The synthetic data was generated using the covariance model parameters (Table 3.1) estimated from inverting this portion of the data, and using appropriate rms noise values and response function.

CHAPTER 4

COMPARISON OF A STOCHASTIC SEAFLOOR MODEL WITH SEA MARC II BATHYMETRY AND SEA BEAM DATA NEAR THE EAST PACIFIC RISE 13° - 15° N

INTRODUCTION

The stochastic model presented in Chapter 2 has so far been only marginally tested. Our primary means of testing is to compare Sea Beam data to synthetic data generated from the model. Although subjective, the eye proves to be a powerful tool in evaluating patterns of randomness. Unfortunately, the limited spatial extent of the Sea Beam system in the across-track direction and lack of significant coverage over large areas severely limits our ability to compare the full 2-D stochastic model with actual bathymetric data, especially with respect to abyssal hill length characteristics. A recent SeaMARC II (SM-II) survey along the flanks and crest of the East Pacific Rise between 13° and 15° N [*Edwards et al.*, 1988] (Figure 4.1) provides a unique opportunity to compare stochastic models of the seafloor against bathymetric data. Although the bathymetric resolution of the SM-II data set examined was not entirely adequate for use in estimating stochastic character (see Appendix C), this survey, which covered over 100 km (70,000 km^2) of off-axis morphology, provides enough bathymetric coverage to portray the full 2-D shape of abyssal hills. The SM-II survey data thus provides a more complete comparison for evaluating the performance of the model synthetics.

Several Sea Beam tracks which are sufficiently long for use in stochastic estimation cross the SM-II survey region (Figure 4.1). The inversion procedure is applied to the Sea Beam swaths to estimate the stochastic character within the region. Estimated stochastic parameters are also used to generate 2-D synthetic realizations used for comparison against

Sea Beam swaths and sections of the gridded SM-II survey data. These comparisons are evaluated for the ability of the model to characterize the low-order stochastic behavior of the seafloor. Seafloor characteristics which are not well-matched by the model for either the Sea Beam or SM-II comparison may provide starting points for improvement in the modeling. The combined Sea Beam and SM-II data set allows us to compare the performance of each bathymetric system with respect to stochastic characterization. Sea Beam data, with better resolution at smaller scales, provides a means of ground-truthing the stochastic characteristics of SM-II bathymetric data, which can cover much larger tracts of seafloor than Sea Beam.

Significant variations are observed in the estimated stochastic parameters with location and can be correlated with spatial and temporal variations in observed ridge crest morphology. The implications of these correlations concerning the ridge crest processes which govern the formation of abyssal hills are discussed.

DESCRIPTIVE MORPHOLOGY OF SEAFLOOR FROM SEAMARC II AND SEA BEAM DATA

The SeaMARC II side looking sonar imagery and bathymetry data used in this study were taken aboard the *RV Moana Wave* on the MW8707 cruise. This survey covered the crest and flanks of the East Pacific Rise from 13° N to 15° N and out to more than 100 km east and west of the ridge crest (Figure 4.1). The SM-II bathymetric data and its geological interpretation are discussed in *Edwards et al.* [1989]. The salient morphological and structural features present in the survey area are briefly described here as they are important to the understanding of the stochastic character of abyssal hill features in the study area.

The East Pacific Rise (EPR) crest at 12° 50' N is characterized by a ~10-15 km wide crestal horst which tapers gradually to <3 km wide at 13° 55' N while deepening about 100 m to the north over this segment of the ridge. North of 13° 55' N the EPR crest is very poorly defined and is characterized by sets of narrow (1-3 km wide), parallel ridges 10-40 km long, whose crests have an average depth of about 2750 m. No continuous depth variation of the EPR crest is evident between ~14°-15° N. This type of discontinuous crestal morphology is thought to correlate with decreased magma supply along a ridge segment [*Macdonald and Fox*, 1988]. The deeper level and lack of a distinct gradient along the crest between 14°-15° N supports this interpretation and may reflect a deeper-seated magma plumbing system that sporadically supplies the EPR crest along this segment. The EPR flanks within the study area also show a marked asymmetry with respect to mean depth and seamount distribution. The Cocos plate (eastern flank) is shallower (200-300 m) than the Pacific plate (western flank), and there are nearly twice as many seamounts on the latter compared to the west flank [*Fornari et al.*, 1988]; these differences are most pronounced in the area south of 14° N.

Based on the SeaMARC II side-looking imagery and the magnetic data it is apparent that the EPR has been propagating northward through the study area [*Edwards et al.*, 1988; *Madsen et al.*, 1990]. Two pseudofaults have been mapped (Figure 4.1) using the structural data, and discrete offsets of the magnetic anomalies 2, and 2A on the Pacific plate support the occurrence of a ridge propagating event that has persisted for the past ~5 Ma [*Madsen et al.*, 1990]. Furthermore, the complex terrain present within the Orozco transform [*Madsen et al.*, 1986], which bounds the survey area to the north, and the morphology of the EPR crest as it sweeps into the eastern Orozco/EPR ridge-transform intersection provide further evidence that this segment of the EPR is propagating northwards and that the tip of the propagator is currently located near the eastern Orozco/EPR intersection.

Sea Beam data from three different cruises were used to estimate the stochastic character of the seafloor within the SM-II survey area (Figure 4.1). The algorithm for stochastic estimation (Chapter 2) study requires that the Sea Beam tracks be approximately straight, sufficiently long, and cut sufficiently orthogonal to the grain of topography (see Chapter 3) to obtain well-resolved results. The track lines shown in Figure 4.1 are the data sets which best satisfy these estimation criteria. With the exception of the Papatua 1 cruise, which surveyed seamounts off-axis, the track lines shown in Figure 4.1 are all sections of ridge surveys and represent the rare occasions when ship tracks continued in fairly long straight lines off axis.

Figure 4.2 shows the Sea Beam ridge-crossing data, which illustrate the variation in ridge characteristics over the survey area. In these and subsequent Sea Beam data plots the depth recorded by each beam is plotted side-by-side as a multichannel time series. (Displaying the data in this manner rather than as contour swaths gives the viewer a better grasp of the geometry and stochastic character of the data.) The northernmost ridge crossing (14.8° N) shows a regional high at the ridge crest (~0800 hrs), but there is no clearly defined crestal horst associated with the rift. The abyssal hills are large and well defined over the entirety of the crest. This implies either that abyssal hill formation occurs very early following crustal accretion or that there are several parallel crestal horsts with the same amplitude and spacing as the adjacent abyssal hills. The next swath south (14.0° N) shows the presence of a fairly well defined structural high (~2100 hrs) but the appearance is still fairly complex. As in the previous example the abyssal hills are large and appear to be everywhere over the ridge crest. There is also a large basin just east of the ridge crest which may be associated with an overlapping spreading center [*Macdonald et al.*, 1984]. In contrast, the two southernmost swaths (13.4° N and 13.2° N) show well developed crestal horsts and smaller abyssal hills on the flanks. There also appears to be a clear point ~3 km to each side of the crestal horst at which significant abyssal hill formation occurs. This distance is roughly consistent with the limit of tectonic activity observed by *Choukroune et al.* [1984] at the EPR crest near 12° 49' N, and roughly corresponds to the off-axis limit of the subaxial magma chamber detected in this region [*Detrick et al.*, 1987].

The propagator pseudofault can be seen on the Sea Beam data. Figure 4.3 shows data from the Papatua 1 swath (Figure 4.1) which crosses it (though in this region it is not within the SM-II survey area). The pseudofault consists of a tandem structural high and low (~0130-0245 hrs) which are considerably broader and larger than the surrounding abyssal hill structures. It appears from this plot that the abyssal hills east of the pseudofault are broader and shorter than those to the west. By applying the inversion method we can quantify this difference.

SEA BEAM RESULTS AND DATA-SYNTHETIC COMPARISONS

The location of the Sea Beam data sets used in an inversion (labeled swaths 1 through 6) are given in Figure 4.4. Details concerning these swaths are listed in Table 4.1. Each side of the northernmost Ceres 2 swath was detrended (by subtracting a best-fitting line along track) and inverted individually. The parameters estimated from the inversion were nearly identical for each side. Only one side is used as an example in this chapter. For the RC2607 swath, because of the short track length, data on either side of the ridge high were detrended individually and the result combined into one data set for use in the inversion. For the southern Ceres 2 swath, only data east of the ridge were used. Three sections of the Papatua 1 swath west of the ridge high were used and each detrended and inverted individually. The sections include a near ridge swath, a swath just east, and one just west of the propagator pseudofault.

The results of the inversions, along with 1-σ errors, are given in Table 4.2. It was not possible to adequately resolve the Hausdorff dimension for any of the swaths. This was due to the fact that the width of the echosounder response (the full width of the beam) is a significant portion of the characteristic length of the topographic profile in the ship direction, thereby masking the behavior of the seafloor covariance near the origin (see Chapter 3). The characteristic abyssal hill widths in this region are among the narrowest of the samples of seafloor that we have observed (see Chapter 5). In all the inversions the Hausdorff dimension was constrained to be 2.5, a value we consider appropriate for rough, unsedimented seafloor. The inverted parameters indicate a large range of stochastic character for the SM-II survey region; each of the swaths is resolvably different at 67% certainty with respect to at least one parameter from each of the other swaths (Table 4.2).

To assess how well the covariance model and its estimated parameters are characterizing the stochastic properties of the seafloor, we need to evaluate more than just the fit of the model covariance to the estimated covariance; we need to compare the model against the original data. We can do this by the procedure described in Chapter 2 for visually comparing the stochastic character of the data and the synthetic. Although subjective, such comparisons can be an intuitively powerful means of gauging the performance of the model and suggest new directions needed to improve it.

Figures 4.5-4.10 show the data synthetic comparison for the 6 swaths shown in Figure 4.4 and listed in Table 4.1. The parameters used to generate the synthetic topography for each case are listed in Table 4.2. In these figures we have plotted 50 km rather than the whole of each swath to facilitate comparison among the swaths. On first inspection, all of these comparisons are favorable; the topographic variation, the characteristic abyssal hill widths, and the lineation azimuths are all well matched by the synthetics. The abyssal hill lengths also appear to be well matched, though the comparison is not clear given the short sampling in the across-track direction. These comparisons suggest that the covariance model (2.21) is generally successful at quantifying the low-order stochastic character of abyssal hill morphology in this region.

The comparisons of Figures 4.5-4.10 are, as we might expect, far from perfect. The differences in stochastic character occur primarily in the finer detail. On swaths 3 and 5 (Figures 4.7 and 4.9), and to a lesser extent on the rest of the swaths, the high-wavenumber character or small-scale roughness seen in the synthetics does not compare well with the data. In these cases the synthetics are rougher at small scales than the data, suggesting that a lower Hausdorff dimension than $D = 2.5$ should have been employed. It may also be the case that we have underestimated the width of the echosounder response function, or are improperly modeling the response as a linear filter. The use of an incorrect

Hausdorff dimension or response function will not significantly affect the estimation of rms height, the lineation azimuth, or the characteristic width and length (see chapter 2).

Closer inspection of the data reveals another possible explanation for the roughness discrepancy. There exists valleys on most of the swaths which are generally greater in amplitude and sharper than the peaks. Representative examples of such features can be found at ~0220 hours on swath 3 (Figure 4.7), and at ~0315 hours on swath 5 (Figure 4.9). Because of their greater amplitude, these features will receive more weight in the estimation of the covariance, and so enrich the small-scale/high wavenumber content. The Gaussian synthetics cannot match this behavior for two reasons; 1) because phase is uncorrelated from wavenumber to wavenumber, it is impossible to localize high wavenumber content, and 2) because the Gaussian distribution is symmetric, we cannot characterize asymmetries in the distribution such as that valleys are deeper and sharper than peaks (or vice versa). It is possible in the Gaussian synthetics to change sign (turn the page upside down) without affecting the stochastic character, whereas in the real data set this creates a noticeable difference. To quantify such vertical asymmetries it is necessary to include higher moments of the joint probability density function in the stochastic model.

It will also be necessary to appeal to higher moments to quantify lateral asymmetries such as abyssal hill tilting. The clearest example of tilting can be found on swath 2 around 1900 hours (Figure 4.6) and swath 3 after 0500 hours (Figure 4.7). In both of these cases the slopes facing the ridge are steeper than those facing away from the ridge. In other examples it is difficult to tell by eye whether or not abyssal hills are tilted. In these cases, quantitative estimation methods may help identify as well as measure tilting.

SEAMARC II DATA-SYNTHETIC COMPARISON

The time series Sea Beam data-synthetic comparison provides a useful means of checking the accuracy of the stochastic estimation, especially with respect to the rms height, the azimuth of lineation, the abyssal hill widths, and the roughness (as represented by the Hausdorff dimension). However, because of the limited Sea Beam swath width, it is very difficult to compare the abyssal hill length characteristics. This is an important check because the average length of an abyssal hill may prove to be an important parameter for describing along-axis morphological and tectonic variations such as ridge crest segmentation or average fault lengths. These variations may, in turn, reflect fundamental differences in the crustal structure and distribution of magma chambers beneath a ridge crest. To evaluate estimates of length characteristics properly, we must compare a full 2-D synthetic field generated from the stochastic model with significant 2-D coverage of the corresponding abyssal hill region used to estimate the parameters of the model.

The relatively narrow Sea Beam swath width (75% of the water depth, or ~2.25 km near the EPR in the study area) has prevented many previous ridge surveys from covering substantial areas of off-axis topography. Hence, there is not presently available a Sea Beam data set for which we can make a full 2-D data-synthetic comparison. The SM-II bathymetric system provides substantially more swath coverage (~10 km), than Sea Beam. The MW8707 SM-II cruise was thus able to obtain overlapping coverage of a large portion of off-ridge topography (over 100 km, 70,000 km^2) on either side of the EPR crest between 13° and 15° N. This off-ridge data provides us with the opportunity to make a more complete 2-D data-synthetic comparison.

It is possible to adapt the multibeam inversion method to use with SM-II data. Analysis of the SM-II data could then provide a more complete picture of the stochastic make-up of the region, and a direct comparison with the 2-D coverage. Unfortunately, the noise characteristics of the SM-II bathymetry collected on the MW8707 cruise make it difficult to use in stochastic estimation. An analysis of the characteristics of SM-II noise in the data collected on the MW8707 cruise is presented in Appendix C. The sole purpose of this analysis is to investigate the usefulness of this SM-II bathymetric data for use in stochastically characterizing small-scale (< 10 km) seafloor morphology. The results do not affect the well known usefulness of the SM-II system for quickly gathering great amounts of large-scale bathymetry as well as simultaneous backscatter information. The noise in the SM-II bathymetry data has two characteristics which inhibit use in stochastic characterization: 1) the rms value of the noise is very large (especially on the port side) with respect to abyssal hill relief, and 2) the noise has a significant correlation distance (i.e. its covariance function has a width substantially greater than the first lag). The rms height of the SM-II noise is found to range from 25 to 75 m (port and starboard). This range is nearly identical to the range in abyssal hill rms heights estimated from Sea Beam data (Table 4.2). The correlation distance is found to be ~1 km. Since the topographic along-track characteristic lengths are generally ~2-5 km (at track azimuths ~45° to the topographic grain), it is nearly impossible to separate the effects of noise from the effects of topography on the beam autocovariances. By comparison, the rms Sea Beam system noise is generally less than 10 m for the swaths listed in Table 4.1, and the noise correlation width appears to be at most 1 lag distance (~37 m), making it indistinguishable from a white noise process whose covariance is a delta-function. Thus, Sea Beam noise significantly affects the beam autocovariances only at zero lag (see Appendix C and Chapter 2), and its effect on the covariance can be separated from that of the topography.

The primary strength of SM-II bathymetry is in providing substantial coverage of larger features. Comparison of a large patch of SM-II bathymetry with synthetic topography should thus be useful for assessing the ability of the model to characterize the overall shape of abyssal hills, especially with respect to characteristic widths and lengths. But rather than derive the model from the SM-II data, we use the Sea Beam lines which cross the SM-II survey area for the parameter estimation. This provides an independent, if not quite direct, data-synthetic comparison. Because of the correlated SM-II noise, we must restrict the comparison to larger scales than for the Sea Beam comparison; i.e. to scales on the order of many abyssal hills.

In this section we make 3 comparisons using a northern, central and southern section of the SM-II survey area. These sections are outlined in Figure 4.4. The sections are all near the ridge, and include a portion of the ridge axis. Sea Beam swaths 1, 2, and 4 were used to estimate model parameters for the generation of synthetic topography for comparison with the sections which each passes through. A square root of age subsidence curve [*Parsons and Sclater*, 1977] was added to each of the synthetic topographies to improve the comparison. For presentation, the SM-II bathymetric data were gridded at 50 m intervals. To reduce the effects of noise, the gridded data were then averaged over 4 × 4 boxes and plotted at 200 m pixel resolution. The synthetic data were generated and plotted at the same resolution Both the SM-II data sections and synthetic topography are plotted as grey-shaded, color-contoured images. The artificial illumination angle is always from the northwest to best highlight the abyssal hill fabric while minimizing the along-track SM-II artifacts.

The Southern Section

We begin with our most favorable comparison (the southern section) and proceed to less favorable comparisons (the central and northern sections). The data-synthetic comparison for the southern section is shown in Figure 4.11. The data contains artifacts, most notably the lack of side-scan data directly beneath the ship and noisy bands associated with half-power transmitters on the port side (now replaced), which make it difficult for the eye to attune to the abyssal hill fabric. Nevertheless, with some squinting and mental filtering, it can be done.

Our initial evaluation of the comparison is quite favorable; the low-order stochastic character of the synthetic (rms height, azimuth of lineation, characteristic widths and lengths) matches that of the real data fairly well. It is also encouraging that the stochastic character of the bathymetric data appears to be fairly consistent (i.e. roughly stationary) over the region shown, suggesting that changes in stochastic character are gradual and that the character of large regions can be estimated from small bathymetric samples. An important litmus test to consider is the character of abyssal hill widths. Since the characteristic widths were found to be well-matched by the synthetics in the Sea Beam data-synthetic comparison (Figure 4.8), we should expect the same result for the SM-II comparison. In this way Sea Beam can serve as a stochastic groung-truthing tool for the less-accurate SM-II data. In Figure 4.11 it does appear that abyssal widths compare favorably. We thus have some measure of confidence in the SM-II data and the validity of this comparison.

Close inspection of the length characteristics reveals a moderate but important discrepancy between the stochastic model and the data. Although it is difficult to trace abyssal hills across swaths, it is fairly clear that on the SM-II data they are more linearly bounded than the synthetic Gaussian hills with aspect ratio of 6.1. The comparison is improved by increasing the abyssal hill lengths. The second synthetic topography shown in Figure 4.11 was generated from the same parameters as the first with the exception of λ_s, which was increased by a factor of 25% (approximately the limit of the 1-σ error). The altered synthetic is clearly an improvement; the edges of the abyssal hills are more linear and the comparison to the data is fairly good. Increasing the abyssal hill lengths by 50% of the estimated value (the third synthetic in Figure 4.11) appears to further improve the comparison. It is therefore likely that in this region the characteristic length is underestimated by the inversion of Sea Beam data.

The most likely causes for underestimating the value of λ_s involve errors in the modeling assumptions. To properly assess the contribution each possible assumption error will require further study. Our preferred explanation is that the covariance function is under-parameterized. In particular, the characteristic length can be underestimated if the aspect ratio is smaller at the scale of the Sea Beam swath width than at the scale of the characteristic length. The current parameterization of the covariance function does not allow for any dependence on scale. A change in aspect ratio with scale could be the result of scale-defined processes acting on the formation of abyssal hills. For example, it is possible that normal surface faulting, creating steep linear scarps with a high degree of anisotropy, is the most influential process forming the abyssal hills at the scales which are evident to the eye in Figure 4.11. At smaller scales (e.g. the width of a Sea Beam swath), constructional volcanism and/or pit collapse, with a probable lesser degree of anisotropy, may be an important influence on the along-strike variation in abyssal hill morphology. This is consistent with deep-tow observations made by *Bicknell et al.* [1987] near the EPR at 19° 30' S that volcanic structural relief generally consists of shorter-wavelength features superimposed on the dominant faulted structure. Increasing the parameterization of the covariance model may enable it to characterize the separate contributions of each of these processes. To test such models, however, we will need extensive 2-D high-resolution coverage of abyssal hill morphology as well as better physical understanding of the processes acting on the formation of oceanic crust.

Central and Northern Sections

The data-synthetic comparisons for the central and northern sections are both shown in Figure 4.12. For the central section, we used data to the west of the ridge rather than to the east (where swath 2 is located) because swath 2 passed near several large seamounts, which overprint and obscure the surrounding abyssal hill fabric. The central and northern comparisons are considered together because the conclusion regarding them is the same: the SM-II bathymetric data collected on the MW8707 cruise are insufficient to capture the stochastic abyssal hill character in this region. Neither of the comparisons in Figure 4.12 pass the litmus test; i.e. the abyssal hill widths displayed by the SM-II data are considerably broader than those displayed by the synthetic image. Since the Sea Beam data-synthetic comparisons (Figures 4.5 and 4.6) were favorable with respect to abyssal hill widths, we conclude that the problem lies with the SM-II data.

Given the characteristics of SM-II noise discussed earlier, this is not a surprising conclusion. The characteristic widths are short in these two sections (1.8 ± 0.43 km for the central section and 1.2 ± 0.32 km for the northern), not much larger than the noise correlation width (~1 km). If noise has a correlation width of 1 km, it is reasonable to assume that the response of the SM-II system in this survey averages the seafloor in some fashion over an area ~1 km wide. Furthermore, if the response is similar to a first arrival echosounder, or if the signal is dominated by strong scatterers, then the averaging effects will be intensified in regions of high relief. The differences between the rms height and characteristic width in the southern region ($H = 44 \pm 3$ m, $\lambda_n = 2.3 \pm 0.51$ km) and those in the central ($H = 68 \pm 5$ m, $\lambda_n = 1.8 \pm 0.43$ km) and northern ($H = 72 \pm 6$ m, $\lambda_n = 1.2 \pm 0.32$ m) regions may be critical in determining whether or not SM-II bathymetric data can be used to accurately portray abyssal hills.

GEOLOGIC CORRELATIONS WITH STOCHASTIC PARAMETERS

The estimated stochastic parameters listed in Table 4.2 represent a quantitative characterization of the abyssal hills near the ridge crest between 13° and 15° N. To form a basis on which these parameters can be interpreted geologically we must first establish empirical correlations between the parameters and geological variables such as spreading rate and direction, ridge morphology, magma supply, etc.

The lineation azimuths shown in Table 4.2 all appear to be well resolved (errors are generally ± 1° or ± 2°). However, these errors are evaluated with respect to ship direction only, and do not include uncertainties in ship navigation. Errors in ship direction are probably on the order of ± 2° or ± 3° so that the resolution of ζ_s for these swaths is likely to range from ± 3° to ± 5°. Within these errors, the near ridge swaths (swaths 1-4) have abyssal hill lineations which are parallel to the trend of the EPR in this region (~349°). The lineation azimuths estimated from the off-ridge swaths on the Papatua 1 track line (swaths 5 and 6) are somewhat more northerly, which is consistent with the change in trend of magnetic lineations [*Klitgord and Mammerickx*, 1982]. The azimuth of 356° ± 1° estimated from swath 5 (located just inside the western propagator pseudofault) may, however, be slightly greater than expected. Though not nearly as pronounced, this difference in expected strike is similar to the change in orientation of abyssal fabric noted by *Kleinrock and Hey* [1989] for topography just inside the outer pseudofaults of the Galapagos 95.5° W propagator.

The remaining three parameters show considerable variation and may contain useful new information about ridge tectonics in this region. In Figure 4.4 the estimated values for H, λ_n and λ_s are shown next to the respective swaths. Plotted in this way the stochastic parameters can be compared with the regional morphology. The near-ridge swaths (swaths 1-4) provide a chance to correlate quantitative seafloor character with observed ridge morphology. The change in stochastic parameters from north to south appears to be well-correlated with the change in ridge crest complexity over the same region. This is clearest for the rms height; the variation of topography about the mean depth is greatest in the north (72 ± 6 m) where the ridge complexity is greatest, and monotonically decreases southward to 44 ± 3 m at the southern end of the SM-II survey area where the ridge crest is defined by a simple, broad and well-defined crestal horst. The characteristic abyssal hill lengths and widths also appear to be correlated with ridge complexity: both length and width are shortest for the northernmost swath and generally increase southward with decreasing ridge crest complexity.

The seafloor recorded by the long Papatua 1 swath (Figure 4.1), extending over 200 km west of the ridge crest, provides information which suggests temporal variations in accretion-related tectonics and volcanism. The three Papatua swaths show significant variation in the three estimated parameters H, λ_n, and λ_s. As with the northernmost swath (swath 1), the swath just east of the western propagator pseudofault (swath 5) represents seafloor generated immediately after passage of the propagator. The characteristic length and width of abyssal hills mapped by these two swaths are similar (8.8 ± 1.7 km and 1.2 ± 0.22 km for swath 5 compared with 7.4 ± 1.6 km and 1.2 ± 0.32 km for swath 1) and in all cases shorter than estimated for all other swaths in this region (though the differences in characteristic length are not well resolved). The rms height for swath 5 (54 ± 2 m) is greater than the near-ridge crest data (44 ± 3 m) at the same latitude, though not as large as the northern data (72 ± 6 m).

To the west of the pseudofault is seafloor that was produced before the propagator disturbed this area. This topography has the lowest average relief (31 ± 2 m) of all the swaths. The characteristic abyssal hill widths in this region (2.4 ± 0.64 km) are similar to those near the ridge crest (2.3 ± 0.51 km) at the same latitude, but the abyssal hill lengths (9.8 ± 3.0 km) are shorter than those near the ridge crest (14.1 ± 3.5 km). The length difference $\Delta\lambda_s$ = 4.3 km is not resolved, however, given the standard deviation $\sigma_{\Delta\lambda_s} = \sqrt{(\sigma_1^2 + \sigma_2^2)}$ = 4.6 km. Both the rms height and the characteristic abyssal hill widths estimated from swath 6 are resolvably different from those estimated from swath 5, just on the other side of the propagator pseudofault.

From the parameters shown in Figure 4.4 for swaths 4, 5, and 6, it is clear that the character of the abyssal hills has changed over time. It appears that we can correlate a significant change (from swath 5 to swath 6) with the time when the propagator traversed this area. It also appears that abyssal hills generated after passage of the propagator in one locale (swath 5) are stochastically similar to those in another locale (swath 1). We therefore hypothesize that the propagator significantly altered the accretionary processes for a substantial enough time after its passage to affect the formation of abyssal hill for 10's of characteristic widths (i.e. enough to measurably alter the statistics of a Sea Beam swath 30-50 km long). Since the morphology of the ridge crest may also be correlated to the flanking abyssal hill character, we also infer that the degree of morphological complexity of the ridge crest and its attendant weakness in magma supply may also depend at least in part on the time since passage of the propagating ridge tip.

CONCLUSIONS AND DISCUSSION

The second-order stochastic model for the seafloor and the Sea Beam inversion procedure provide good initial means of quantitatively describing the low-order characteristics of the seafloor. This description provides estimates of physical characteristics of abyssal hill morphology, including rms height, azimuth of lineation, characteristic lengths and widths, aspect ratio, and Hausdorff dimension. The Sea Beam data-synthetic comparisons indicate that we are generally successful in estimating rms height, lineation direction, and characteristic abyssal hill widths. The comparisons also indicate the need to include a description of higher order moments in the stochastic characterization to detect and quantify abyssal hill asymmetries and peakiness. The SM-II data-synthetic comparison for the southern section (Figure 4.11) suggests that, at the scale plotted for this comparison, the inversion underestimates the characteristic abyssal hill length. This discrepancy may be due to under-parameterization of the covariance function description of topography. A more realistic covariance model may need to include the variation of anisotropy with scale. The northern SM-II data-synthetic comparisons (Figure 4.12) indicate more about the limitations of SM-II data than about the stochastic modeling.

It has been proposed that abyssal hills in fast spreading regions are formed primarily by ridge-parallel normal faulting [*Bicknell et al.*, 1987; *Pockalny, et al.*, 1989]. It is therefore a potentially useful exercise to interpret the stochastic properties of abyssal hill in terms of the faulting process alone. For example, the characteristic abyssal hill width may be related to the average spacing of large offset faults. The rms height may be related to the amount of offset on the faults, and the length may be related to the average length of the surface breaking faults (or the coherence of faulting along-strike). If faulting characteristics can also be related to the ridge characteristics, information concerning the lengths of abyssal hills may provide insight into the along-strike variation in ridge morphology. There is much ground-truthing work to be done, however, before these relationships can be made quantitative, if such relationships can, in fact, be defined.

If faulting is the principal abyssal hill forming process in this region at the scale of characteristic abyssal hill widths and lengths, it is possible that at smaller scales constructional volcanism plays a more important role, decreasing the degree of anisotropy with decreasing feature scale. It is difficult with the present data sets to determine what the influence of each abyssal hill forming process is at different scales. As we stated previously, constructional volcanism may have an important effect in this region at the scale of a Sea Beam swath width (~2.25 km). In other regions, such as the north Atlantic [*Pockalny, et al.*, 1989] and the Juan de Fuca ridge [*Kappel and Ryan*, 1986], constructional volcanism may the the principal abyssal hill forming process. We should expect that with varying spatial and temporal tectonic factors (e.g. magma supply, episodicity and flow type, or presence or absence of an axial valley), the relative contributions of tectonism and volcanism to the formation of abyssal hills should also vary. Data with greater spatial resolution than either Sea Beam or SM-II data, applicable over a wide range of scales, will be needed to perform an adequate study of the variation in stochastic characteristics with scale.

The stochastic parameters derived from the inversion (Table 4.2, Figure 4.4) change significantly from one swath to the next. We can make the following initial correlations with the observed morphological structures in the region. The ridge has been shown to be complex and ill-defined in the northern half of the SM-II survey area. South of 14° N, the ridge crest is characterized by a single, well-developed high which broadens to the south. The near-axis stochastic character of the abyssal hills undergoes a corresponding change from north to south. In the north the abyssal hills have large average relief (72 ± 6 m) and short length (7.4 ± 1.6 km) and width (1.2 ± 0.32 km) (swath 1). In the southern portion of the survey area, the relief monotonically decreases to 44 ± 3 m and the characteristic length and width generally increase to 14.1 ± 3.5 km and 2.3 ± 0.51 km respectively at the southernmost swath (swath 4).

With the long east-west Papatua 1 track line (Figure 4.1) we can correlate changes in stochastic character with temporal changes in ridge activity. A change in abyssal hill morphology apparently coincided with the passage of the propagating rift. Before the propagator (swath 6), the abyssal hills formed with low average relief (31 ± 2 m) and (by the standards of the region) fairly wide characteristic widths (2.4 ± 0.64 km) and moderate lengths (9.8 ± 3.0 km). After the propagator (swath 5), relief increased to 54 ± 2 m, the characteristic widths decreased to 1.2 ± 0.22 km, and the lengths decreased to 8.8 ± 1.7 km (although the change in length is not well resolved). Near present (swath 4), the relief has decreased back down to 44 ± 3 m, the widths have increased to 2.3 ± 0.51 km, and the lengths have increased to 14.1 ± 3.5 km. The first post-propagator swath (swath 5) is similar in temporal/spatial proximity to the propagator as the far northern swath (swath 1). Characteristic lengths and widths estimated from the two swaths are also similar, though their rms heights differ significantly.

These correlations suggest a scenario for the SM-II survey region in which, as the propagator tip passes, it leaves in its wake a complex ridge with associated abyssal hill faulting which is more frequent (shorter characteristic width), produces higher relief, and is less coherent along the length of the ridge (shorter characteristic lengths) than the abyssal hills generated before the propagator. In time the ridge settles down to its previous, simpler state with a clearly defined crestal horst, and producing wider and lower abyssal hills which are more coherent along-strike. From the southern SM-II data-synthetic comparison it appears that the abyssal hills are longer than estimated by the Sea Beam data alone. This should also be the case for the estimates from westernmost Papatua 1 swath (swath 6). Since the average relief is lower in this case, the effects of a decrease in anisotropy with decreased scale on biasing the estimation of λ_s should be greater. Thus the topography shown in swath 6 (Figure 4.10) may represent the steady state toward which the abyssal hill forming processes are headed after being disturbed by the passage of the propagator.

From the increase in the rms height across the propagator and from the decrease in relief from north to south, it appears clear that the topographic relief has been influenced by the time since passage of the propagator. However, just how much an effect it has had is uncertain. The relief estimated from swath 5, just east of the propagator in the south, is significantly less than for the two northern swaths (swaths 1 and 2), which are respectively the same distance as and farther from the propagator than swath 5. It appears that more than just the propagator has influenced the rms height; perhaps proximity to the Orozco Fracture Zone is also an important factor in determining this parameter.

If the complex, deep ridge crest in the north of the SM-II survey area characteristically produces relatively high relief and short length and width abyssal hill morphology, then we may, in turn, associate such abyssal hill morphology with the weakness in magma supply attributed to such ridge crest type. The further possible association of this type of abyssal hill morphology with the recent propagation of the ridge consequently prompts us to hypothesize that a weak magma supply is also associated with recent ridge propagation. This series of relationships is tenuous at best and requires further data to substantiate. However, the hypothesis they suggest is certainly reasonable since it should take time to set up a steady-state magma chamber and well-developed plumbing system for a new rift. This hypothesis was earlier forwarded by *Christie and Sinton* [1981; 1986] and *Sinton et al.* [1983] on the basis of variations in crystal fractionation throughout the evolution of the Galapagos 95.5° W propagator. It is also consistent with the tectonic model proposed by *Kleinrock and Hey* [1989] for the evolution of the same propagator. In their model, volcanism does not begin until 6.5 km behind the tectonic initiation of the propagating rift. Volcanism, furthermore, does not become localized into a neovolcanic zone until 4.5 km beyond the initiation of volcanism and the full rate of spreading is not reached until 10 km beyond the neovolcanic tip, ~21 km beyond the initial rift. Given the rate of propagation of

~52 km/my [*Kleinrock and Hey*, 1989], this translates to ~0.4 my after rift initiation. Although the dynamics of a slow spreading ridge propagator may be substantially different than for a fast one, the implication of this model is that magma supply slowly increases and becomes more organized with increase in age since passage of the propagator tip. The propagation velocity for the propagator in the vicinity of 13°-15° N is approximately 108 km/my [*Madsen et al.*, 1990]. Application of *Kleinrock and Hey*'s [1989] model to the 13°-15° N propagator in terms of time since propagation suggests that we might not expect to see the ridge crest dynamics return to normal until at least 50 km south of the crack tip. However, for the 13°-15° N propagator, the crestal horst does not become clearly defined until ~14° N, 100 km south of the propagator tip. This may imply that the faster spreading-rate propagator requires more time to organize into a stable rift system than does the slower spreading-rate propagator, or, again, that proximity to the Orozco Fracture Zone also has an important influence on the formation of abyssal hills.

TABLE 4.1. Sea Beam Data Used for Parameter Estimation.

Swath	Cruise	Ship	Starting Date	Starting Time	Starting Latitude, deg. N	Starting Longitude, deg. E	Ending Time	Length of Data, km	Number of Data Points	Reference
1	Ceres 2	*Thomas Washington*	July 29, 1982	0600	14.84	-103.97	0800	41	708	Macdonald
2	Ceres 2	*Thomas Washington*	July 27, 1982	1715	14.07	-103.61	2030	56	1152	Macdonald
3	RC2607	*Robert Conrad*	June 07, 1985	0200	13.41	-104.34	0630	33[a]	2676	Detrick
4	Papatua 1	*Thomas Washington*	Oct. 14, 1985	0530	13.17	-104.62	0800	54	1484	McClain
5	Papatua 1	*Thomas Washington*	Oct. 14, 1985	0300	13.16	-105.13	0530	55	1486	McClain
6	Papatua 1	*Thomas Washington*	Oct. 13, 1985	2230	13.13	-106.04	0100	54	1486	McClain

[a] Excluding data from 0415 to 0515 hours

TABLE 4.2. Stochastic Parameters Derived from Inversion.

Swath	H, m	ζ_s^a, deg	λ_n, km	λ_s, km	a	D^b
1	72 ± 6	347 ± 2	1.2 ± 0.32	7.4 ± 1.6	6.2 ± 1.7	2.5
2	68 ± 5	351 ± 2	1.8 ± 0.43	11.3 ± 3.2	6.3 ± 1.6	2.5
3	57 ± 4	353 ± 1	1.6 ± 0.33	10.5 ± 1.9	6.7 ± 1.5	2.5
4	44 ± 3	351 ± 2	2.3 ± 0.51	14.1 ± 3.5	6.1 ± 1.6	2.5
5	54 ± 2	356 ± 1	1.2 ± 0.22	8.8 ± 1.7	7.6 ± 1.6	2.5
6	31 ± 2	354 ± 4	2.4 ± 0.64	9.8 ± 3.0	4.0 ± 1.3	2.5

[a] Lineation errors do not include the effects of navigation uncertainties.

[b] Hausdorff dimension fixed in inversion.

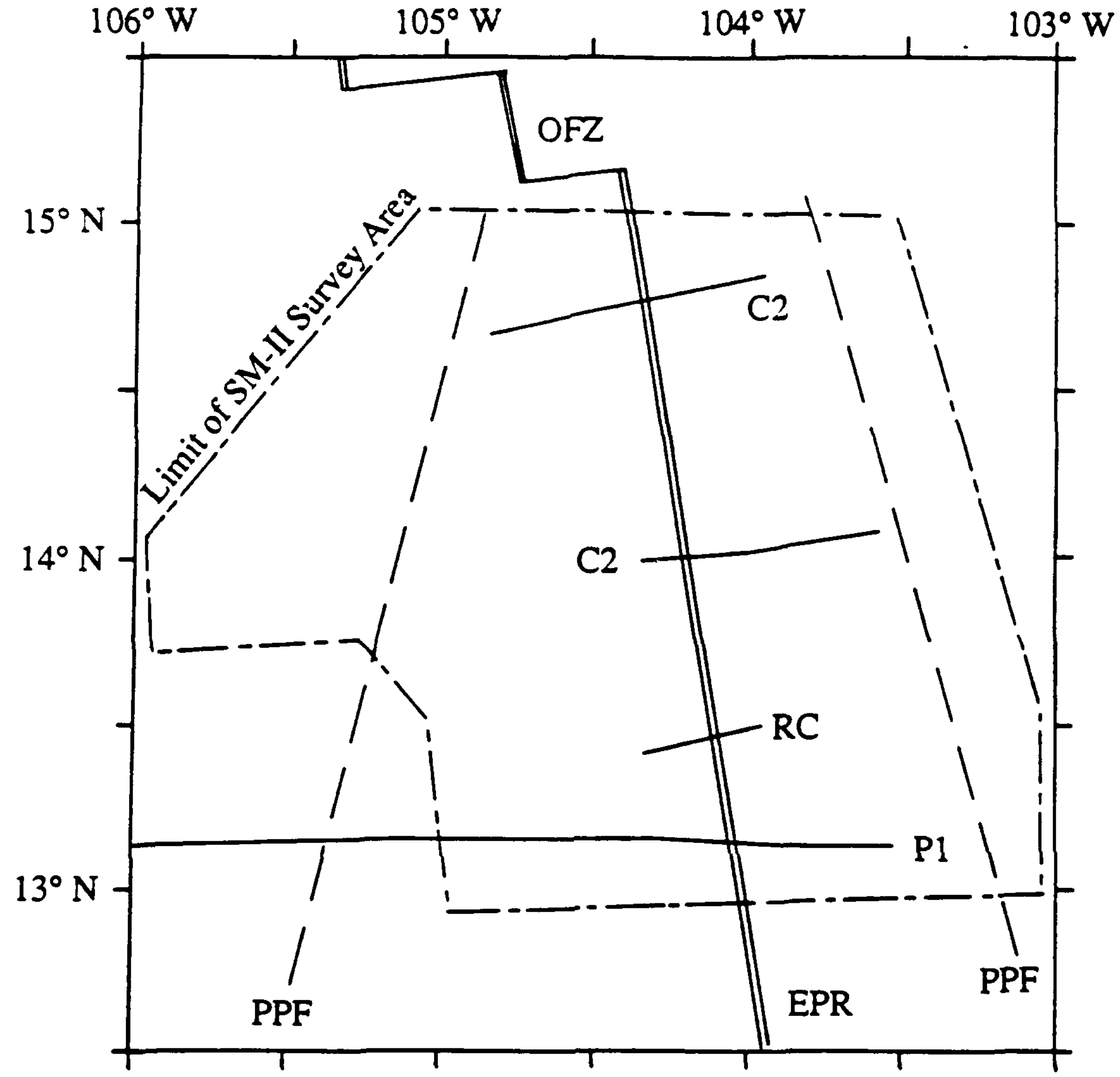
106° W
105° W
104° W
103° W
15° N
14° N
13° N
OFZ
Limit of SM-II Survey Area
C2
C2
RC
P1
PPF
EPR
PPF

Figure 4.1. Map of the SM-II survey region showing the location of the East Pacific Rise (EPR), the Orozco Fracture Zone (OFZ), and the propagator pseudofault (PPF). Also shown are the track lines of the Sea Beam data considered in this paper from cruises Papatua 1 (P1) and Ceres 2 (C2) on the *RV Thomas Washington* and RC2607 (RC) on the *RV Robert Conrad.*

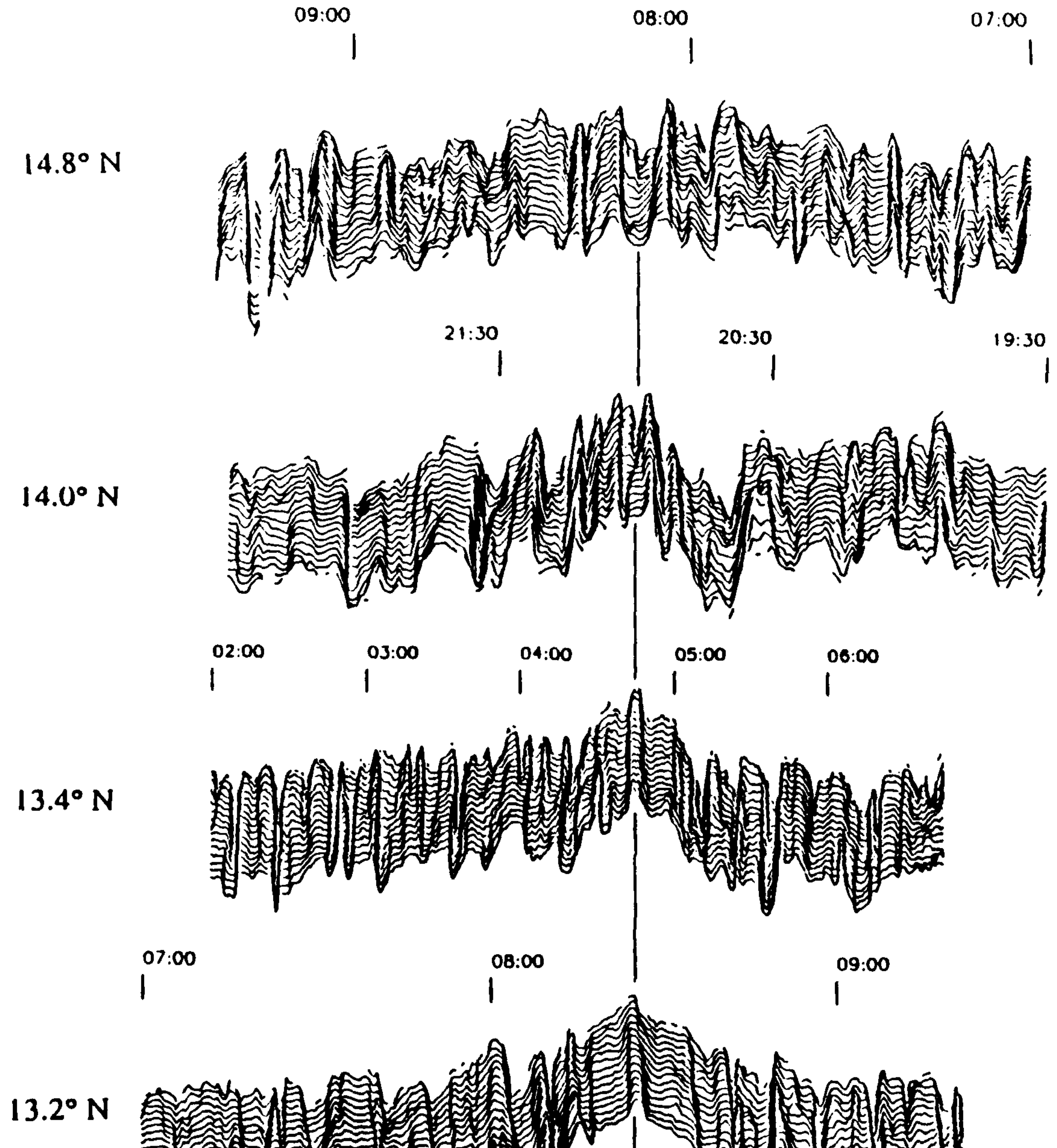

Figure 4.2. Four examples of Sea Beam data crossing the East Pacific Rise within the SM-II survey area. The depth recorded by each beam is plotted separately. The beam spacing for each swath varies as a function of beam angle, but averages to approximately 145 m in each case. Top panel: from the Ceres 2 cruise of the *RV Thomas Washington* near 14.8° N. The average along-track data spacing is 58 m. Second panel: from the Ceres 2 cruise of the *RV Thomas Washington* near 14.0° N. The average along-track data spacing is 49 m. Third panel: from the RC2607 cruise of the *RV Robert Conrad* near 13.4° N. The average along-track data spacing is 16 m. Bottom panel: from the Papatua 1 cruise of the *RV Thomas Washington* near 13.2° N. The average along-track data spacing is 36 m.

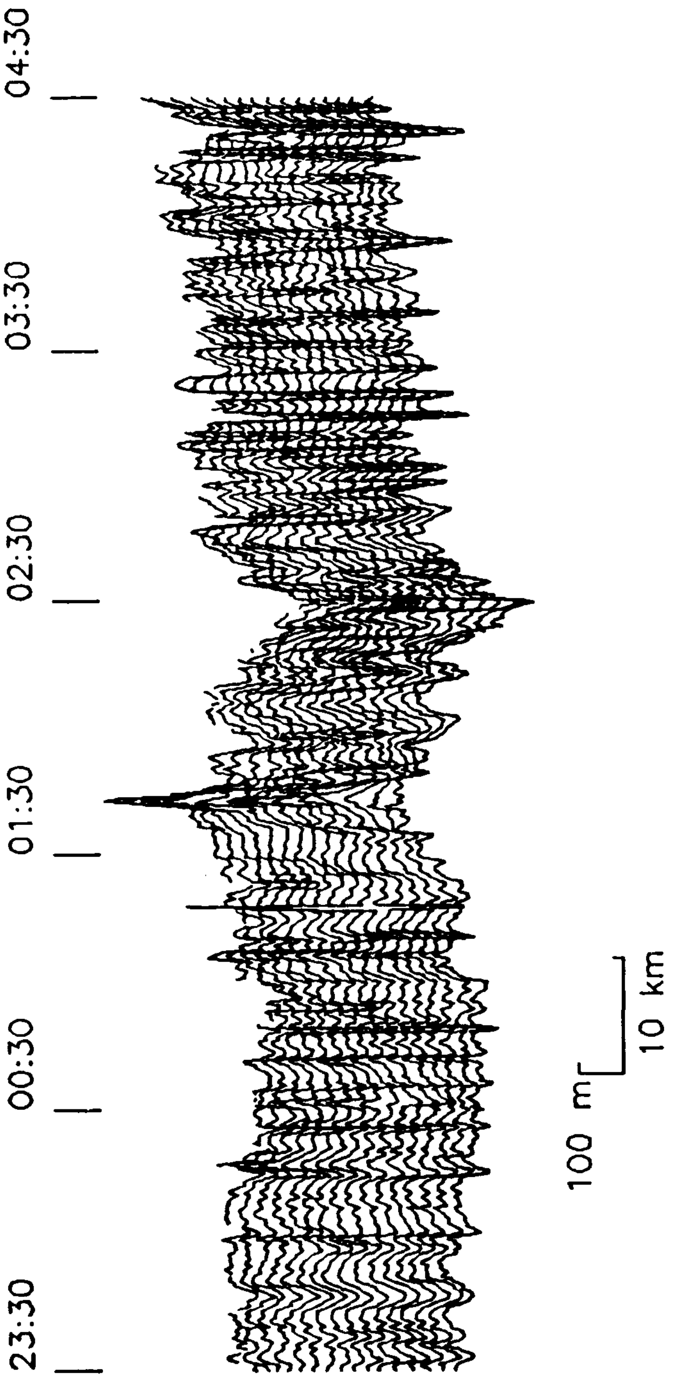

Figure 4.3. Sea Beam data from the Papatua 1 cruise of the *RV Thomas Washington* (See Figure 4.1) crossing the propagator pseudofault ~120 km west of the EPR near 13.1° N. The depth recorded by each beam is plotted separately. The average along-track data spacing is 36 m and the average beam spacing is 155 m.

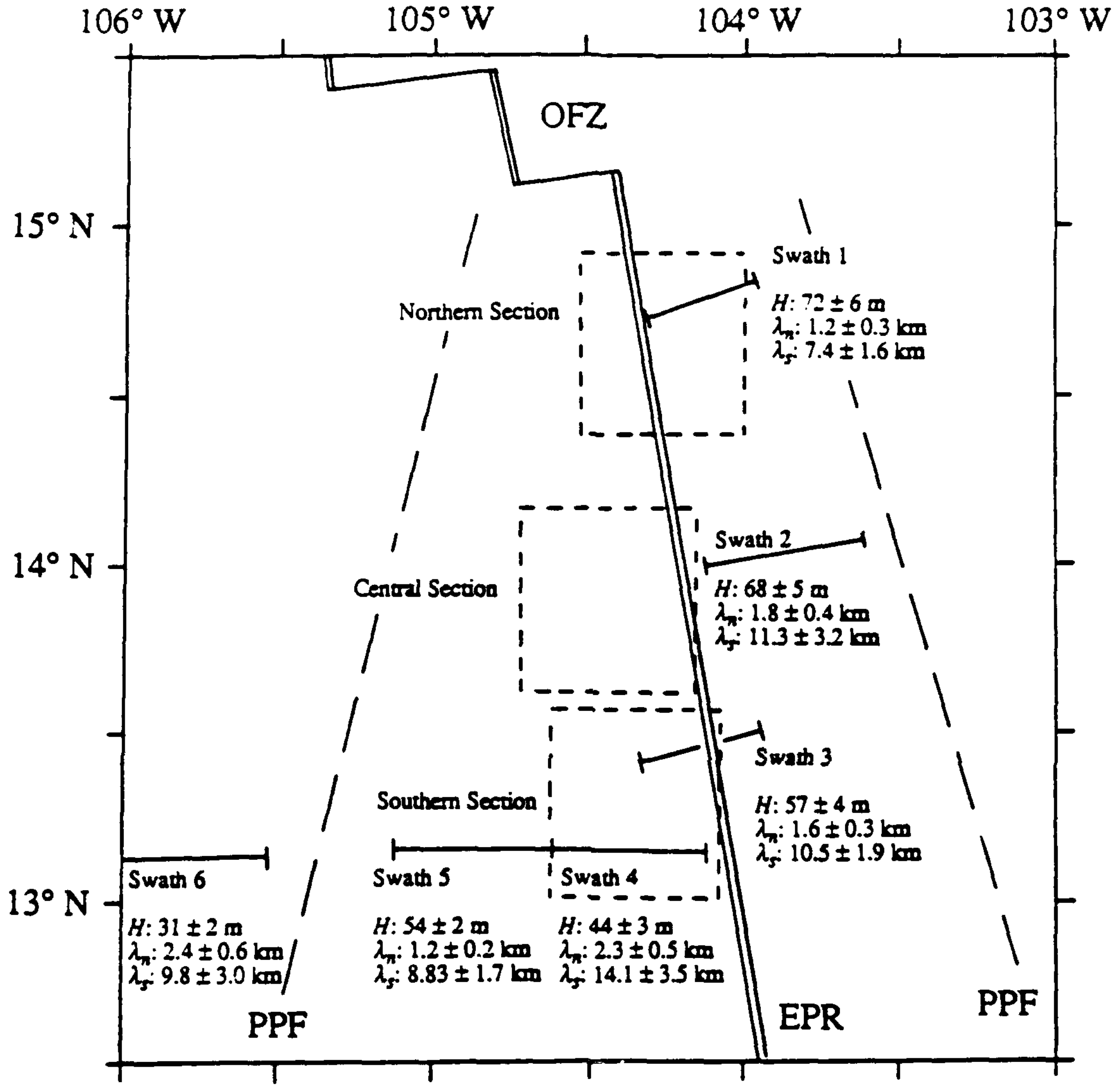
106° W
105° W
104° W
103° W
15° N
14° N
13° N
OFZ
Swath 1
H: 72 ± 6 m
λn: 1.2 ± 0.3 km
λs: 7.4 ± 1.6 km
Northern Section
Swath 2
H: 68 ± 5 m
λn: 1.8 ± 0.4 km
λs: 11.3 ± 3.2 km
Central Section
Swath 3
H: 57 ± 4 m
λn: 1.6 ± 0.3 km
λs: 10.5 ± 1.9 km
Southern Section
Swath 6
H: 31 ± 2 m
λn: 2.4 ± 0.6 km
λs: 9.8 ± 3.0 km
Swath 5
H: 54 ± 2 m
λn: 1.2 ± 0.2 km
λs: 8.83 ± 1.7 km
Swath 4
H: 44 ± 3 m
λn: 2.3 ± 0.5 km
λs: 14.1 ± 3.5 km
PPF
EPR
PPF

Figure 4.4. Map of the SM-II survey area showing swaths 1-6 used for the estimation of stochastic parameters. The estimated values of H, λ_n and λ_s are listed next to each swath. Also shown are the outlines of the three SM-II sections used for data-synthetic comparisons in Figures 4.11 and 4.12.

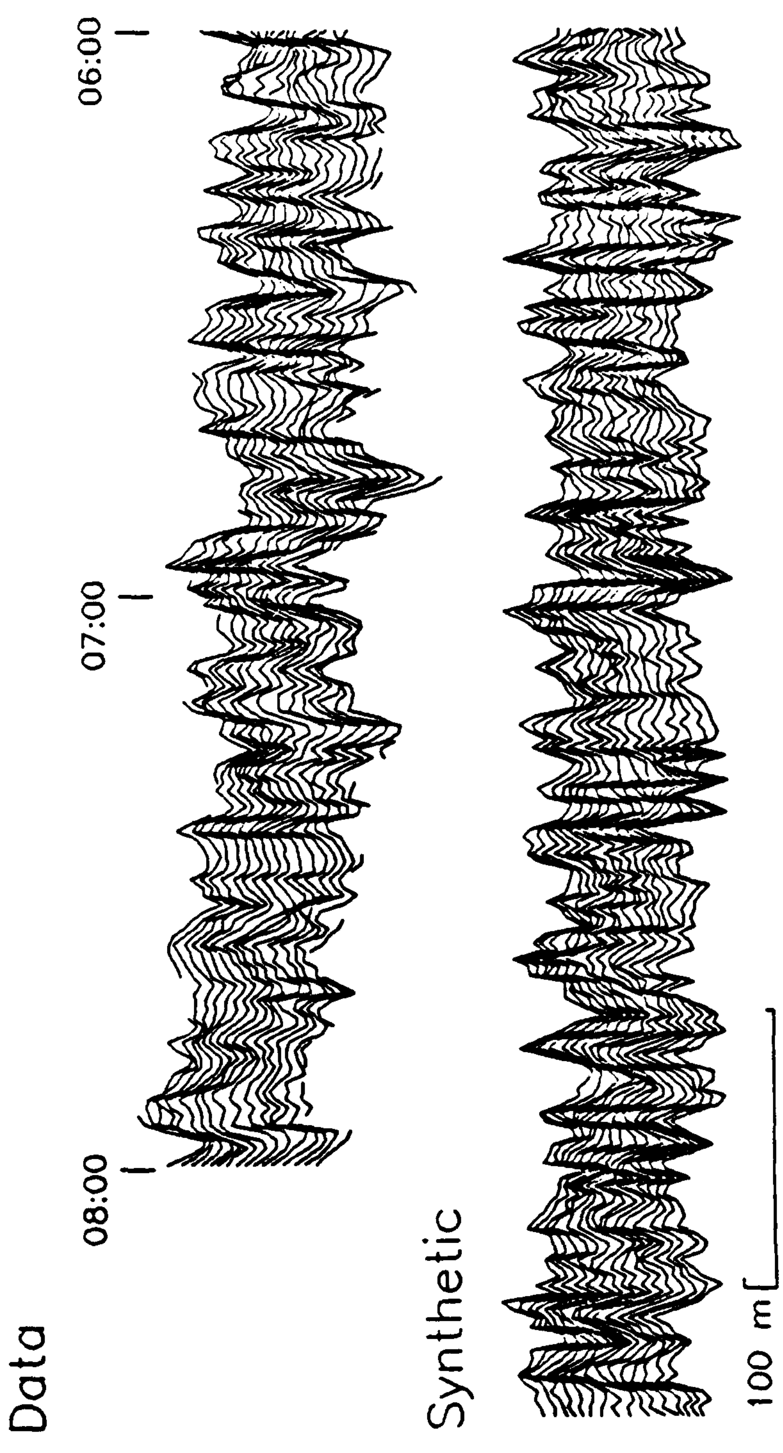

Figure 4.5. Comparison of Sea Beam data from swath 1 (Table 4.1, Figure 4.4) with synthetic data generated from the covariance parameters estimated from an inversion of this data set (Table 4.2). Appropriate Sea Beam noise and response were applied to the synthetic data set and both data and synthetic have been averaged over 5 pings. The depth recorded by each beam is plotted separately.

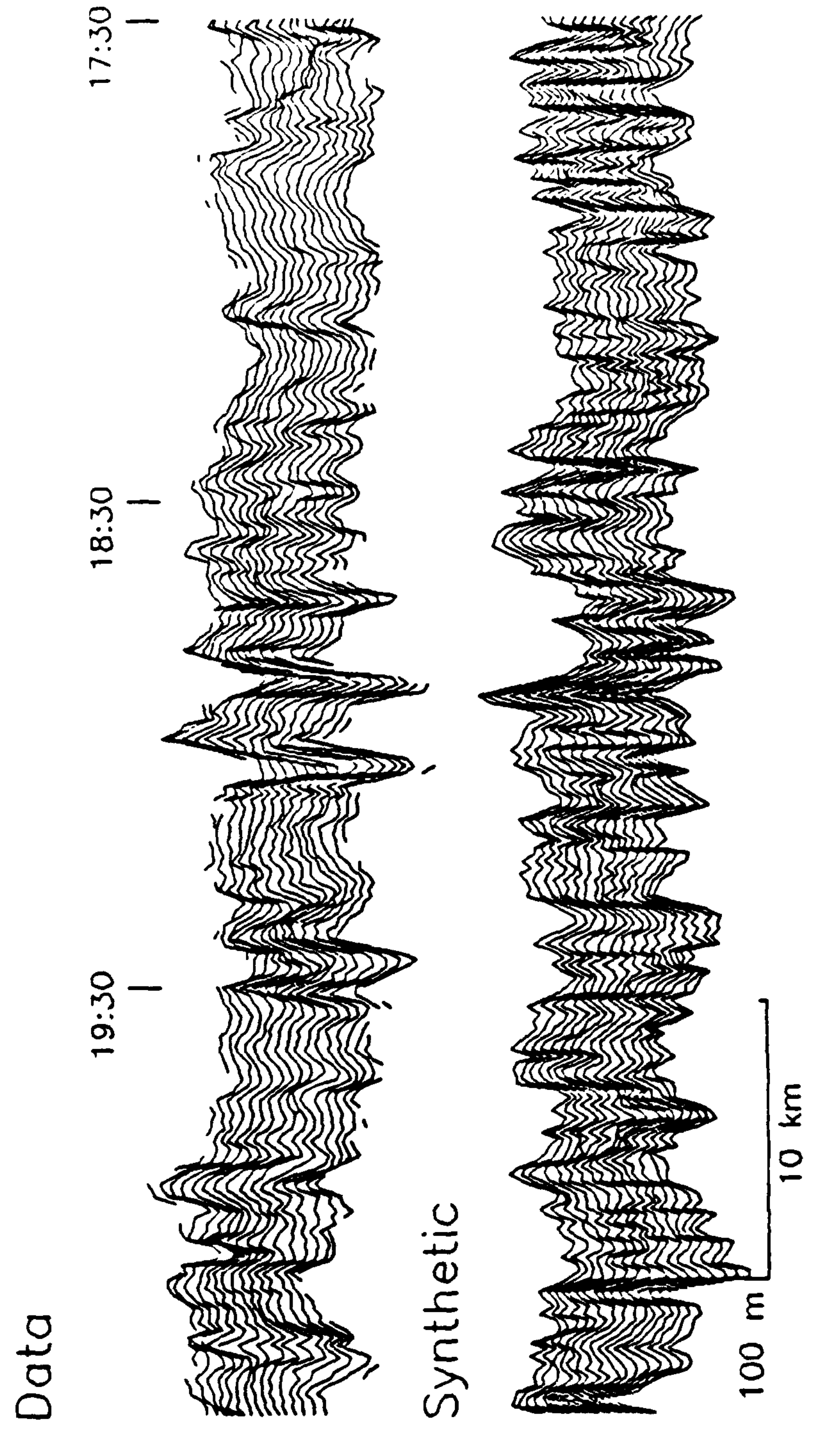

Figure 4.6. Data-Synthetic comparison for swath 2. See Figure 4.5 for further details.

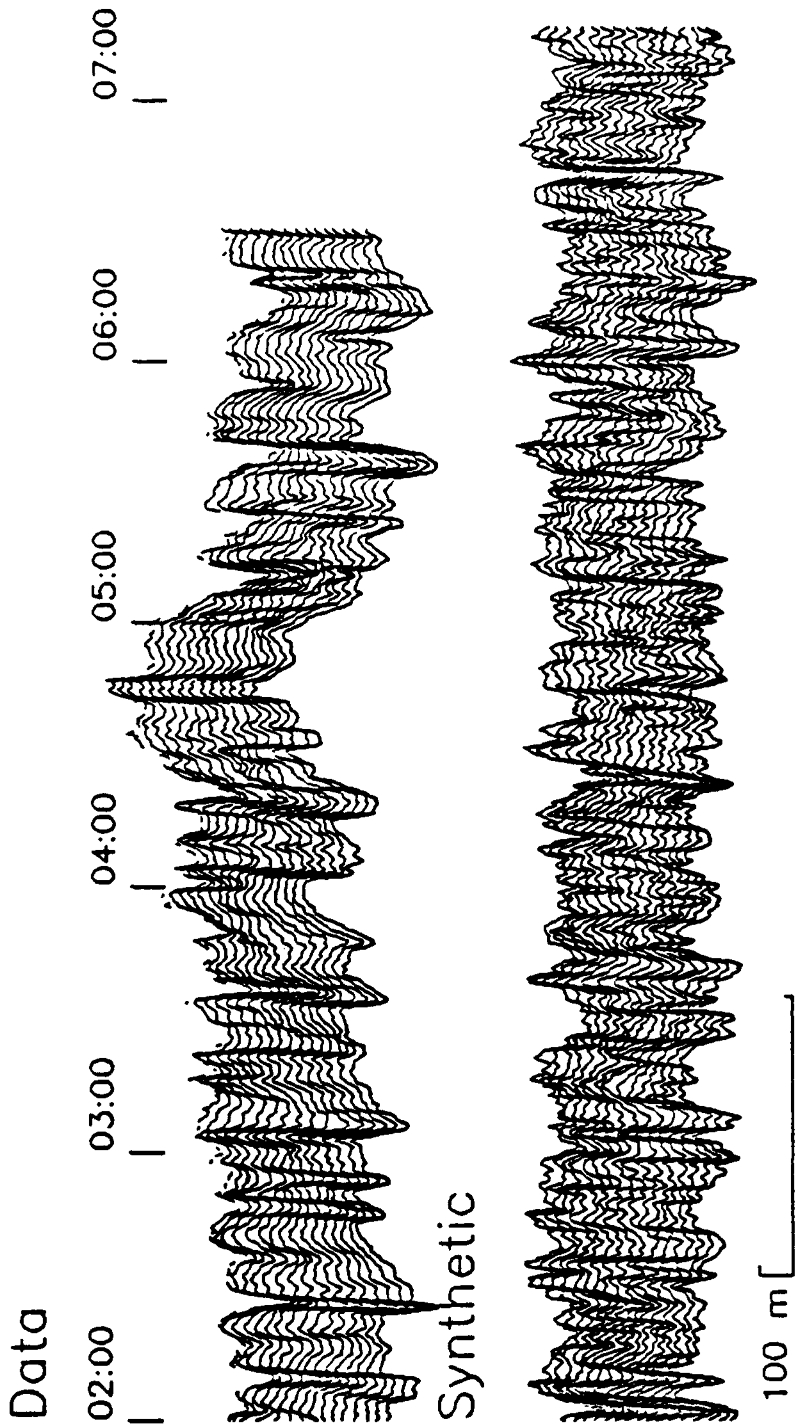

Figure 4.7. Data-Synthetic comparison for swath 3. See Figure 4.5 for further details.

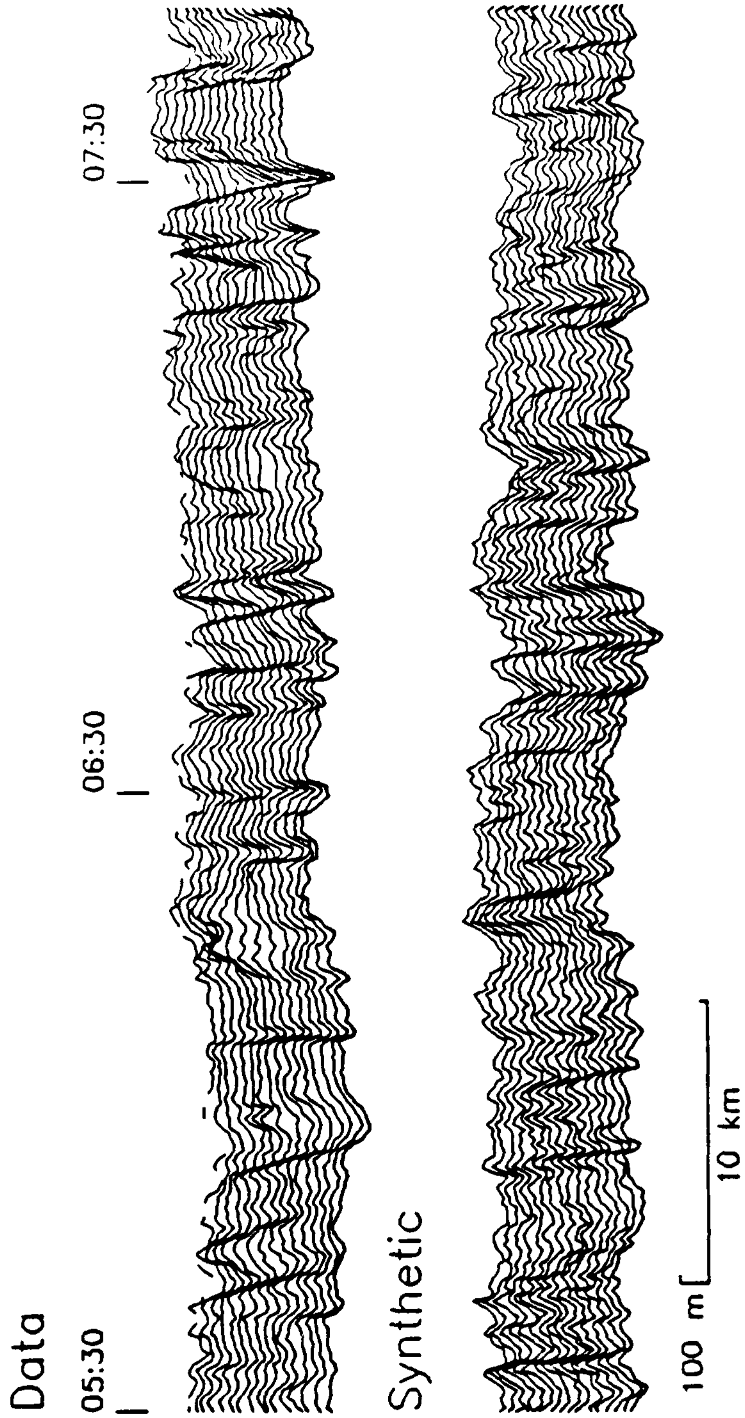

Figure 4.8. Data-Synthetic comparison for swath 4. See Figure 4.5 for further details.

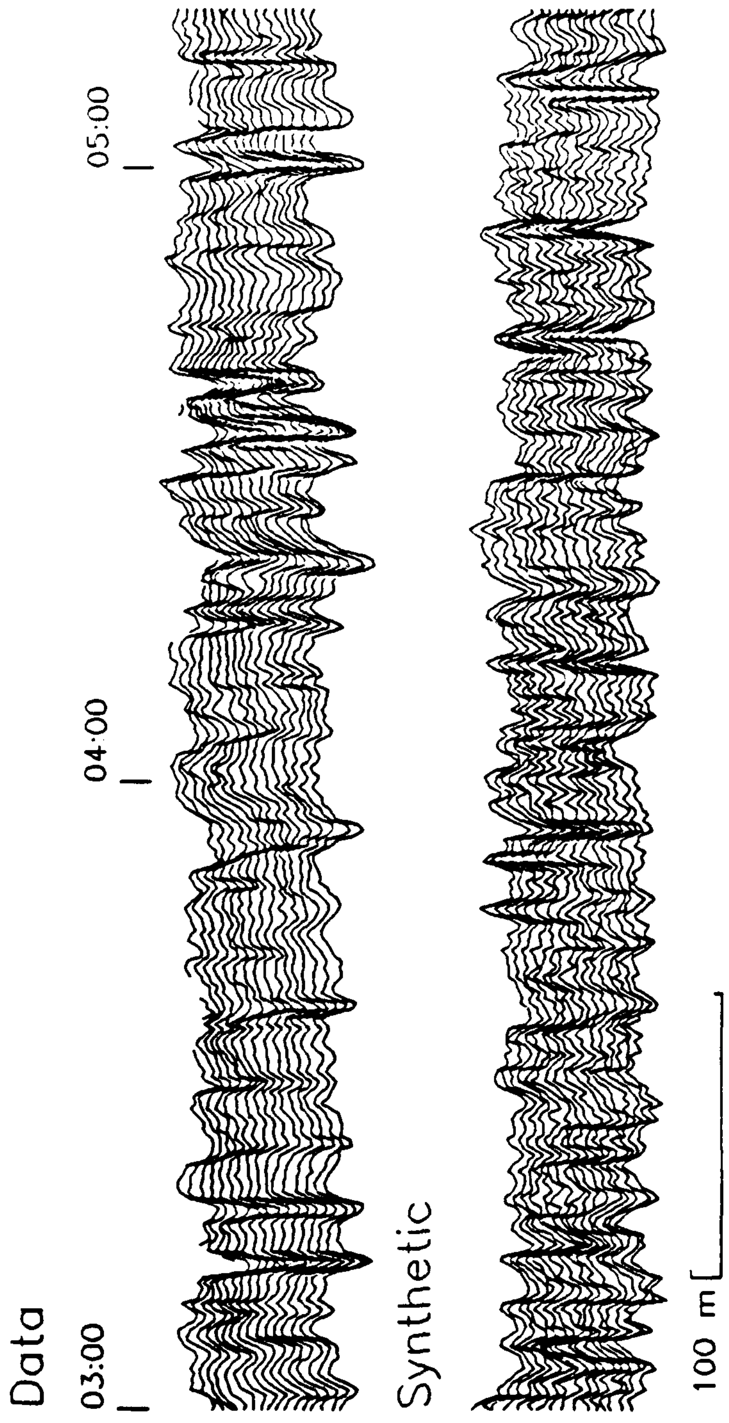

Figure 4.9. Data-Synthetic comparison for swath 5. See Figure 4.5 for further details.

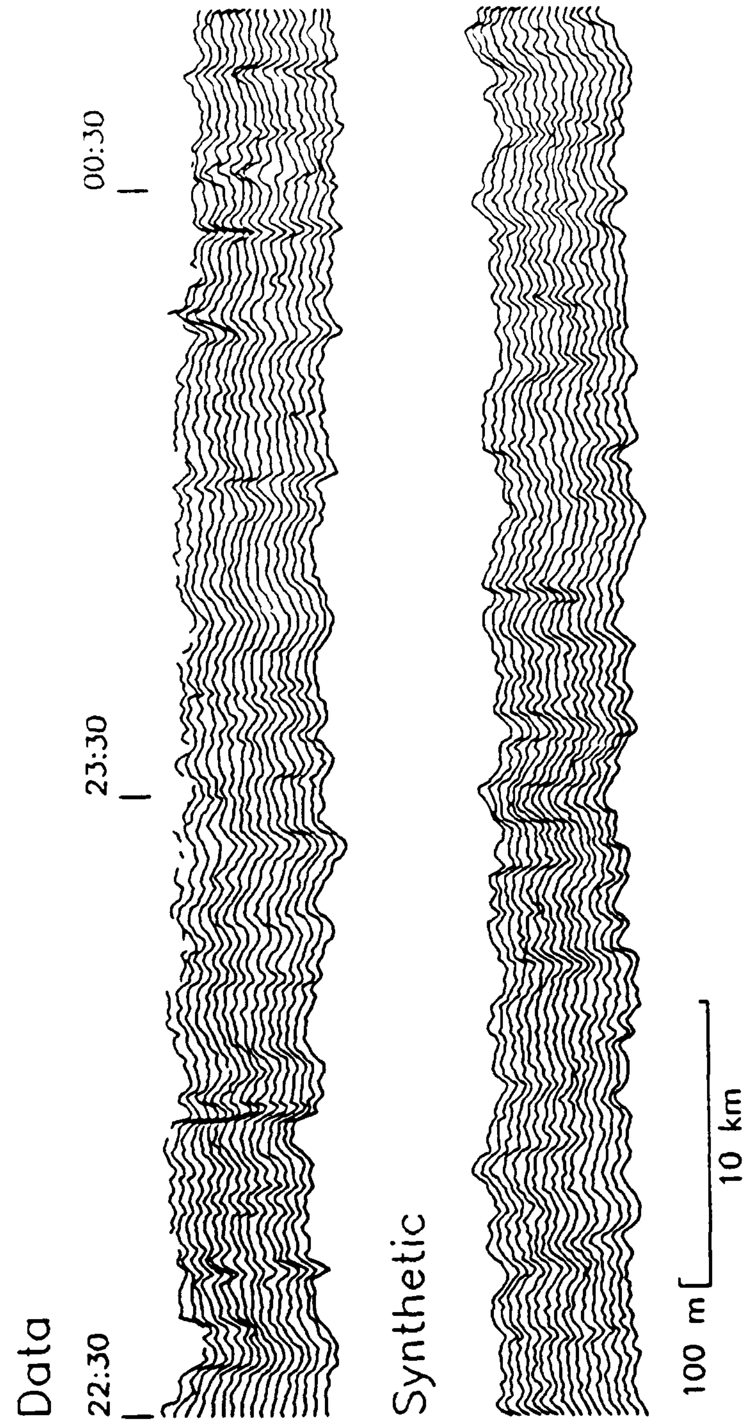

Figure 4.10. Data-Synthetic comparison for swath 6. See Figure 4.5 for further details.

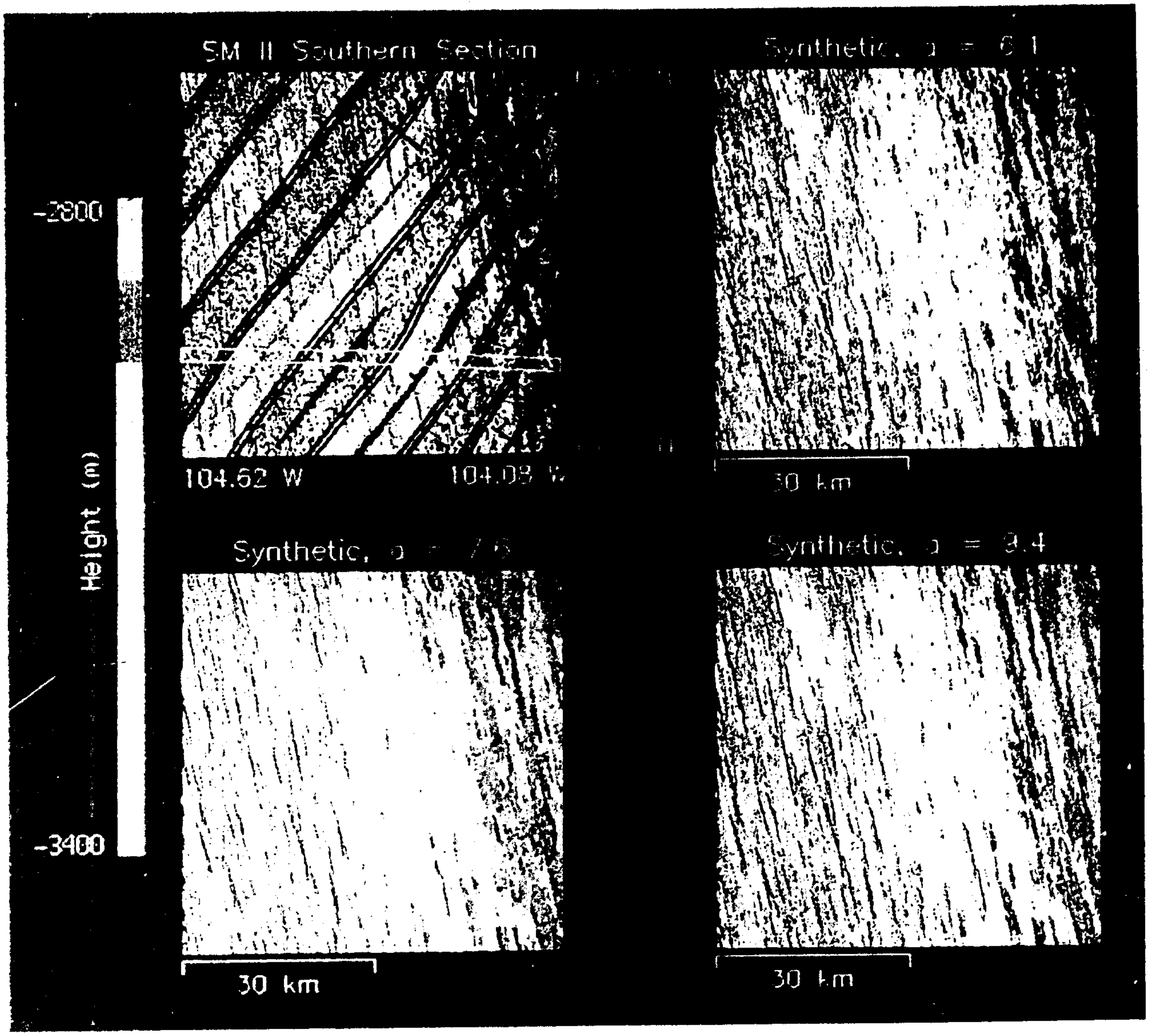

Figure 4.11. Comparison of grey-shaded color relief images of SM-II bathymetry data from the southern section (Figure 4.4) to a synthetic surface generated from the covariance model. The SM-II data, originally gridded at 50 m spacing, has been averaged over 4 × 4 boxes and plotted at 200 m pixel spacing. The synthetic topography was also generated at 200 m spacing. The parameters used to generate the first synthetic surface (upper right panel) were estimated from the inversion of swath 4 (Table 4.2). The Papatua 1 swath, from which swath 4 was taken, is shown on the data image in white. The second two synthetic surfaces were generated using the same parameters as the first with the exception of λ_s (originally 14.1 ± 3.5 km), which was increased by 25% (lower left panel) and 50% (lower right panel). Square root of age curves have also been added to the synthetics to simulate deterministic ridge morphology. Both surfaces are artificially illuminated from a sun azimuth of 45°. This angle emphasizes abyssal hill texture while minimizing SM-II swath effects.

Best Available Copy

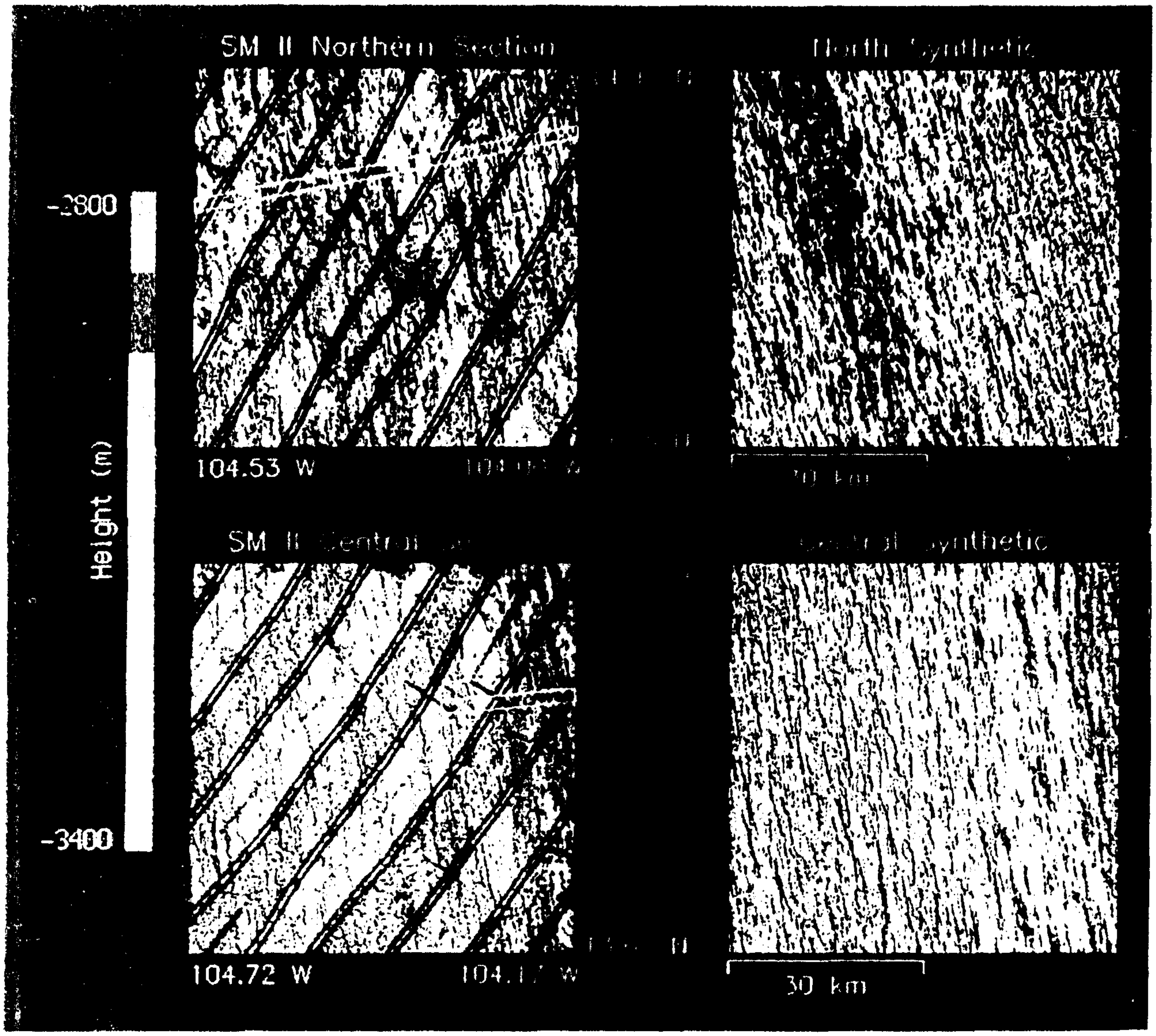
SM II Northern Section
North Synthetic
-2800
Height (m)
-3400
104.53 W
30 km
SM II Central
Central Synthetic
104.72 W
30 km

Figure 4.12. Comparison of grey-shaded color relief images of SM-II bathymetry data from the northern section (Figure 4.4) (upper two panels) and the central section (Figure 4.4) (lower two panels) to synthetic surfaces generated from the covariance model. The parameters used to generate the synthetic surfaces were estimated from an inversion of swath 1 (Table 4.2) for the northern section and from an inversion of swath 2 for the central section. See Figure 4.11 for more details.

Best Available Copy

CHAPTER 5

A GLOBAL AND REGIONAL ANALYSIS OF NEAR-RIDGE ABYSSAL HILL MORPHOLOGY

INTRODUCTION

The second-order stochastic model and parameter estimation methodology introduced in Chapter 2 provides a valuable new tool for the investigation of morphological processes which form and reshape abyssal hills. In the previous chapter we made use of this tool to perhaps gain some new insight into the time-dependent effects of a propagating rift on ridge processes. A cornerstone of this study was our ability to characterize the ridge and near-ridge morphology in order to interpret abyssal hill statistics away from the ridge. The current relationship between ridge and abyssal hill characteristics will be important in any study which involves the characterization of abyssal hills far enough away from the ridge so that either the processes forming abyssal hills have changed or secondary processes (e.g. sedimentation, mass wasting, or off-axis volcanism) have significantly altered their morphology. Without these relationships as a reference, interpretation is difficult if not impossible.

We have compiled a data set of 64 near-ridge Sea Beam swaths (Table 5.1, Figures 5.1-5.3) to characterize near ridge abyssal hill morphology and its relationship to ridge properties. These data are gleaned from available Sea Beam records, and so in general do not comprise a very coherent or uniform sampling of the world's ridge system. Much of the data (27 swaths) comes from cruises to the Pacific-Cocos spreading section of the East Pacific Rise between 9° and 15° N. These data provide very good abyssal hill coverage of this well-mapped and studied ridge section and form the basis of a regional analysis of the correlation between ridge morphology and stochastic abyssal hill parameters. We also have data from near the Rivera (9) and Nazca (7) spreading sections of the East Pacific Rise, the Mid-Atlantic Ridge (18), and the SW Indian Ridge (3). Though spotty, this constitutes a good initial global data set for the analysis of correlations among covariance parameters and between parameters and ridge characteristics, especially spreading rate.

THE FORMATION OF ABYSSAL HILLS

Abyssal hills form primarily through a complex combination of tectonic (surface faulting) and constructional (volcanic) processes which occur at or near the ridge axis. Several studies have ventured to track to one degree or another the formation of surface morphology from the moment of rifting to the cessation of tectonic and volcanic activity along the flanks of the ridge. These include studies along the Rivera [*Lewis*, 1979; *CYAMEX*, 1981; *Macdonald and Luyendyk*, 1985], Cocos [*Choukrone et al.*, 1984] and Nazca [*Lonsdale*, 1977; *Searle*, 1984; *Renard et al.*, 1985; *Bicknell et al.*, 1987] spreading sections of the East Pacific Rise and portions of the northern Mid-Atlantic Ridge [*Needam and Francheteau*, 1974; *Harrison and Stieltjes*, 1977; *Macdonald and Luyendyk*, 1977; *Macdonald and Atwater*, 1978; *Kong et al.*, 1988].

Based on submersible observations along the Rivera spreading section of the East Pacific Rise a generic series of stages for the formation of abyssal hills was developed by *CYAMEX* [1981] and modified by *Macdonald and Luyendyk* [1985] (Figure 5.4). These include: (1) ridge axis volcanism, including flood basalts and edifice formation, (2) fissuring and horst and graben formation, with no polarization in faulting direction, (3) polarized normal faulting with larger inward facing faults driven by necking of the lithosphere [*Tapponnier and Francheteau*, 1978; *Phipps-Morgan et al.*, 1987], and leading to the formation of a rift valley, and finally (4) the inactive zone, where abyssal hill construction has ceased, and their morphology is slowly modified by mass-wasting, sedimentation, and occasional off-axis volcanism. These volcanic and structural zones are also observed along the Mid-Atlantic Ridge [*CYAMEX*, 1981]. The principle morphological differences between the slow (e.g. Mid-Atlantic Ridge) and medium (e.g. Pacific-Rivera Ridge) spreading are (1) that the zone volcanism is almost always expressed as edifice formation in the former, often to the size of flanking abyssal hills [*CYAMEX*, 1981 and references therein; *Kong et al.*, 1988], as opposed to a mixture of edifice and flood basalts in the latter, and (2) polarized faulting is much larger at the slower spreading ridge, creating rift valleys over 1 km deep and up to 30 km wide [*Needham and Francheteau*, 1974]. The rift valley at the medium-rate spreading ridge, by contrast, has only 50-200 m of relief [*Macdonald*, 1982], on the order of the size of flanking abyssal hills.

Harrison and Stieltjes [1977] and *Macdonald and Atwater* [1978] argue that there must be an additional tectonic zone (noted as phase 3b on Figure 5.4) for the slow-spreading ridge; as the seafloor is rafted over the top of the rift mountains, it changes from sloping, on average, steeply upward to slightly downward. To accommodate this transition either one or more of the following must occur: back tilting of the faulted blocks, reverse faulting on relict normal faults, or the formation of outward facing normal faults. In the medium-rate spreading ridge, there is no large-scale change in the average slope. The rift mountains (or hills) can be rafted away, without additional back-tilting, to take their place among abyssal hills, and a new rift mountain is formed by one or two new inward facing faults. For both medium and slow spreading ridges, the locus of volcanic activity is generally discontinuous, implying that the magma supply feeding the ridge volcanism is erratic, or episodic, and that magma chambers, if they exist, are transient and spatially discontinuous. [*Macdonald and Luyendyk*, 1977; *Macdonald and Luyendyk*, 1985; *Kong et al.*, 1988].

Fast spreading ridges apparently undergo only the first two of the abyssal hill forming stages (Figure 5.4). Rather than a rift valley, the plate boundary is marked by a ridge crest which is likely an isostatic response to a buoyant, steady-state magma chamber and zone of partial melt in the upper mantle beneath the rift [*Madsen et al.*, 1984]. The large volume of flood basalts erupting from the rift create a morphology akin to a linear shield volcano [*Lonsdale*, 1977]. The locus of volcanic activity is generally continuous within a spreading section [*Lonsdale*, 1977], implying that the magma supply is predominantly steady state, though subject to temporal and spatial variations in intensity [*Macdonald and Fox*, 1988].

The lid of the magma chamber beneath fast-spreading ridges is approximately 1.2-2.4 km deep and 4-6 km wide [*Detrick et al.*, 1987]. Because of a thin brittle layer atop the magma chamber, it is difficult to establish large relief in the beginning stages of fissuring and horst and graben formation. Large-scale horst and graben formation, leading to the full size of abyssal hills, is observed to begin, often abruptly, 2-10 km from the ridge crest [*Lonsdale*, 1977; *Choukrone et al.*, 1984, *Bicknell et al.*, 1987] (labeled as phase 2b in Figure 5.4). *Lonsdale* [1977] attributed this onset to the end of the subaxial magma chamber. *Lister* [1977] also postulated that with the transition between magma chamber and deep brittle crust comes a sudden onslaught of hydrothermal penetration, perhaps sufficiently cooling the upper crust to initiate large extensional structures.

By measuring cumulative throw on faults, *Bicknell et al.* [1987] found that there was a preference for inward facing faults on the flanks of the East Pacific Rise at 19° 30' S. Assuming that lithospheric necking (i.e. rift valley formation) is not significant in the faster spreading regions, they forward the suggestion, made earlier by *Tapponnier and Francheteau* [1978] and *Searle* [1984], that inward facing faults rupture a thinner brittle layer, and so require less energy to form. This hypothesis will be discussed in chapter 6 when we investigate asymmetries in abyssal hill morphology.

Figure 5.5 presents a summary of the several proposed mechanisms which may contribute to abyssal hill formation. One of the primary goals of the global study is to assess the relative contribution of each at various spreading rates in light of previous work on the subject. Much of this work strongly suggests that we can expect considerably larger abyssal hill features on the flanks of slower spreading ridges than near faster spreading ridges. Large differences in temperature profiles [*Phipps-Morgan et al.*, 1987] indicate that the lithosphere immediately adjacent to the rift axis of a slow spreading ridge will have greater elastic thickness [*McNutt*, 1984] than the lithosphere adjacent to the axis of a fast spreading ridge. Consequently, we can expect that abyssal hills, which at scale lengths less than 100 km are elastically supported loads [*Black and Mcadoo*, 1988], may obtain much larger sizes in slower spreading regions. Differences in the size distribution of microearthquakes [*Ouchi et al.*, 1982 (East Pacific Rise); *Toomey et al.*, 1988 (Mid-Atlantic Ridge)] and teleseismic centroid depths [*Huang and Solomon*, 1988] indicate that the brittle failure zone extends much deeper at slower spreading ridges. Larger fault offsets, and thus larger features associated with faulting, can therefore be generated adjacent to slower spreading ridges. Also, the difference in style of extruded volcanics (pillow lavas at slow spreading ridges vs. flood basalts at fast spreading ridges) [*CYAMEX*, 1981] favors the formation of taller volcanic edifices at slow spreading ridges.

At fast spreading rates we would like to establish whether volcanic construction or surface tectonism by means of horst and graben formation is predominate. *Lonsdale* [1977] interpreted a deep-tow profile taken across the East Pacific Rise at 3° 25' S almost entirely as faulted in origin. *Bicknell et al.* [1987] did the same for profiles at 19° 30' S, stating that the intermediate wavelength (2-8 km) topography off-axis has a faulted origin while the short wavelength topography (a few hundred meters) has a volcanic origin.

At slow spreading ridges, either volcanic edifice formation and tectonic processes resulting from lithospheric extension may dominate the formation of abyssal hills. From a study of abyssal hills east of the Mid-Atlantic Ridge near 23° N, *Rona et al.* [1974] concluded that both volcanic and tectonic processes play an important role. *Kong et al.* [1987] observed that a large volcanic edifice formed in the rift valley near 23° N was similar in size and shape to abyssal hill structures off axis, and thus proposed that abyssal hills in this region are extinct volcanic edifices which have been rafted away. However, before a volcanic edifice can be rafted away, it must pass over the rift mountains, and in the process be subjected to severe normal faulting with individual fault throws on the order of hundreds of meters [*Macdonald and Luyendyk*, 1977]. On the other hand, *Macdonald and Luyendyk* [1977] found that faults preferentially formed along the edges of volcanic edifices, so that it is perhaps possible to preserve volcanic constructs to a large degree as they are transported over the rift mountains. It is, however, not very clear from these studies whether we can expect either processes to dominate the formation of abyssal hills in slow spreading regions.

On the regional scale we expect to address more detailed questions concerning the ridge crest processes which influence abyssal hill formation. For example, how might abyssal hill formation be affected by regional variations in magma supply, proximity to small or large offset transforms, or small deviations in the stress fields from what might be expected adjacent to a linear (or idealized) ridge? We expect that important clues to answering these questions will be provided by establishing well-resolved correlations between quantitative abyssal hill characteristics and salient ridge parameters or features.

GLOBAL ANALYSIS

The stochastic parameters estimated from the near-ridge Sea Beam swaths (Table 5.1) are listed in Table 5.2. These form the basis of both the global and regional analysis of near-ridge morphology. Since this is the first time this type of analysis has been performed, much of what we do here is purely exploratory. There are a myriad of ways that the estimated parameters can be plotted. Some are enlightening, some curious, and others confusing. There are two general methods of plotting that we will pursue in the global analysis. The first is to plot parameters as a function of other parameters to investigate general aspects of abyssal hill characteristics. The second is to plot individual parameters versus the spreading rate of the nearby ridge to investigate the dependence of the parameters on first-order ridge characteristics. To highlight regional variations in both types of plots, different symbols are used to indicate different spreading regions.

Inter-Parameter Correlations

Characteristic abyssal hill widths (λ_n) are plotted versus corresponding rms height (H) in Figure 5.6. The overall trend is what we might expect on the basis of physical arguments: as the height of abyssal hills increases, so does their girth. If, however, we restrict attention to the Pacific-Cocos data, which dominates the lower end of both axes, then this trend is reversed. We quantify these trends by a weighted least-squares inversion for the best-fitting linear trend. The best-fitting slope to the Pacific-Cocos data is $b = -0.021 \pm .010$, and for the rest of the data $b = 0.0164 \pm 0.002$. The implications of this are, perhaps, that there are at least two major processes which dominate the formation of abyssal hills at different scales; one which at the larger scales produces a positive correlation between λ_n and H, and one at smaller scales which produces a negative correlation between λ_n and H. This view differs with that of others [e.g. *Searle*, 1984] who contend that the process of abyssal hill formation is essentially the same regardless of spreading rate.

Abyssal hill aspect ratios (a), or average length-to-width ratios, are plotted versus corresponding rms height (H) in Figure 5.7. This figure also displays a difference between the behavior of the smaller-scale Pacific-Cocos data and the rest of the global data set. While the Pacific-Cocos data show a large increase in a from ~3 at $H = 30$ m to ~6-16 at $H = 80$ m (estimated slope $b = 0.76 \pm 0.29$), the rest of the data are nearly constant at approximately $a = 1.5$-4 (estimated slope $b = 0.003 \pm 0.002$). As with Figure 5.6, this figure suggests that smaller-scale abyssal hills are formed by a very different process than larger-scale abyssal hills. A plot of the aspect ratio versus characteristic width shows much the same thing (Figure 5.8). In this plot there is a general monotonic decay in a with increasing λ_n,. The Pacific-Cocos data aspect ratios are larger in general, and exhibit a much steeper negative correlation with λ_n ($b = -14.3 \pm 10.4$) than the rest of the data ($b = -0.14 \pm 0.06$).

For the sake of completeness we have also included a plot of characteristic lengths (λ_s) versus the corresponding characteristic width (λ_n) (Figure 5.9). This plot contains the same information as in Figure 5.8, but in this format it is more difficult to interpret. As expected, there is a general positive correlation between the width and length of abyssal hills. Close inspection reveals that the Pacific-Cocos data tends to follow a steeper gradient than the remaining data, indicating, as before, that they tend to have greater aspect ratios.

Spreading Rate Correlations

The rms abyssal hill height (H), characteristic width (λ_n), length (λ_s), and aspect ratio (a) are plotted versus spreading rate in Figures 5.10, 5.11, 5.12, and 5.13 respectively. From these plots we observe that the tallest, widest, longest and least anisotropic abyssal hills are found at some of the slowest spreading rates. Although coverage is spotty, it appears that H, λ_n, and perhaps λ_s tend to decrease and a tends to increase with increased spreading rate up to the Pacific-Cocos data. The results from the Pacific-Nazca data, at some of the fastest observed spreading rates in the world, bear more resemblance in each of these plots to the medium spreading rate Pacific-Rivera data than to the Pacific-Cocos data.

The variation in estimates of H, λ_n, and λ_s is also much greater at lower spreading rates than elsewhere. This indicates that the process of abyssal hill formation is much more complex, variable, and/or episodic in the slower-spreading regions. The absolute variation of a is greatest for the Pacific-Cocos data, but the relative variation is fairly constant throughout.

In Figure 5.14 we have plotted the difference $\Delta\zeta_s$ between the abyssal hill lineation azimuths (ζ_s) and the normal to the RM2 [*Minster and Jordan*, 1978] spreading direction. $\Delta\zeta_s$ thus provides some measure of the relative anomaly in ζ_s. At this point we do not wish to draw attention to any particular values of $\Delta\zeta_s$ (some values, such as the Pacific-Rivera and African-Indian data are likely primarily due to errors in assumed spreading direction), but rather simply to the large variation in values among separate spreading sections, especially in the Pacific-Cocos data where ζ_s is best resolved. This indicates that abyssal hill lineations are subject to significant perturbation from the ridge strike and/or plate-motion normal directions, and may yield important physical information. The content of such information is probably best understood, however, in the regional analysis.

The final figure in this section plots the Hausdorff, or fractal dimension (D) versus spreading rate (Figure 5.15). It appears from this plot that D is slightly larger in the faster-spreading data (Pacific-Cocos average = 2.28 ± 0.05) than in the slower spreading data (Mid-Atlantic Ridge average = 2.21 ± 0.02).

Interpretation

Summarizing statements made above, we have the following primary observations from stochastically modeling near-ridge abyssal hill morphology: at large scales the rms height (H) and characteristic width (λ_n) tend to be positively correlated, while at small scales they appear negatively correlated; the aspect ratio (a) tends to be much larger at small scales (both vertical and horizontal) than at large scales; a also has a strong positive correlation with H at small scales while it is nearly constant over larger values of H; and, neglecting the Pacific-Nazca data, H and λ_n tend to be negatively correlated and a tends to be positively correlated with spreading rate. At this point we interpret these results in light of previous work concerning the formation of abyssal hills in different regions.

The negative correlation of H and λ_n with spreading rate up to ~13 cm/yr (Figures 5.10 and 5.9) is perhaps one of the strongest of our observations. A likely factor in this relationship is that at slower spreading rates the lithosphere at and near the ridge axis is colder [*Phipps-Morgan et al.*, 1987], its elastic thickness is therefore greater [*McNutt*, 1984], and it is thus able to elastically support larger surface loads than at faster spreading ridges. This suggests that the maximum size of abyssal hills in any region may reflect the maximum load which can be elastically supported by the lithosphere at the point of formation. Also, the differences, stated earlier, in the probable size of faulted features as inferred from seismic evidence [*Ouchi et al.*, 1982; *Toomey et al.*, 1988; *Huang and Solomon*, 1988] and in style of volcanic edifice formation [*CYAMEX*, 1981] between slow and fast spreading ridges suggests that abyssal hill forming processes tend to produce larger features at slower spreading ridges. The observation of larger H and λ_n for the Pacific-Nazca data than for the Pacific-Cocos data does not appear to support these statement (Figures 5.10 and 5.11). However, these data are all located near the Easter Island Microplate (Figure 5.2), a region with a complex tectonic history [*Hey et al.*, 1985], and may be anomalous with respect to the rest of the Nazca spreading section of the East Pacific Rise. The similarity in stochastic character with the medium spreading Pacific-Cocos region suggests that the region just south of the microplate may be akin to the Australian-Antarctic discordant zone [e.g. *Weissel and Hayes*, 1974]. To properly put this region in context, however, will require increased data coverage of the flanks of the Pacific-Nazca Ridge.

Previous work [e.g. *Lonsdale*, 1977; *Bicknell et al.*, 1987] indicates that surface tectonic processes related to cooling of the lithosphere are the primary abyssal hill forming processes at fast spreading rates, where lithospheric necking is not observed. Some of the observations listed above for the Pacific-Cocos data support these assertions in that they are inconsistent with the contrary assertion that volcanic edifice formation is the primary abyssal hill forming process in this region. Observational studies limit the slopes of submarine volcanic constructs to at most 25° [*Menard*, 1964; *Fornari et al.*, 1984; *Barone and Ryan*, 1985; *Smith and Jordan*, 1988]. Thus, as the height of a volcanic edifice grows, so too must its width, contrary to the negative correlation between H and λ_n observed at small scales (Figure 5.6). Also, if an eruption is derived from a magma source which is limited in the along-axis direction, we can expect the width of an edifice to grow proportionally faster than the length as its height also grows. Although not conclusive, this suggests that volcanic edifices are not consistent with the strong positive correlation between aspect ratio and rms height that is observed at small scales in Figure 5.7. Faulting and fissuring, however, are not inconsistent with either of these observed relationships. In particular, there is no limit on the slope of a fault, allowing for a possible negative correlation between H and λ_n.

If we accept the statement that horst and graben formation is predominant in the fast spreading Pacific-Cocos region, then it is likely, based on the stated differences in inter-parameter correlations over different scales, that a very different process controls abyssal hill formation at slower spreading rates and larger scales. If preferential faulting driven by lithospheric necking is predominant, then we must seek to explain why there should be such a difference between this type of faulting and fissuring and horst and graben formation. This no doubt could be done, but it is easier at this point to assume, as suggested by *Kong et al.* [1987], that volcanic edifice formation is predominant, which is, perhaps, more consistent with some of the very low aspect ratios observed at slow spreading rates (and for the Pacific-Nazca data) on Figure 5.13. However, the large variation in both H and λ_n at slow spreading rates probably indicates that there is a complex interplay between these two processes, perhaps on regional scales which we cannot discern with the present data set. We thus concur with the conclusion of *Rona et al.* [1974] that both volcanic construction and surface tectonism are important in the formation of abyssal hills at slow spreading rates.

As a final point we add that the observed average difference in the Hausdorff dimension between the Pacific-Cocos data and Mid-Atlantic Ridge data (Figure 5.15), though slight, may reflect the fact that topography produced by surface faulting will generally be rougher (with more power at smaller scales relative to larger scales) than topography more strongly influenced by constructional volcanism.

REGIONAL ANALYSIS

The East Pacific Rise between 9° and 15° N is among the most well surveyed and studied portions of the world's mid-ocean rift system [e.g. *Choukrone et al.*, 1984; *Macdonald et al.*, 1984; *Detrick et al.*, 1987; *Crane*, 1987; *Macdonald and Fox*, 1988, *Edwards et al.*, 1989]. Not coincidentally, it is also the region of densest coverage of the near-ridge Sea Beam swaths (27 of the 64, Figure 5.1), allowing us to conduct a detailed comparison between variations in abyssal hill morphology with variations in ridge morphology over this region. This analysis extends the previous chapter's analysis of the region between 13° and 15° N.

Ridge Morphology and Magma Supply

The morphology of the East Pacific Rise crest undergoes several transitions within the study region. South of the Orozco Fracture Zone (15° N) to 13° 55' N, the ridge axis is poorly defined and is characterized by narrow (1-3 km wide), parallel ridges 10-40 km long, whose crests have an average depth of about 2750 m. South of 13° 55' N, the ridge axis is well-defined by a single crestal horst which gradually shoals to ~2600 m and broadens to ~10-15 km wide near 13° N [*Edwards et al.*, 1989]. South of 13° N, the crestal horst narrows and deepens again to ~2750 m where it meets a large overlapping spreading center at 11° 45' N [*Macdonald et al.*, 1984]. Based on a fault patterns on the ridge flanks, *Crane* [1987] argues that this overlapper has migrated southward. South of 11° 45' N, the crestal horst shoals rapidly to ~2550 m, and persists near that depth until 11° N where it begins to narrow and drop precipitously to ~2900 m at 10° 15' N where the East Pacific Rise enters the Clipperton Transform Fault [*Macdonald and Fox*, 1988]. Just south of Clipperton, the ridge crest is shallow (~2550 m) and the crestal horst is broad and remains so until it encounters an overlapping spreading center at 9° 03' N [*Macdonald and Fox.*, 1988]. *Crane* [1987] argues for a southward propagation of the 9° 03' N overlapper.

The crest of the East Pacific Rise in the region between 9° and 15° N thus rises and falls (Figure 5.16) and the crestal horst correspondingly broadens and narrows several times.

Macdonald and Fox [1988] found that there is an excellent correlation between the rise crest highs and the presence of magma chamber reflectors found by *Detrick et al.* [1987]. They thus argue that the systematic variations in ridge morphology correspond to variations in magmatic budget along the length of the ridge. Where the magma supply is relatively abundant, the shallow-level magma chamber is kept well supplied, is therefore large (4-6 km), and will cause a broad and tall isostatic bulge (the crestal horst). Where the magma supply is less abundant, the magma chamber, if it exists, will be thinner (< 2 km), and thus produce a thinner and shorter axial bulge.

H and λ_n

The pattern of rising (and broadening) and falling (and narrowing) rise crests (Figure 5.16) is closely mimicked by the second-order stochastic parameters estimated from the near-ridge Sea Beam swaths in this region. Figure 5.17 plots both the rms abyssal hill height (H) and the characteristic width (λ_n) of the Pacific-Cocos data as a function of the average latitude over the length of the swath. Plotting parameters simultaneously gives the reader a better sense of how geographic variations in different parameters are correlated. H, the most well-resolved parameter, provides the most coherent correlation with ridge morphology. Where the ridge crest is high and the crestal horst is broad, the average abyssal height is relatively small (as low as 30 m). Where the ridge is low and the crestal horst thin or poorly defined, the average abyssal height is relatively large (as high as 80 m). The pattern of characteristic widths, though less well resolved, appears to be negatively correlated with H, which is consistent with the observation noted on Figure 5.6. We therefore suggest, consistent with statements made in the previous chapter, that abyssal hills in this region tend to be shorter and wider where the rise crest is shallow and wide and the magma supply relatively abundant, and taller and thinner where the rise crest is deep and thin and the magma supply relatively reduced.

The combination of large H and small λ_n indicates (provided that faulting is the principal process driving abyssal hill formation, and that fault dip is relatively constant) that the amount of crustal extension observed at the surface is greater in the regions of low magma supply than in regions of greater magma supply. If extension is purely proportional to rms height, then we may be observing a factor of 2 variation in crustal extension. Differences in λ_n should increase this range since the largest faults will be more densely spaced where λ_n is small than where λ_n is relatively large.

Observations of greater crustal extension in colder regions may contradict intuition, since we might expect hotter regions to undergo more cooling, and thus undergo more extensional deformation than colder regions. However, in the previous chapter we remarked that full-scale abyssal hill formation appears to begin much earlier in the former case, due perhaps to the shorter off-axis extent of the magma chamber. Thus, where the axial magma chamber is small, off-axis surface deformation is probably coupled sooner to deeper crustal deformation during the most rapid buildup of extensional stress. This would result, perhaps, in surface deformation which reflects a larger volume of extensional deformation. On the other hand, the axial magma chamber might also act as a thermal buffer, allowing the uppermost layer of the crust to cool slowly for a time before allowing significant cooling of the lower crust. Thus, where the magma supply is more abundant, the crust will not cool as rapidly (i.e. less rapid stress buildup) at the point of elastic coupling between upper and lower crust, resulting, perhaps, in a reduced amount of brittle deformation.

a and $\Delta\zeta_s$

The difference between expected (normal to plate motions) and observed abyssal lineations ($\Delta\zeta_s$) and abyssal hill aspect ratios (a) for the Pacific-Cocos data are plotted together as a function of latitude in Figure 5.18. If we momentarily disregard the complexities in parameters estimated from data south of the Clipperton Transform Fault, then these two parameters also display a marked correlation with ridge morphology; $\Delta\zeta_s$ tends to be positive (a counter-clockwise anomaly) and a tends to be lower where the ridge crest is shallower and broader. Although the error bars on the estimated aspect ratios are large compared with the regional variation in the estimates, the strong similarity with the regional variation of other parameters suggests that the pattern is real.

A lower aspect ratio in the hotter ridge sections perhaps indicates that volcanic constructs play more of a role in abyssal hill formation. This is a strong possibility since off-axis volcanism is observed near each of the ridge highs in this region [*Crane*, 1987]. Alternatively, lower aspect ratios may indicate that while faults are more amply spaced (greater λ_n), they tend to have smaller offsets and so their along-axis extent (and hence abyssal hill aspect ratio) is reduced. We note, without attempting explanation, exceptions to the correlation of a with ridge morphology on the two data points closest to the Clipperton Transform Fault near 10° 45' N.

The strong correlation between $\Delta\zeta_s$ and ridge morphology between the Clipperton and Orozco transform faults is perhaps surprising. Why would the presence of a strong magma chamber cause a reorientation of abyssal hill lineation of up to 10°? A clue toward answering this question may be found by comparing the lineation azimuth predicted by plate motion models to the strike of the adjacent ridge axis. Based on maps by *Klitgord and Mammerickx* [1982], the East Pacific Rise between the Orozco and Clipperton transform faults has a strike of ~349°, whereas between the Clipperton and Siquieros it is ~355°. The normal to the spreading direction in this region, based on model RM2 [*Minster and Jordan*, 1978] generally ranges between 353° and 355°, consistent with the latter ridge axis strike. Thus, between the Orozco and Siquieros transforms (15° N - 10° N), there may be a 5° discrepancy between ridge strike and the normal to the spreading direction. This is similar in magnitude and direction to the values of $\Delta\zeta_s$ observed along the flanks of the shallower portions of the ridge crest (Figure 5.18).

As stated earlier, the steady-state presence of a large magma chamber may serve to decouple deeper lithospheric deformation from upper crustal deformation during the most active phase of lithospheric extension. When horst and graben formation first occurs in this situation, the direction of faulting should be dominated by the ridge-perpendicular extension driven by cooling following emplacement of magma at the ridge axis. Where the ridge is deeper and the magma chamber smaller or non-steady state, we expect a stronger coupling between deeper lithospheric and surface crustal deformation and thus a more accurate surface expression of deeper lithospheric stresses related to plate cooling.

An important question to address is whether or not we can observe any off-axis signature of the two large overlapping spreading centers at 9° 03' N and 11° 45' N. If these overlappers have migrated southward as suggested by *Crane* [1987], then we should expect to see a signature in the variation of estimated parameters, if any exists, somewhat north of their present locations. Although the larger scale (i.e. > 100 km or so) variations in all parameters plotted in Figures 5.17 and 5.18 can easily be correlated with the variations in ridge depth, strong short-scale, or swath-to-swath variations, which are not so easily explained, occur in all parameters near 9° 45' N and 12° 45' N. This erratic behavior may indicate that we are sampling locally transient phenomena which may constitute the off-axis trails of the overlapping spreading center.

CONCLUSIONS

Important results from the global analysis are summarized as follows:

(1) The characteristic length (λ_n) is generally positively correlated, and the aspect ratio (a) generally negatively correlated with the rms height of abyssal hills (H). For the Pacific-Cocos data, however, these trends are reversed. a and λ_n are generally negatively correlated with each other.

(2) Although coverage is spotty, the rms height (H), characteristic width (λ_n) and length (λ_s) all generally decrease with spreading rate, with the greatest variation in all these parameters occurring at slow spreading rates. The aspect ratio (a) generally increases with spreading rate. All of these "trends" appear to reverse between the Pacific-Cocos and Pacific-Nazca data, which bears more resemblance to the medium rate spreading Pacific-Rivera data than to the Pacific-Cocos data.

(3) Variations in the difference between expected and observed lineation azimuths ($\Delta\zeta_s$) can exceed 30° over an individual spreading data set.

(4) The Hausdorff (fractal) dimension appears to be slightly greater at faster spreading rates.

We have compared these observations to the proposals of others for formation of abyssal hills, and as a result support the following assertions. At slow-spreading ridges, the lithosphere at and flanking the ridge axis is relatively cold, its brittle and elastic layer thicker, and is therefore likely to be capable of elastically supporting the formation of much larger abyssal hill features than can the hotter fast-spreading ridges. Constructional volcanism at the ridge crest of slow-spreading ridges episodically produces large edifices which, after being strongly modified by faulting during passage out of the rift valley, become principle building blocks of abyssal hills. In contrast, volcanism at fast-spreading ridges is primarily expressed as flood basalts and, because the near-ridge crust is likely underlain by a large fluid magma chamber, cannot build up large edifices despite the large volume of erupted material. Only when the crust has ridden off the magma chamber (or some low viscosity region) can features of larger size be produced, and then primarily by brittle extension of the crust in response to rapid cooling of the surface (probably aided or even initiated by deep hydrothermal circulation). A possible consequence of these assertions is that a primary indicator of the difference between tectonism and volcanic construction may be the aspect ratio, which is likely larger for horst and graben features than for volcanic features.

For the Pacific-Cocos regional data set we find a correlation between the variation of abyssal hill parameters and the variation in ridge morphology associated with magma supply abundance. Where the ridge crest is shallow and the crestal horst broad and well-defined, indicating an abundant magma supply, λ_n and $\Delta\zeta_s$ tend to be larger, and H and a tend to be smaller than where the ridge crest is deep and the crestal horst narrow and/or poorly defined. To explain most of these correlations we suggest that the axial magma chamber serves to decouple for a time deeper lithospheric deformation from surface crustal deformation. Where the magma chamber is small or temporally sporadic (deep ridge with narrow crestal horst), surface and deeper lithospheric deformation couple quickly so that a greater component of surface topography is a reflection of deeper brittle failure. In this case, the total volume of extension coupled to the surface, and hence the rms height of horst and graben formation observed at the surface will be greater. More rapid coupling may also cause the azimuth of abyssal hill lineation to be more reflective of larger scale plate stresses where they may differ from stresses associated only with the morphology of the ridge. Where the magma chamber is large, the formation of horst and graben features is severely limited for a time by the shallowness of the brittle layer over the chamber. During this phase of abyssal hill formation, any deeper lithospheric deformation that may occur will be entirely decoupled from surface topography by the intervening weak zone, and the direction of extensional faulting in response to surface cooling should be controlled by ridge morphology rather than plate stresses. What surface faulting does form, however, will provide pre-existing zones of weakness for further surface tectonism when the magma chamber ceases and surface deformation is finally coupled to lithosphere deformation

TABLE 5.1. Sea Beam Data Used for Parameter Estimation.

Swath	Cruise	Ship	Starting Date	Starting Time	Starting Latitude, deg N	Starting Longitude, deg E	Length of Data, km	Spreading Rate, mm/yr^b
1	Papatua 1	*TW*	Sep. 20, 1985	1730	21.48	-109.71	64	60.3
2	Pascua 1	*TW*	Jan. 08, 1983	0500	21.23	-109.87	75	60.6
3	Ceres 4	*TW*	Oct. 23, 1982	0415	20.93	-109.27	65	60.4
4	Ariadne 3	*TW*	Apr. 25, 1982	0100	20.84	-109.43	86	60.6
5	Pascua 1	*TW*	Jan. 08, 1983	0830	20.74	-109.38	54	60.7
6	Ceres 4	*TW*	Oct. 23, 1982	0030	20.69	-108.69	60	60.3
7	Papatua 1	*TW*	Sep. 20, 1985	2230	20.64	-109.20	62	60.8
8	Ceres 4	*TW*	Oct. 21, 1982	1830	20.51	-108.76	46	60.5
9	Ceres 4	*TW*	Oct. 22, 1982	1200	20.50	-108.76	48	60.5
10	Ceres 2	*TW*	Jul. 29, 1982	0830	14.70	-104.42	43	100.6
11	Ceres 2	*TW*	Jul. 29, 1982	0600	14.84	-103.97	41	100.3
12	Ceres 2	*TW*	Jul. 27, 1982	1715	14.07	-103.61	56	103.3
13	2607	*RC*	Jun. 07, 1985	0200	13.41	-104.34	33	105.4
14	Papatua 1	*TW*	Oct. 14, 1985	0530	13.17	-104.62	54	106.5
15	2607	*RC*	Jun. 09, 1985	1000	13.10	-103.70	38	107.1
16	Papatua 1	*TW*	Sep. 23, 1985	2100	12.89	-104.81	64	107.4
17	Papatua 1	*TW*	Oct. 12, 1985	2130	12.80	-104.13	57	108.1
18	2607	*RC*	Jun. 08, 1985	1400	12.82	-103.61	25	108.1
19	2607	*RC*	Jun. 08, 1985	1830	12.73	-104.03	27	108.3
20	2607	*RC*	Jun. 02, 1985	0430	12.56	-103.80	32	108.6
21	2607	*RC*	Jun. 01, 1985	2200	12.25	-104.24	44	109.7
22	Ceres 2	*TW*	Jul. 26, 1982	0330	12.15	-103.15	54	110.9
23	2L25	*AII*	May 31, 1985	0800	11.58	-103.66	72	111.8
24	2607	*RC*	Jun. 01, 1985	0530	11.51	-103.71	48	112.7
25	2L26	*AII*	Jun. 07, 1985	0800	11.33	-103.01	81	115.8
26	2607	*RC*	May 31, 1985	2300	11.14	-104.10	37	113.9
27	2607	*RC*	May 31, 1985	1840	10.97	-103.78	51	114.8
28	2607	*RC*	May 31, 1985	1300	10.84	-103.28	40	115.5
29	2607	*RC*	May 31, 1985	0730	10.68	-103.57	22	116.2
30	2607	*RC*	May 30, 1985	2200	10.53	-104.35	23	116.4
31	2607	*RC*	Jun. 12, 1985	0500	9.91	-103.75	40	119.0
32	2607	*RC*	Jun. 16, 1985	1500	9.76	-104.21	23	119.4
33	2607	*RC*	May 27, 1985	0830	9.74	-103.07	42	119.8
34	2607	*RC*	Jun. 16, 1985	1000	9.70	-104.63	30	119.5
35	2607	*RC*	Jun. 17, 1985	0000	9.45	-103.90	27	120.5
36	2607	*RC*	Jun. 17, 1985	0530	9.41	-104.33	19	120.5
37	Pascua 4	*TW*	Apr. 10, 1983	1100	-22.60	-114.21	76	169.6
38	Pascua 4	*TW*	Apr. 10, 1983	0445	-22.52	-115.37	73	169.6
39	Pascua 3	*TW*	Mar. 06, 1983	1600	-29.06	-110.79	66	171.0
40	Pascua 3	*TW*	Mar. 07, 1983	2100	-29.95	-111.43	138	171.1
41	Pascua 3	*TW*	Mar. 08, 1983	0700	-30.13	-110.02	103	171.1
42	Pascua 3	*TW*	Mar. 09, 1983	1300	-31.20	-113.14	96	171.1
43	Pascua 3	*TW*	Mar. 09, 1983	2130	-31.49	-111.76	75	171.1
44	2509	*RC*	Jul. 30, 1984	0300	46.41	-30.15	199	23.6
45	4L2	*AII*	May 19, 1986	1500	27.85	-50.39	177	26.1
46	2511	*RC*	Sep. 18, 1984	1500	23.58	-47.04	140	26.8
47	4L2	*AII*	Jun. 13, 1986	2100	23.21	-45.38	179	26.8

Table 5.1. Continued.

Swath	Cruise	Ship	Starting Date	Starting Time	Starting Latitude, deg N	Starting Longitude, deg E	Length of Data, km	Spreading Rate, mm/yr[b]
48	2602	*RC*	Feb. 18, 1985	2300	1.44	-30.79	123	35.9
49	2602	*RC*	Feb. 16, 1985	0000	0.03	-22.66	126	36.5
50	2602	*RC*	Feb. 15, 1985	0200	-1.26	-18.55	131	36.9
51	2602	*RC*	Feb. 14, 1985	0500	-2.58	-14.65	107	37.4
52	2806	*RC*	Jun. 12, 1987	1300	-3.70	-15.42	173	37.6
53	2515	*RC*	Jan. 08, 1985	2000	-8.32	-16.57	163	38.5
54	2711	*RC*	Dec. 12, 1986	1430	-25.54	-12.12	115	39.5
55	2711	*RC*	Dec. 13, 1986	0200	-26.04	-14.42	95	39.5
56	2711	*RC*	Dec. 20, 1986	1330	-26.27	-13.80	117	39.5
57	2711	*RC*	Dec. 13, 1986	2200	-27.18	-13.29	118	39.4
58	2711	*RC*	Dec. 13, 1986	1500	-27.38	-14.60	82	39.4
59	Marathon 10	*TW*	Jan. 06, 1985	0930	-35.67	-16.12	101	38.5
60	Marathon 10	*TW*	Jan. 08, 1985	1600	-36.87	-17.44	75	38.3
61	Marathon 10	*TW*	Dec. 22, 1984	1100	-37.04	-21.14	84	38.3
62	2709	*RC*	Oct. 03, 1986	0300	-21.83	57.46	91	47.1
63	2709	*RC*	Oct. 03, 1986	1630	-24.21	57.51	83	49.2
64	2709	*RC*	Oct. 04, 1986	0000	-25.50	57.45	119	50.4

[a] *AII*: *RV Atlantis II*, *RC*: *RV Robert Conrad*, *TW*: *RV Thomas Washington*.

[b] Spreading rates from model RM2 [*Minster and Jordan*, 1978].

TABLE 5.2. Stochastic Parameters Derived From Inversion.

Swath	H, m	ζ_s, deg	λ_n, km	λ_s, km	a	D
1	76 ± 8	20.9 ±1.8	2.8 ± 0.6	12.9 ± 3.6	4.7 ± 1.3	2.15 ± 0.21
2	116 ± 14	19.0 ± 3.3	5.2 ± 1.0	13.4 ± 3.3	2.6 ± 0.7	2.21 ± 0.13
3	110 ± 14	9.9 ± 3.7	4.3 ± 0.9	11.5 ± 2.9	2.7 ± 0.7	2.20 ± 0.17
4	104 ± 15	17.5 ± 1.7	6.8 ± 1.7	34.0 ± 11.3	5.0 ± 1.7	2.33 ± 0.20
5	85 ± 10	19.0 ± 3.5	3.5 ± 0.7	9.5 ± 2.0	2.7 ± 0.6	2.20 ± 0.19
6	73 ± 9	40.9 ± 2.4	5.1 ± 1.3	19.6 ± 6.5	3.9 ± 1.3	2.42 ± 0.13
7	99 ± 23	20.2 ± 5.0	9.4 ± 3.8	23.6 ± 9.8	2.5 ± 1.1	2.52 ± 0.10
8	73 ± 6	44.4 ± 4.2	3.1 ± 0.8	7.4 ± 2.0	2.4 ± 0.7	2.23 ± 0.24
9	80 ± 8	34.5 ± 3.6	3.1 ± 0.6	7.9 ± 1.5	2.6 ± 0.6	2.20 ± 0.30
10	67 ± 4	352.0 ± 2.0	1.2 ± 0.3	8.3 ± 2.0	7.1 ± 2.0	2.50^a
11	72 ± 6	347.0 ± 2.0	1.2 ± 0.4	7.4 ± 2.0	6.1 ± 1.9	2.50^a
12	68 ± 5	351.0 ± 2.7	1.8 ± 0.4	11.3 ± 3.2	6.3 ± 1.9	2.50^a
13	57 ± 4	352.7 ± 1.1	1.6 ± 0.3	10.5 ± 1.9	6.7 ± 1.5	2.50^a
14	44 ± 3	350.9 ± 2.0	2.3 ± 0.5	14.1 ± 3.5	6.1 ± 1.6	2.39 ± 0.30
15	48 ± 3	345.5 ± 2.0	1.5 ± 0.4	10.9 ± 3.3	7.1 ± 2.2	2.50^a
16	46 ± 4	349.8 ± 2.0	4.2 ± 1.0	18.9 ± 5.0	4.5 ± 1.3	2.48 ± 0.13
17	58 ± 3	349.9 ± 1.8	2.0 ± 0.4	9.8 ± 2.0	4.8 ± 1.1	2.50^a
18	48 ± 5	340.5 ± 3.5	2.3 ± 0.7	8.8 ± 3.0	3.9 ± 1.4	2.38 ± 0.22
19	58 ± 5	344.6 ± 1.5	1.6 ± 0.5	16.6 ± 5.9	10.3 ± 3.8	2.50^a
20	72 ± 13	348.7 ± 3.0	4.2 ± 1.7	28.3 ± 17.0	6.8 ± 4.0	2.10 ± 0.15
21	60 ± 6	354.9 ± 1.3	2.2 ± 0.6	35.4 ± 22.1	16.4 ± 9.5	2.25 ± 0.15
22	58 ± 4	353.3 ± 1.9	2.0 ± 0.5	11.3 ± 3.2	5.6 ± 1.7	2.34 ± 0.39
23	57 ± 4	353.6 ± 1.8	2.2 ± 0.6	17.7 ± 6.6	7.9 ± 2.9	2.50^a
24	39 ± 4	343.0 ± 5.0	2.7 ± 0.8	8.1 ± 2.5	3.0 ± 1.0	2.17 ± 0.19
25	62 ± 3	348.0 ± 1.4	1.6 ± 0.3	14.9 ± 3.9	9.5 ± 2.5	2.17 ± 0.15
26	44 ± 4	348.2 ± 2.6	2.0 ± 0.6	11.8 ± 4.4	6.0 ± 2.3	2.13 ± 0.17
27	55 ± 5	345.2 ± 1.8	2.0 ± 0.6	16.6 ± 5.9	8.3 ± 3.0	2.29 ± 0.20
28	70 ± 5	348.0 ± 1.4	1.4 ± 0.4	15.7 ± 6.1	11.1 ± 4.2	2.50^a
29	70 ± 7	354.1 ± 1.9	1.5 ± 0.4	11.3 ± 3.6	7.5 ± 2.6	2.50^a
30	83 ± 9	354.8 ± 3.6	1.9 ± 0.6	8.3 ± 2.9	4.4 ± 1.7	2.06 ± 0.45
31	49 ± 4	1.5 ± 1.5	2.2 ± 0.6	16.6 ± 4.9	7.6 ± 2.3	2.22 ± 0.20
32	34 ± 4	341.9 ± 5.0	2.1 ± 0.7	7.3 ± 2.6	3.4 ± 1.3	2.09 ± 0.26
33	56 ± 4	356.0 ± 1.2	1.9 ± 0.5	14.9 ± 3.9	7.7 ± 2.2	2.54 ± 0.21
34	37 ± 4	338.4 ± 3.5	2.2 ± 0.7	8.3 ± 2.7	3.7 ± 1.3	2.47 ± 0.17
35	54 ± 7	3.3 ± 1.9	2.2 ± 0.7	18.9 ± 8.8	8.5 ± 3.9	2.28 ± 0.20
36	43 ± 5	356.1 ± 2.4	1.4 ± 0.5	9.1 ± 3.2	6.4 ± 2.4	2.50^a
37	67 ± 7	26.4 ± 6.3	5.0 ± 1.5	14.1 ± 5.7	2.8 ± 1.1	2.38 ± 0.12
38	54 ± 4	0.4 ± 2.7	3.4 ± 0.9	16.6 ± 6.9	4.9 ± 2.0	2.51 ± 0.15
39	132 ± 16	3.2 ± 5.3	3.6 ± 0.9	13.4 ± 6.4	3.7 ± 1.7	2.10 ± 0.10
40	127 ± 15	355.2 ± 27.8	8.0 ± 1.7	10.1 ± 3.4	1.3 ± 0.4	2.13 ± 0.08
41	70 ± 9	6.5 ± 15.4	7.6 ± 2.5	13.8 ± 6.3	1.8 ± 0.8	2.35 ± 0.09
42	75 ± 6	308.9 ± 57.4	4.6 ± 1.1	5.1 ± 1.2	1.1 ± 0.3	2.23 ± 0.12
43	99 ± 12	337.3 ± 50.0	5.8 ± 1.2	8.5 ± 4.5	1.5 ± 0.7	2.32 ± 0.09
44	126 ± 14	354.0 ± 4.0	11.4 ± 2.9	26.7 ± 6.7	2.3 ± 0.7	2.21 ± 0.07
45	226 ± 18	15.3 ± 4.9	5.2 ± 1.0	11.1 ± 3.5	2.1 ± 0.6	2.11 ± 0.18
46	226 ± 23	8.1 ± 3.5	6.0 ± 1.0	18.8 ± 6.6	3.1 ± 1.0	2.22 ± 0.09
47	292 ± 32	0.6 ± 3.2	7.6 ± 1.4	20.9 ± 6.5	2.8 ± 0.8	2.05 ± 0.09
48	207 ± 39	355.3 ± 5.6	11.9 ± 3.5	29.3 ± 13.3	2.5 ± 1.1	2.40 ± 0.06
49	105 ± 20	357.0 ± 9.2	15.2 ± 5.3	60.9 ± 134.5	4.0 ± 8.4	2.34 ± 0.09
50	179 ± 21	350.8 ± 2.0	7.3 ± 1.3	27.9 ± 7.0	3.8 ± 0.9	2.07 ± 0.12
51	216 ± 34	351.7 ± 3.2	8.8 ± 1.9	21.7 ± 5.8	2.5 ± 0.7	2.17 ± 0.10
52	164 ± 15	358.0 ± 7.0	7.9 ± 1.8	15.8 ± 4.7	2.0 ± 0.6	2.26 ± 0.10
53	115 ± 20	0.4 ± 9.0	20.2 ± 7.2	40.4 ± 23.1	2.0 ± 1.1	2.36 ± 0.07
54	299 ± 33	351.2 ± 2.9	6.3 ± 1.1	13.4 ± 3.2	2.1 ± 0.5	2.02 ± 0.10
55	184 ± 22	328.4 ± 2.1	5.8 ± 1.1	17.6 ± 4.6	3.1 ± 0.8	2.10 ± 0.11

Table 5.2. Continued.

Swath	H, m	ζ_S, deg	λ_n, km	λ_S, km	a	D
56	276 ± 42	357.5 ± 6.3	8.8 ± 2.3	30.4 ± 33.2	3.5 ± 3.5	2.10 ± 0.09
57	209 ± 28	349.2 ± 2.1	9.2 ± 2.2	33.6 ± 11.2	3.7 ± 1.2	2.36 ± 0.07
58	170 ± 19	347.1 ± 1.8	4.3 ± 0.7	15.9 ± 3.8	3.7 ± 0.9	2.10 ± 0.10
59	177 ± 30	323.0 ± 22.0	5.7 ± 1.9	11.2 ± 8.6	2.0 ± 1.4	2.10 ± 0.10
60	214 ± 50	0.0[b]	7.0 ± 2.2	0.0[b]	0.0[b]	2.10 ± 0.10
61	123 ± 21	338.6 ± 37.0	4.7 ± 1.4	6.4 ± 4.6	1.4 ± 0.9	2.10 ± 0.10
62	116 ± 12	313.1 ± 3.1	3.6 ± 0.8	16.7 ± 5.9	4.7 ± 1.6	2.10 ± 0.10
63	51 ± 3	312.7 ± 3.1	3.1 ± 0.7	14.1 ± 4.2	4.6 ± 1.4	2.37 ± 0.25
64	70 ± 7	306.7 ± 4.0	4.4 ± 1.0	15.9 ± 5.3	3.6 ± 1.2	2.06 ± 0.18

[a] Parameter fixed in inversion.
[b] Unstable parameter.

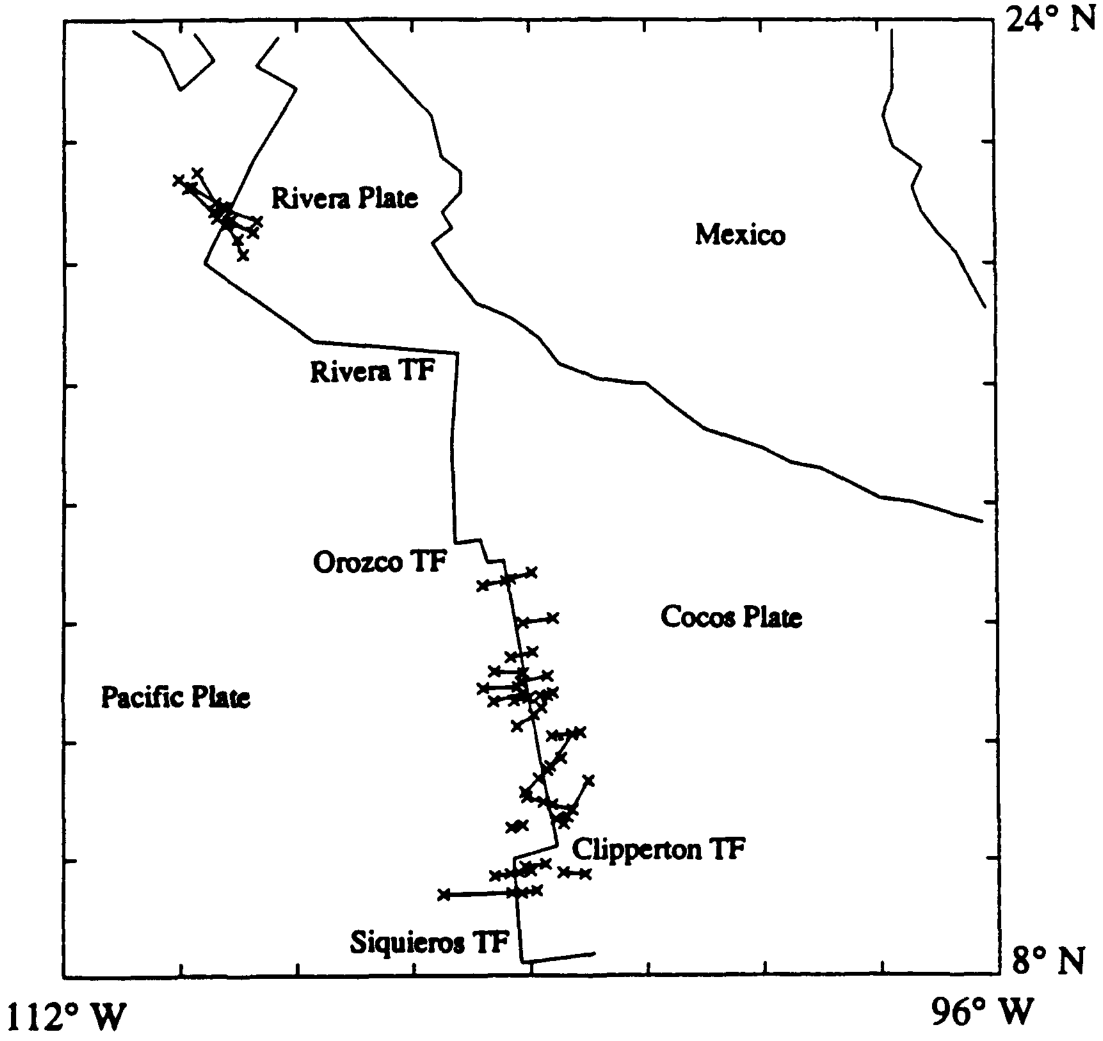
24° N
8° N
112° W
96° W
Rivera Plate
Mexico
Rivera TF
Orozco TF
Cocos Plate
Pacific Plate
Clipperton TF
Siquieros TF

Figure 5.1. Pacific-Rivera and Pacific-Cocos Sea Beam swaths listed in Table 5.1. X's mark the beginning and end of track lines used in the inversion for stochastic parameters.

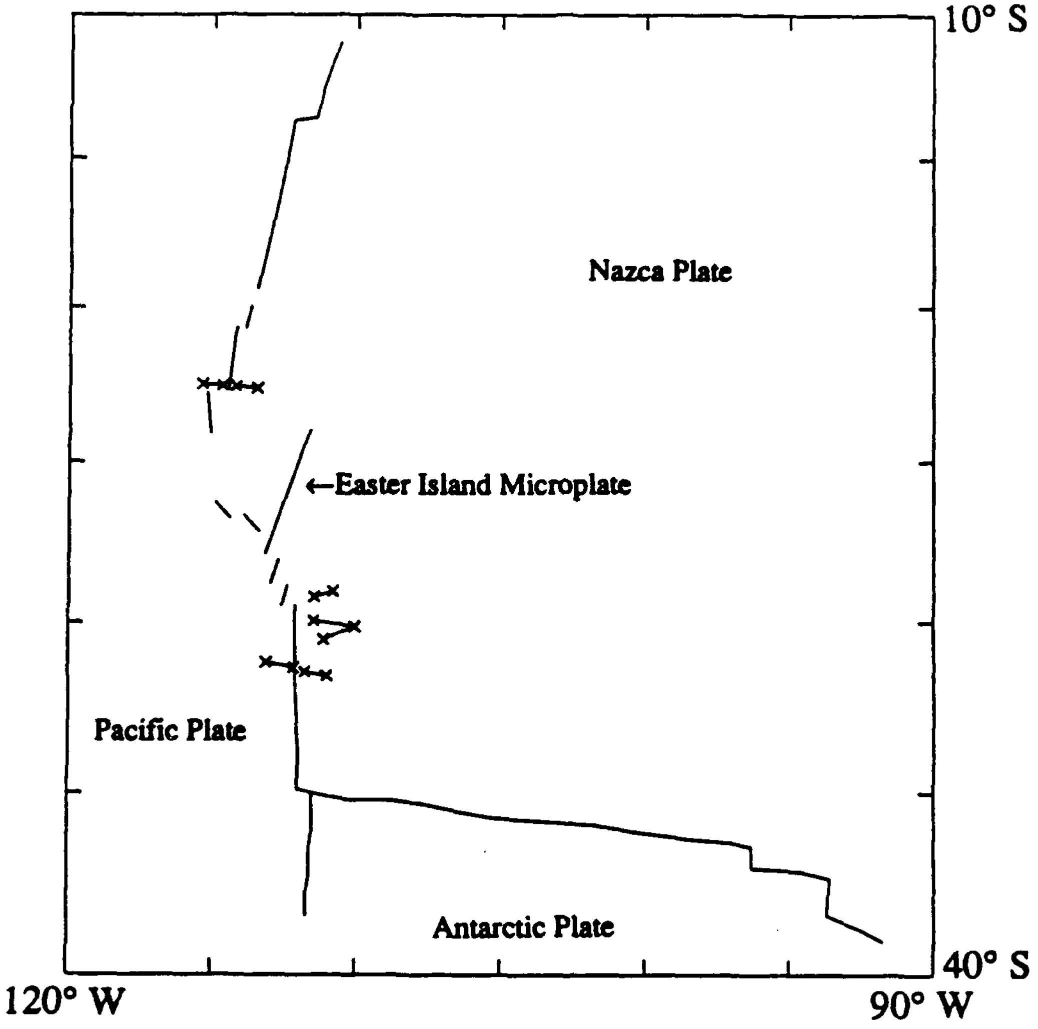
10° S
Nazca Plate
←Easter Island Microplate
Pacific Plate
Antarctic Plate
40° S
120° W
90° W

Figure 5.2. Pacific-Nazca Sea Beam swaths listed in Table 5.1. X's mark the beginning and end of track lines used in the inversion for stochastic parameters.

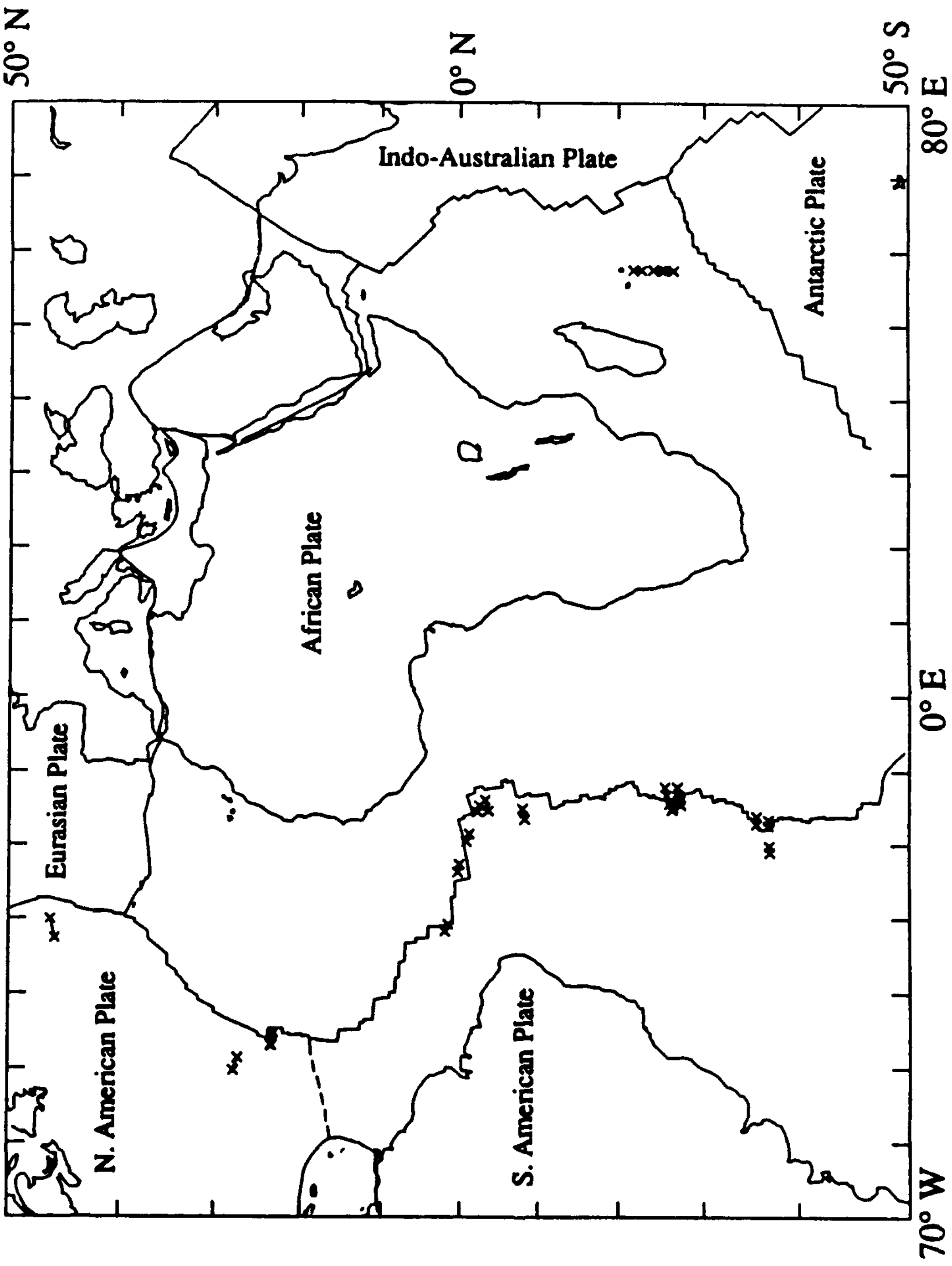
50° N
0° N
50° S
80° E
0° E
70° W
Indo-Australian Plate
Antarctic Plate
African Plate
Eurasian Plate
N. American Plate
S. American Plate

Figure 5.3. Mid-Atlantic Ridge and Africa-India Sea Beam swaths listed in Table 5.1. X's mark the beginning and end of track lines used in the inversion for stochastic parameters.

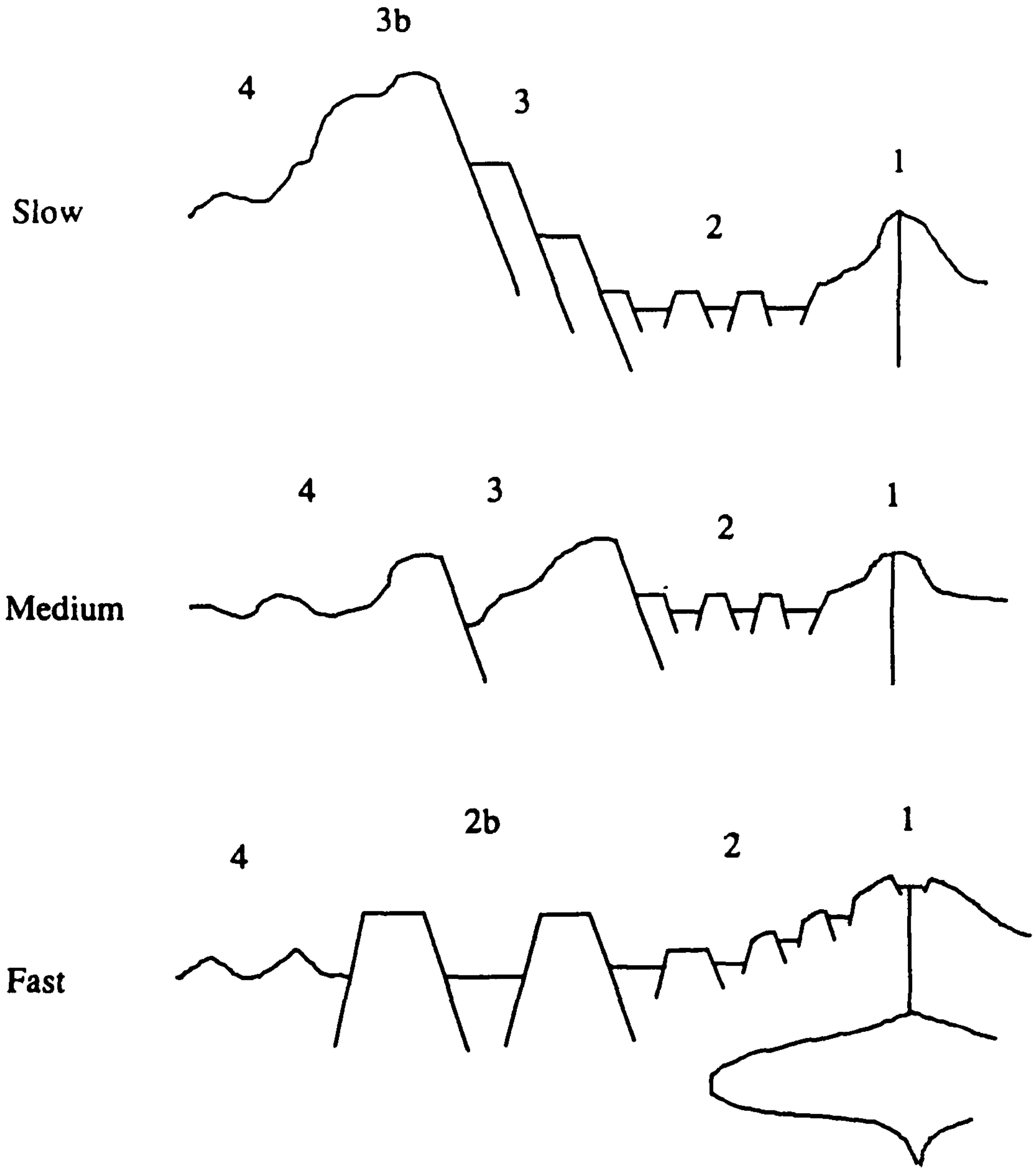

Figure 5.4. Stages in the evolution of abyssal hills (adapted from *CYAMEX* [1981]) illustrated for slow, medium, and fast spreading ridges: 1) axial zone of volcanic extrusion, 2) formation of rifted and horst and graben relief, 3) predominantly inward facing faults associated with lithospheric necking, and 4) the inactive zone, where abyssal hills are slowly modified by mass wasting, sedimentation, and occasional off-axis volcanism. In slow spreading regions, *Harrison and Stieltjes* [1977] propose an additional phase of tectonic activity (noted as 3b) to allow for the steady state rift mountains. Stage 3 is not observed at fast spreading regions, but and additional phase to stage 2 (noted as 2b) represents observations of a sudden onset of large scale normal faulting leading to the full size of flanking abyssal hills. The region below the axis of the fast spreading ridge represents the axial magma chamber and/or low viscosity region postulated to help explain stage 2b. See text for further discussion.

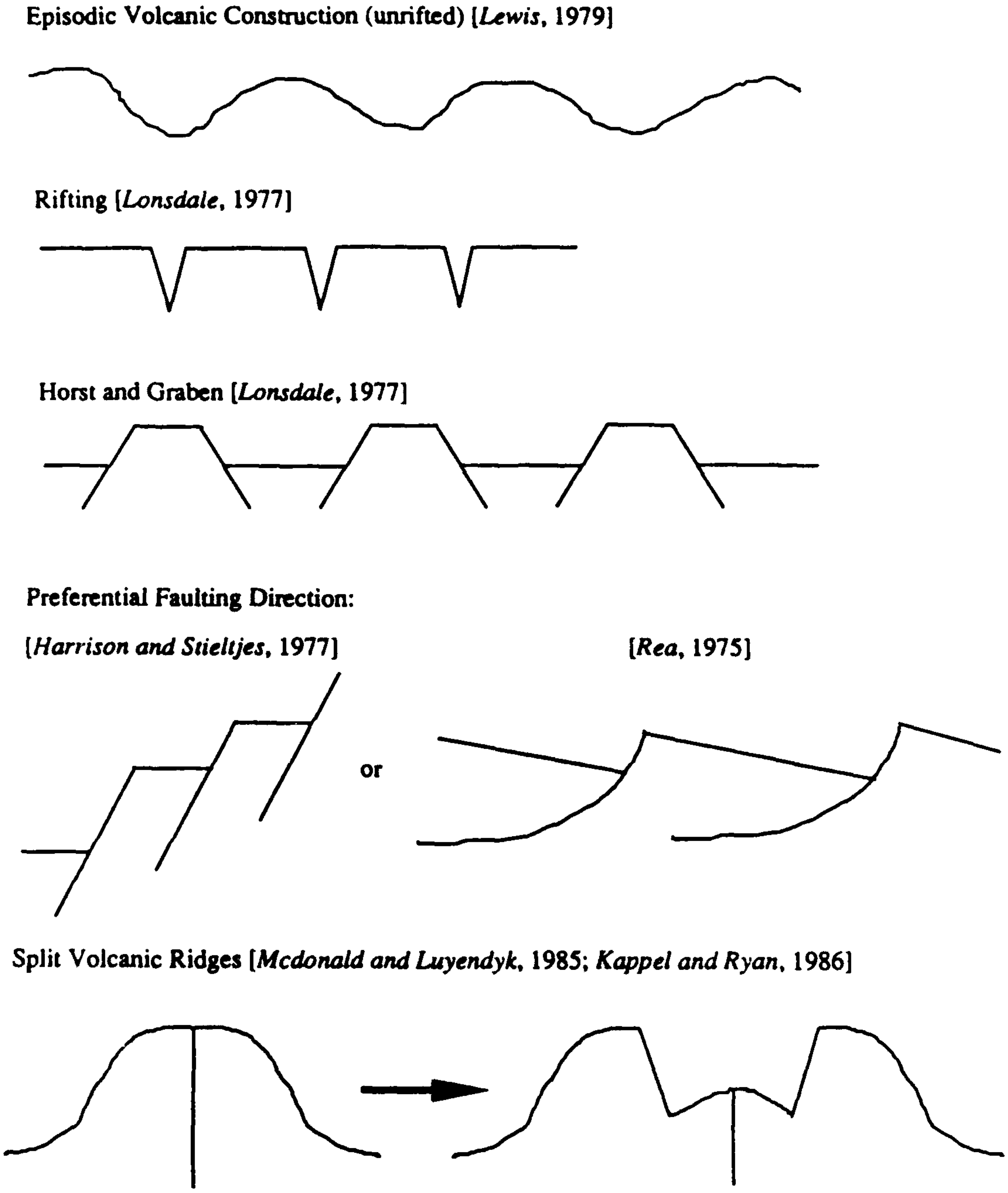

Episodic Volcanic Construction (unrifted) [*Lewis*, 1979]

Rifting [*Lonsdale*, 1977]

Horst and Graben [*Lonsdale*, 1977]

Preferential Faulting Direction:

[*Harrison and Stieltjes*, 1977]

[*Rea*, 1975]

Split Volcanic Ridges [*Mcdonald and Luyendyk*, 1985; *Kappel and Ryan*, 1986]

Figure 5.5. Various proposed mechanisms for the formation of abyssal hills.

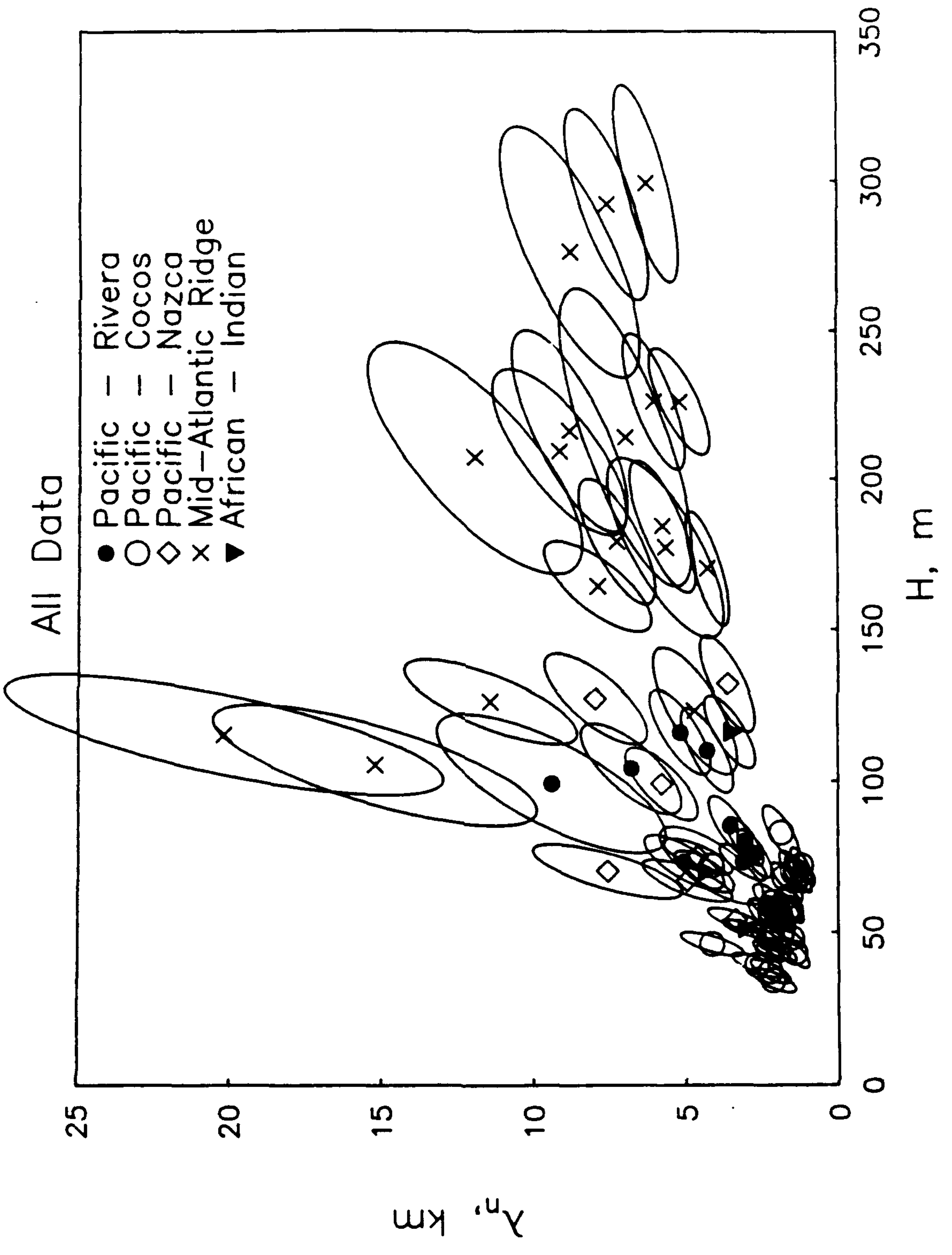

Figure 5.6. Estimated values of characteristic width (λ_n) plotted as a function of rms height (H). Values are listed in Table 5.2. Ellipses represent 1-σ errors about each estimation. Different symbols represent data from different spreading regions as indicated.

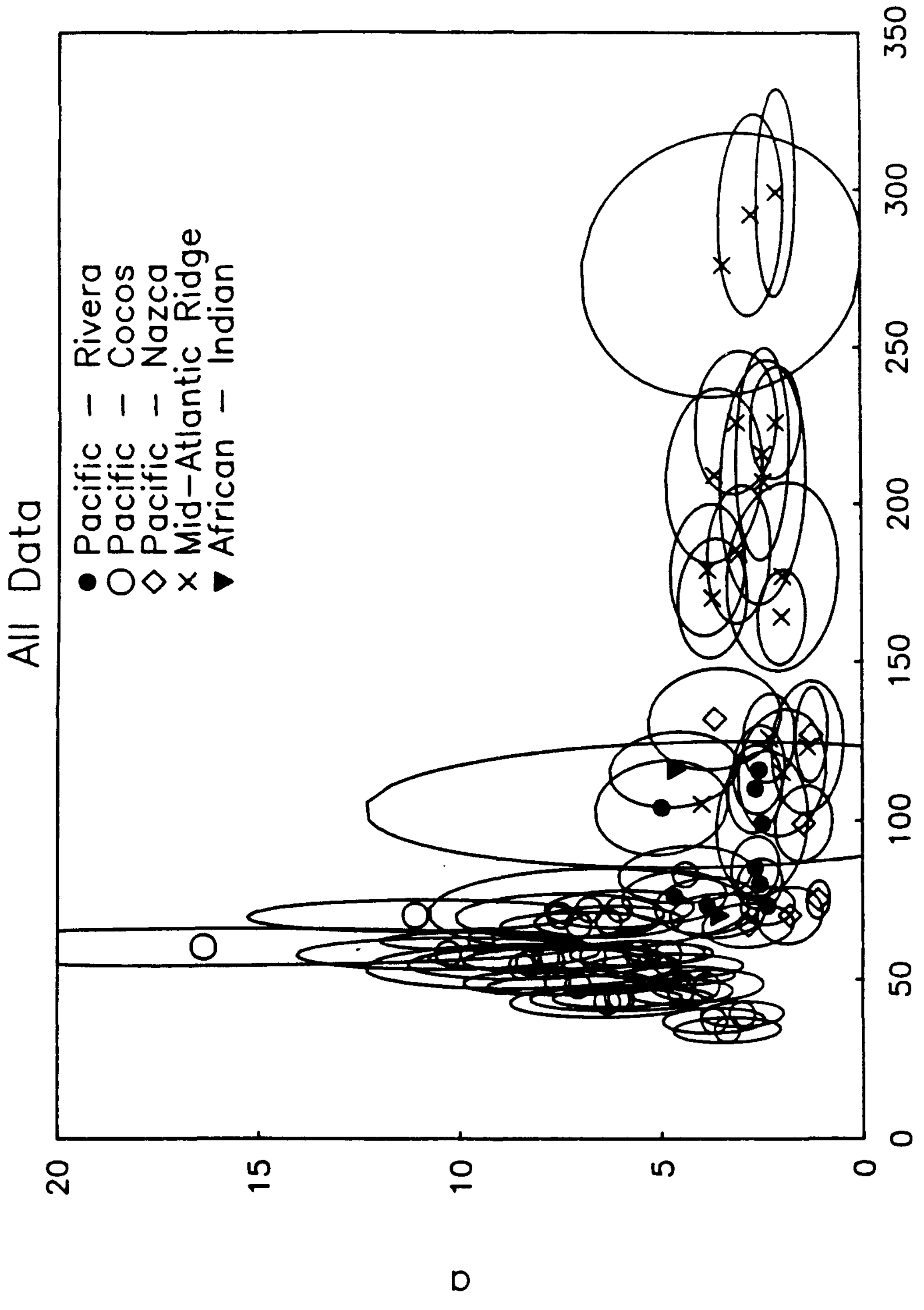

Figure 5.7. Estimated values of aspect ratio (*a*) plotted as a function of rms height (*H*). Values are listed in Table 5.2. Ellipses represent 1-σ errors about each estimation. Different symbols represent data from different spreading regions as indicated.

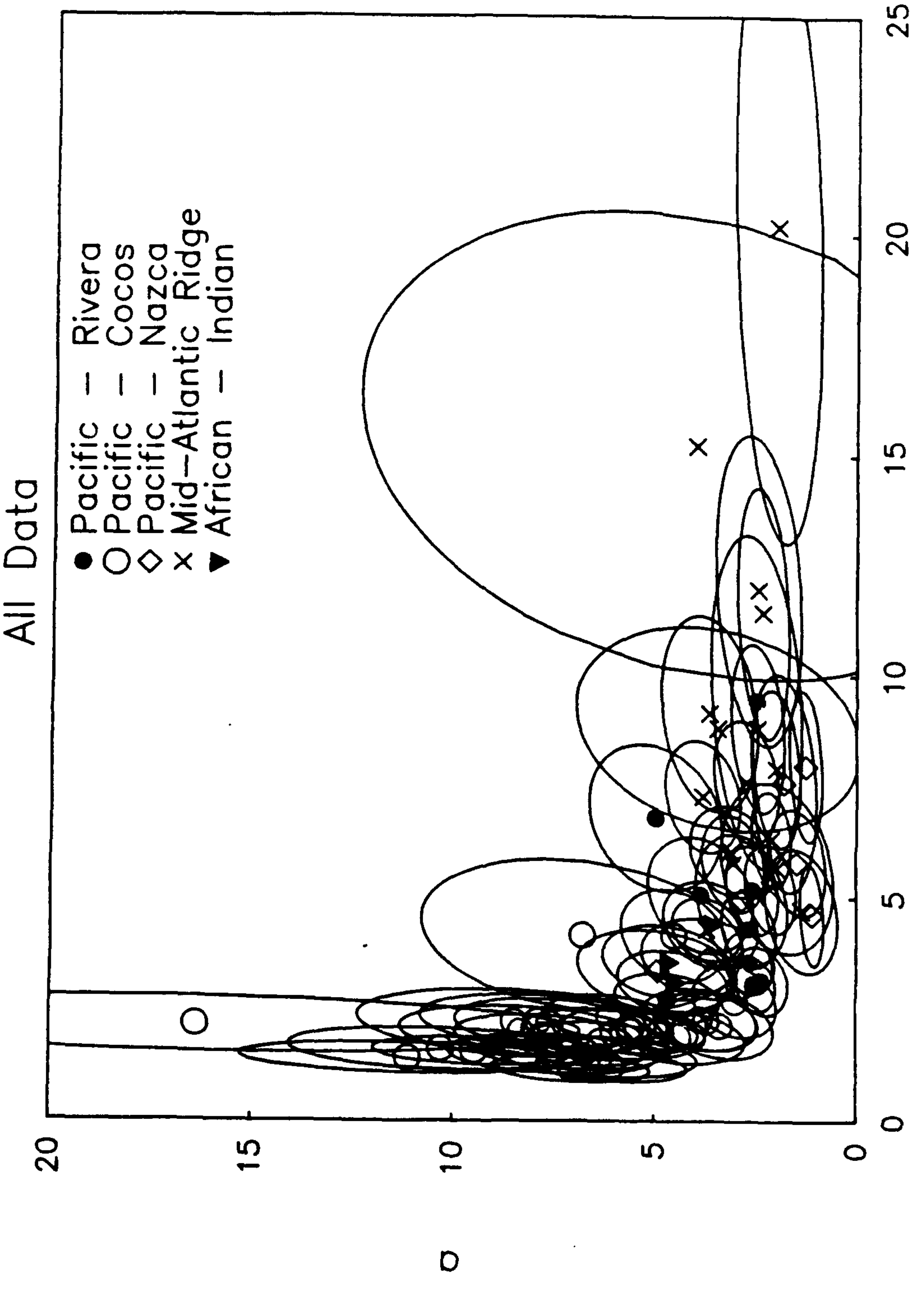

Figure 5.8. Estimated values of aspect ratio (a) plotted as a function of characteristic width (λ_n). Values are listed in Table 5.2. Ellipses represent 1-σ errors about each estimation. Different symbols represent data from different spreading regions as indicated.

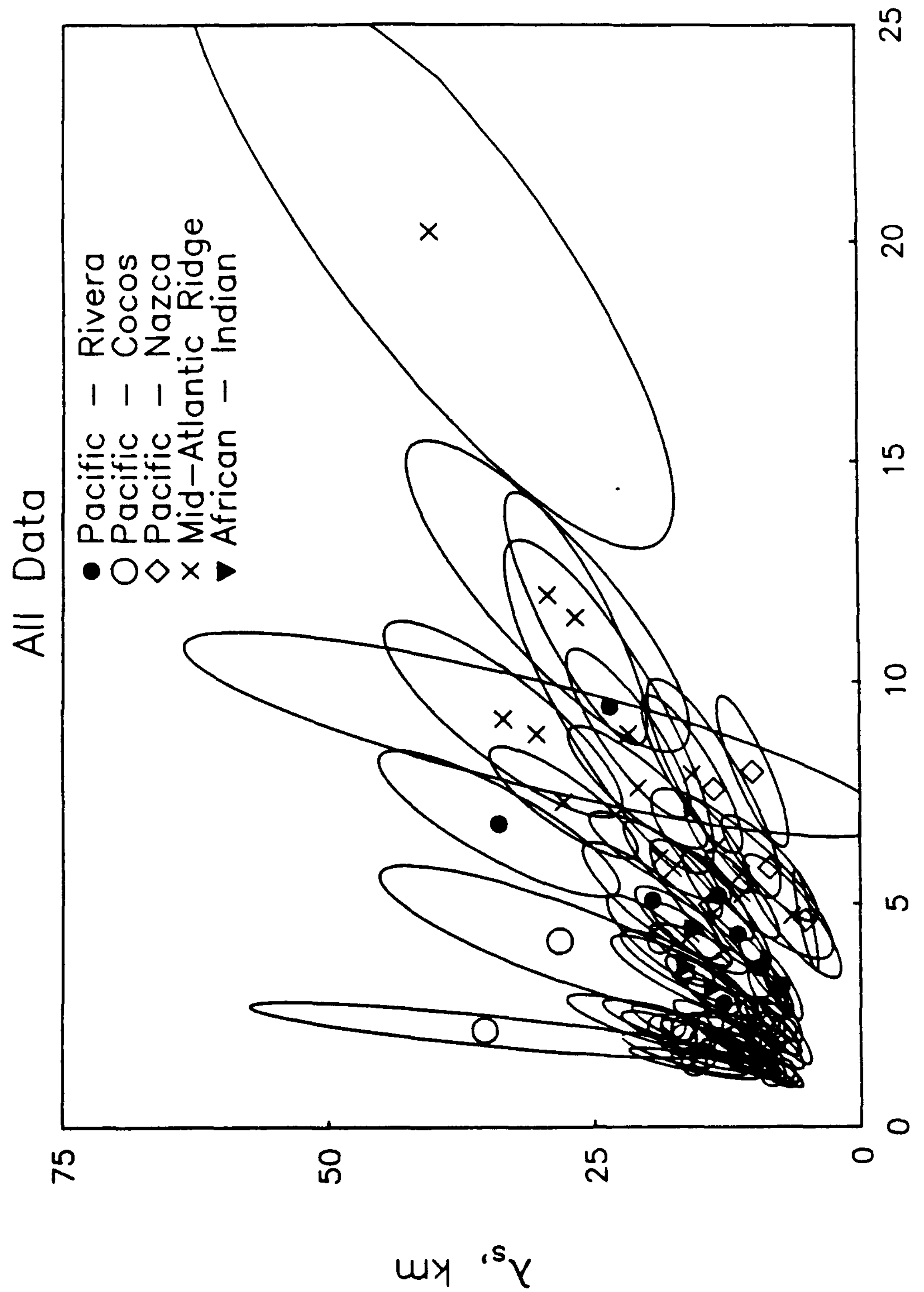

Figure 5.9. Estimated values of characteristic length (λ_s) plotted as a function of characteristic width (λ_n). Values are listed in Table 5.2. Ellipses represent 1-σ errors about each estimation. Different symbols represent data from different spreading regions as indicated.

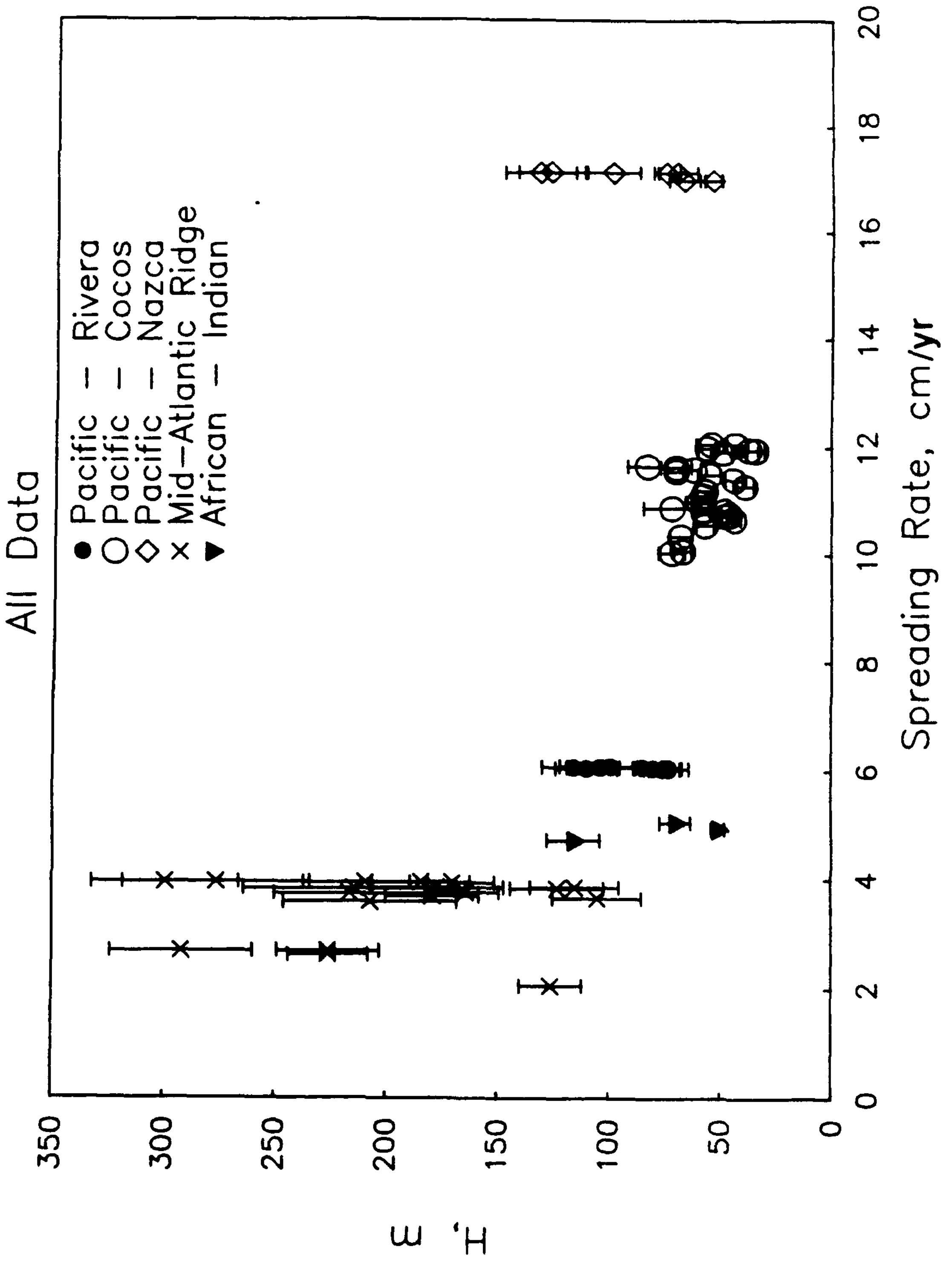

Figure 5.10. Rms height (*H*) (Table 5.2) plotted as a function of spreading rate (Table 5.1) as determined by model RM2 [*Minster and Jordan*, 1978]. Bars represent 1-σ errors about each estimation. Different symbols represent data from different spreading regions as indicated.

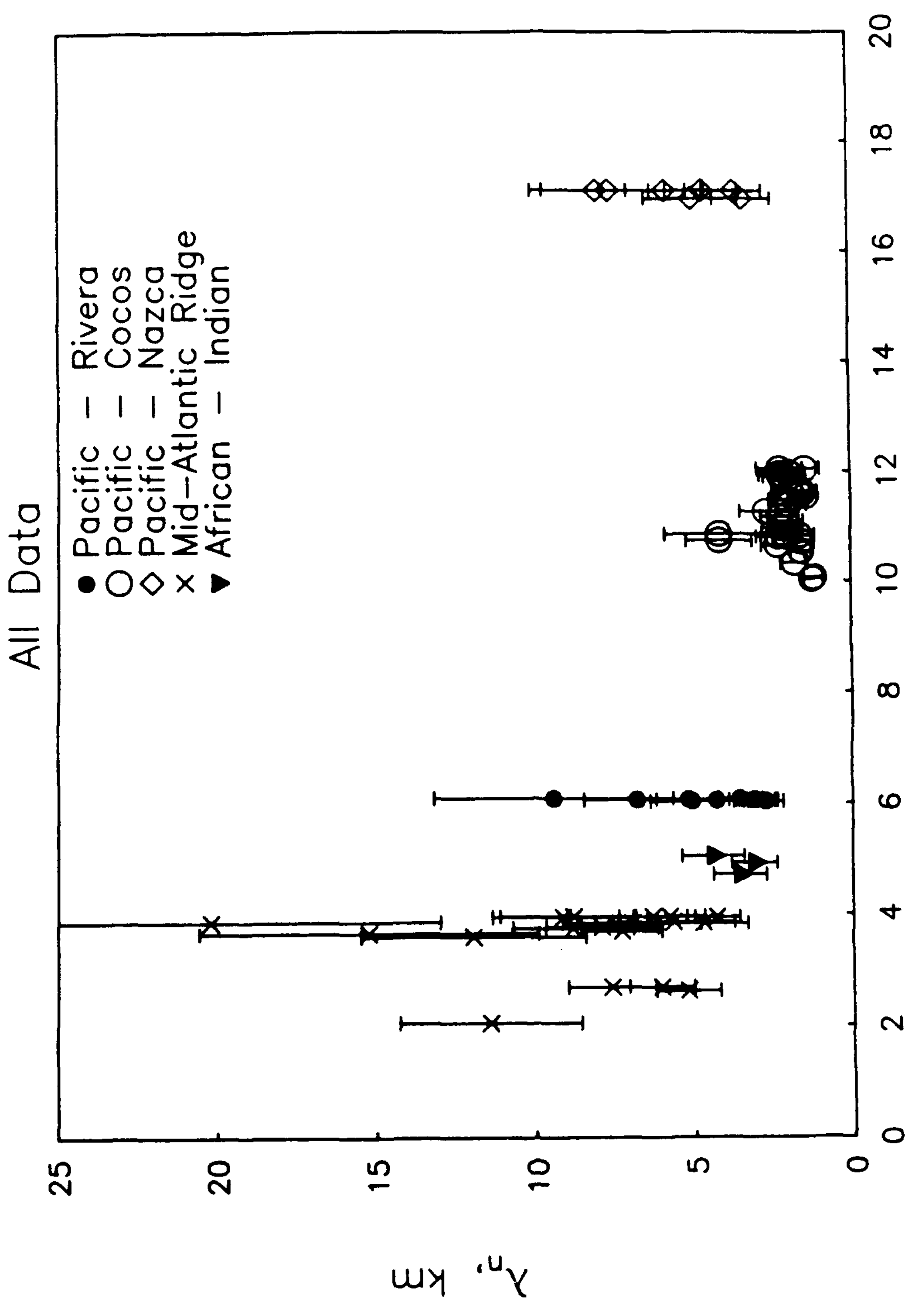

Figure 5.11. Characteristic width (λ_n) (Table 5.2) plotted as a function of spreading rate (Table 5.1) as determined by model RM2 [*Minster and Jordan*, 1978]. Bars represent 1-σ errors about each estimation. Different symbols represent data from different spreading regions as indicated.

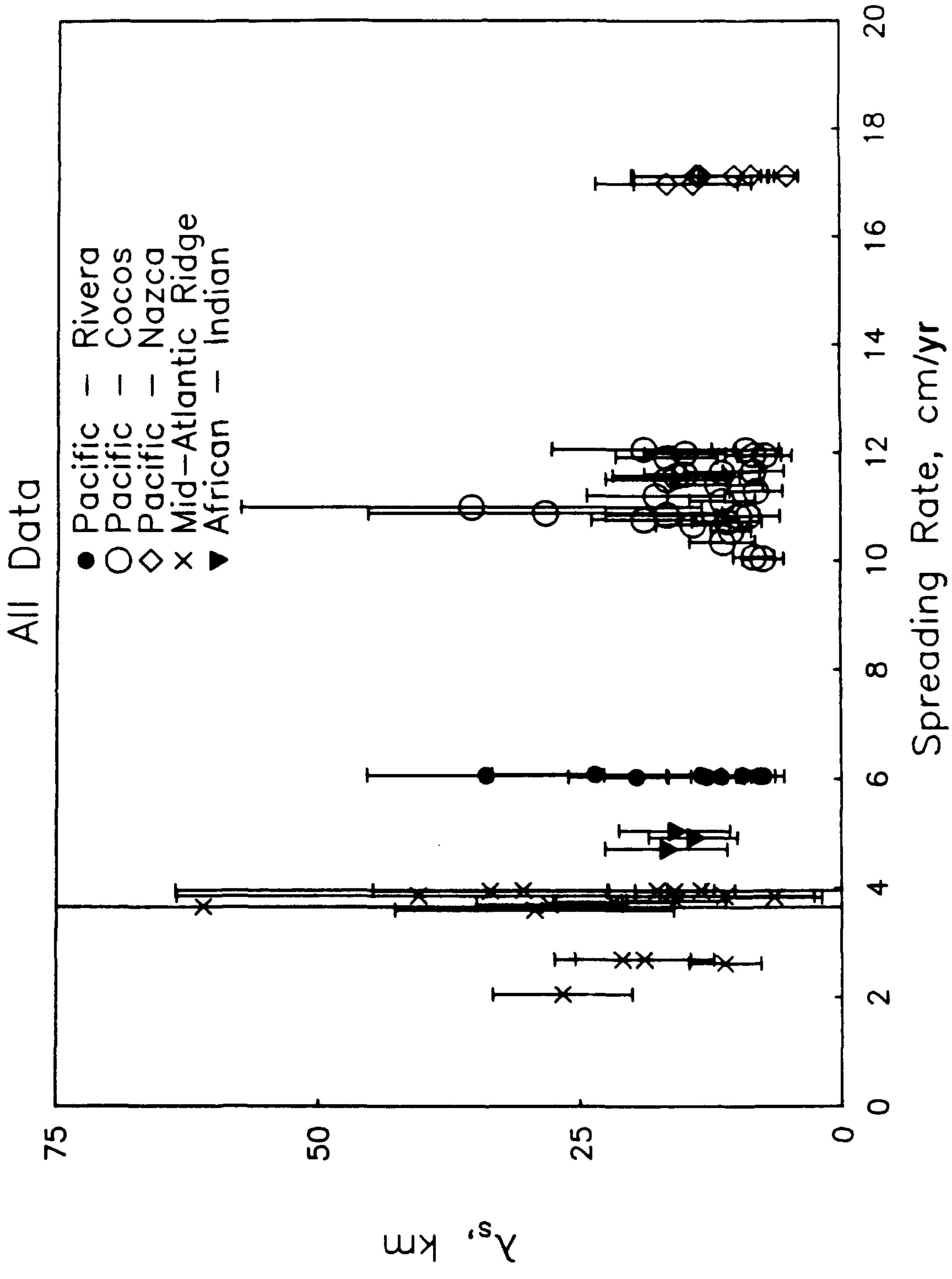

Figure 5.12. Characteristic length (λ_S) (Table 5.2) plotted as a function of spreading rate (Table 5.1) as determined by model RM2 [*Minster and Jordan*, 1978]. Bars represent 1-σ errors about each estimation. Different symbols represent data from different spreading regions as indicated.

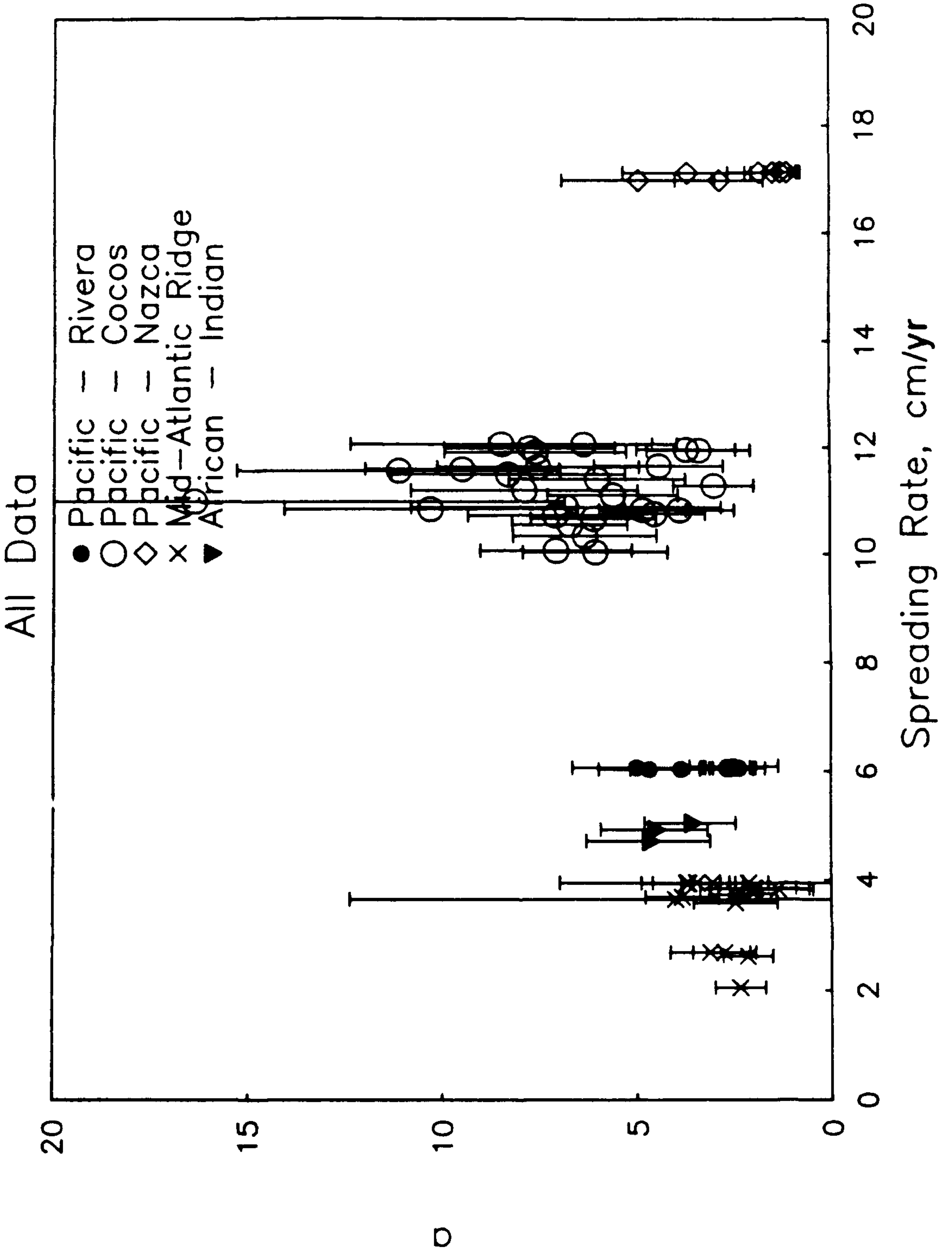

Figure 5.13. Aspect ratio (*a*) (Table 5.2) plotted as a function of spreading rate (Table 5.1) as determined by model RM2 [*Minster and Jordan*, 1978]. Bars represent 1-σ errors about each estimation. Different symbols represent data from different spreading regions as indicated.

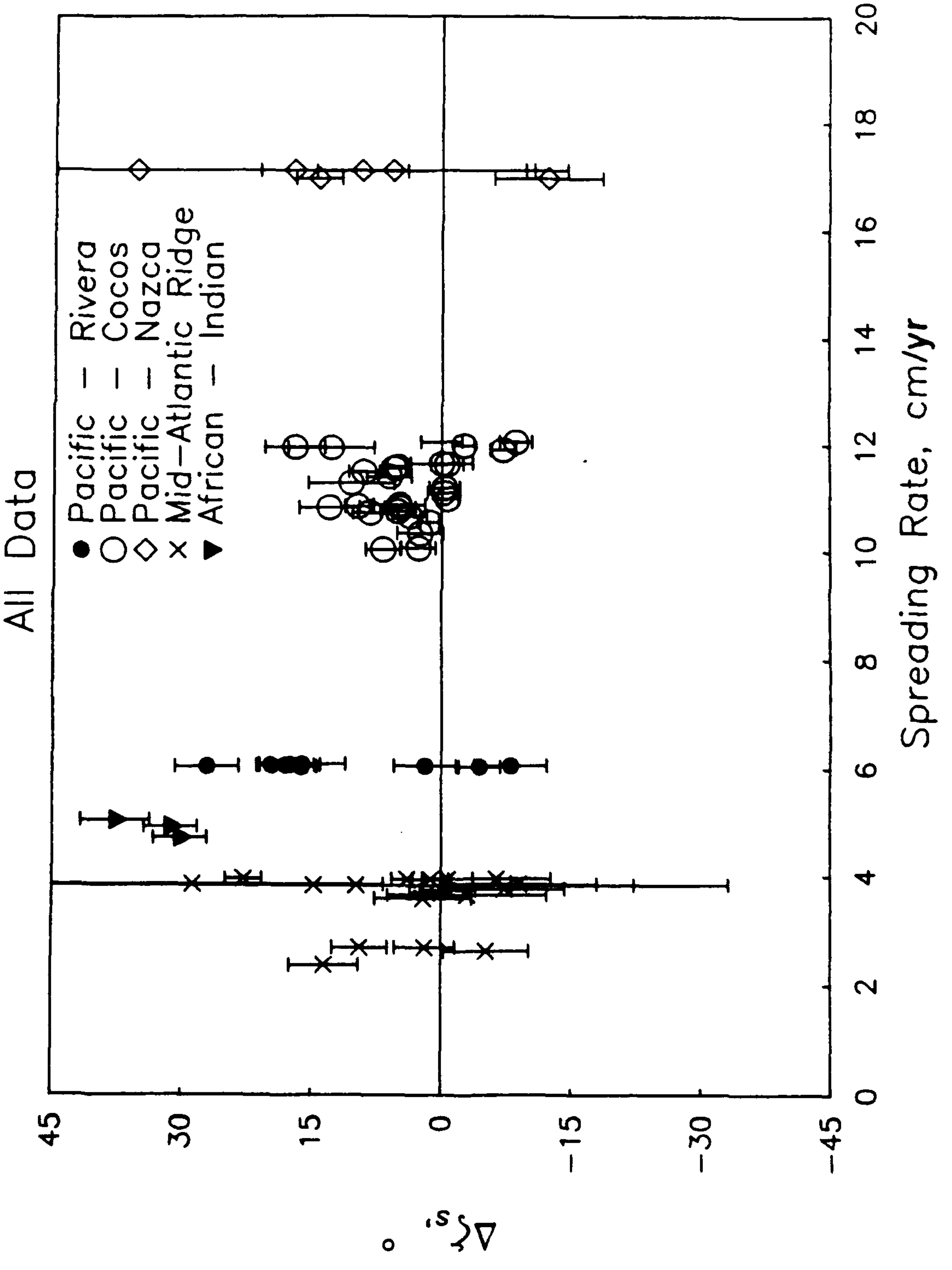

Figure 5.14. Difference ($\Delta\zeta_s$) between the normal to spreading direction and estimated abyssal hill lineation (ζ_s) (Table 5.2) plotted as a function of spreading rate (Table 5.1) as determined by model RM2 [*Minster and Jordan*, 1978]. Bars represent 1-σ errors about each estimation. Different symbols represent data from different spreading regions as indicated.

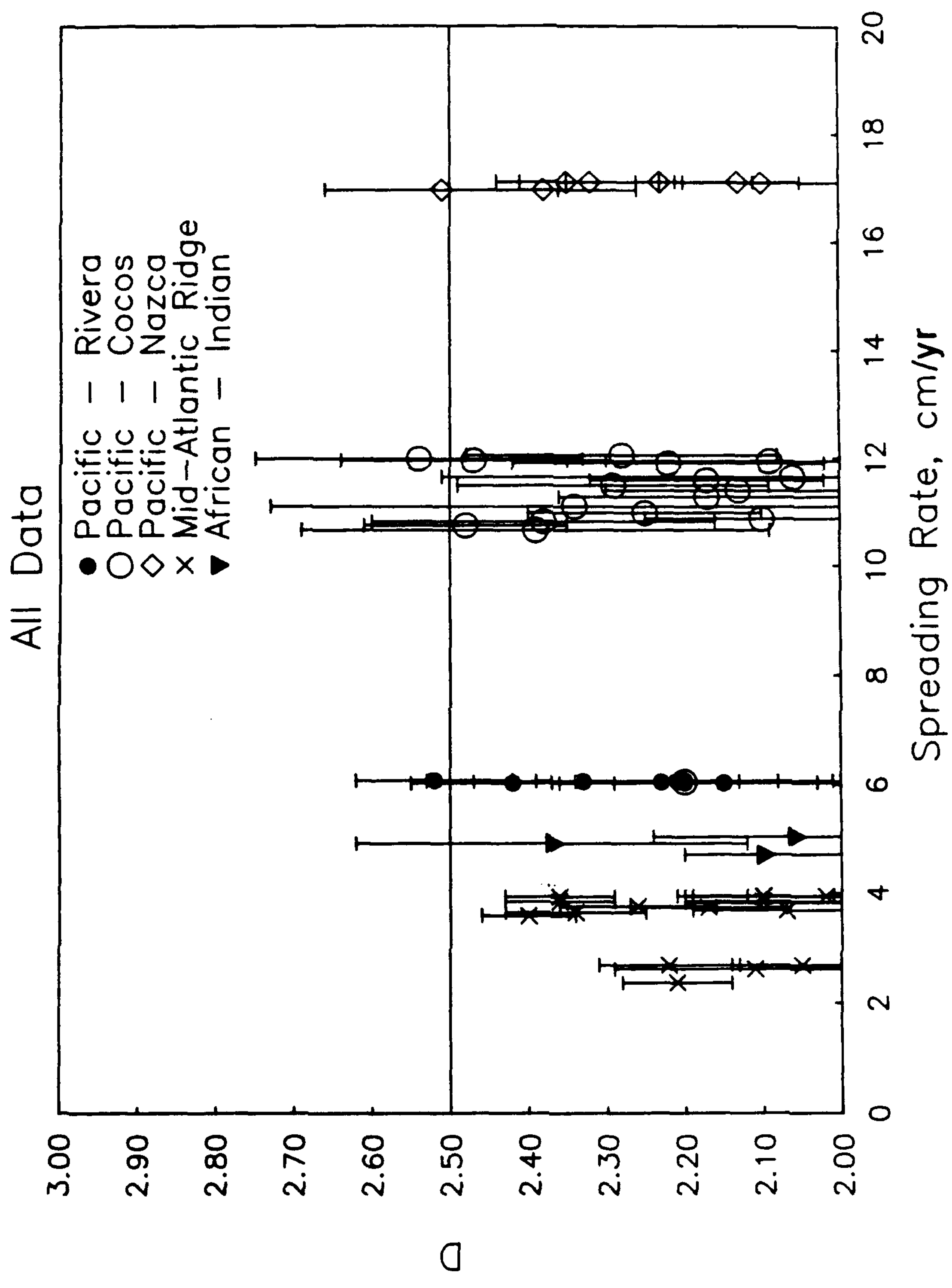

Figure 5.15. Hausdorff dimension (D) (Table 5.2) plotted as a function of spreading rate (Table 5.1) as determined by model RM2 [*Minster and Jordan*, 1978]. Bars represent 1-σ errors about each estimation. Different symbols represent data from different spreading regions as indicated.

Macdonald et al.: East Pacific Rise From Siqueiros to Orozco Fracture Zones

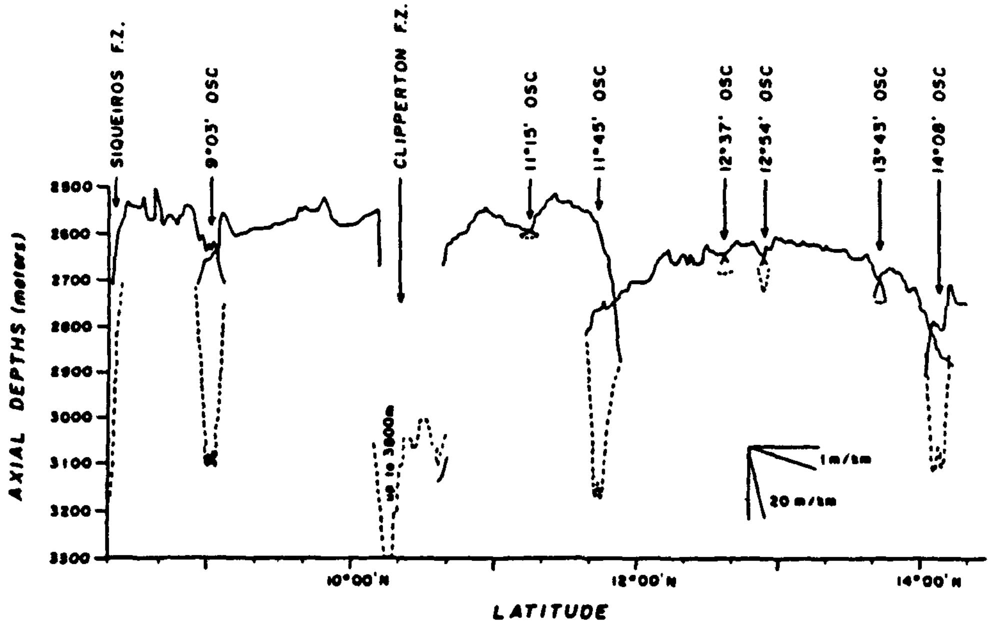

Fig. 3. Longitudinal profile of the depth of the shallowest point of the neovolcanic zone, plotted versus latitude (solid line). A bathymetric point is picked every minute of latitude from 10-m interval charts which provide continuous coverage of the axial neovolcanic zone. Dashed lines show the maximum depths attained at fracture zones and at overlap basins between OSC's. In general, there is a correlation between the depth of the rise and its cross-sectional shape (see text for discussion).

Figure 5.16. Depth to shallowest point of the East Pacific Rise crest plotted as a function of latitude. Reprinted from *Macdonald et. al.* [1984].

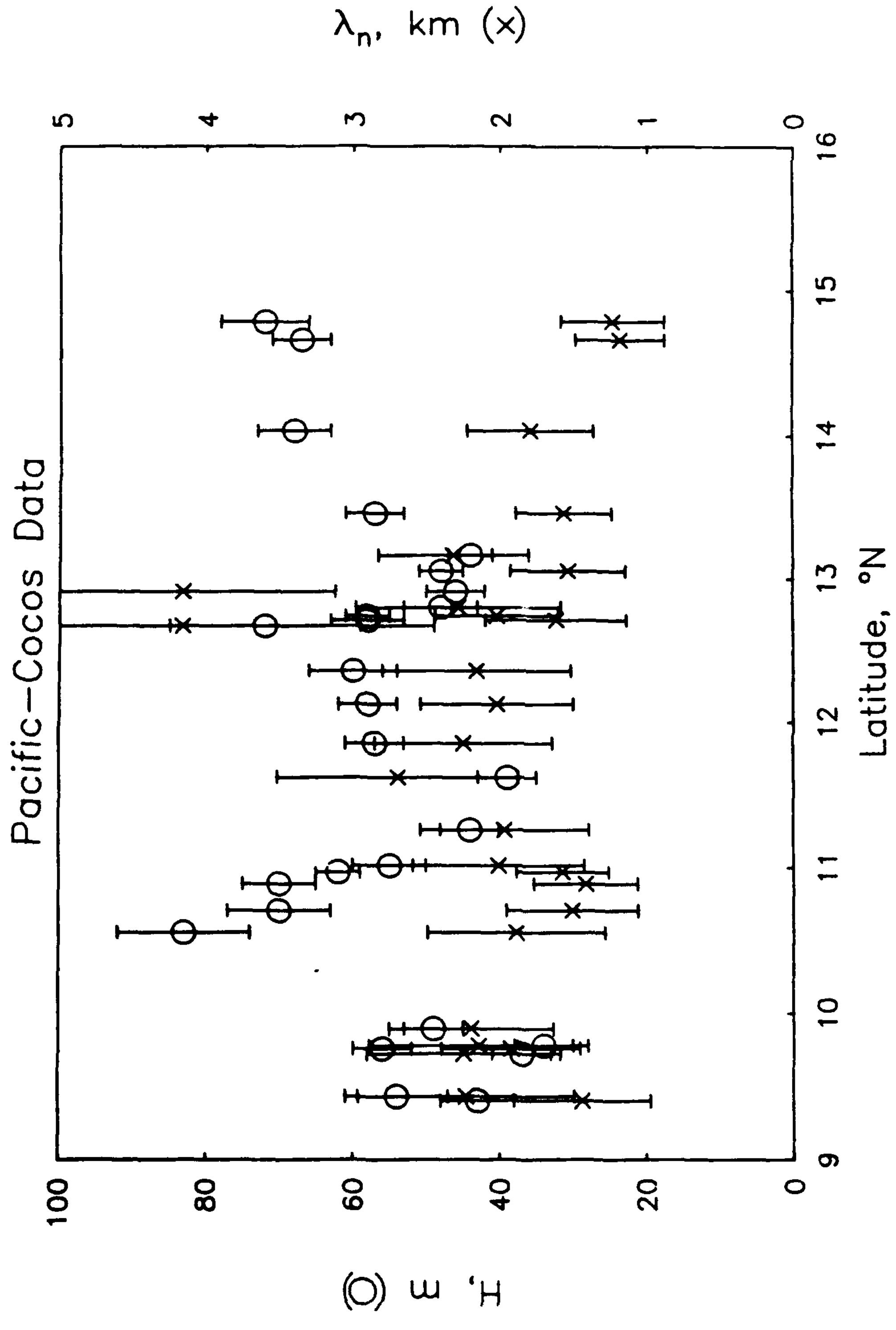

Figure 5.17. Rms height (H) and characteristic width (λ_n) (Table 5.2) for the Pacific-Cocos data plotted as a function of average latitude of each swath. Bars represent 1-σ errors about each estimation.

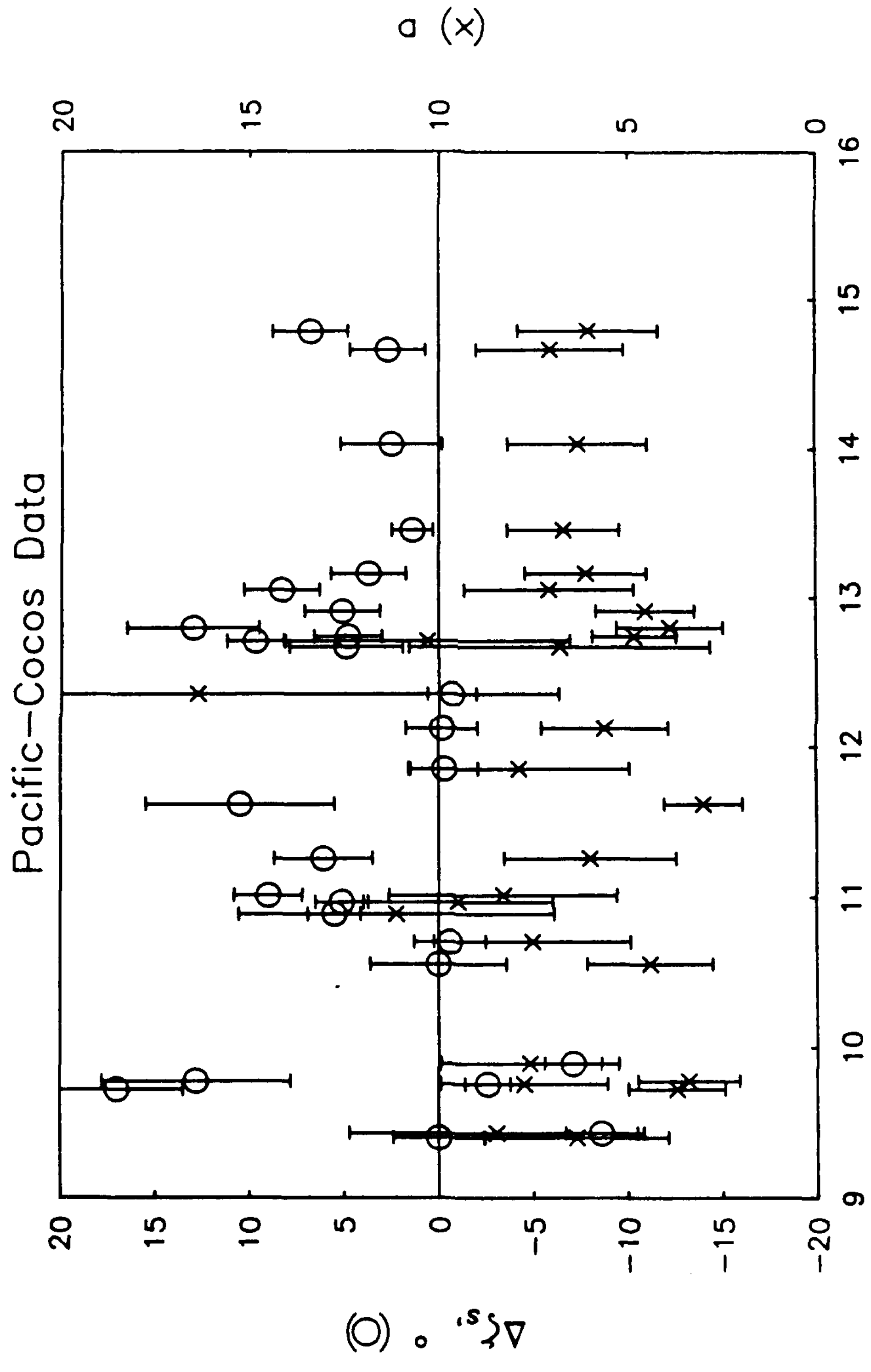

Figure 5.18. Difference ($\Delta\zeta_s$) between the normal to spreading direction (model RM2 [*Minster and Jordan*, 1978]) and estimated abyssal hill lineation (ζ_s) (Table 5.2) and aspect ratio (a) (Table 5.2) for the Pacific-Cocos data plotted as a function of average latitude of each swath. Bars represent 1-σ errors about each estimation.

CHAPTER 6

NON-GAUSSIAN STOCHASTIC ANALYSIS OF THE SEAFLOOR

INTRODUCTION

The work presented in this thesis till now has focused on the use of second-order (Gaussian) statistics in the characterization of abyssal hill morphology. As we have shown in previous chapters, this work provides a very useful low-order quantitative description which can be applied to the geophysical study of ridge-crest and abyssal hill forming processes. However, second-order statistics are, in a sense, only half the statistical picture. In the wavenumber domain they only provide information regarding the amplitude of the spectrum, with no constraint on the phase. In the space domain second-order statistics provide no means of describing, for example, asymmetries in the distribution. Asymmetries in the vertical distribution can tell us whether or not peaks tend to be larger and sharper than troughs (or vice verse). This type of parameter can be related to the amount of sediment ponding or, perhaps, to the degree to which the morphology was constructionally (e.g by extrusive volcanics) or destructionally (e.g. by rifting or faulting) formed. Asymmetries in the lateral distribution, such as that slopes facing one direction tend to be steeper or more gradual than those facing the opposite direction, can also be important. Lateral asymmetries may be related to the style of normal faulting contributing to abyssal hill formation. Another important characteristic unmodeled by second-order statistics is the size of the tails of the probability density. Large tails allow for occasional large peaks to exist in the topography. This "peakiness" may be related to the degree to which the formation of abyssal hills is non-uniform or episodic. Quantifying such higher-order characteristics may be an important means of evaluating the validity of various models for the formation of abyssal hill (Figure 5.5).

To quantify these higher-order features we must appeal to higher statistical moments than order two. In this chapter we introduce a mathematical framework for the study of higher moments of a topographic field. This framework is built upon the concept that lower-order moment provide the groundwork for studying the higher-order moments. Following this general discussion we propose a very simple 1-D parameterized model for moments up to order 4. This model includes two parameters for the third moment, describing vertical and lateral asymmetries, and one for the fourth moment, which describes the peakiness of topography. We then describe initial methods for estimating these parameters from bathymetric profiles. Finally, we present a general comparison of results from near ridge data from the Pacific and Atlantic oceans, and discuss these results with reference to abyssal hill forming processes.

FRAMEWORK FOR THE STUDY OF HIGHER-ORDER MOMENTS

In this section we present a framework for the study of higher-order moments based on decomposition of moments by the process of "iterated" expectation. Through this decomposition, a statistical moment is represented in terms of two-point conditional expectations, lower moments, and the vertical (disjoint) moment of the same order. We shall also show in this section that we can determine the conditional expectation if we are given a morphological model expressed in terms of an invertible mapping from a topographic field with known statistics (e.g. a Gaussian). (Such mapping models are useful both for the fact that they can be very intuitive, and for their utility in generating non-Gaussian synthetic topography.) Any moment of the model can thus be computed if we know the lower order moments and the vertical moment of the same order (which, as we will see in the next section, can be a parameter in the mapping). This yields a forward problem, allowing for the formulation of an inverse problem which estimates model parameters from estimates of topographic moments.

Decomposition of the N-Point Moment

The N-point moment was introduced in Chapter 2, equation (2.3). Using "iterated" expectations, we decompose the N-point moment in the following way [e.g. *Taylor and Karlin*, 1984, p. 47]:

$$\mathrm{E}[h_1 h_2 h_3 \dots h_n] = \mathrm{E}[h_1\, \mathrm{E}[h_2 h_3 \dots h_n \mid h_1]] \tag{6.1}$$

where $h_i = h(\mathbf{x}_i)$. In the following discussion, the index i represents an arbitrary coordinate index, whereas the index j is used interchangeably as a second arbitrary coordinate index or, when added to i, as a lag index. We express each h_j in terms of a component which is dependent on h_1 and a component which is independent of h_1:

$$h_j = \mathrm{E}[h_j \mid h_1] + X_j^{(1)} \tag{6.2}$$

By this construction, $X_j^{(1)}$ is uncorrelated with h_1; i.e. if we multiply (6.2) by h_1 and take the expected value, we obtain

$$\mathrm{E}[h_1 h_j] = \mathrm{E}[h_1\, \mathrm{E}[h_j | h_1]] + \mathrm{E}[h_1 X_j^{(1)}] \tag{6.3}$$

The first term on the right-hand-side is simply the iterated expectation of $\mathrm{E}[h_1 h_j]$. Thus the second term of the right-hand-side of (6.3) is zero; i.e. $X_j^{(1)}$ is uncorrelated with h_1. It is also clear that the two right-hand terms in (6.2) are uncorrelated with each other. This is shown by multiplying (6.2) by $\mathrm{E}[h_1 h_j]$ and again taking the expected value. Since

$E[h_jE[h_j|h_1]] = E[E[h_j|h_1]\,E[h_j|h_1]]$ (again by iterated expectation) we must have $E[E[h_j|h_1]\,X_j^{(1)}] = 0$, or that $X_j^{(1)}$ is uncorrelated with $E[h_j|h_1]$.

$E[h_j|h_1]$ is a function of h_1 and lag $(j-1)$ whose expected value, as is that of h_1, is zero. To emphasize this dependence we write it as $f_j(h_1)$. Inserting (6.2) into (6.1) then yields

$$E[h_1h_2h_3...h_n] = E[h_1\,E[(f_2(h_1)+X_2^{(1)})(f_3(h_1)+X_3^{(1)})...(f_n(h_1)+X_n^{(1)})|h_1]] \qquad (6.4)$$

The inner conditional expectation can easily be computed with this construction; conditioned on h_1, $f_j(h_1)$ is a constant, and $X_j^{(1)}$ is independent of h_1, so that the inner conditional expectation is simply a computation of various moments of $X_j^{(1)}$ up to order n-1 multiplied by constants. Using (6.2), these moments can be computed if we know the moments of h to order n-1 and the functions $f_j(h_i)$. The third moment provides a useful example:

$$\begin{aligned} E[h_1h_2h_3] &= E[h_1\,E[(f_2(h_1)+X_2^{(1)})(f_3(h_1)+X_3^{(1)})|h_1]] \\ &= E[h_1f_2(h_1)f_3(h_1)] + E[h_1f_2(h_1)E[X_3^{(1)}]] + E[h_1f_3(h_1)E[X_2^{(1)}]] + E[h_1E[X_2^{(1)}X_3^{(1)}]] \qquad (6.5) \end{aligned}$$

By taking the expected value of both sides of equation (6.2), we find that $E[X_j^{(1)}] = 0$. Thus the second and third terms of the right-hand-side of (6.5) are zero. Also, since $E[h_1] = 0$, the last term in (6.5) is also zero (we don't need to calculate $E[X_2^{(1)}X_3^{(1)}]$ at this stage). We are thus left with

$$E[h_1h_2h_3] = E[h_1f_2(h_1)f_3(h_1)] \text{ or } E[h_1E[h_2|h_1]E[h_3|h_1]] \qquad (6.6)$$

Using equation (6.6), the full third moment of h can be computed by integrating the argument of the outer expectation over the (disjoint) probability density of h, which requires that we be able to specify the density to third order and the $f_j(h_i)$ functions.

Mapping Models and the Calculation of $f_j(h_i)$

For visualization purposes, we represent $f_j(h_i)$ in terms of its Gaussian and non-Gaussian components:

$$\mathrm{E}[h_j|h_i] = f_j(h_i) = r_{ij}h_i + g_j(h_i) \tag{6.7}$$

r_{ij} is the correlation function ($r_{ij} = C_{hh}(\mathbf{x}_i - \mathbf{x}_j)/H^2$) between h_i and h_j. $g_j(h_i)$ is thus the change in conditional expectation from what it would be if h were Gaussian distributed. An important constraint on $g_j(h_i)$ is derived by taking the covariance between h_i and h_j:

$$\mathrm{E}[h_ih_j] = C_{hh}(\mathbf{x}_j - \mathbf{x}_i) = H^2 r_{ij} = \mathrm{E}[h_i\,\mathrm{E}[h_j|h_i]] \tag{6.8}$$

By inserting (6.7) into the right-hand-side of (6.8), we see that $\mathrm{E}[h_i\, g_j(h_i)] = 0$. We also find, by taking the expected value of equation (6.7), that $\mathrm{E}[g_j(h_i)] = 0$.

$f_j(h_i)$ and $g_j(h_i)$ can be calculated if we know the conditional probability density function for two points:

$$\mathrm{E}[h_j|h_i] = \int_{-\infty}^{\infty} h_j'\, p(h_j'|h_i)\, dh_j' \tag{6.9}$$

At this point we part with complete generality so that we can do something useful. We now assume that we intend to apply the study of higher order moments to a morphological model. In particular, this model is one which is expressed by a one-to-one, onto (i.e.

invertible) mapping $M^{G \to P}$ (with inverse mapping $M^{P \to G}$) of a topographic field with known statistics h_i^G (presumably, but not necessarily Gaussian), such that

$$h_i = M^{G \to P}(h_i^G), \quad h_i^G = M^{P \to G}(h_i) \tag{6.10}$$

We also assume that the mapping preserves second-order statistics, so that the mean and covariance of h is identical to that of h^G. As we shall see in the next section, such mappings can be very convenient both for our ability to intuitively grasp their effect on the topography and in their utility for generating synthetic realizations with non-Gaussian statistics.

The following equation allows us to numerically calculate $p(h_j|h_i)$, and thus $f_j(h_i)$, for a given mapping:

$$p(h_j|h_i)dh_j = p(h_j^G|h_i^G)\,dh_j^G, \quad dh_j^G = (h_j + \frac{dh}{2})^G - (h_j - \frac{dh}{2})^G \tag{6.11}$$

The validity of (6.11) can be seen in the following way. Consider first all positions i of a finite topographic field for which the value $= c_i$, the total number of which $= N(c_i)$. We then express the conditional probability that at position $i + j$ the value is h_{i+j} within a given interval Δh:

$$P(h_{i+j} - \frac{\Delta h}{2} < h_{i+j}' \le h_{i+j} + \frac{\Delta h}{2} | \, c_i) = \frac{N(h_{i+j} - \frac{\Delta h}{2} < h_{i+j}' \le h_{i+j} + \frac{\Delta h}{2})}{N(c_i)}$$

$$\cong p(h_{i+j}|c_i)\,\Delta h \tag{6.12}$$

If the mapping is invertible, then

$$\begin{gathered} N(c_i^G) = N(c_i) \\ N((h_{i+j}-\frac{\Delta h}{2})^G < h_{i+j}^{G\,\prime} \le (h_{i+j}+\frac{\Delta h}{2})^G) = N(h_{i+j}-\frac{\Delta h}{2} < h_{i+j}' \le h_{i+j}+\frac{\Delta h}{2}) \end{gathered} \tag{6.13}$$

Using these substitutions in (6.12) and taking the limit as the size of the topographic field becomes arbitrarily large and as $\Delta h \rightarrow 0$ yields (6.11).

We are thus able, given a morphological mapping model, to calculate any moment of the resulting field, providing a critical link between our primary tool for estimation and a parameterized representation of topography which is intuitively clear and can be used to generate synthetic topography.

A SIMPLE THIRD AND FOURTH MOMENT MODEL

In the previous section we showed that, given an invertible morphological mapping, we can determine all the moments of the resulting topographic field. In this section we will present a combination of two 1-D mapping models which provide three parameters describing vertical and lateral asymmetries and peakiness in the distribution. The asymmetries can be estimated using the third moment and peakiness by the fourth.

Vertical Asymmetry and Peakiness

For describing vertical asymmetry we propose to use the topographic skewness $\mu_3 = \mathrm{E}[h^3(\mathbf{x})]/H^{3/2}$. The skewness will be positive if peaks tend to be sharper and broader than troughs, and will be negative if the reverse is true. For describing peakiness we propose to use the topographic kurtosis $\mu_4 = \mathrm{E}[h^4(\mathbf{x})]/H^2$. For a Gaussian field, $\mu_4 = 3$. At larger values of μ_4, larger peaks and troughs will become more exaggerated while topography nearer the mean will be shifted even closer to the mean. An increase in peakiness also results in an increase in boxiness.

The skewness and kurtosis are well known parameters and we do not require the framework described above to estimate or understand them. Without the framework, however, these parameters do not provide a complete description of the third and fourth moments of the topographic field. For example, if we know the covariance and the value of μ_3, can we also determine $E[h_1 h_2 h_3]$? Also, how do we synthesize topography with non-zero μ_3 and/or non-Gaussian μ_4? To answer the latter question (and provide a means of answering the former) we construct a mapping of a topographic field with a Gaussian density to a field with a density having the same second moment and with skewness and kurtosis given by desired values of μ_3 and μ_4. We can formulate such a density using Hermite polynomials, whose terms are perturbations to a Gaussian function with coefficients given by the statistical moments μ_i ($i > 2$). To fourth order, these are given by [*Papoulis*, 1965]

$$p_H(h,\sigma,\mu_3,\mu_4) = \frac{1}{\sigma\sqrt{2\pi}} \exp(-h^2/2\sigma^2) \left[1 + \frac{\mu_3}{3!\sigma^3}\left(\frac{h^3}{\sigma^3} - \frac{3h}{\sigma}\right) + \frac{1}{4!}\left(\frac{\mu_4}{\sigma^4} - 3\right)\left(\frac{h^4}{\sigma^4} - \frac{6h^2}{\sigma^2} + 3\right)\right] \tag{6.14}$$

where $\sigma = (\mu_2)^{1/2}$. Equation (6.14) is plotted in Figure 6.1 at various values of μ_3 and μ_4. Note that where μ_3 is non-zero while $\mu_4 = 3$ (top panel), the function can become negative, which is not acceptable for a probability density. This reflects the fact that when μ_3 is non-zero, either the peaks or the troughs are "peaky", which is the topographic property of kurtosis. It is thus not surprising that the negative portions of p_H can be eliminated by increasing the value of μ_4 in (6.14) (bottom panel of Figure 6.1). Thus non-Gaussian values of μ_4 must be considered when non-Gaussian values of μ_3 are as well. Equation

(6.14) also becomes negative at vales of $\mu_4 > 7$ (middle panel), indicating perhaps that higher moments than 4 should also be considered when μ_4 is large.

Using (6.14) the Hermite mapping algorithm proceeds as follows:

1. A Gaussian realization (see Appendix B) is generated from the desired covariance model.

2. For each value of the Gaussian realization $h^G{}_i$, the probability distribution at that value is calculated by integrating the probability density

$$P_H(h_i^G,\sigma,0,3) = \int_{-\infty}^{h^G} p_H(h_i^G,\sigma,0,3)\; dh_i^{G\prime} \tag{6.15}$$

3. The value h_i is then found for which $P_H(h_i,\sigma,\mu_3,\mu_4) = P_H(h_i^G,\sigma,0,3)$.

Figure 6.2 shows a Gaussian profile and the mapping of this profile into Hermite probability spaces with various values of μ_3 and μ_4. From these plots the reader can gain an intuitive sense of the meaning of vertical asymmetry and peakiness.

Armed with a morphological mapping, we can now address the question of what is the general third and fourth moment of a mapped field. The first step is to calculate $g_j(h_i)$ using, in order, equations (6.11), (6.9), and (6.7). Figure 6.3 shows $g_j(h_i)$ calculated in this manner at different values of μ_3 and μ_4. We have also calculated these functions numerically by generating 50 synthetic profiles using the mapping algorithm, and then binning and averaging the difference between observed conditional values and the expected conditional value under the Gaussian hypothesis; i.e. each bin is the average of all differences $h_{i+j} - r_j h_i$ where h_i falls within an interval $c_i \pm \Delta h$. The close match between each of the two plots if Figure 6.3 indicates that we are generally successful in calculating the functions $g_j(h_i)$ for the Hermite mapping model.

Using equation (6.6) we can now calculate $\mathrm{E}[h_i h_{i+j} h_{i+k}] = C_{hhh}(\mathrm{x}_j,\mathrm{x}_k)$ by integrating $h_i f_j(x_i) f_k(x_i)$ over the probability density for h (6.14). There are many redundancies in the third moment. For example, for a 1-D profile the axis $x_j = 0$ is identical to the axis $x_k = 0$, and the axis $x_j = -x_k$ is identical to the axis $x_j = 2x_k$. In all there are six redundant regions on the lag coordinate plane [*Nikias and Raghuveer*, 1987]. We restrict consideration to the cases $x_k \leq 0 \leq x_j$, and $x_j \leq 0 \leq x_k$, where $|x_k| \leq |x_j|$. Figure 6.4 shows three axes of $C_{hhh}(x_j,x_k)$ calculated using (6.6) for the case $\mu_3 = 0.5$, and covariance parameters $k_\theta = 1.0$ and D = 1.5. The three axes correspond to the cases $x_k = 0$, $x_j = -2x_k$, and $x_j = -x_k$, presenting the widest possible variation in the region of consideration. Also shown in Figure 6.4 are estimated third moment axes generated by averaging the following summation over 50 synthetic profiles:

$$\tilde{C}_{hhh}(x_j,x_k) = \frac{1}{N_i} \sum_{i=1}^{N_i} h_i h_{i+j} h_{i+k} \tag{6.16}$$

The match for all three axes is very good, indicating that we are successful in predicting the general form of the third moment under the Hermite mapping described above.

Lateral Asymmetry

We use the following mapping algorithm to generate synthetic profiles whose slopes facing in one direction are on average steeper than slopes facing in the opposite direction:

1. A Gaussian profile is generated from the desired covariance model.

2. Each value of the Gaussian realization $h^G(x_i)$ is mapped to a new coordinate position using the equation

$$h(x_i + \alpha h^G(x_i)/H) = h^G(x_i) \tag{6.17}$$

3. The tilted profile is then resampled at the original data spacing by linear interpolation between nearest neighbor points.

We call this algorithm the uniform tilt mapping since features of identical shape but different scale will continue to have the same relative shape and scale after mapping. If we follow this mapping algorithm with the Hermite distribution mapping, we can produce a synthetic realization with all three characteristics that we are trying to model. Figure 6.5 shows several examples of profiles generated using various combinations of the two mapping algorithms. Where α is positive, slopes facing to the right are steeper than those facing the left. This is particularly accentuated on the large peaks in the case $\mu_3 = 1.0$, $\alpha = 0.4$, and $\mu_4 = 7.0$ (bottom panel).

The uniform tilt mapping does not change the vertical distribution of h. The skewness is therefore zero, and $C_{hhh}(x_j,x_k)$ will be an odd function. The Hermite mapping on the other hand only produces an even contribution to $C_{hhh}(x_j,x_k)$. We shall therefore be able to study the vertical and lateral asymmetries separately simply by separating the third moment into even and odd components.

Although the uniform tilt mapping produces very nice tilted synthetics, it has an important flaw: it is not completely invertible. The problem is that there is a strong probability, given a fractal surface, that there exists topographic points which are close enough to each other and sufficiently separated vertically before mapping to have their order reversed after mapping (i.e. they will produce an overhang). When the surface is resampled in step 3 we must effectively discard one of the points. This problem is apparent in the discrepancy between the calculated and numerically constructed $g_j(h_i)$ functions (Figure 6.6), which is most pronounced near $h = 0$. The region near $h = 0$ is, unfortunately, where $p_H(h)$ is greatest. We can therefore expect a strong effect on the calculation of $C_{hhh}(x_j,x_k)$ when calculated using equation (6.6). Calculated and numerically constructed axes of $C_{hhh}(x_j,x_k)$ for $\mu_3 = 0.5$ and $\alpha = 0.1$ are shown in Figure 6.7. On the axes where $x_j \neq -x_k$, rather than decay monotonically to zero, the calculated functions initially level off at non-zero values (either positive or negative depending on the sign of the lag). This problem is made especially clear when we plot the odd portion of $C_{hhh}(x_j,x_k)$ (Figure 6.8, larger dashed lines).

We can better solve for one axis of $C_{hhh}(x_j,x_k)$ in the case of the uniform tilt mapping if we restrict consideration to the skewness of the difference function $D(x_i, x_j) = h(x_i + x_j) - h(x_i)$. The skewness of the difference is related to $C_{hhh}(x_j,x_k)$ in the following way

$$\mathrm{E}[D^3(x_j)] = 6\,\mathrm{E}[h^2(x_i)\,h(x_{i+j})]^{\mathrm{o}} \tag{6.18}$$

where the superscript o indicates the odd part. Because the field is stationary, there is no dependence on x_i. As shown in Appendix A, if the topography is Gaussian distributed, then the differences will also be Gaussian distributed with zero mean and variance given by $2(C_{hh}(0) - C_{hh}(j))$. The probability density function $p_{x_j}(D)$ (the probability that, over a lag x_i, the difference $= D$) for $D(x_i,x_j)$ of a field generated under the uniform tilt mapping can be constructed in a manner similar to (6.11):

$$\begin{gathered} p_{x_j}(D)\,dD = p_{x_j - \alpha D^G}(D^G)\,\frac{x_j - \alpha D^G}{x_j}\,dD^G \\ D^G = D, \quad dD^G = \left(D + \frac{dD}{2}\right)^G - \left(D - \frac{dD}{2}\right)^G \end{gathered} \tag{6.19}$$

The weighting factor on the right-hand-side of (6.19) accounts for the fact that, where the difference interval in the tilted profile x_j is shorter than the difference interval for the Gaussian profile $x_j - \alpha D^G$, the total number of chances to find the difference D is greater in the tilted profile than the Gaussian profile. At small values of x_j this construction will break down because of the overhang problem. As an artificial remedy, we allow $p_{x_j}(D)$ to be negative, where $x_j - \alpha D < 0$. This reflects the fact that such mappings are impossible, and compensates for the excessive probability which (6.19) gives to cases where $x_j - \alpha D$ is small and positive. The skewness of the differences is then determined by the integral

$$E[D^3(x_j)] = \frac{1}{2}\int_{-\infty}^{\infty} D^{3\prime}\, p_{x_j}(D')\, dD' \tag{6.20}$$

The factor of 1/2 comes from the fact that $p_{x_j}(D)$ measures the total probability density of a difference value D occurring over a lag distance $|x_j|$, so that to consider either only positive or negative lag we must divide by 2. Computed in this way, the function $C_{hhh}(x_j,0)^{o}$ is also plotted in Figure 6.8 (smaller dashed lines). The comparison to the numerically constructed curve is very good. We are therefore encouraged that we can use $C_{hhh}(x_j,0)^{o}$ for the estimation of lateral asymmetry.

The form of the function $C_{hhh}(x_j,0)^{o}$ is very dependent on the form of the covariance function as well as the value of α. The location of the peak on either side of zero lag $\pm x_{peak}$ is entirely dependent on the width of the covariance function or the characteristic length λ_θ, with the empirical relationship $x_{peak} \equiv \lambda_\theta/4$. The height of the peak, on the other hand, is dependent both on the value of α and λ_θ. The dependence on λ_θ emphasizes the point that in order to understand the third moment we must first understand the second.

INITIAL ATTEMPTS AT ESTIMATION OF HIGHER MOMENT PARAMETERS

Having solved the forward problem of determining the form of the third and fourth moments of a profile given the mapping models and values of their parameters μ_3, μ_4, and α, we now turn our attention to posing and solving the inverse problem of estimating these parameters from the estimated third and fourth moments of bathymetric profiles. As in the previous section, the skewness and kurtosis will be considered separately from the tilting parameter. Unfortunately, various factors which will be described below make it difficult to estimate the asymmetry parameters, and we are forced to adopt procedures which, while maximizing resolution of a particular estimate (i.e. its 1-σ errors), sacrifice accuracy (i.e. they are biased). It is therefore prudent at this time to restrict our goals to estimating the sign of the asymmetries rather than their magnitude.

Vertical Asymmetry and Peakiness

To illustrate the difficulty in estimating the skewness, consider a set of N uncorrelated samples h_i of a process whose mean is 0 and whose variance, skewness and kurtosis are given by $\mu_2 = 1$, $\mu_3 = 0.5$ and $\mu_4 = 4.0$ respectively. To estimate each moment we take the following sums:

$$\tilde{\mu}_n = \frac{1}{N} \sum_{i=1}^{N} h_i^n \tag{6.21}$$

The variance of each estimate is then given by

$$E[\tilde{\mu}_n^2] = \frac{1}{N} (E[\mu_{2n}] - E[\mu_n]^2) \tag{6.22}$$

μ_6 and μ_8 are calculated using the Hermite probability density:

$$\mu_n = \int_{-\infty}^{\infty} h^n \, p_H(h,\sigma,\mu_3,\mu_4) \, dh \tag{6.23}$$

For this example, $\mu_6 = 30$ and $\mu_8 = 315$. The variance of the estimate for μ_3 is approximately an order of magnitude greater than for μ_2, and an order of magnitude less than for μ_4. The 1-σ errors on the estimates (the square root of the variance), as measured proportionally to the expected value of the estimate, shows that μ_3 is the hardest parameter to estimate: the proportional errors for μ_3 are ~6.3 times the proportional errors for μ_2, and ~2.5 times the proportional errors for μ_4. Since 1-σ errors are inversely proportional to the square root of N (see 6.22), we see that we need $6.3^2 \cong 40$ times more data to resolve the third moment than is needed to resolve the second at the same resolution.

Problems in estimating μ_3 are exacerbated in cases such as topography where the samples are highly correlated. The correlation greatly reduces the total effective amount of independent information which contributes to the estimation (see Chapter 3). In most cases, the length of data required to directly estimate μ_3 from a single bathymetric profile may be prohibitive, if not seriously jeopardize the non-stationary assumption. Correlation is, however, a second-order property, which we estimate by other means and is only a hindrance in the estimation of μ_3. We can greatly improve the resolution of both μ_3 and μ_4 by reducing $h(x)$ to its uncorrelated component $h^p(x)$. This can be done by prewhitening, the steps of which are the following: (1) Fourier transform a topographic profile, (2) divide each value of the resulting complex spectrum by its absolute value, and (3) retransform back into the space domain. The result is constrained to be an uncorrelated profile with variance = 1. Equation (6.21) can then be used to estimate the values of $\mu^p{}_3$ and $\mu^p{}_4$ (where p indicates the prewhitened profile) from this profile with errors in the estimation given by equation (6.22).

How do $\mu^p{}_3$ and $\mu^p{}_4$ compare with μ_3 and μ_4? Through numerical experiments on synthetic profiles, we find that $\mu^p{}_3$ and $\mu^p{}_4$ tend to be biased toward Gaussian values of 0 and 3 respectively. $\mu^p{}_3$ is most strongly affected. It is typically about 1/2 the value of μ_3 and, under certain conditions, can be less than 1/4 the value of μ_3. $\mu^p{}_4$, however, is not as strongly biased, and usually is not more than 0.5 less than the value of μ_4. The amount of bias is strongly dependent on several factors, including echosounder response width, noise statistics, data spacing, correlation width and Hausdorff dimension. It beyond the present scope of this work to determine the degree of contribution of each factor. We shall be content at present to estimate the value of μ_4 to within ~0.5 plus the resolution error and the general sense of asymmetry (i.e.whether μ_3 is positive or negative).

Despite the magnitude ambiguity in the estimation of these parameters, it is still a very useful exercise to compare bathymetric profiles with synthetics generated from the estimated covariance parameters and some educated guess as to the values of μ_3 and μ_4. Figure 6.9 shows such comparisons for both an Atlantic and Pacific Sea Beam profile. There are clear differences between these two profiles in the second-order statistics; both the rms height and characteristic length are substantially larger on the Atlantic profile ($H = 292 \pm 32$ m, $\lambda_\theta = 7.6 \pm 1.5$ km) than on the Pacific profile ($H = 54 \pm 2$ m, $\lambda_\theta = 1.2 \pm 0.22$ km). There are also visual differences which go beyond these quantities and which the higher-order measures begin to address. The vertical skewness is negative on the Pacific profile ($\mu_3 \sim -0.75$), and positive on the Atlantic profile ($\mu_3 \sim 1.0$). The kurtosis, meanwhile, is perhaps only slightly larger on the Atlantic profile ($\mu_4 \sim 6.0$) than on the Pacific profile ($\mu_4 \sim 5.5$). In each case, the Hermite mapping synthetic provides a better visual comparison than the Gaussian synthetic, indicating that we are somewhat successful at characterizing some of the higher-order properties of the seafloor.

Lateral Asymmetry

The proposed means for estimating the tilt parameter α from bathymetric profiles is through the skewness of differences function $E[D^3(x_j)]/6 = C_{hhh}(x_j,0)^o$ (Figure 6.8). As with estimating second-order statistics, it is important to understand the effect of echosounder response on the model function. In Figure 6.10 we have plotted $C_{hhh}(x_j,0)^o$ for both the case of the ideal echosounder and for a realistic echosounder with response width of 0.4 km. Both numerically constructed (equation (6.16)) and calculated (equation (6.20)) functions are plotted. The principal effect of response is to reduce the size of the peak and to laterally shift it outward by approximately 1/2 the response width.

Also plotted if Figure 6.10 are 1-σ errors on the null hypothesis that $C_{hhh}(x_j,0)^o$ is 0 for all x_j. The errors were generated by computing the standard deviation of the estimated functions from 50 synthetic profiles used to construct $C_{hhh}(x_j,0)^o$ numerically. The error curves provide important information regarding our ability to make estimates. We can reasonably expect to resolve $C_{hhh}(x_j,0)^o$ from one profile only at lags where the expected value surpasses the error curves. The errors increase dramatically from zero at zero lag to, at large lag, being much larger than the function we are trying to estimate. There is, fortunately, a significant region on either side near zero lag including the peaks where we should expect to be able to resolve $C_{hhh}(x_j,0)^o$ in this case. We are therefore hopeful that we will be able to detect lateral asymmetry if it exists by the behavior of the estimated skewness of differences near zero lag.

Before attempting a very difficult and time consuming formalized inverse problem, we have formulated the following simplified inverse procedure for estimating α which depends only on estimating the value of $C_{hhh}(x_{peak},0)^o$. After estimating the second-order parameters (Chapter 2), $C_{hhh}(x_{peak},0)^o/k_\theta$ is first estimated using equation (6.16). This value is then converted to an estimate of α using a look-up table, calculated using (6.20), that displays $C_{hhh}(x_{peak},0)^o/k_\theta$ as a function of k_θ for several values of α (Figure 6.11). The look-up table is sensitive to different values of the Hausdorff dimension and echosounder response length, so that several must be produced. The error in the estimation of α is assumed to be proportional to the error in $\tilde{C}_{hhh}(x_{peak},0)^o/k_\theta$, which is calculated numerically. This assumption is generally supported by the nearly linear variation in α with $C_{hhh}(x_{peak},0)^o/k_\theta$ in Figure 6.11.

An example of an estimated skewness of differences function calculated from a synthetic profile is shown in Figure 6.12. The synthetic profile was generated with a value of k_θ = 1.2, and α = 0.1. The large tick on the lag axis marks the position of $x_{peak} = \lambda_\theta/4$ + response length/2. The estimated value of $C_{hhh}(x_{peak},0)^o$ is —0.045 ± .008. From the look-up table in Figure 6.11 (after dividing by k_θ), this translates to a value of $\alpha = 0.095 \pm .017$, very close to the value of $\alpha = 0.1$ used to generate the synthetic profile.

The applicability of this or any other estimation procedure to actual seafloor profiles depends on whether or not the uniform tilt model is an accurate description of lateral abyssal hill asymmetries. To explore this question we examine various Sea Beam profiles and their $\tilde{C}_{hhh}(x_j,0)^o$ functions. If inward facing slopes (slopes facing the ridge) tend to be steeper than outward facing slopes, then $\tilde{C}_{hhh}(+x_{peak},0)^o$ will be negative where a profile runs toward the ridge, and positive where a profile runs away from the ridge. The parameter α is defined such that it is positive if steeper slopes face the ridge, and negative otherwise.

Our first example, shown in Figure 6.13, is from a Sea Beam profile taken near the East Pacific Rise along the Cocos-Pacific spreading section. The second-order stochastic parameters estimated from this section are $H = 44 \pm 3$ m, and $\lambda_\theta = 2.3 \pm 0.51$ km (D was assumed to be 2.5). We have also estimated the skewness and kurtosis at $\mu_3 \sim -0.6$ and $\mu_4 \sim 5.0$. The estimated skewness of differences function (top panel) shows well defined peaks near $\pm x_{peak}$ which rise well above the 1-σ errors plotted about the null hypothesis, indicating that we are very likely detecting lateral asymmetry in this case. The estimated value for the tilt parameter is $\alpha = 0.11 \pm 0.04$. The profile used for this estimation is also shown is Figure 6.13 (top profile of bottom panel). It is not difficult to be convinced that steeper slopes face the ridge in this data set. It is particularly noticeable in some of the deeper basins (e.g. at 0730 h). There are also many features at smaller scales which appear to be tilted. Below the data we compare two synthetic profiles, one which is generated from the Hermite mapping of a profile generated from the second-order parameters and one generated by also applying the uniform tilt mapping with $\alpha = 0.11$. The comparison between the data and the tilted synthetic is fairly good, and superior to the comparison with the non-tilted synthetic. We conclude that for this case at least the uniform tilting model is an acceptable means of quantifying lateral asymmetry.

The uniform tilting model noticeably fails to characterize abyssal hill asymmetry when the tilting does not occur uniformly at all scales. Figure 6.14 shows an example of this from a Sea Beam profile taken in the same region as the previous example. For this profile, the estimation of $C_{hhh}(x_j,0)^o$ (top panel) exhibits very large peaks on either side of zero lag. However, the peaks are clearly not centered at the values of $\pm x_{peak}$ derived from the second-order characteristics. We are thus at a loss as to how to interpret such a curve in terms of the uniform tilt model. Two large asymmetric basins (~1900 hrs) are the likely cause of the mislocation of the peaks. These features are anomalously large compared with the surrounding abyssal hill character, and will tend to dominate the estimation of the third moment more than they will the second. The amount of tilting at the these scales is more than can be accounted for by the simple model. The kurtosis in this case is also adversely affected, with an absurdly high estimate of $\mu_4 = 12 \pm 2$. The large basins are an example of non-stationarity, or episodicity which is not presently accounted for by our modeling. Despite the ambiguity in interpreting the value of the tilt parameter in this case, estimation of α ($0.20 \pm .03$) still provides a strong measure of which direction the profile is tilted and of how well resolved that measure is.

Three examples of the estimation of $C_{hhh}(x_j,0)^o$ for different Pacific Sea Beam profiles, shown in Figure 6.15, exhibit another form of non-uniform tilt. In each of these cases, despite the existence of resolvable positive tilt at $\pm x_{peak}$, at small lags the estimated functions either remain near zero or have the opposite sign out to larger values of $|x_j|$ than can reasonably be accommodated by the uniform tilt model. This suggests that in these cases the smaller scales exhibit no tilt or are actually tilted in the opposite direction from that of the larger scale features. If polarized listric faulting [*Rea*, 1975] (Figure 5.5) is the cause of measured tilting, then there are two reasonable physical mechanisms to produce back tilting at smaller scales; either small scale features can be rotated by piggy-backing on the larger-scale features, or antithetic faulting [*Macdonald and Luyendyk*, 1985] can occur on the hanging wall (Figure 6.15).

The unfortunate (yet challenging) conclusion from examining $\tilde{C}_{hhh}(x_{peak},0)^o$ functions estimated from various Sea Beam profiles is that the uniform tilt model is not flexible enough to properly characterize the variation in lateral asymmetries that abyssal hills exhibit. As with our conclusion regarding the abyssal hill aspect ratios in Chapter 4, future modeling of the third moment should consider the dependence of parameterization on scale. For this thesis, however, we will be content to address the problem of whether or not abyssal hills are vertically and/or laterally asymmetric, and if so, then with what sign. For this purpose, estimation of the parameters μ_{P_3} and α by the procedures described above will suffice.

RESULTS AND DISCUSSION

The results for the estimation of μ_{P_3} for the near-ridge data set (Table 5.1, Figures 5.1-5.3) are plotted as a function of spreading rate in Figure 6.17. The estimated values of μ_{P_3} near the slower-spreading ridge sections (below 7 cm/yr) are very consistently positive; i.e. the abyssal hill peaks tend to be larger than the troughs. This suggests that, in the slower spreading regions, abyssal hill morphology is predominantly formed by constructional features; i.e. perhaps by periodic formation of volcanic edifices. This is consistent with the working hypothesis proposed in the previous chapter and with the conclusions of *Kong et al.* [1988] and *Pockalny et al.* [1989] on the basis of visual similarity of flanking abyssal hills to volcanic ridges within the median valley. In their view, volcanic ridges pass out of the rift valley essentially intact to become abyssal hills. We know, however, that as new seafloor is rafted over the rift mountains it becomes very severely faulted, with throws up to hundreds of meters [*Macdonald and Luyendyk*, 1977]. The evidence suggests that, although volcanic ridges may not remain completely intact after passing out of the rift valley, they still retain their essentially constructional character.

Along the Pacific-Cocos spreading section, μp_3 is generally negative. μp_3 also appears to be negative on the portion of the Pacific-Nazca spreading just north of the Easter Island Microplate (see also Figure 5.2). If we limit consideration to these and the data from slower spreading ridges, we can construct the following plausible scenario, consistent with the working hypothesis of the previous chapter, for abyssal hill formation. The slower-spreading ridges are cold and strong, and can therefore support large constructional features. The magma supply is likely episodic [*Macdonald and Luyendyk*, 1977; *Kong et al.*, 1988], thereby allowing individual volcanic ridges to form at the spreading axis which are subsequently rafted (and faulted) away, likely leading to a positive value of μp_3. In this case faulting is a secondary abyssal hill-forming process to volcanic construction. As the spreading rate increases, the magma supply becomes more consistent, the axial magma chamber becomes steady state and broader, and the near-ridge lithosphere becomes hotter and weaker, making it very difficult to elastically support loads from large volcanic constructs [*Lonsdale*, 1977] forming at the ridge axis. As the other end-member of this scenario we would expect faulting and rifting caused by cooling to become the primary abyssal hill forming process, leading, perhaps, to a negative value of μp_3. Unfortunately, the very consistent estimated positive values for μp_3 found south of the Easter Island Microplate (Figure 6.17, see also Figure 5.2), some of the fastest spreading in the world, do not fit into this model. As we pointed out in the previous chapter, this region seems very anomalous, bearing more resemblance to slow-to-medium spreading rate regions than to the Pacific-Cocos data. The data shown in Figure 6.17 lend further weight to this observation.

The results for the estimation of μp_4 for the near-ridge data set are shown in Figure 6.18. The results are all similar and not at all surprising given the strong non-zero estimations of μp_3; in nearly every case the estimation of μp_4 is significantly greater than the Gaussian value of 3. There does appear, however, to be a greater tendency toward larger μp_4 at slower spreading rates. We interpret this to mean that the abyssal hill-forming processes are less uniformly distributed over scales and more episodic at slower spreading rates than at faster spreading rates.

The results for the estimation of α for the near-ridge data set are shown in Figure 6.19. The strongest evidence that steeper slopes face the ridge comes from the Pacific-Rivera and Pacific-Cocos data. The Mid-Atlantic Ridge data indicates only marginal evidence for positive tilt. For the Pacific-Cocos region, this evidence is consistent with submersible observations, made by *Macdonald and Luyendyk* [1985], that inward-facing faults tend to be larger than outward facing faults in this region. They also observed several split volcanic ridges with fault surfaces facing inward.

Reviewing some of the previous chapter, the formation of polarized faulting along the Rivera-Pacific rise is described by *CYAMEX* [1981]. They identify four zones of tectonic activity: (1) volcanism, including flood basalts and edifice formation, (2) fissuring and horst and graben formation, with no polarization in faulting direction, (3) polarized normal faulting with larger inward facing faults, leading to the formation of a rift valley, and finally (4) the inactive zone, where abyssal hill construction has ceased, and their morphology is slowly modified by mass-wasting, sedimentation, and occasional off-axis volcanism. These zones are also observed along the Mid-Atlantic Ridge. The principle morphological differences between the slow and medium spreading are that the zone volcanism is almost always expressed as edifice formation in the former as opposed to a mixture of edifice and flood basalts in the latter, and the polarized faulting is much larger in the slower spreading, creating rift valleys over 1 km deep and up to 30 km wide. The rift valley in the medium spreading ridge, by contrast, has 50-200 m of relief [*Macdonald*, 1982], on the order of the size of the flanking abyssal hills.

Given the observations of strong polarized faulting in the Atlantic, it may be surprising that there is only marginal evidence there for lateral asymmetry (Figure 6.19). However, it is clear that there must be an additional tectonic zone for slow spreading regions based on geometric arguments [*Harrison and Stieltjes*, 1977, *Macdonald and Atwater*, 1978]. As the seafloor is rafted over the top of the rift mountains, it changes from sloping, on average, upward to slightly downward. To accommodate this transition either one or more of the following must occur: back tilting of the faulted blocks, reverse faulting on relict normal faults, or the formation of outward facing normal faults. The net effect should be to significantly reduce or even eliminate the lateral asymmetry. In the medium spreading ridge, this stage need not occur as the rift mountains (actually hills) can be rafted away to take their place among abyssal hills, and a new rift mountain is formed by one or two new inward facing faults.

The strong evidence for lateral asymmetry along the Cocos-Pacific ridge system (Figure 6.19) is mildly problematic; fast spreading ridges are generally characterized by highs associated with linear shield volcanoes [e.g. *Lonsdale*, 1977; *Macdonald*, 1982] rather than by axial rift valleys; i.e. no zone 3 tectonic activity is observed. There is thus no obvious means of producing the differential vertical motions necessary to produce polarized faulting [*Choukroune et al.*, 1984] and thus lateral asymmetry. We must therefore look for other mechanisms to produce asymmetry. Observations by *Rea* [1975] of asymmetric abyssal hills on the flanks of the East Pacific Rise near 11° S prompted him to propose that polarized listric faulting with preferential inward facing faults, forming as a result of the tensile stresses from surface cooling, is the dominant mechanism for producing abyssal hills on fast spreading ridges. Significant evidence of outward facing faults near the East Pacific Rise has lead others [e.g. *Lonsdale*, 1977; *Choukrone et al.*, 1984] to favor a horst and graben model. *Bicknell et al.* [1987] found, however, that while both outward and inward facing faults tend to form on fast-spreading ridge flanks, inward facing faults tend to have greater accumulated throw. They forward the suggestion, made earlier by *Tapponnier and Francheteau* [1978] and *Searle* [1984], that inward facing faults rupture a thinner brittle layer, and so require less energy to form. Some block tilting must occur, however, to accommodate the difference in accumulated throw, and also to explain the possible observed back tilting (Figures 6.15 and 6.16), and so perhaps *Rea*'s [1975] model is at least partially correct.

CONCLUSIONS

In this chapter we have developed a general framework for the analysis of the moments of a topographic field greater than 2. This framework uses "iterated" expectation to reduce the statistical moment to component parts involving the vertical moment, lower moments, and conditional expectation. The latter can be computed if we presume an invertible morphological model which maps a topographic field with known statistic (i.e. a Gaussian) to a field with desired properties. We illustrated the utility of this framework by calculating the third moment for two mapping models; the Hermite polynomial probability density and the uniform tilting.

These models contain parameters which provide very useful descriptions of the morphological properties of vertical and lateral asymmetry and peakiness. We have described initial methodologies for estimating these parameters from bathymetric profiles. In the case of vertical asymmetry, μ_3, estimation is unfortunately hampered by the need for large quantities of data. This can be circumvented to a degree by prewhitening, which eliminates the correlated component of the profile. Estimates of the vertical asymmetry from the prewhitened profile are, however, biased toward 0, and the amount of bias is dependent on several factors. For now we can only reliably estimate the sign of vertical asymmetry. Estimation of the peakiness parameter, μ_4, is also biased by prewhitening, though not as severely. Estimation of the lateral asymmetry, α, is complicated by the fact that the uniform tilt model is not general enough to characterize the observed skewness of differences from bathymetric profiles. As with vertical asymmetry, we can at present only reliably estimate the sign of lateral asymmetry.

The results for vertical asymmetry generally indicate that slower spreading ridges tend to produce abyssal hill morphology in which peaks are generally larger than the troughs. This indicates that constructional features such as volcanic edifices probably play a dominant role in abyssal hill formation. Faster spreading ridges, on the other hand, tend to have abyssal hill with troughs bigger than peaks, indicating that destructional features such as rifts or narrow grabens are dominant. The peakiness is everywhere larger than for a Gaussian probability distribution, and tends to be larger for the slower spreading regions than for the faster spreading regions. This may indicate that the abyssal hill forming processes are more continuous in the Pacific.

Where lateral asymmetry is detected it almost always indicates that inward facing slopes are steeper than outward facing slopes. At medium-rate spreading centers such as the Rivera-Pacific section of the East Pacific Rise, the asymmetry is likely caused by preferential inward faulting associated with rift valley formation. At slow spreading rates, only marginal evidence for lateral asymmetry is observed despite observations that at slow spreading axes there exists large amounts of preferential inward faulting. This asymmetry can be nullified, however, at the crest of the rift mountains, where a change in slope must be accommodated by either block tilting, reverse faulting on relict faults, or the formation of outward facing normal faults. A strong component of lateral asymmetry is also observed on fast spreading ridges such as the Cocos-Pacific section of the East Pacific Rise, despite the fact that a rift valley is not formed there. Asymmetry in this case must be accommodated by some degree of polarized listric faulting forming as a result of the tensile stresses from surface cooling.

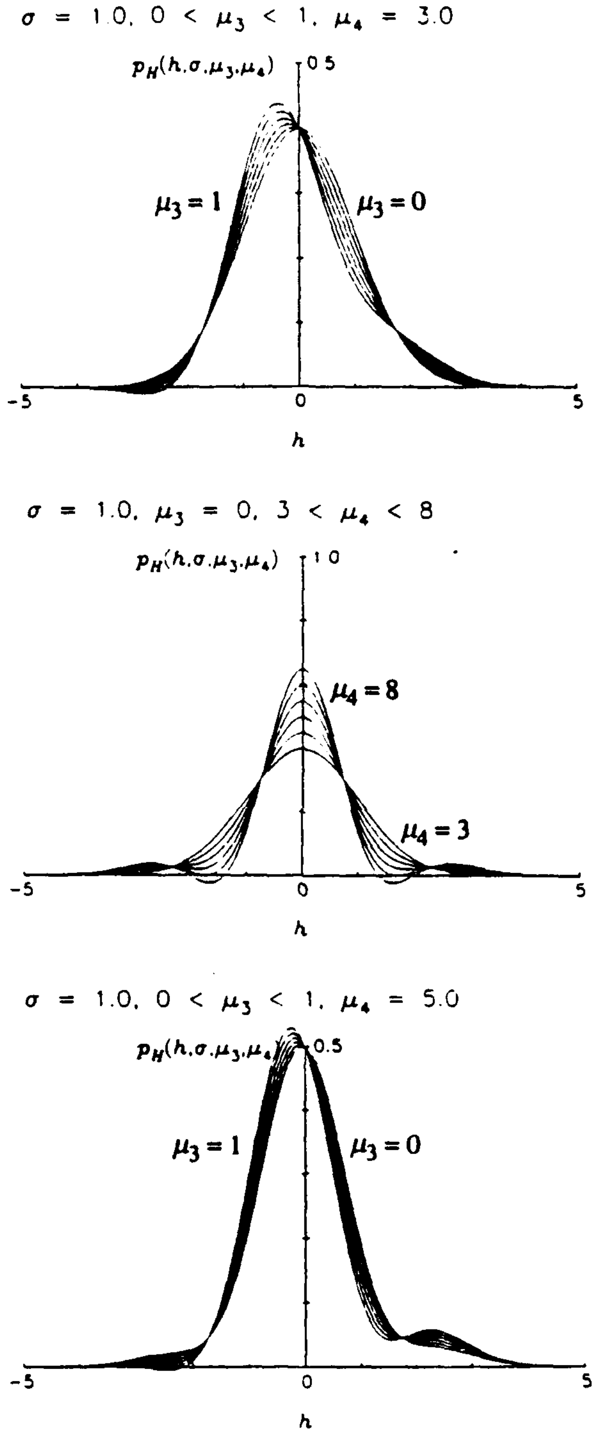

Figure 6.1. Hermite polynomial function (6.14) plotted at various values of μ_3 and μ_4.

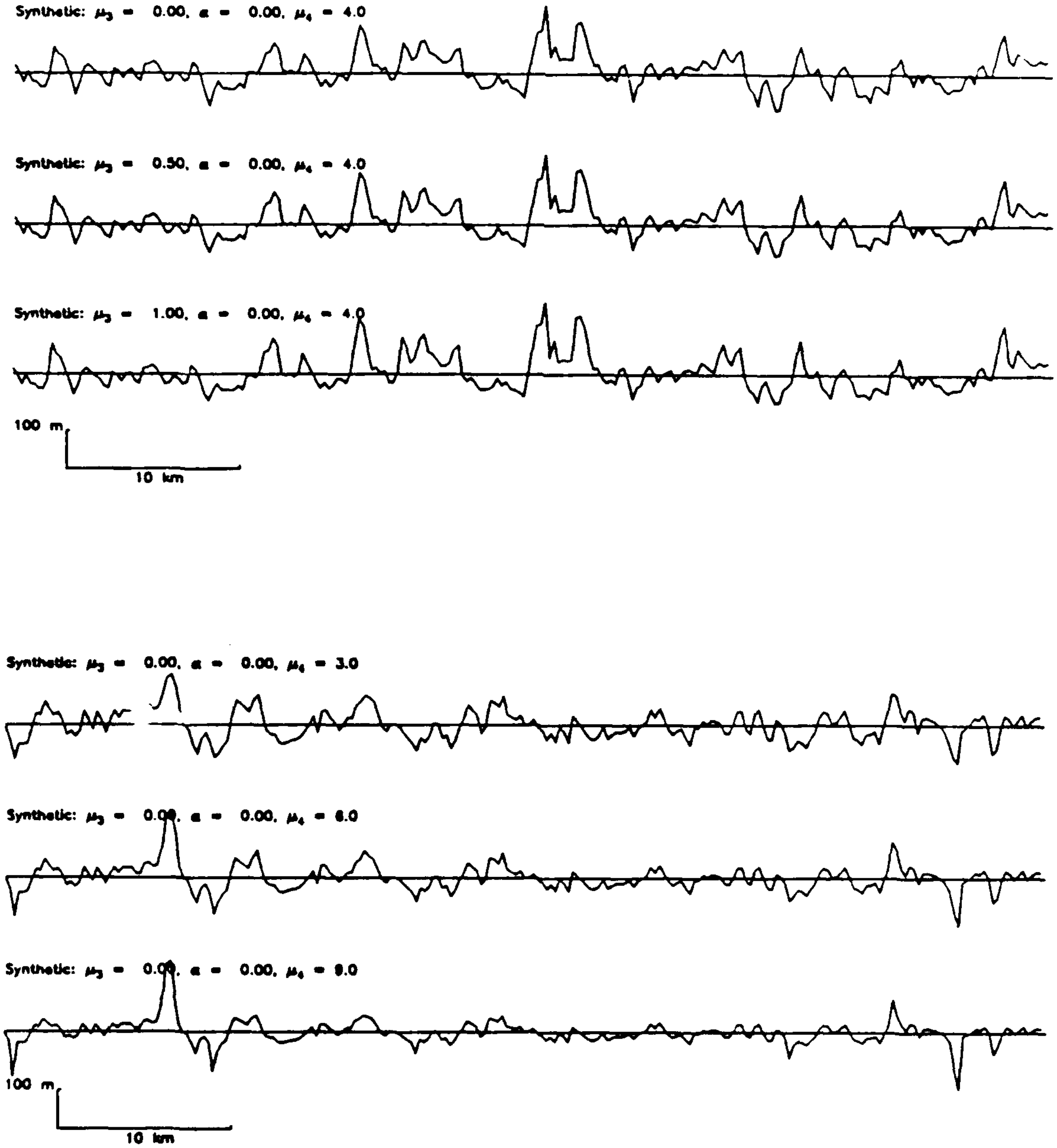

Figure 6.2. Various synthetic profiles generated using the Hermite mapping algorithm (see text). The Gaussian profiles from which each was mapped are also shown at the top of each panel ($\mu_3 = 0.0$, $\alpha = 0.0$, and $\mu_4 = 3.0$). The second-order parameters for all profiles shown are $H = 50$ m, $\lambda_\theta = 2.4$ km, and D = 1.5.

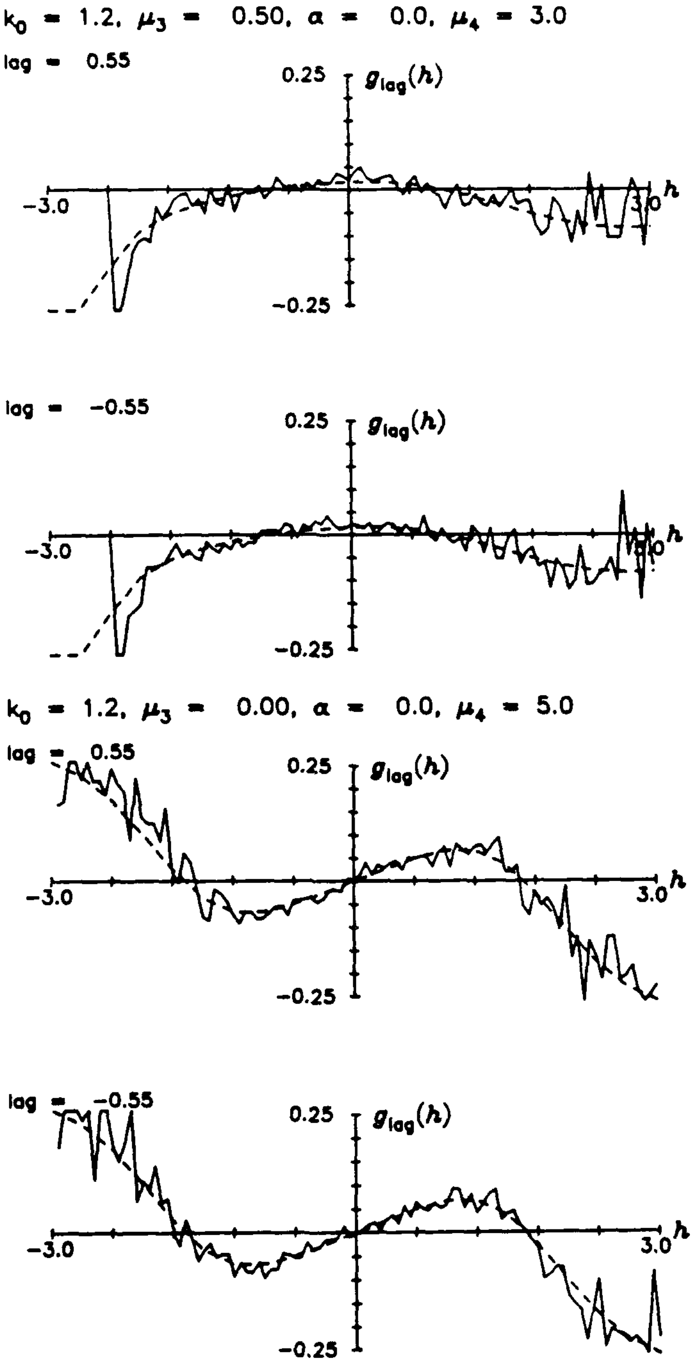

Figure 6.3. Calculated (dashed) and numerically constructed (solid) $g_{lag}(h)$ functions for a non-Gaussian value of μ_3 (top panel) and μ_4 (bottom panel) at both a positive and negative lag.

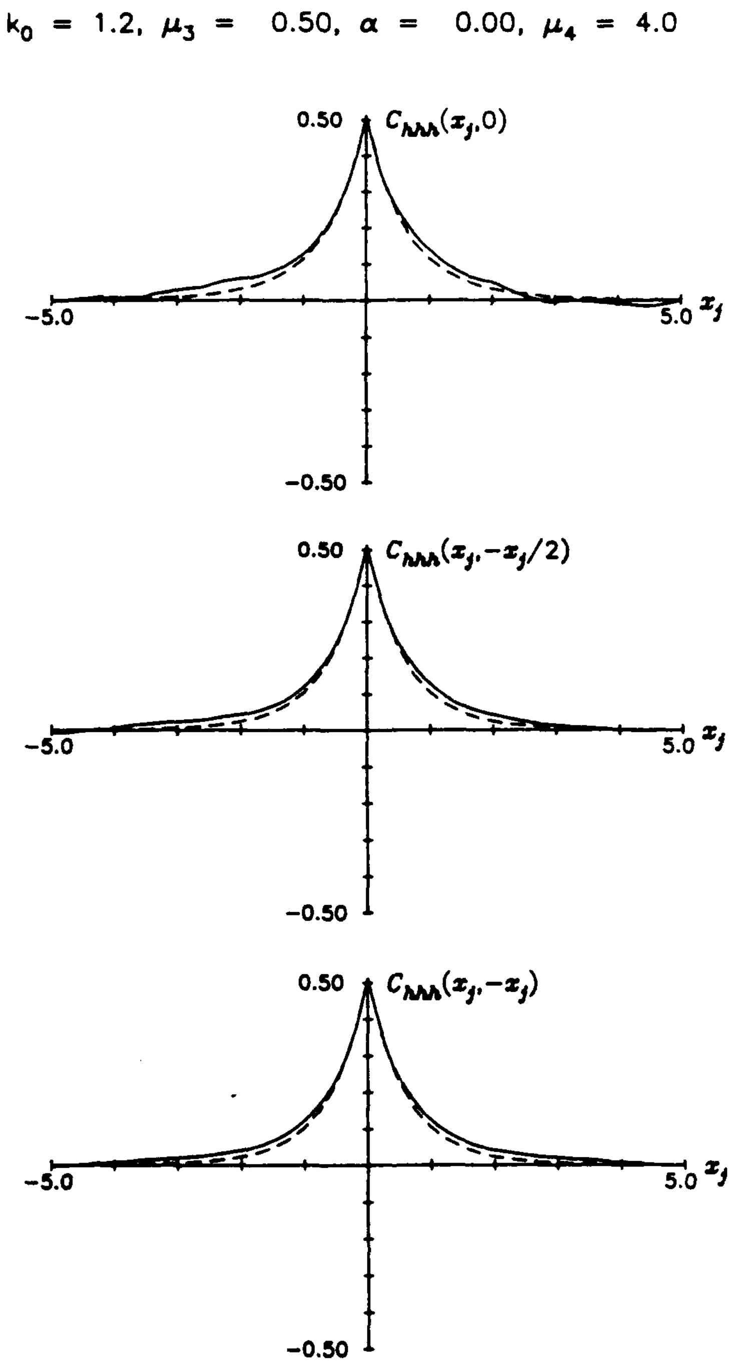

Figure 6.4. Calculated (dashed) and numerically constructed (solid) $C_{hhh}(x_j,x_k)$ functions along three axes for a non-Gaussian μ_3 and μ_4.

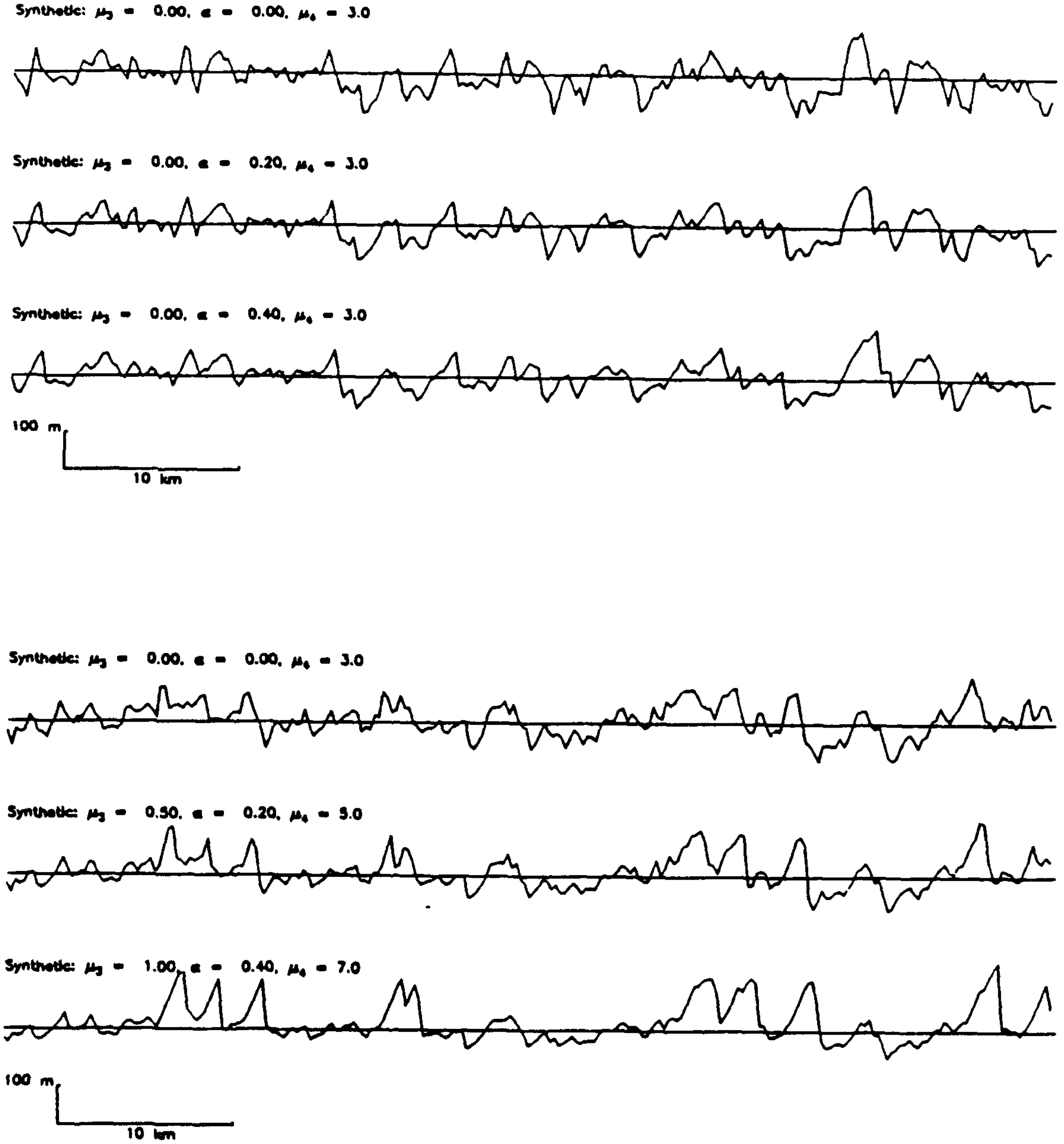

Figure 6.5. Various synthetic profiles generated using the uniform tilt mapping (top panel) and both it and the Hermite mapping algorithm (bottom panel) (see text). The Gaussian profiles from which each was mapped are also shown at the top of each panel (μ_3 = 0.0, α = 0.0, and μ_4 = 3.0). The second-order parameters for all profiles shown are H = 50 m, λ_θ = 2.4 km, and D = 1.5.

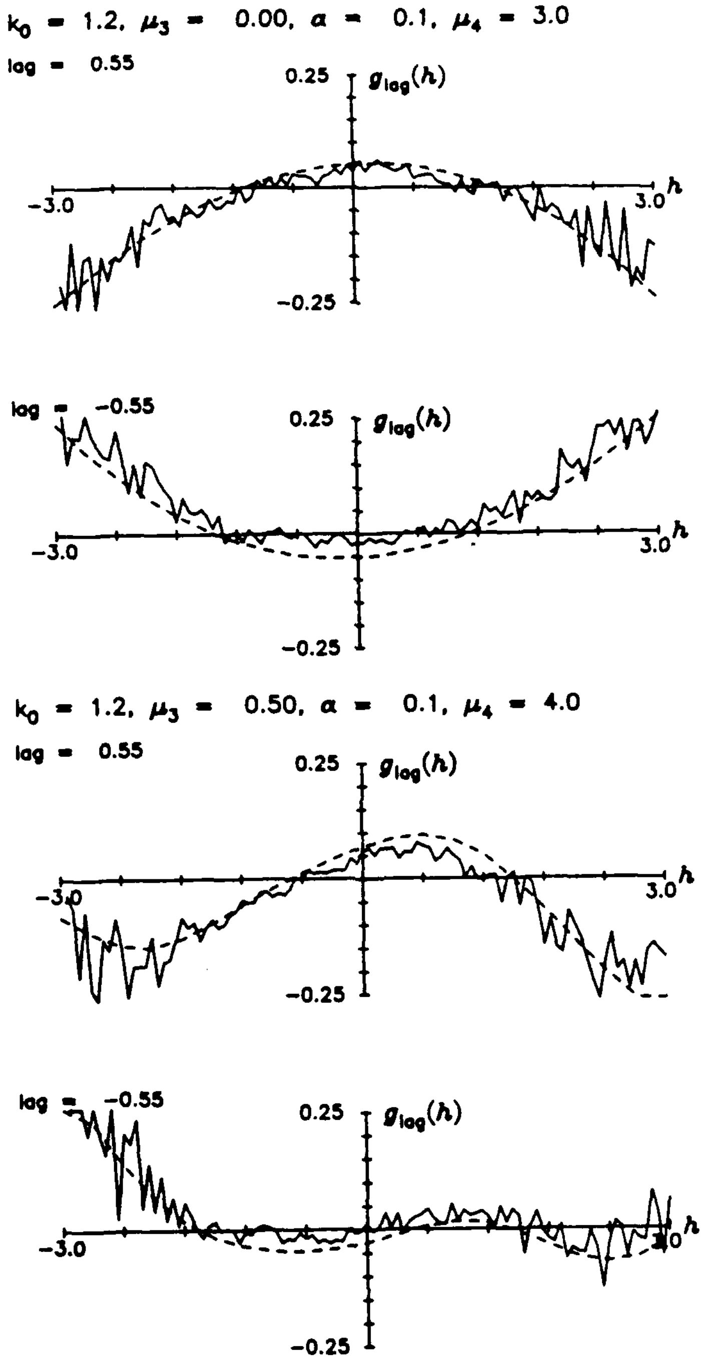

Figure 6.6. Calculated (dashed) and numerically constructed (solid) $g_{lag}(h)$ functions for a non-Gaussian value of α (top panel) and α, μ_3, and μ_4 (bottom panel) at both a positive and negative lag.

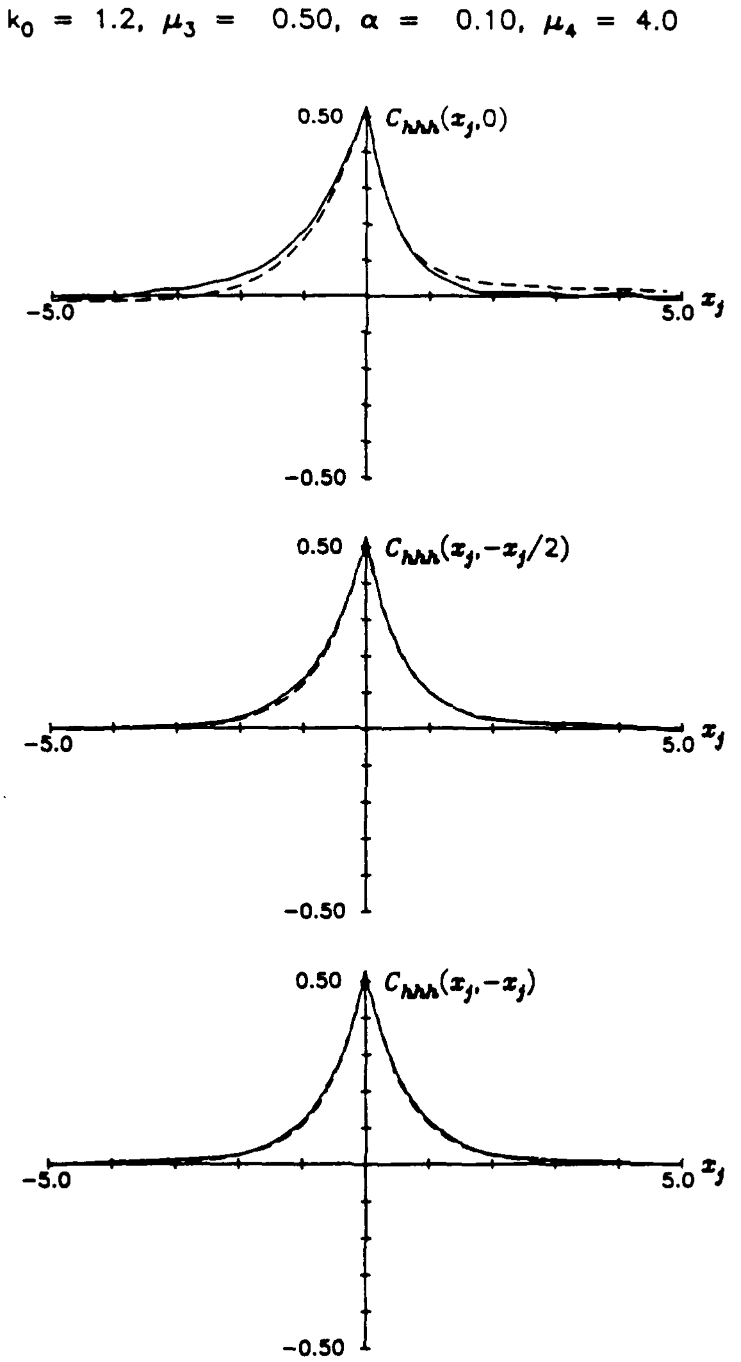

Figure 6.7. Calculated (dashed) and numerically constructed (solid) $C_{hhh}(x_j,x_k)$ functions along three axes for a non-Gaussian α, μ_3, and μ_4.

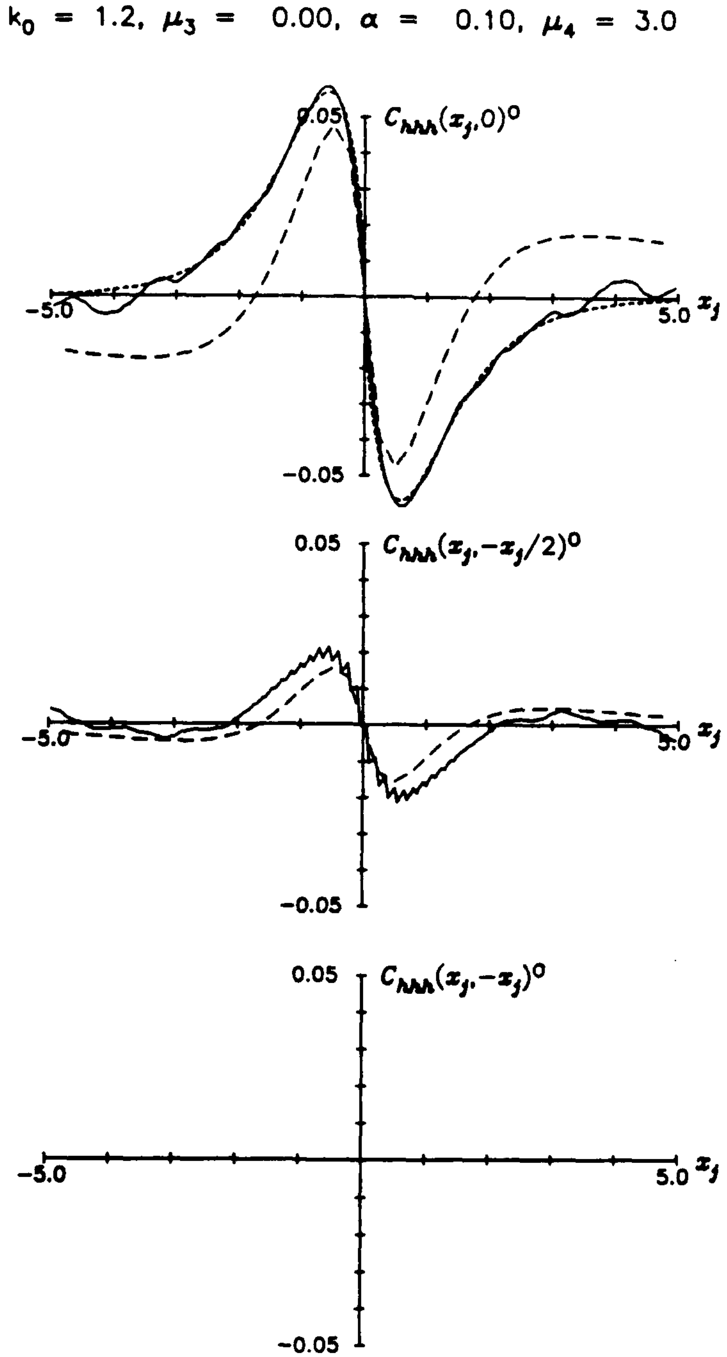

Figure 6.8. Calculated (dashed) and numerically constructed (solid) $C_{hhh}(x_j,x_k)^o$ functions along three axes for a non-Gaussian α. Two methods were used to calculate $C_{hhh}(x_j,x_k)^o$ in the top panel; iterated expectation (6.6) (long dash) and skewness of differences (6.20) (short dash).

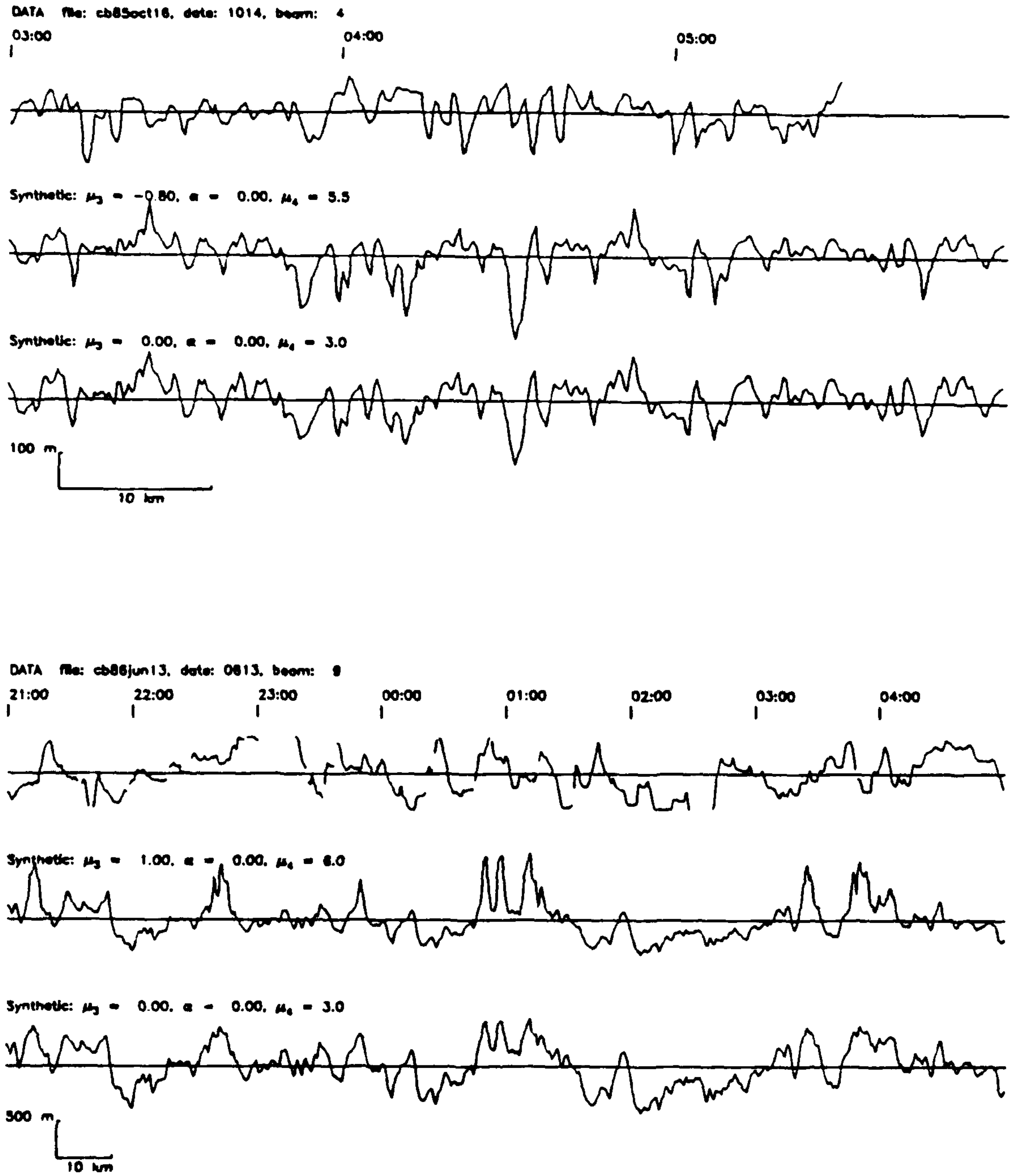

Figure 6.9. Comparison of Pacific (top panel) and Atlantic (bottom panel) Sea Beam profile with synthetics generated from the estimated second-order parameters (bottom profile of each panel) and estimated second-, third- (excluding α), and fourth-order parameters (middle profile). The Pacific profile was taken from the Papatua 1 leg of the *RV Thomas Washington*, near the East Pacific Rise at ~13.1° N. The second-order parameters estimated from this profile are $H = 54 \pm 2$ m, and $\lambda_\theta = 1.2 \pm 0.22$ km. D was assumed to be 2.5. The Atlantic profile was taken from the AII4L2 cruise of the *RV Atlantis II*, near the Mid-Atlantic Ridge, just south of the Kane Fracture Zone. The second-order parameters estimated from this profile are $H = 292 \pm 32$ m, and $\lambda_\theta = 7.6 \pm 1.5$ km, and D = 2.1 ± 0.9.

$k_0 = 1.2, \alpha = 0.10$

Response = 0.0 km

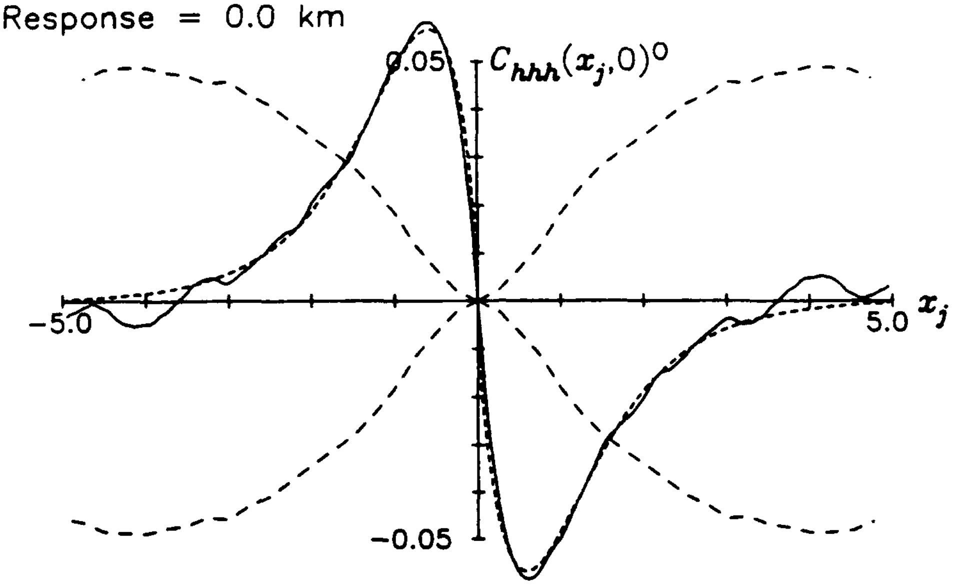

Response = 0.4 km

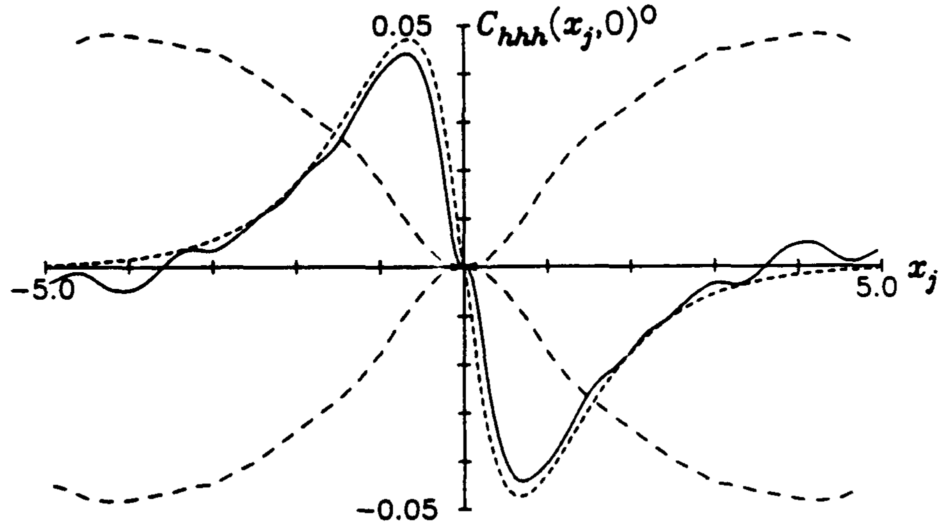

Figure 6.10. Calculated (short dashed) and numerically constructed (solid) $C_{hhh}(x_j,0)^o$ functions for an ideal echosounder (top panel) and a finite beamwidth echosounder (bottom panel). $C_{hhh}(x_j,0)^o$ was calculated using skewness of differences (6.20). Numerically constructed 1-σ errors (long dash) on the null hypothesis that $\tilde{C}_{hhh}(x_j,0)^o = 0$ are also plotted.

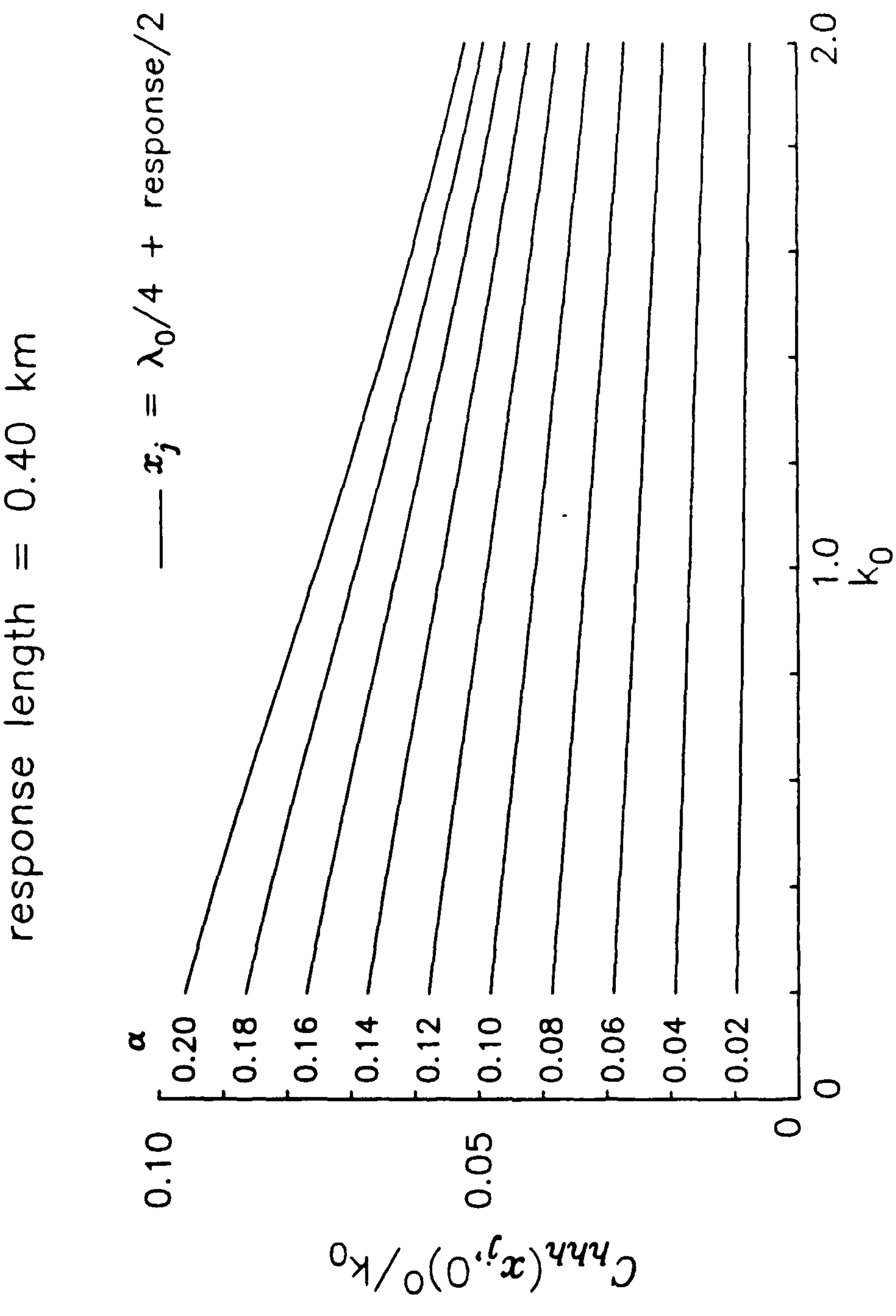

Figure 6.11. Look-up table for converting values of $\tilde{C}_{hhh}(x_{peak},0)^{o}/k_{\theta}$ into estimations of α.

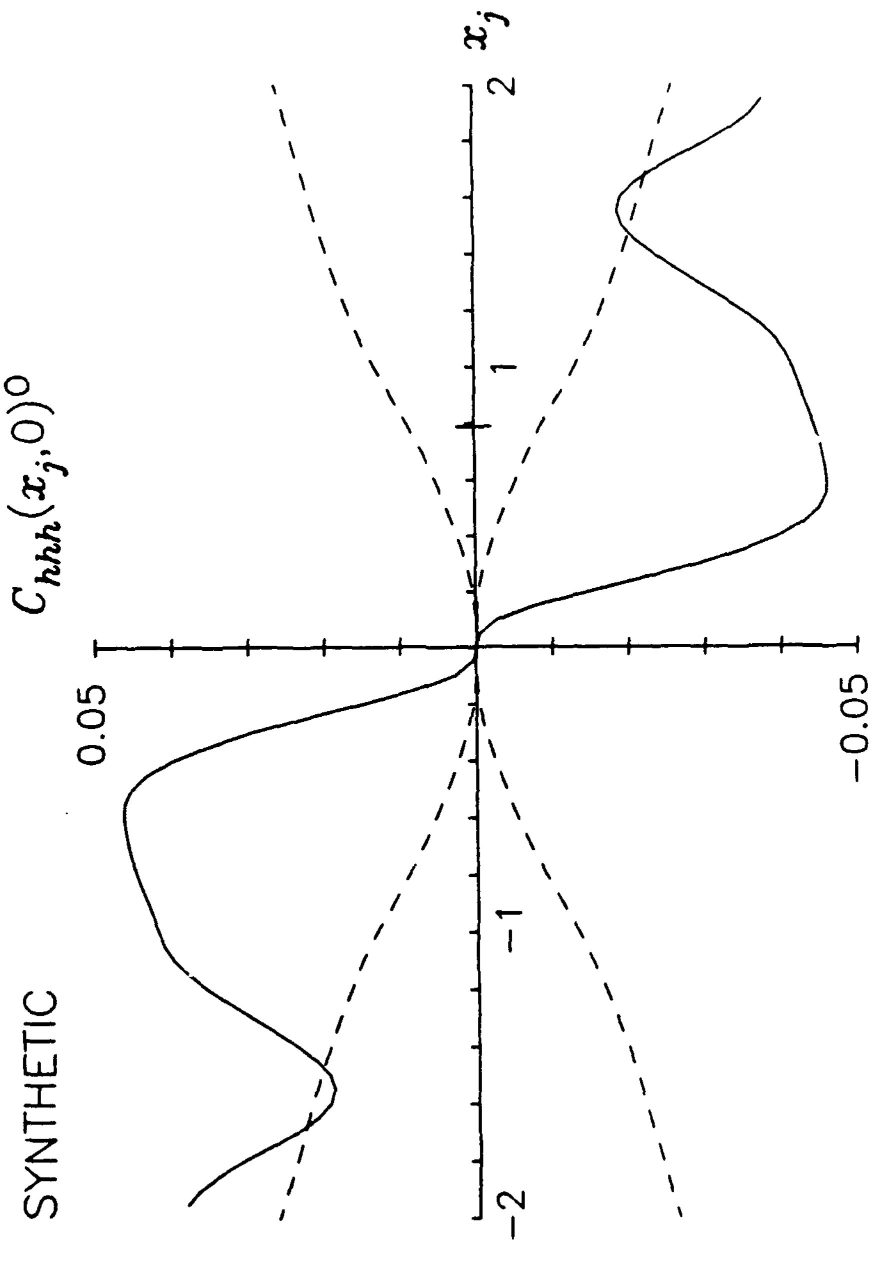

Figure 6.12. $\tilde{C}_{hhh}(x_{peak},0)^{\mathrm{O}}$ (solid) calculated from a synthetic profile generated using the uniform tilt mapping with $\alpha = 0.1$ and second-order parameters $H = 50$ m, $\lambda_\theta = 2.4$ km, and $D = 2.5$. The numerically constructed 1-σ errors on the null hypothesis that $\tilde{C}_{hhh}(x_{peak},0)^{\mathrm{O}} = 0$ are also plotted (dashed).

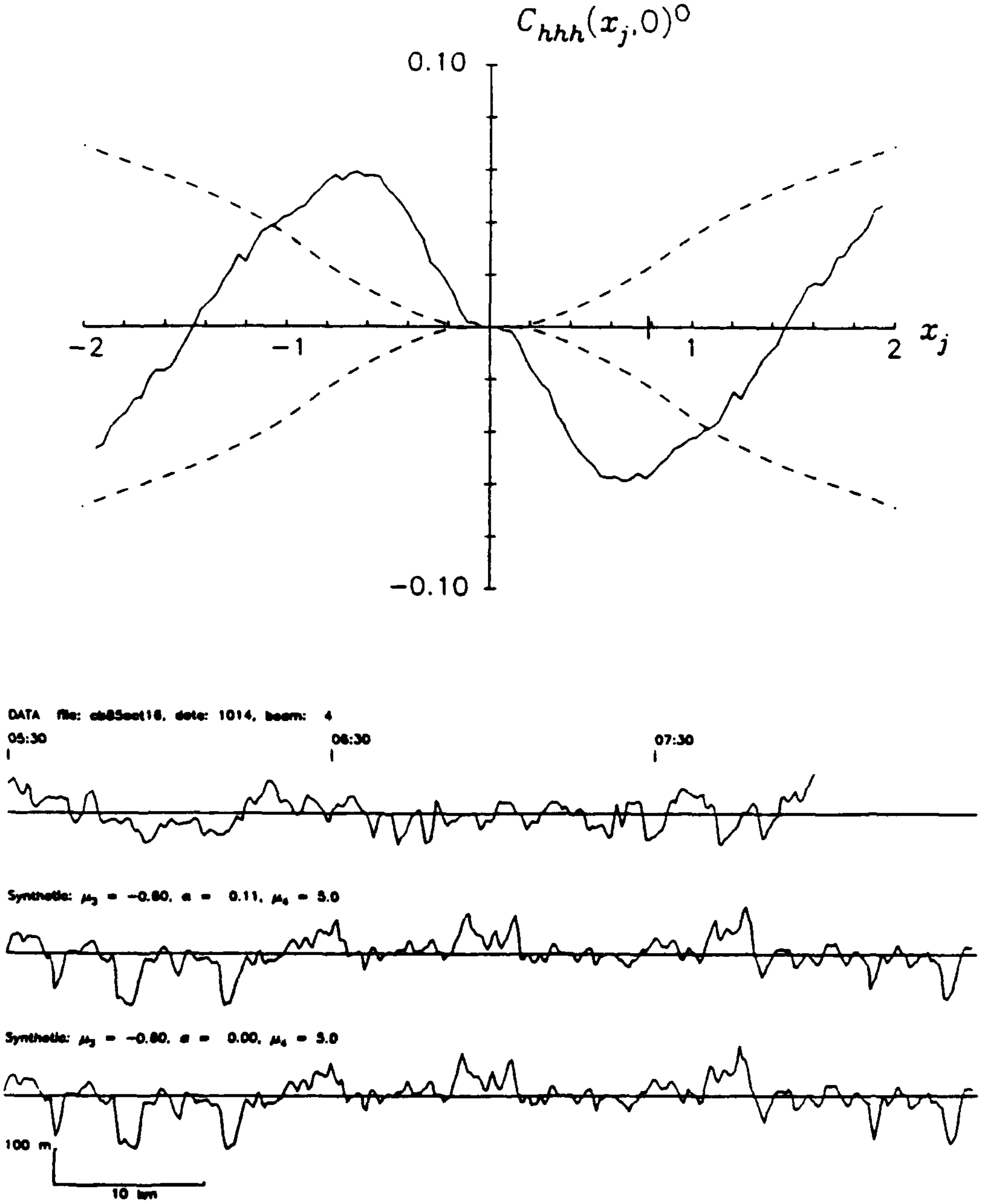

Figure 6.13. $\tilde{C}_{hhh}(x_{peak},0)^o$ (solid, top panel) with numerically constructed errors on the null hypothesis that $C_{hhh}(x_{peak},0)^o = 0$ (dashed, top panel), and data-synthetic comparison (bottom panel) for a Pacific Sea Beam profile. The data was taken on the Papatua 1 leg of the *RV Thomas Washington*, near the East Pacific Rise at ~13.1° N. The second-order parameters estimated from the profile, and used in the generation of the synthetics, are $H = 292 \pm 32$ m, and $\lambda_\theta = 7.6 \pm 1.5$ km, and $D = 2.1 \pm 0.9$.

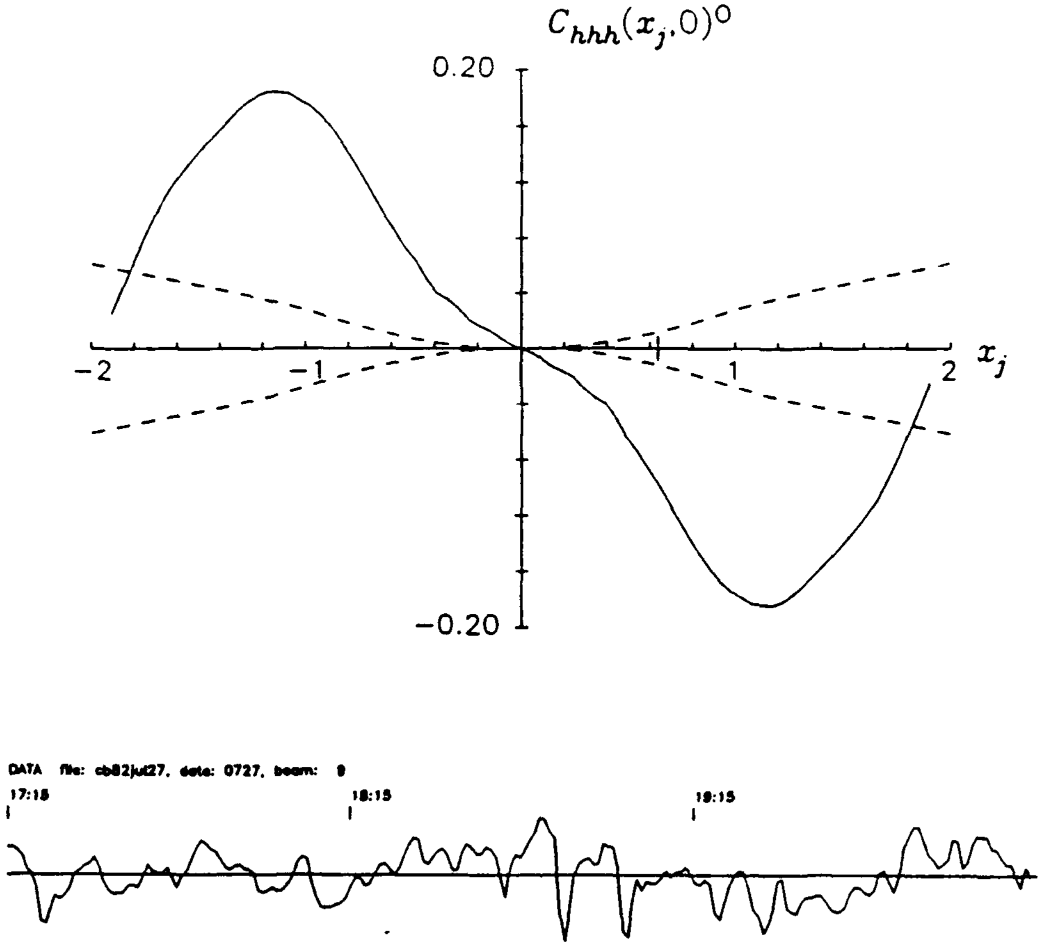

Figure 6.14. $\tilde{C}_{hhh}(x_{peak},0)^{o}$ (solid, top panel) with numerically constructed errors on the null hypothesis that $\tilde{C}_{hhh}(x_{peak},0)^{o} = 0$ (dashed, top panel), and the Pacific Sea Beam profile from which it was calculated (bottom panel). The data was taken on the Ceres 2 leg of the *RV Thomas Washington*, near the East Pacific Rise at ~14.0° N.

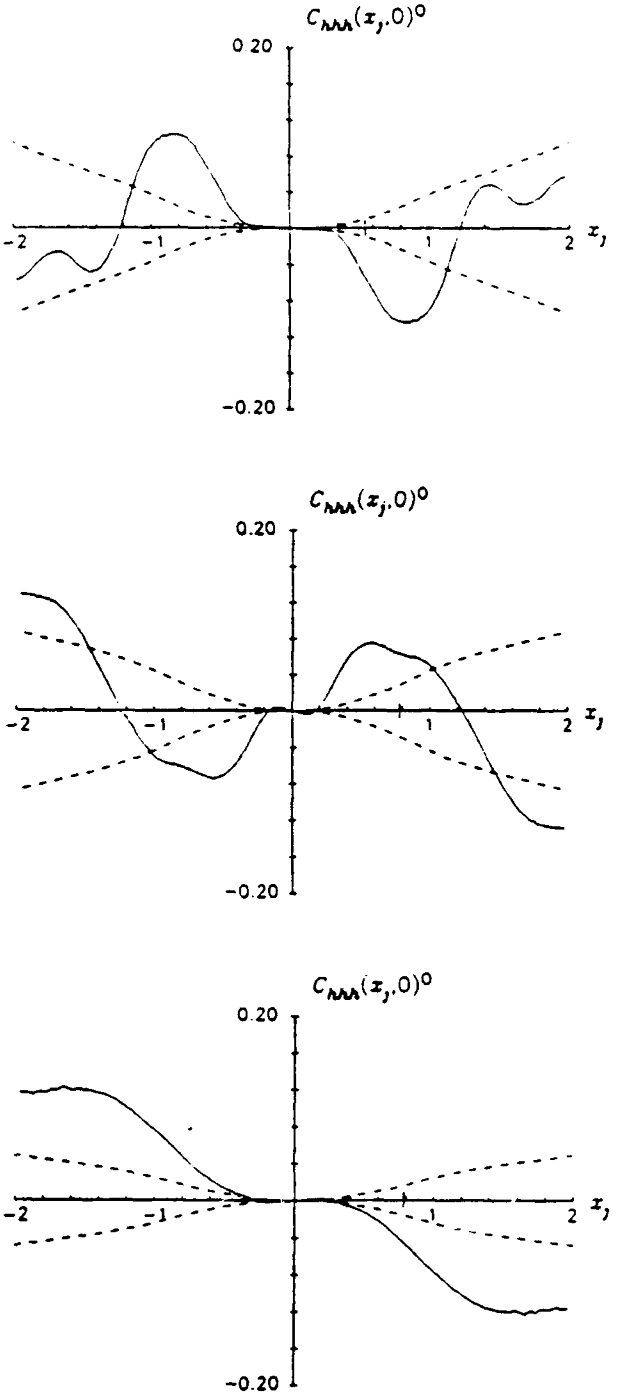

Figure 6.15. Three examples of $\tilde{C}_{hhh}(x_{peak},0)^0$ (solid) from Pacific Sea Beam profiles exhibiting possible back-tilt at smaller scales (see text). Also shown are numerically constructed errors on the null hypothesis that $\tilde{C}_{hhh}(x_{peak},0)^0 = 0$ (dashed). Top panel is from data taken aboard the RC2607 leg of the *RV Robert Conrad*, near the East Pacific Rise at ~9.4° N. The middle panel is from data taken aboard the same leg near the East Pacific Rise at ~11.0° N. The bottom panel is from data taken aboard the AII2L26 leg of the *RV Atlantis II*, just south of the juncture between the Clipperton Transform Fault and the East Pacific Rise.

Piggy-Back Features

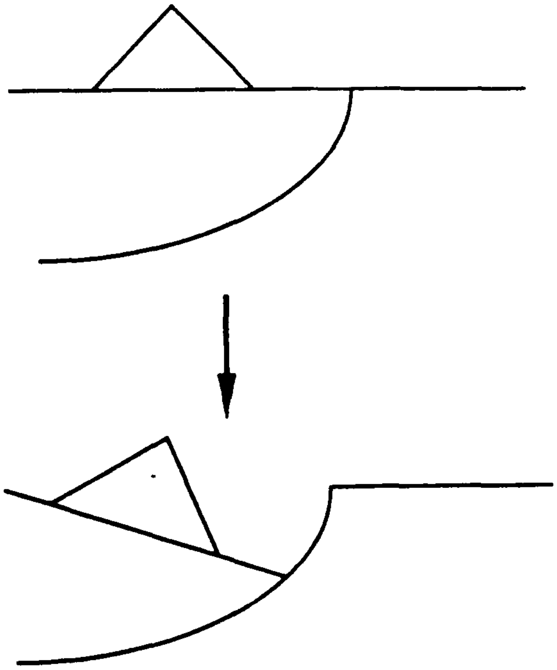

Antithetic Faulting
[*Mcdonald and Luyendyk*, 1985]

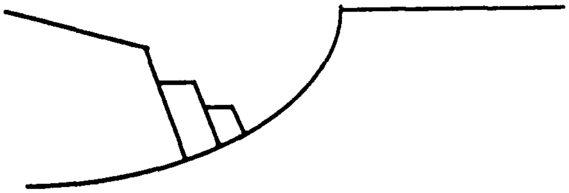

Figure 6.16. Possible causes of back tilting at small scales provided that polarized listric faulting is the primary cause lateral asymmetry at larger scales.

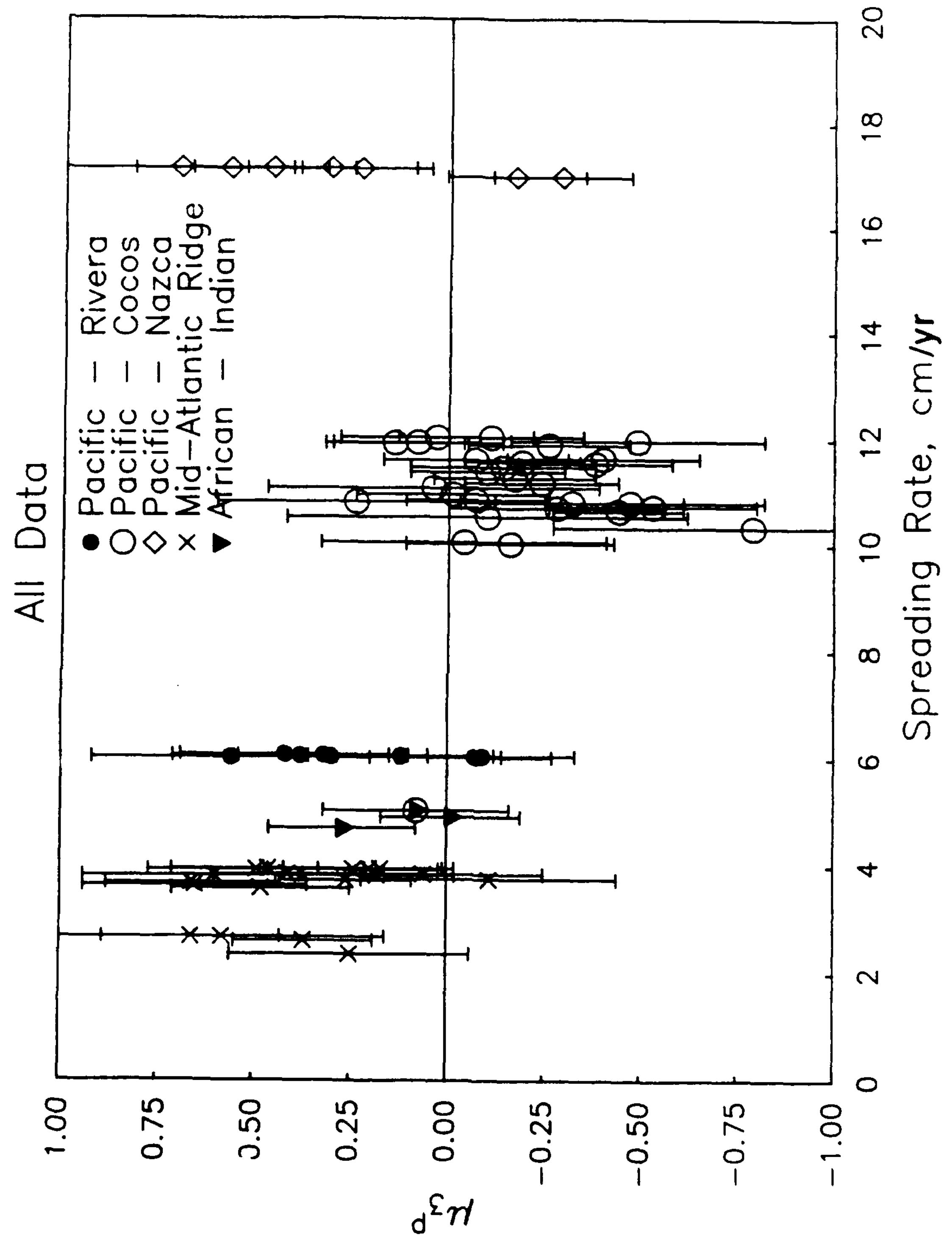

Figure 6.17. $\mu_3 P$, estimated from the near-ridge Sea Beam data (Table 5.1), plotted as a function of spreading rate (Table 5.1) as determined by model RM2 [*Minster and Jordan*, 1978]. Bars represent 1-σ errors about each estimation. Different symbols represent data from different spreading regions as indicated.

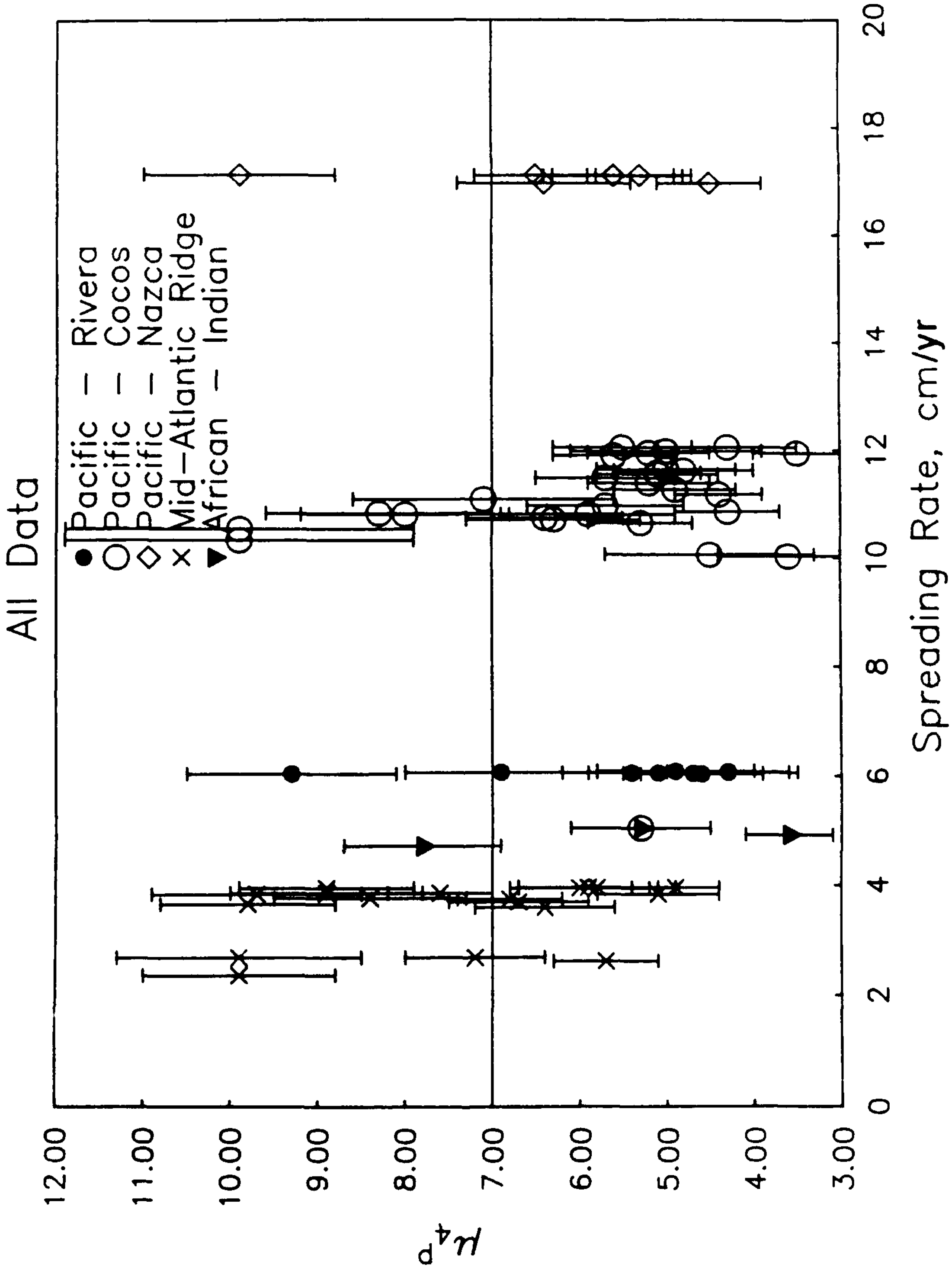

Figure 6.18. μ_4^p estimated from the near-ridge Sea Beam data (Table 5.1), plotted as a function of spreading rate (Table 5.1) as determined by model RM2 [*Minster and Jordan*, 1978]. Bars represent 1-σ errors about each estimation. Different symbols represent data from different spreading regions as indicated.

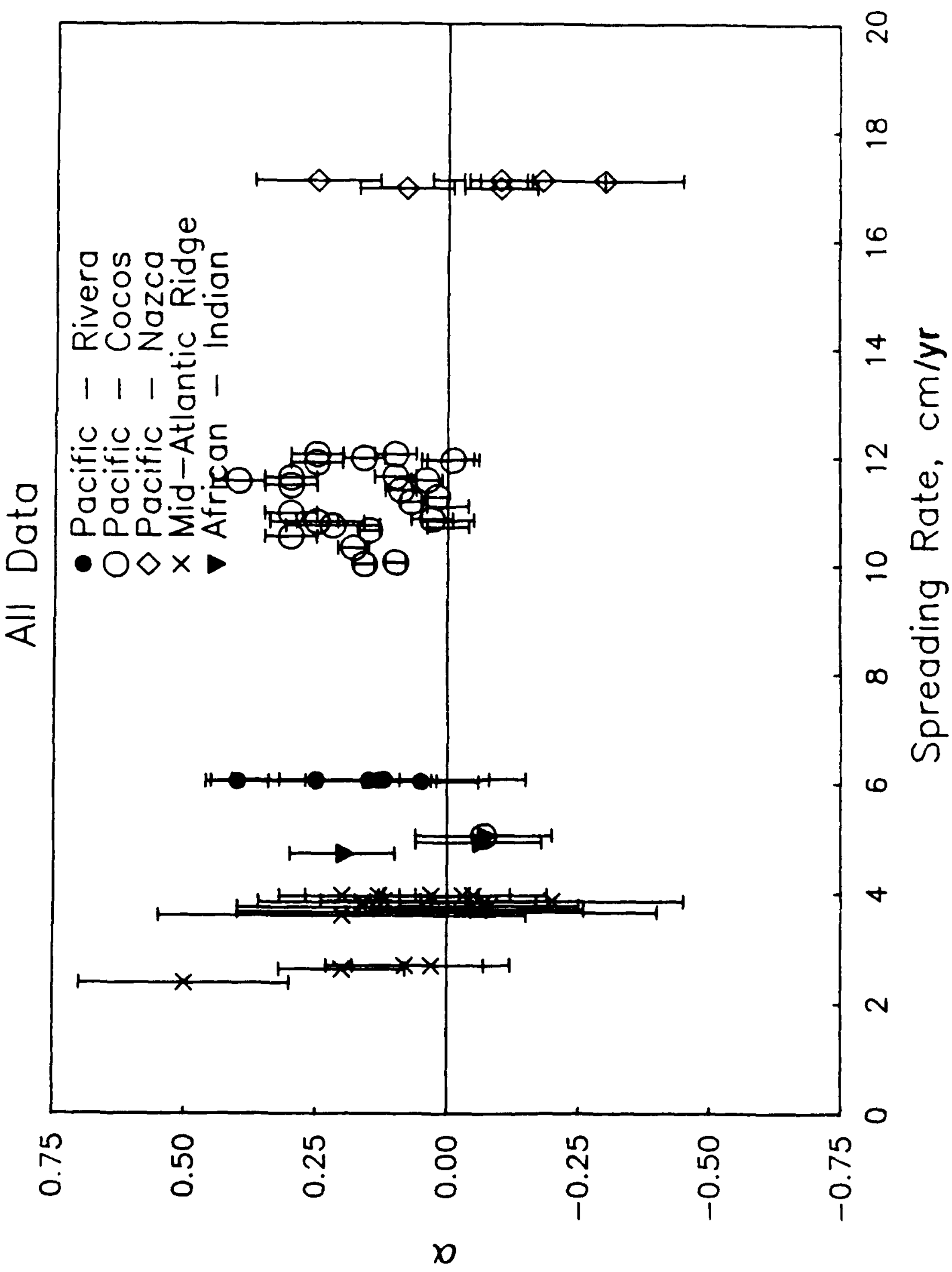

Figure 6.19. α estimated from the near-ridge Sea Beam data (Table 5.1), plotted as a function of spreading rate (Table 5.1) as determined by model RM2 [*Minster and Jordan*, 1978]. Bars represent 1-σ errors about each estimation. Different symbols represent data from different spreading regions as indicated.

APPENDIX A

A COVARIANCE FUNCTION FOR SEAFLOOR TOPOGRAPHY

The seafloor covariance model given by (2.21) is specified in terms of the function

$$G_\nu(r) = r^\nu K_\nu(r) \qquad 0 \le r < \infty \qquad \nu \in [0,1] \tag{2.20}$$

A correlation function of this form was first proposed by *von Kármán* [1948] for characterizing the random velocity field of a turbulent medium. It has since been frequently used, with one value of ν or another, in the turbulence literature [e.g., *Tatarski*, 1961] as well as other studies involving random fields, such as wave scattering [e.g., *Chernov*, 1960]. Its importance has also been recognized in the statistical literature. For example, *Matérn* [1970] identified it specifically as belonging to the class of continuous correlation functions. Workers such as *Whittle* [1954], *Bartlett* [1966], and *Moran* [1973] derived (2.20) at several values of ν as correlation functions uniquely corresponding to random fields that are solutions to stochastic differential equations of the form

$$\left[\nabla^2 + \kappa^2\right]^{(1+\nu)/2} h(\mathbf{x}) = \varepsilon(\mathbf{x}) \tag{A.1}$$

where $\varepsilon(\mathbf{x})$ is a continuous, white noise process on the plane and κ is a constant wave number. The case $\nu = 0$ corresponds to a two-dimensional Markov field. The case $\nu = 1$ corresponds to an autoregressive field; the correlation function corresponding to this value was called the elementary correlation in two dimensions by *Whittle* [1954]. *Lord* [1954], taking a slightly different tack, considered equations of the form of (2.20) as probability distributions for random fields of arbitrary dimension.

The Power Spectrum

The power spectrum corresponding to a random field whose covariance function is given by (2.21) is simply the Fourier transform of the covariance function:

$$P_h(\mathbf{k}) = \int_{-\infty}^{\infty}\int_{-\infty}^{\infty} C_{hh}(\mathbf{x})\, e^{-i\,\mathbf{k}\cdot\mathbf{x}}\, d^2\mathbf{x} \tag{2.7}$$

In the symmetric case, the power spectrum and covariance function can be related via an N-dimensional Hankel transform [*Lord*, 1954]:

$$P_h(u) = (2\pi)^{N/2}\, u^{-N/2+1} \int_0^{\infty} r^{N/2} J_{N/2-1}(ru)\, C_{hh}(r)\, dr \tag{A.2}$$

$$C_{hh}(r) = (2\pi)^{-N/2}\, r^{-N/2+1} \int_0^{\infty} u^{N/2} J_{N/2-1}(ru)\, P_h(u)\, du \tag{A.3}$$

where $J_{N/2-1}$ is the Bessel function of order $N/2 - 1$. The Hankel transform pair for $G_\nu(r)$ has been derived by *Lord* [1954]:

$$P_h(u) = \frac{\Gamma(\nu + N/2)}{2^{1-N-\nu}\, \pi^{N/2}} (1 + u^2)^{-\nu - N/2} \tag{A.4}$$

Applying a change of variables specified by (2.13) to (2.7) for the anisotropic case and normalizing $G_\nu(r)$ as in (2.21), we obtain, for the two-dimensional case,

$$P_h(\mathbf{k}) = 4\pi \nu H^2 |\mathbf{Q}|^{-1/2}[u^2(\mathbf{k}) + 1]^{-(\nu+1)} \tag{2.22}$$

where $u(\mathbf{k})$ and $\mathbf{Q}$ are defined in the text.

Calculation of the Hausdorff Dimension

The most typical method for calculating the fractal dimension of a random field is to measure the asymptotic roll-off rate of the power spectrum [e.g., *Fox and Hayes*, 1985]. A space-domain method follows the definitions given by *Adler* [1981] which relate the Hausdorff dimension D to the asymptotic properties of the covariance function near zero lag. We define N and d to be the coordinate and field dimensions, respectively. We thus consider $h(\mathbf{x})$ to be a stationary Gaussian field with $N = 2$, $d = 1$, and a continuous covariance function $C_{hh}(r)$. We define the incremental variance function:

$$\sigma^2(r) \equiv \langle | h(\xi + \mathbf{x}) - h(\xi) |^2 \rangle = 2[C_{hh}(0) - C_{hh}(r)] \tag{A.5}$$

Where $\sigma(r)$ exhibits a power-type behavior, we can define the β index of the field h by

$$\begin{aligned} \beta &= \sup \{ \beta\colon \sigma(r) = o(r^{\beta}),\ r \downarrow 0 \} \\ &= \inf \{ \beta\colon r^{\beta} = o(\sigma(r)),\ r \downarrow 0 \} \end{aligned} \tag{A.6}$$

β may be said to be a measure of how erratic the local behavior of the field is. *Adler* [1981] shows that the Hausdorff dimension is then given by

$$\mathsf{D} = \min \left[\frac{N}{\beta},\ N + d(1 - \beta) \right] \tag{A.7}$$

To examine the property of $\sigma(r)$ as $r \rightarrow 0$, we make use of the Frobenious series expansion [*McLachlan*, 1955]:

$$K_\nu(r) = \frac{\pi}{2 \sin \nu\pi} \left[I_{-\nu}(r) - I_\nu(r) \right] \tag{A.8}$$

$$I_\nu(r) = \left(\frac{r}{2}\right)^\nu \sum_{n=0}^{\infty} \frac{\left(\frac{1}{4} r^2\right)^n}{n!\, \Gamma(n + \nu + 1)} \tag{A.9}$$

where I_ν is the modified Bessel function of the first kind. We now define

$$A_\nu = \frac{\pi}{2 \sin \nu\pi} \frac{H^2}{G_\nu(0)} \tag{A.10}$$

$$E_\nu(r) = \left(\frac{1}{2}\right)^\nu \sum_{n=0}^{\infty} \frac{\left(\frac{1}{4} r^2\right)^n}{n!\, \Gamma(n + \nu + 1)} \tag{A.11}$$

and note that $0 < E_\nu(0), E_{-\nu}(0) < \infty$. We may then write

$$C_{hh}(r) = A_\nu \left[E_{-\nu}(r) - r^{2\nu} E_\nu(r) \right] \tag{A.12}$$

As $r \rightarrow 0$, $\sigma(r)^2 \rightarrow 2A_\nu E_\nu(0) r^{2\nu}$. Thus $\sigma(r) \sim r^\nu$ as $r \rightarrow 0$. From (A.6) it is then clear that $\beta = \nu$ and, in the case $N = 2$ and $d = 1$, $D = 3 - \nu$.

Self-Affine Scaling at Small Scales

An interesting surface property related to the Hausdorff dimension is self-affine scaling. We adopt the following definition, based on definitions given by *Mandelbrot* [1983, 1985] and consistent with the notation established in this paper: A topographic surface $h(\mathbf{x})$ is a self-affine fractal surface if there exists an $\alpha \in [0,1]$ such that, for all $R > 0$ the topographic difference function $d(\mathbf{x} - \mathbf{x}_0) = h(\mathbf{x}) - h(\mathbf{x}_0)$ is identical in distribution to $R^{-\alpha}d(R\mathbf{x} - R\mathbf{x}_0)$. Where $\alpha = 1$, $h(\mathbf{x})$ is a self-similar fractal surface. For surfaces corresponding to power spectral forms such as (2.11), this relationship will hold for all scales. However, for surfaces which have corner wave numbers in their power spectral forms, this relationship holds only for small scales. To take this behavior into account we can easily modify the self-affine definition in the following way: $h(\mathbf{x})$ is a bounded self-affine fractal surface if there exists a scale L such that the self-affine relationship holds for $|\mathbf{x} - \mathbf{x}_0| \ll L$.

To solve for α in the case of a Gaussian distribution, we set the mean and variance of $d(\mathbf{x} - \mathbf{x}_0)$ equal to the mean and variance of $R^{-\alpha}d(R\mathbf{x} - R\mathbf{x}_0)$ (identical distribution). Taking the mean of both gives

$$\langle d(\mathbf{x} - \mathbf{x}_0)\rangle = \langle R^{-\alpha}d(R\mathbf{x} - R\mathbf{x}_0)\rangle = 0 \tag{A.13}$$

regardless of the value of R or α. We must therefore use the variances to constrain α:

$$\langle (d(\mathbf{x} - \mathbf{x}_0))^2\rangle = \langle (R^{-\alpha}d(R\mathbf{x} - R\mathbf{x}_0))^2\rangle \tag{A.14}$$

The left-hand side of (A.14) is simply the incremental variance function (A.5) so that, in the isotropic case with $k_n = k_s = k_0$, we have, for $k_0|\mathbf{x} - \mathbf{x}_0| \ll 1$ (i.e. $L = k_0^{-1}$)

$$\begin{aligned} \langle (d(\mathbf{x} - \mathbf{x}_0))^2\rangle &= c\,|\mathbf{x} - \mathbf{x}_0|^{2\nu} \\ c &= 2A_\nu E_\nu(0)k_0 = \text{constant} \end{aligned} \tag{A.15}$$

Applying (A.15) to (A.14) gives

$$c\,|\mathbf{x}-\mathbf{x}_0|^{2\nu} = R^{-2\alpha}R^{2\nu}c\,|\mathbf{x}-\mathbf{x}_0|^{2\nu} \qquad \text{(A.16)}$$

Thus $\alpha = \nu$. In the anisotropic case it is clear that that we may set $L = k_n$, and the same relationship will hold with the constant in (A.15) directionally dependent.

Asymptotic Equation

The behavior of the covariance at large lag is also affected by the parameter ν, but to a lesser extent than the behavior near the origin. Using the asymptotic expansion for $K_\nu(r)$, from *McLachlan* [1955], we compute, for r » 1,

$$G_\nu(r) \sim \sqrt{\frac{\pi}{2}}\, r^{\nu-1/2} e^{-r} \left\{ 1 + \frac{(4\nu^2-1^2)}{1!\,8r} + \ldots \right.$$

$$\left. + \frac{(4\nu^2-1^2)\ldots[4\nu^2-(2n-3)^2]}{(n-1)!\,(8r)^{n-1}} + .. \right\} \qquad \text{(A.17)}$$

Thus, the smaller the value of ν, the greater the rate of decay at large r. This fact has important implications for the estimation of scale parameters, since the rate of decay in the covariance function with increasing lag is the primary determinant of the scale parameters. A trade-off between these parameters is therefore to be expected. The behavior of the covariance function at both small and large lag is illustrated in Figure 2.1.

Calculation of Characteristic Length

Consider a profile, taken in the $\hat{\mathbf{e}}_\theta$ direction, of a random surface with covariance given by (2.21). A simple and commonly used definition for the characteristic length along such a profile [e.g., *Tatarski*, 1961; *Bell*, 1975*b*] is the inverse of the scale parameter, given by

$\lambda_\theta \equiv k_\theta^{-1} = [\hat{\mathbf{e}}_\theta^T \mathbf{Q} \hat{\mathbf{e}}_\theta]^{-1/2}$. Characteristic length can also be defined by the width of the covariance function in the direction of the profile, which can be formulated in terms of the variance about zero lag of the autocovariance function for the profile:

$$\lambda_\theta = 2\sqrt{\frac{\mu_2}{\mu_0}} \tag{A.18}$$

where μ_p are the p^{th} moments of the autocovariance function

$$\mu_p = 2\int_0^\infty x_\theta^p C_{hh}(x_\theta)\, dx_\theta \; . \tag{A.19}$$

and x_θ is length in the $\hat{\mathbf{e}}_\theta$ direction. Making use of (2.21), we can rewrite (A.19) as

$$\mu_p = \frac{2H^2}{G_\nu(0)} \frac{1}{k_\theta^{p+1}} \int_0^{+\infty} (k_\theta x_\theta)^{\nu+p} K_\nu(k_\theta x_\theta)\, d(k_\theta x_\theta) \tag{A.20}$$

An equation of the form (A.20) is solved in the integral tables of *McLachlan* [1955], yielding

$$\mu_p = \frac{2^{\nu+p} H^2}{G_\nu(0)\, k_\theta^{p+1}} \Gamma\{\frac{1}{2}(p-1)\}\, \Gamma\{\frac{1}{2}(2\nu+p+1)\} \tag{A.21}$$

Returning to equation (A.18), we have the result:

$$\lambda_\theta = \frac{2\sqrt{2\nu + 1/2)}}{k_\theta} \tag{2.24}$$

This definition of the characteristic length is preferable to the previous one because it explicitly accounts for the effect of the Hausdorff dimension as well as the scale parameter on the width of the covariance function. In fact, it is likely that most of the D-k_θ trade-off is well described by (A.22) with λ_θ fixed. Thus, while resolution of D and k_θ are degraded by the trade-off, λ_θ remains a well-resolved parameter.

Slope Statistics

Because the covariance function (2.21) is discontinuous at the origin for $\nu < 1$, the random field has fractal character, and its spatial derivatives do not exist. Therefore, it is necessary to measure slopes in terms of topography differences over finite intervals. The slope function is defined as

$$s(\mathbf{x}_1,\xi_1) = \frac{h(\mathbf{x}_1 + \xi_1) - h(\mathbf{x}_1)}{|\xi_1|} \tag{A.25}$$

where $|\xi_1|$ is the slope interval. If the probability density function for h is stationary and normally distributed with known second moment, as in (2.21), then the probability density function for s will also be stationary and normally distributed with zero mean and variance given by

$$\langle s^2(\mathbf{x}_1,\xi_1)\rangle = \frac{2(C_{hh}(0) - C_{hh}(\xi_1))}{|\xi_1|^2} \tag{A.26}$$

At small lag, (A.12) can be used to show that the slope variance is proportional to $|\xi^1|^{2(\nu-1)}$. Thus, for fractal topography with $\nu < 1$, slopes become arbitrarily steep as the slope interval decreases. In the case of the Euclidean surface ($\nu = 1$), the variance of slopes is constant over all slope intervals.

Equation (A.26) can be generalized to the slope autocovariance function:

$$C_{ss}(\mathbf{x},\xi_1,\xi) = \langle s(\mathbf{x}_1,\xi_1)\, s(\mathbf{x}_1 + \mathbf{x},\xi_1 + \xi)\rangle = \frac{C_{hh}(\mathbf{x} + \xi) - C_{hh}(\xi_1 - \mathbf{x}) - C_{hh}(\mathbf{x} + \xi_1 + \xi) + C_{hh}(\mathbf{x})}{|\xi_1|\,|\xi_1 + \xi|} \tag{A.27}$$

We can also calculate the slope-height covariance

$$C_{sh}(\xi_1) = \frac{C_{hh}(\xi_1) - C_{hh}(0)}{|\xi_1|} \tag{A.28}$$

In one dimension, the case $\nu = 0.5$ (exponential covariance) yields a Markov process (the Ornstein-Uhlenbeck process) [*Feller*, 1971]. The Markov property can be demonstrated by considering the 1-D form of (A.27) for $k_\theta \xi \ll 1$:

$$C_{ss}(x,\xi_1,\xi) = \begin{cases} \dfrac{2H^2 k_\theta}{|\xi_1|}\,\dfrac{(\xi_1 - x)}{(\xi_1 + \xi)}, & \xi_1 > x \\ 0, & \xi_1 \le x \end{cases} \tag{A.29}$$

Thus, when slope intervals do not overlap ($\xi_1 < x$), the slopes are uncorrelated. Using the asymptotic forms form $\nu \neq 0.5$, we find that the slopes for non-overlapping intervals are positively correlated where $\nu > 0.5$, and negatively correlated where $\nu < 0.5$.

APPENDIX B:

NESTED STOCHASTIC SEAFLOOR REALIZATIONS

This appendix details the algorithm developed to generate nested synthetic seafloor sections from a second-order stochastic model such as (2.21). This algorithm can be applied to any situation in which gridded, course-resolution data is used as a constraint for data (stochastically generated or not) which is rendered at finer-scale resolution. An important application of this algorithm is the stochastic interpolation of known (i.e. deterministic) bathymetry based on a given stochastic model. The scale at which "known" and "interpolated" topography are separated is arbitrary, so that a map may be constructed at any scale before it is stochastically interpolated. Through the molding algorithm, synthetic realizations can be combined with large-scale bathymetric maps, such as DBDB5, to stochastically interpolate known ocean-bottom bathymetry.

Deterministic and Stochastic Components of Seafloor Topography

We let $z(\mathbf{x})$ be the height of the seafloor above some mean reference level at a position $\mathbf{x}$, and we suppose we have a map of this topography, denoted $z_M(\mathbf{x})$. Because the map is based on limited data, it may accurately represent age-dependent subsidence, thermal swells, major fracture zones, oceanic plateaus, and other "large-scale" features, but does not contain topographic variations with horizontal dimensions below some "cutoff scale" x_M. We assume the map can be approximated as the output of some filter $M[z(\mathbf{x})]$. To the extent that the mapping cutoff is sharp — i.e., M passes features larger than x_M with no distortion but completely annihilates features smaller than x_M — this filter is a projection operator: $z_M(\mathbf{x}) = M[z_M(\mathbf{x})]$. An example of $z_M(\mathbf{x})$, the one used in this appendix, is the

DBDB5 bathymetry, which is specified on a 5' × 5' grid (9.25-km knot spacing) and has an effective cutoff of $x_M \approx 50$ km.

We seek to supplement this deterministic description of the seafloor with some stochastic representation of the small-scale features. Let $h(\mathbf{x})$ be a stochastic process, or random field, which represents the statistics of the topographic variation at all length scales. We define $h_M(\mathbf{x}) = \mathcal{M}[h(\mathbf{x})]$ and take as our model of seafloor topography

$$\tilde{z}(\mathbf{x}) = z_M(\mathbf{x}) + h(\mathbf{x}) - h_M(\mathbf{x}) \tag{B.1}$$

In other words, we replace the stochastic components of the field with scale lengths greater than the cutoff x_M by the known ("deterministic") components. If $\mathcal{M}$ is a projection operator, then applying it to this model recovers the map: $\mathcal{M}[\tilde{z}(\mathbf{x})] = z_M(\mathbf{x})$.

The Nesting Algorithm

The algorithm for generating nested synthetics involves two basic steps. The first is to generate a master realization from the desired covariance function on a large-scale grid. The second is to take a compact rectangular subset of the master realization and use it as a constraint in generating a synthetic realization with finer resolution. The latter involves a procedure for "molding" an arbitrary topographic array to values specified on a coarser grid. The nested synthetic is then regarded as a master realization, and the nesting is iterated to produce realizations on finer grids.

To generate unconstrained synthetic topography, we compute the Fourier spectrum on a regularly spaced wave number grid by multiplying the square root of the power spectrum (2.22) by a phase factor $\exp(i\phi)$ where ϕ is a random number uniformly distributed on the interval $[0, 2\pi)$ [*Priestly*, 1981]. The space domain image is then obtained from a two-dimensional, fast Fourier transform. To minimize edge effects associated with aliasing, a larger realization than required is generated, so that the edges may simply be discarded. An example of such a realization, displayed as a color-contoured, grey-shaded relief plot, is shown in Figure B.1.

The algorithm for generating a nested synthetic realization includes the following steps:

1. A rectangular ($m \times n$ array) compact subset of the master realization is selected for nesting. As an example we use the square shown in the first panel of Figure B.1. The realization is a 1000×1000 array and the subset $m = 100 \times n = 100$. (In practice, arrays are 20% larger than stated throughout the algorithm, so that we may discard the edges to reduce adverse aliasing effects.)

2. The subset is interpolated, using a bilinear (or bicubic) algorithm [*Press et al.*, 1986], at the resolution that will be required for the stochastic interpolation. This results in an $em \times en$ array, where e is the enlargement factor. The second panel of Figure B.1 shows the bilinear interpolation of the box shown in the first panel with $e = 10$, which results in another 1000×1000 array.

3. A stochastic realization is generated from the covariance model at the resolution and scale required for the stochastic interpolation. The bilinear interpolation of the subset is Fourier transformed, obtaining a spectrum with discrete wavenumbers (k_{x_i}, k_{y_j}) indexed $-em/2 < i < em/2$ and $-en/2 < j < en/2$. Phases of the wavenumbers indexed $-m/2 < i < m/2$ and $-n/2 < j < n/2$, the portion of the spectrum sampled by the master realization, are then input as the phases for the identically indexed wavenumbers of the spectrum of the stochastic realization. The Fourier transform of this spectrum produces a realization whose low wavenumber characteristics are similar to those of the interpolated subset (compare the second and third panels of Figure B.1).

4. The final step is the molding the finer-scale realization generated in step 3 to the master realization generated in step 1. The former is first sampled on the coarse grid, resulting in an $m \times n$ array. This array is then interpolated using the same algorithm used in step 2, yielding another $em \times en$ array. The difference between this interpolated array and that obtained in step 2 is subtracted from the finer-scale realization, thus constraining it

to coincide with the master on the coarser grid. The fourth panel in Figure B.1 shows the final product.

The effect of the molding algorithm is to replace the smoother features of the unconstrained stochastic realization with those obtained from the master without significantly altering the power spectrum.

Stochastic Interpolation of Gridded Bathymetric Data

The molding algorithm can be used to stochastically interpolate a gridded bathymetric map, such as DBDB5, by using the map as the master realization. The following model parameters were used to generate two stochastic realizations to interpolate DBDB5 data:

Model	H (m)	ζ_s (deg)	λ_n (km)	λ_s (km)	D
SM1-P	50	170	2.3	19	2.5
SM1-A	225	10	5.9	22	2.2

Model SM1-P was obtained from Sea Beam data taken near the East Pacific Rise between the Orozco and Siquieros fracture zones (see chapter 4), and model SM1-A from Sea Beam data taken just south of the Kane fracture zone.

Two sets of DBDB5 bathymetry, gridded at 10 km spacing and covering 100 km on a side, are shown in Figure B.2. These data sets have been linearly interpolated to 100 m spacing, the resolution at which we will stochastically interpolate. The molding algorithm superimposes a stochastic realization generated from the model parameters onto the interpolated DBDB5 bathymetry. The results are also shown in Figure B.2.

Aliasing

If the spectrum of a spatially unlimited topographic field $h(\mathbf{x})$ is sampled on an $N \times N$ grid of spacing Δk, its space-domain image will be an aliased version of $h(\mathbf{x})$. The covariance function of the aliased field will be the sum of the covariance function $C_{hh}(\mathbf{x})$ with copies centered on a grid with spacing $N\Delta x$ [*Bracewell*, 1978]. When $N\, \Delta x$ is large compared to the characteristic length λ_s, such as in the case of the master realization of each series, aliasing will not be significant, since the amplitude of the copies is small where $C_{hh}(\mathbf{x})$ is large. However, when $N\Delta x$ is small compared to the characteristic length, such as in the second-level and third-level nestings of each series, the spacing between copies is small enough that the aliased covariance function will be significantly different from the model.

Fortunately, the effect of aliasing is to add power to the field only at the largest scales. The combined contribution of nearby diametrically placed copies will be approximately a constant. Adding a constant to the covariance simply adds a constant to the topography, which is removed in the molding procedure.

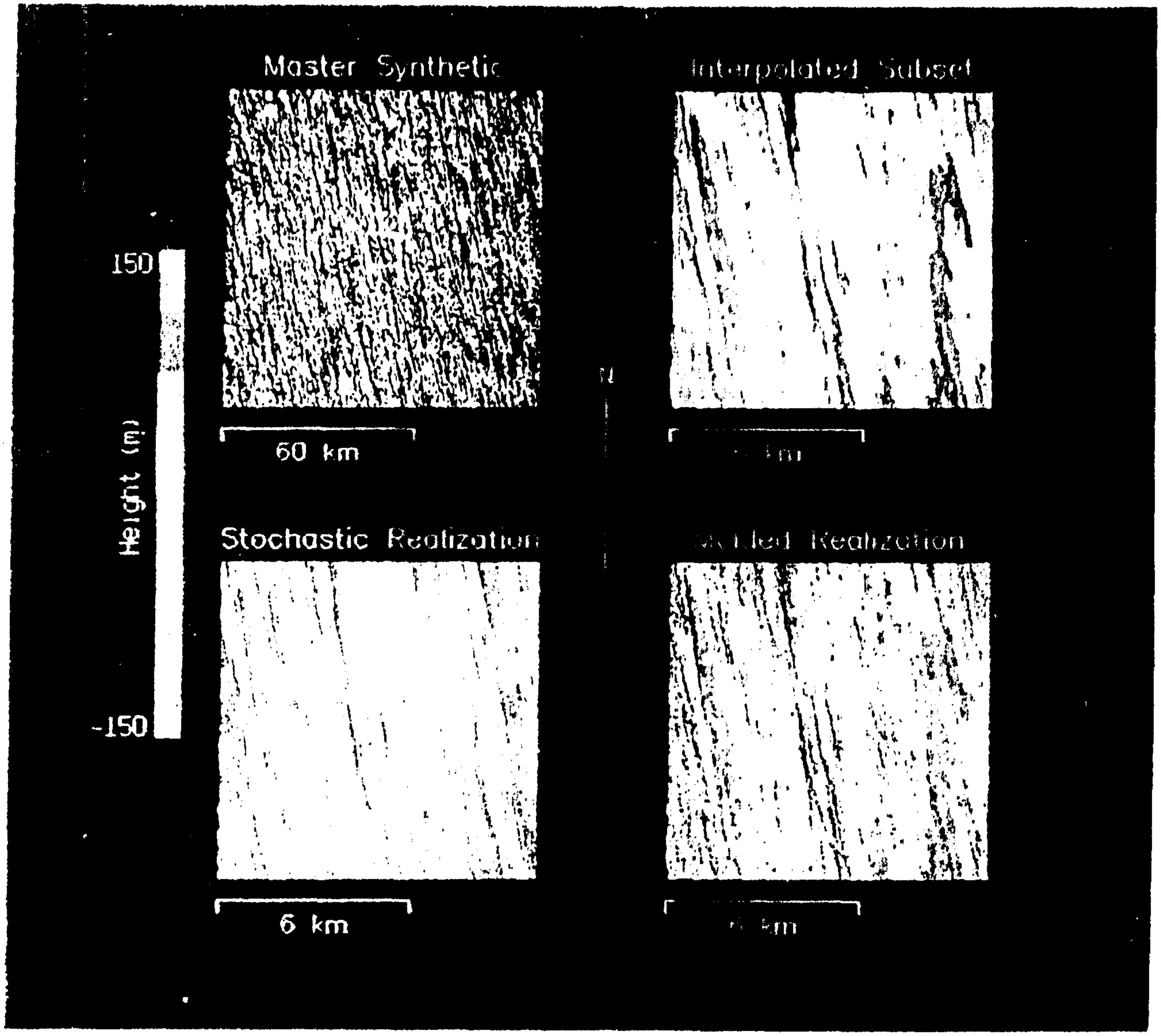

Figure B.1. Example of the nesting algorithm described in the text. Each panel is a color contoured, grey-shaded relief plot of seafloor topography. First panel (upper left) is the unconstrained master realization, generated from the parameters for SM1-P. This realization array contains 1000 × 1000 elements, and is 100 km on each side. The outlined box in the middle of this panel is the subset chosen for nesting. This box is 100 × 100 elements (10 km × 10 km). The second panel (upper right) is the bilinear interpolation of the subset. This panel contains 1000 × 1000 elements and has a dimension of 10 km × 10 km. The third panel (bottom left) is another stochastic realization generated over the finer-scale grid of the second panel. The phases from the lowest 50 wavenumbers from the Fourier spectrum of the second panel were used as phases for the identical wavenumbers in generating the third panel. The fourth panel (lower right) was then generated by molding (see text) the second panel to the constraints provided by the master.

Best Available Copy

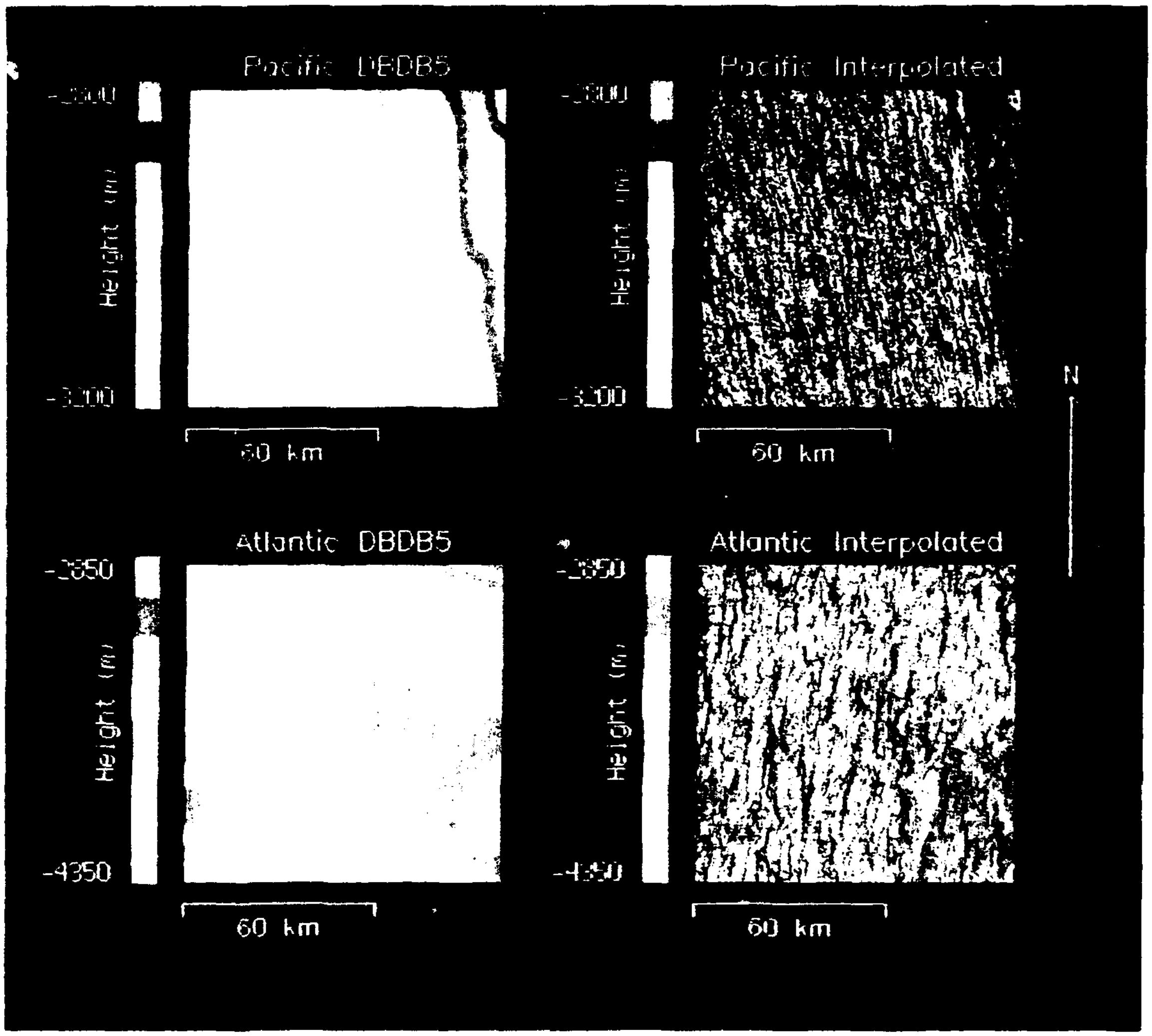
Pacific DBDB5
-2300
Height (m)
-3300
60 km
Pacific Interpolated
-2300
Height (m)
-3300
60 km
N
Atlantic DBDB5
-3350
Height (m)
-4350
60 km
Atlantic Interpolated
-3350
Height (m)
-4350
60 km

Figure B.2. Color-contoured, grey-shaded plots of the Pacific and Atlantic DBDB5 sections provided in the release and the superposition of these data sets with the (molded) stochastic realizations (see text). These topographic models are designated SM1-P and SM1-A, respectively Latitude and longitudes represent the location of the lower-left corner of each DBDB5 section.

APPENDIX C

STATISTICAL ANALYSIS OF SEAMARC II NOISE

This appendix is a statistical analysis of the noise characteristics for the SM-II bathymetric data taken aboard the MW8707 cruise. The purpose of this analysis is to investigate the suitability of this data set as it is made available in the standard HIG .zx format (A. Shor, personal communication, 1990) for use in stochastic characterization of abyssal hill morphology at small scales (< 10 km). It does not affect the well-known usefulness of the SM-II system for quickly gathering large quantities of bathymetric data, suitable for characterizing larger scale features, as well as simultaneous backscatter data. This appendix is concerned only with characterizing the effects of SM-II noise so that we can, in turn, understand how it affects the statistics of the seafloor bathymetry which it is measuring. A detailed examination of the causes of SM-II noise characteristics is beyond the scope of this paper. For a recent description of SM-II noise we refer the reader to *Matsumoto* [1990]. This analysis is based on methods developed in Chapter 2 for Sea Beam data.

To facilitate the study, SM-II .zx files are formed into 16 "beams" to simulate an idealized Sea Beam data geometry; for each SM-II ping, the data point chosen to represent each beam corresponds to the point closest to a preset cross-track distance. Other than the center beam, the cross-track distances used to form the beams begin at 0.75 km on either side of the center line and index every 0.45 km thereafter. This algorithm results in a 7.8 km wide swath width. Results for two SM-II data sets are shown in Figures C.1 and C.2. Figure C.1 is 5-ping averaged data from the MW8707 cruise, taken just west of the EPR near 13° N. (The 5-ping averaging is necessary to reduce the level of noise sufficiently to view the data. In the actual analysis only unaveraged data is used.) Figure C.2 is 5-ping averaged data from the same cruise, crossing the Siquieros Fracture Zone west of the ridge-transform intersection. In each figure, the 16 formed beams are plotted individually. Port (negative) beams are at top. (Plotting the data as time series rather than as contours allows the reader a better intuitive understanding of the noise characteristics.) Noise is evident on each plot as high-frequency variability superimposed on the topography. The port side is much noisier than the starboard due to a significant difference in transmit power between the two sides prior to October, 1987 (A. Shor, personal communication, 1990). Figure C.1 is an example of fairly typical abyssal hill topography for the EPR region. The abyssal hills appear as coherent lineated features which slant diagonally. These are difficult to see on the port side because the noise, which is less coherent from beam to beam, is greater in amplitude than the abyssal hills themselves. On Figure C.2 there is no problem picking out the major topographic features (the fracture zone). However, there are also at least two regions where several beams simultaneously become extremely negative. These are likely due to time errors (A. Shor, personal communication, 1990).

We represent the time series for the *p*th beam by an equation of the form (2.25). This linear approximation works well for Sea Beam which calculates depth based on the centroid of the arrival time of acoustic energy reflecting from a finite area of seafloor. Sea Beam thus averages the seafloor in some fashion (though not exactly linearly) over a region $A_p(t)$. Noise is likely an expression of uncertainty in picking the correct centroid time. It is more difficult to predict the form of SM-II response and noise. In the following discussion, equation (2.25) provides only a framework for comparison and its validity with respect to SM-II bathymetry is not critical. In more general terms, we consider system effects which filter high wavenumber behavior of the seafloor to be the response, and those which enrich high wavenumber behavior to be the noise.

Topography is expected to have a covariance function given by (2.21). We also expect the cross-correlation of noise from beam to beam to be small so that the second order noise properties can be described by (2.30). Equation (2.31) represents the forward problem in relating the second-order statistics of the seafloor to the statistics of a multibeam data set. The echosounder response, acting like a filter, will tend to smooth the cross-covariance function and noise will add a sharp spike (assuming its correlation distance is small) to the top of the autocovariance ($p = q$) function. These effects are illustrated in Figure 2.6 both for the autocovariance function and its Fourier transform, the power spectrum, assuming a white noise ($\rho_{nn}(t) = \delta(t)$). The dashed line represents the autocovariance for an unmodified seafloor. These effects can be seen on the autocovariance of the SM-II center beam (beam 0) and power spectrum (Figure C.3). The SM-II center line, unlike the side-scan bathymetry, is a simple first-arrival echosounder and thus is similar to a Sea Beam system. The "spike" at the top of the autocovariance in Figure C.3 (see inset figure) is very sharp; its correlation width appears to be less than the data spacing (~0.037 km). Correspondingly, the part of the power spectrum dominated by noise effects (high wavenumbers) is flat. The noise in this case can thus be treated as a white process. The variance of the noise can easily be measured by the height of the spike, or the difference between the 0th and 1st lag.

Figure C.4 shows the autocovariance and power spectrum for the 6th port-side beam (beam -6) from the center beam of the SM-II data shown in Figure C.2. The autocovariance in this case is dominated by the two large features of the fracture zone. The effects of noise, which is also large on the port beams, is clearly in evidence as a spiky "cap" on top of the autocovariance. Unlike the center line (or Sea Beam), however, the along-track correlation distance (defined by the width of the correlation function) for $\rho_{nn}(t)$, ~1 km, is considerably larger than the data spacing. Correspondingly, the noise portion of the power spectrum is sloping rather than flat. The effects of SM-II noise are even more dramatic in Figure C.5, which shows the autocovariance and power spectrum of the -6 beam from Figure C.1. In this case noise dominates both the data and the autocovariance function. The noise correlation distance is again ~1 km. The slope of the power spectrum in Figure C.5 is very gradual, indicating a high fractal dimension for the noise process of

~1.8. Figure C.6 shows the autocovariance and power spectrum of the +3 beam in Figure 1. In this case, although the topographic covariance is a much larger portion of the total beam autocovariance, the portion which is due to noise is still large. Because the noise correlation is similar in size and shape to the topographic contribution to the beam autocovariance, it is impossible, without further information, to separate the two effects. However, because we can reasonably quantify the effects of the center echosounder profile (see Figure C.3), we can use its autocovariance as an approximate constraint. In Figure C.6, the dashed line represents the fit-by-eye model autocovariance shown in Figure C.3 (without system effects). The difference between the sample autocovariance and this model, enlarged and plotted in the inset, represents the approximate combined effects of SM-II noise and response in this profile. Again it is clear on this plot that the noise correlation has a width of ~1 km. Perhaps because of the significant correlation distance of the noise, the effects of response (if it exists), which should show as negative regions on the inset of Figure C.6, cannot easily be detected as in Figure C.3.

It is possible to make a rough estimate of the SM-II noise variance by differencing the autocovariance at 0 lag with the autocovariance at a lag sufficiently far to capture most of the noise variance but little of the topographic variance. We are aided in this by the assumed presence of an echosounder response, which should flatten the top of the topographic autocovariance in the absence of additive noise. For the SM-II examples in this study, we feel that differencing at a lag of 0.25 km provides a close (perhaps slightly underestimated) measure of the noise variance. Figures C.7 and C.8 show the rms noise estimated in this manner for each beam of the data in Figures C.1 and C.2 respectively. The noise-beam pattern is nearly identical for each case: the port (negative) beams exhibit the greatest amount of noise, and the center beam (calculated by differencing the 0th and 1st lag of the autocovariance) exhibits much less noise than does the side-scan bathymetry. The overall noise variation is greater for the data which has the strongest topographic component (Figure C.8). It is difficult to tell whether this results from a correlation of topography and noise or from leakage of topographic variance into the noise estimate.

There are several questions raised by this analysis that need to be addressed. Primarily we need to better understand the mechanism of response and noise for both multi-beam and side-scan bathymetric systems. Once done we may then come to an understanding of why SM-II noise is strongly correlated and Sea Beam noise is not, and of what the significance is of the correlation width and fractal dimension of SM-II noise. Work in this area is presently being carried out by Tom Reed at HIG (personal communication, 1989), who has noted the correlated noise as an artifact shingled textured to SM-II bathymetry data and attributed it to dispersed arrivals from strong reflectors. He has developed an algorithm to recognize and remove these effects. It is hoped that both through the improved power amplification hardware which has recently been installed, new transducers which have yet to be installed, and improved processing techniques that SM-II bathymetry data can be rendered suitable for the quantitative analysis of small-scale features.

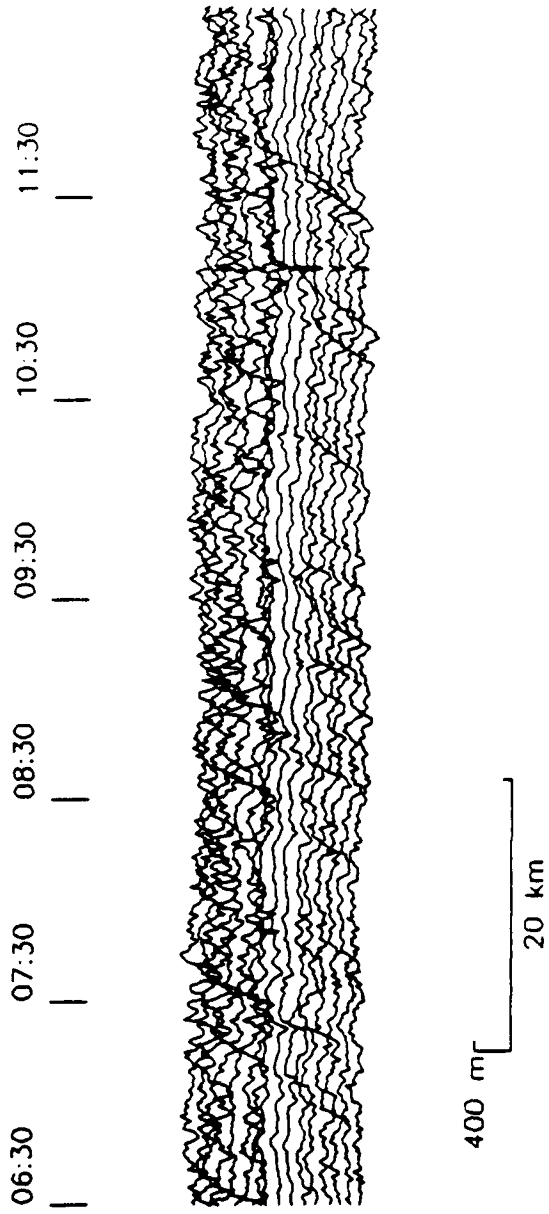

Figure C.1. 5-ping averaged SM-II data from the MW8707 cruise, taken just west of the EPR crest near 13° N. The SM-II z-x data are formed into 16 beams to simulate Sea Beam geometry (see text). The 16 formed beams are plotted individually. Port (negative) beams are at top. Ship direction is left-to-right.

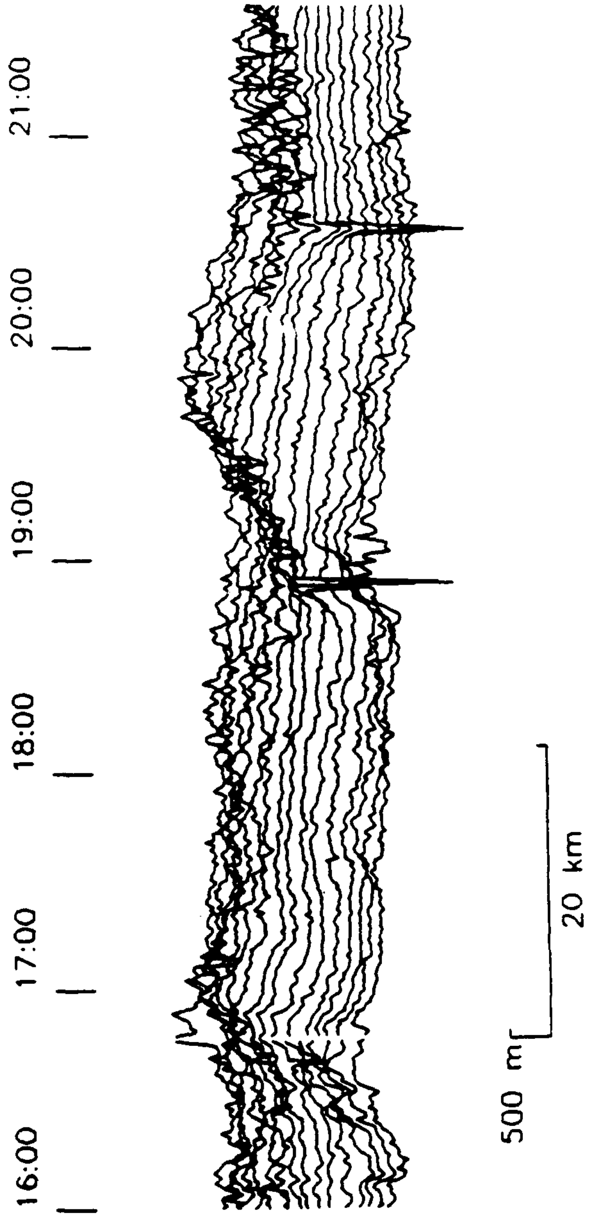

Figure C.2. Same as Figure C.1 for SM-II data from the MW8707 cruise crossing the Siquieros Fracture Zone just west of the ridge-transform intersection.

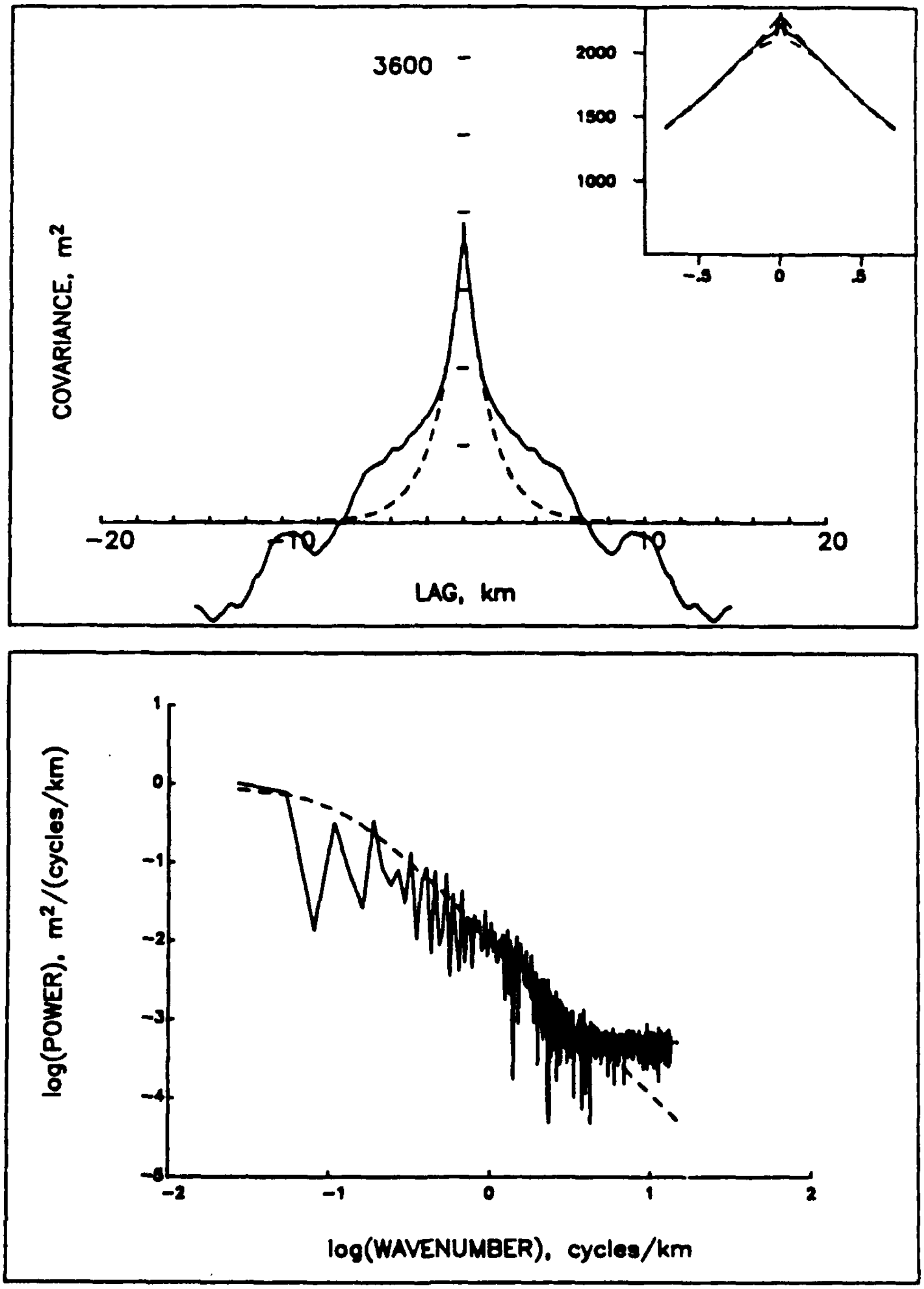

Figure C.3. Autocovariance (top), with inset showing enlargement of the origin, and power spectrum (bottom) calculated from the center beam (+0) of the data in Figure C.1. Also shown, in dashed lines, are fit-by-eye model functions both with and without system effects (compare with Figure 2.6).

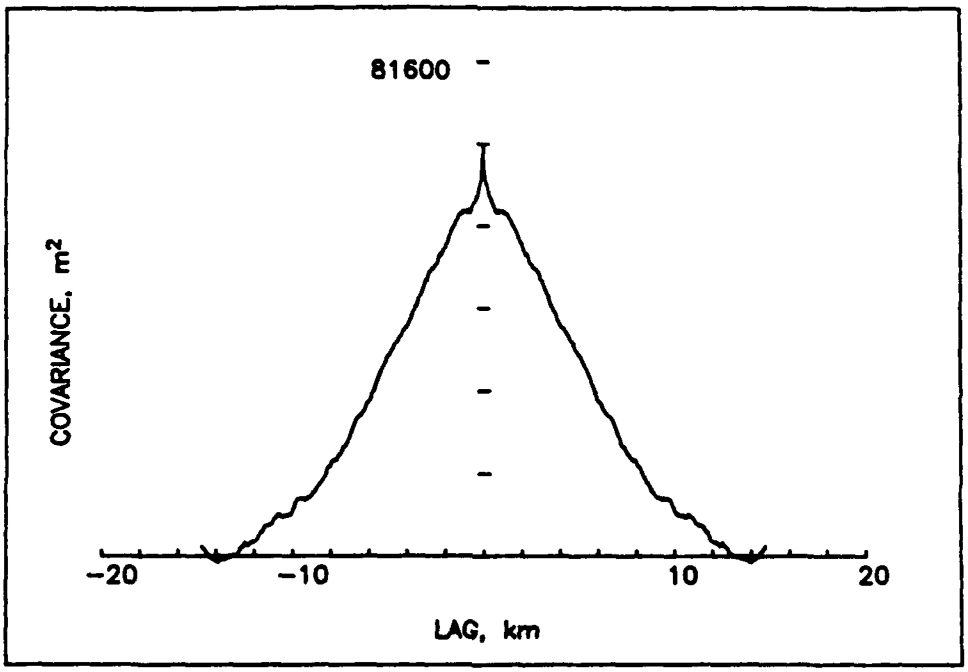

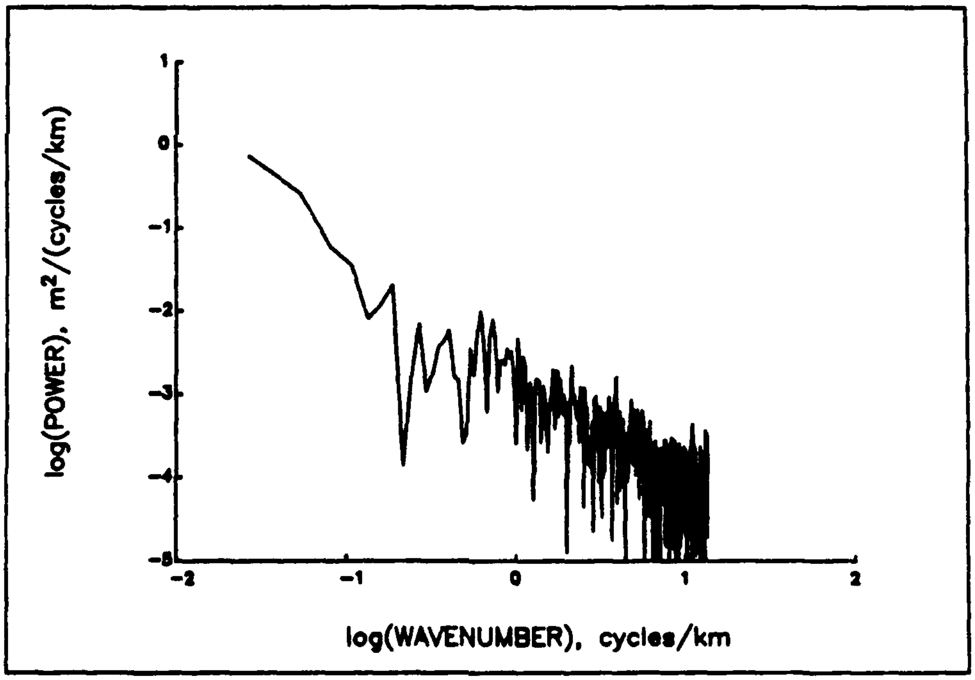

Figure C.4. Autocovariance (top) and power spectrum (bottom) calculated from the -6 beam of the data shown in Figure C.2.

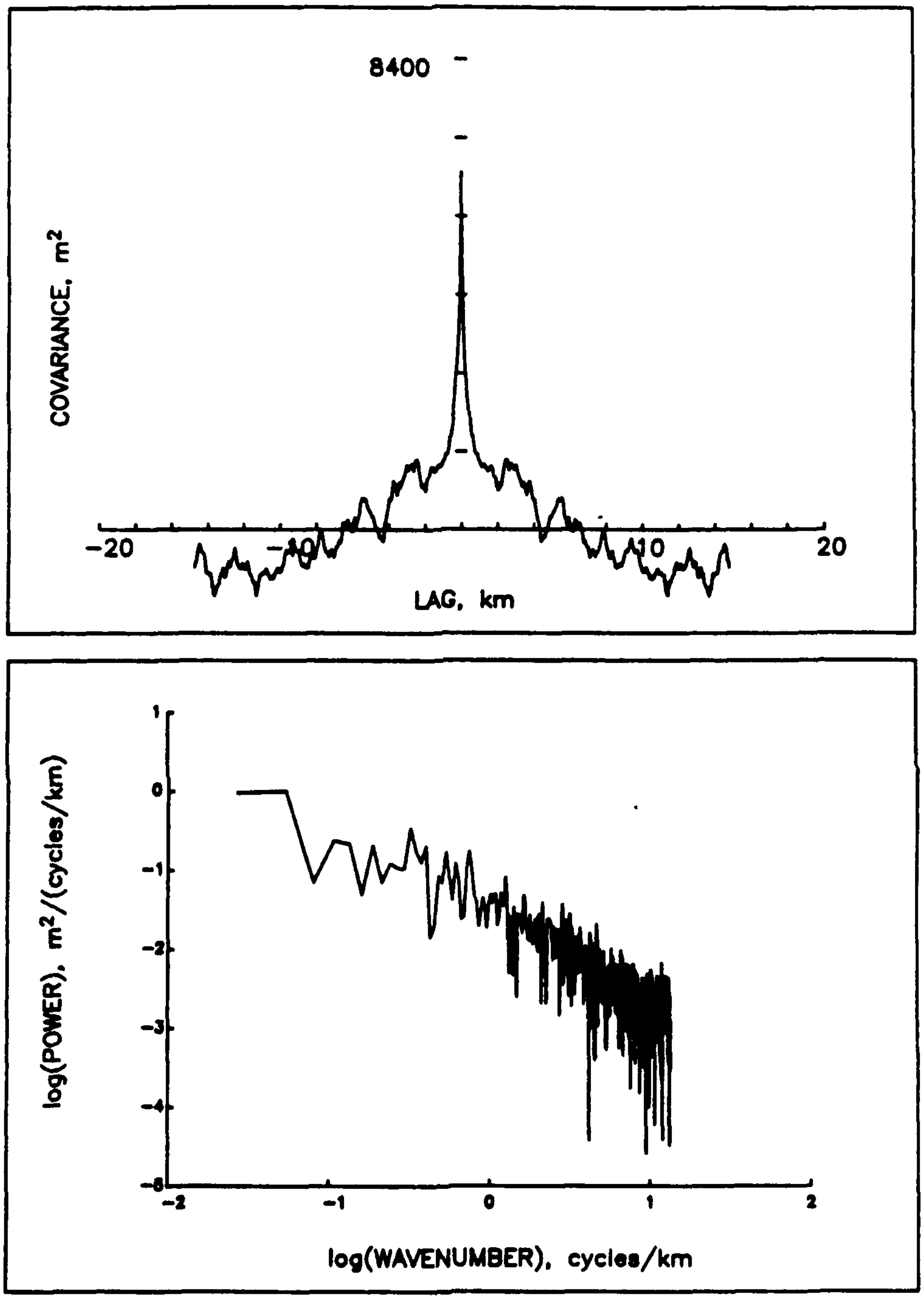

Figure C.5. Autocovariance (top) and power spectrum (bottom) calculated from the -6 beam of the data shown in Figure C.1.

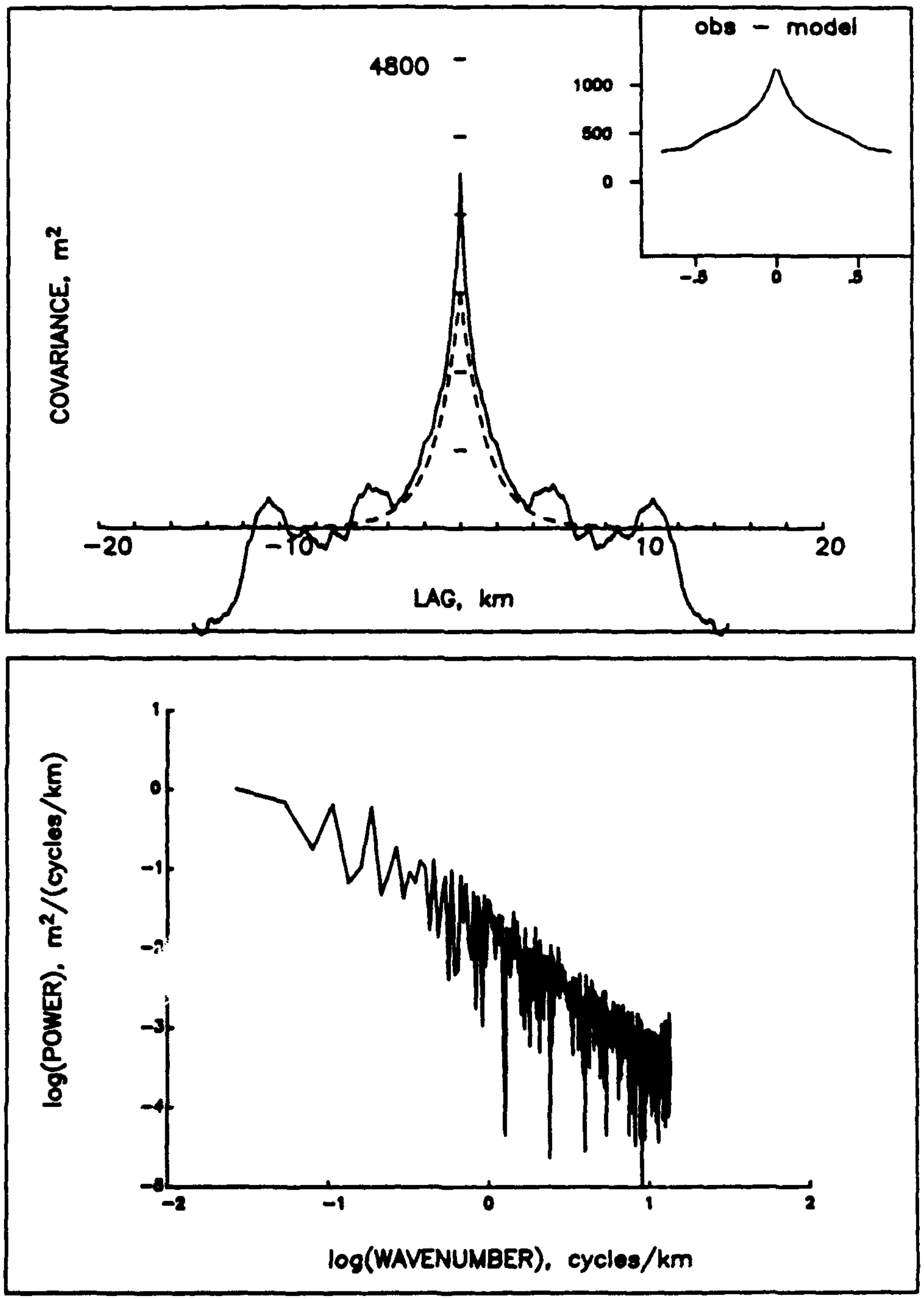

Figure C.6. Autocovariance (top) and power spectrum (bottom) calculated from the +3 beam of the data shown in Figure C.1. The dashed line is the same model autocovariance (without system effects) shown in Figure C.4. An enlargement of the difference between these near the origin is shown in the inset.

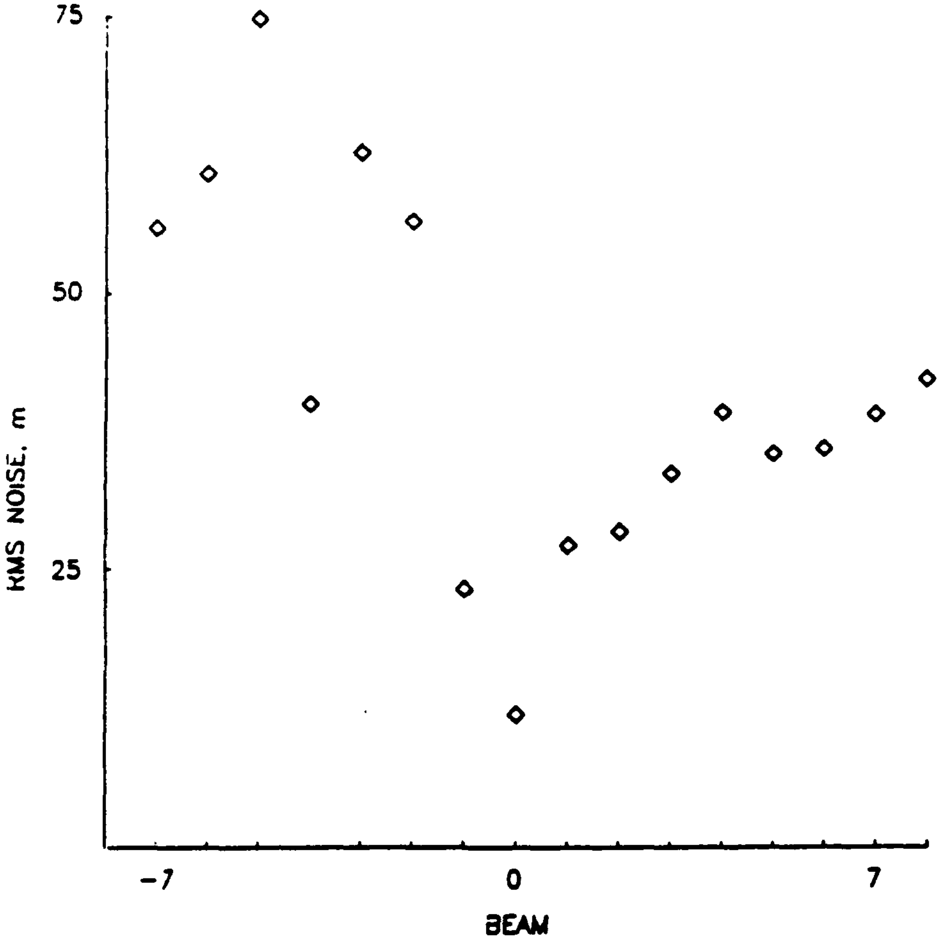

Figure C.7. Estimates of the rms noise for each of the beams shown in Figure C.1 (see text)

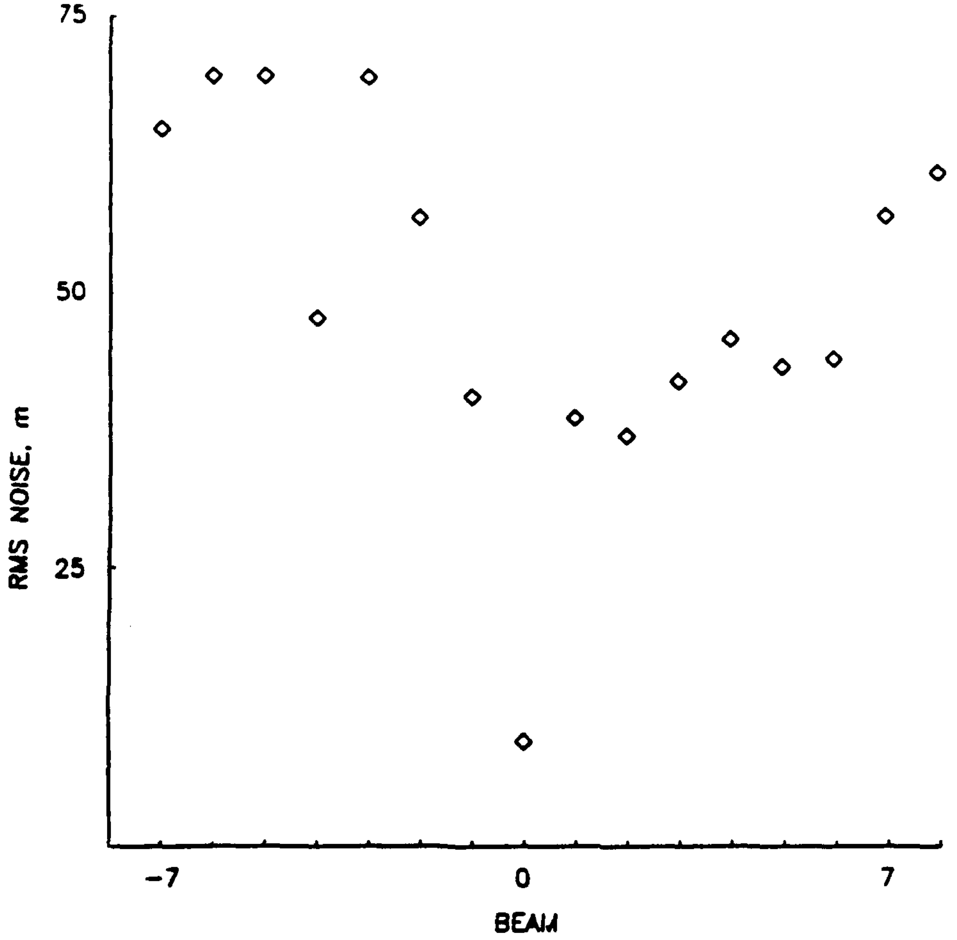

Figure C.8. Estimates of the rms noise for each of the beams shown in Figure C.2 (see text)

REFERENCES

Adler, R. J., *The Geometry of Random Fields*, 280 pp., John Wiley, New York, 1981.

Backus G., and F. Gilbert, Uniqueness in the inversion of inaccurate gross earth data, *Philos. Trans. R. Soc. London, Ser. A, 266,* 123–192, 1970.

Bard, Y., *Nonlinear Parameter Estimation,* 341 pp., Academic, San Diego, Calif., 1974.

Barone, A. M., and W. B. F. Ryan, Along-axis variations within the plate boundary zone of the southern segment of the Endeavor Ridge, *J. Geophys. Res., 93,* 7856-7868, 1988.

Bartlett, M. S., *An Introduction to Stochastic Process With Special Reference to Methods and Applications*, 362 pp., Cambridge University Press, New York, 1966.

Bell, T. H., Topographically generated waves in the open ocean, *J. Geophys. Res., 80,* 320–327, 1975*a*.

Bell, T. H., Statistical features of sea-floor topography, *Deep Sea Res., 22,* 883–892, 1975*b*.

Bell, T. H., Mesoscale sea floor roughness, *Deep Sea Res., 26A,* 65–76, 1978.

Beran, M. J., *Statistical Continuum Theories,* 424 pp., Wiley-Interscience, New York, 1968.

Bicknell, J. D. J.-C. Sempere, K. C. Macdonald, and P. J. Fox, Tectonics of a fast spreading center: A Deep-Tow and Sea Beam survey on the East Pacific Rise at 19° 30' S., *Mar. Geophys. Res., 9,* 25-45, 1987.

Black, M. T., and D. C. Mcadoo, Spectral analysis of marine geoid heights and ocean depths: Constraints on models of lithospheric and sublithospheric processes, *Mar. Geophys. Res., 10,* 157-180, 1988.

Bracewell, R., *The Fourier Transform and Its Application,* 381 pp., McGraw-Hill, New York, 1978.

Carrier, G. F., Stochastically driven dynamical systems, *J. Fluid Mech.*, *44*, 249–264, 1970.

Chernov, L. A., *Wave Propagation in a Random Medium*, 168 pp., McGraw-Hill, New York, 1960.

Choukroune, P., J. Francheteau, and R. Heikinian, Tectonics of the East Pacific Rise near 12° 50' N: a submersible study, *Earth Planet. Sci. Lett.*, *68*, 115-127, 1984.

Christie, D. M. and J. M. Sinton, Evolution of abyssal lavas along propagating segments of the Galapagos spreading center, *Earth Planet. Sci. Lett.*, *56*, 321-335, 1981.

Christie, D. M. and J. M. Sinton, Major element constraints on melting, differentiation and mixing of magmas from the Galapagos 95.5° W propagating rift system, *Contr. Min Petr.*, *94*, 274-288, 1986.

Clay, C.S., and H. Medwin, *Acoustical Oceanography: Principles and Applications*, 544 pp., Wiley-Interscience, New York, 1977.

Crane, K., Structural evolution of the East Pacific Rise axis from 13° 10' N to 10° 35' N: Interpretations from SeaMARC I data, *Tectonophysics*, *136*, 65-124, 1987.

CYAMEX, First manned submersible dives on the East Pacific Rise at 21°N (project RITA): General results, *Mar. Geophys. Res.*, *4*, 345-379, 1981.

de Moustier, C., and M. C. Kleinrock, Bathymetric artifacts in Sea Beam data: How to recognize them and what causes them, *J. Geophys. Res.*, *91*, 3407–3424, 1986.

de Moustier, C., State of the art in swath bathymetry survey systems, *Int. Hydrog. Rev.*, *65*, 25-54, 1988.

Detrick, R. S., P. Buhl, E. Vera, J. Mutter, J. Orcutt, J. Madsen, and T. Brocher, Multichannel seismic imaging of a crustal magma chamber along the East Pacific Rise, *Nature*, *326*, 35-41, 1987.

Edwards,M. H., D. J. Fornari, A. Malinverno, W. B. F. Ryan, J. A. Madsen, D. G. Gallo, M. R. Perfit, and A. N. Shor, Digital image processing of SeaMARC II data from the crest and flanks of the East Pacific Rise 13°-15° N: Implications for tectonic and thermal processes at medium-fast spreading centers (abstract), *Eos Trans. AGU, 69*, 1478, 1988.

Edwards, M. H., D. J. Fornari, A. Malinverno, W. B. F. Ryan, J. A. Madsen, D. G. Gallo, M. R. Perfit, and A. N. Shor, High resolution mapping using SeaMARC II over an intermediate to fast spreading segment of the East Pacific Rise 13°-15° N: quantitative structural data and implications for the fine-scale tectonic evolution of the Mid-Ocean Ridge crest and flank, *Proceedings of IGARSS-89/12th Canadian Symposium on Remote Sensing*, Vancouver, July, 1989.

Elter, J. F., and J. E. Molyneux, The long-distance propagation of shallow water waves over an ocean of random depth, *J. Fluid Mech., 53*, 1–15, 1972.

Farr, H. K., Multibeam bathymetric sonar: SEA BEAM and HYDRO CHART, *Mar. Geod., 4*, 1980.

Feller, W., *An Introduction to Probability Theory and Its Applications*, vol. 1, 509 pp., John Wiley, New York, 1968.

Feller, W., *An Introduction to Probability Theory and Its Applications*, vol. 2, 669 pp., John Wiley, New York, 1971.

Fornari, D. J., W. B. F. Ryan, and P. J. Fox, The evolution of craters and calderas on young seamounts: insights from Sea MARC I and Sea Beam sonar surveys of a small seamount group near the axis of the East Pacific Rise at 10° N, *J. Geophys. Res., 89*, 11,069-11,083, 1984.

Fornari, D. J., M. H. Edwards, A. Malinverno, J. A. Madsen, D. G. Gallo, M. R. Perfit, and A. N. Shor, Morphology of the East Pacific Rise from the axis of seafloor 4 ma old between 13°-15° N: bathymetric anomalies and local variations in subsidence along a ridge segment (abstract), *Eos Trans. AGU, 69*, 1485, 1988.

Fox, C. G., and D. E. Hayes, Quantitative methods for analyzing the roughness of the seafloor, *Rev. Geophys., 23*, 1–48, 1985.

Franklin, J. N., Well-posed stochastic extensions of ill-posed linear problems, *J. Math. Anal. Appl.*, *31*, 682–716, 1970.

Gilbert, L. E., and A. Malinverno, A characterization of the spectral density of residual ocean floor topography, *Geophys. Res. Lett.*, *15*., 1401-1404, 1988.

Goff, J. A., and T. H. Jordan, Stochastic Modeling of Seafloor Morphology: Inversion of Sea Beam data for second-order statistics, *J. Geophys. Res.*, *93*, 13 589-13 608, 1988.

Goff, J. A., and T. H. Jordan, Stochastic Modeling of Seafloor Morphology: a parameterized, Gaussian model, *Geophys. Res. Lett.*, *16*, 45-48, 1989*a*.

Goff, J. A., and T. H. Jordan, Stochastic Modeling of Seafloor Morphology: resolution of topographic parameters by Sea Beam data, *IEEE J. Ocean Eng.*, *14*, 326-337, 1989*b*.

Goff, J. A, T. H. Jordan, M. H. Edwards, and D. J. Fornari, Comparison of a stochastic seafloor model with SeaMARC II bathymetry and Sea Beam data near the East Pacific Rise 13° - 15° N, submitted to *J. Geophys. Res.*, 1990*a*

Goff, J. A., and T. H. Jordan, Pacific and Atlantic models of small-scale seafloor topography, *Office of Naval Research S. R. P. on Acoustic Reverberation*, Technical Report No. 1, 1990*b*.

Harrison, C. G. A., and L. Stieltjes, Faulting within the median valley, *Tectonophysics*, *38*, 137-144, 1977.

Hey, R. N., D. F. Naar, M. C. Kleinrock, W. J. Phipps-Morgan, E. Morales, and J. -G. Schilling, Microplate tectonics along a superfast seafloor spreading system near Easter Island, *Nature*, *317*, 320-325, 1985.

Huang, P. Y., and S. C. Solomon, Centroid depths of mid-ocean ridge earthquakes: dependence on spreading rate, *J. Geophys. Res.*, *93*, 13,445-13,477, 1988.

Jordan, T. H., H. W. Menard, and D. K. Smith, Density and size distribution of seamounts in the eastern Pacific inferred from wide-beam echosounding data, *J. Geophys. Res.*, *88*, 10,508–10,518, 1983.

Kappel, E. S., and W. B. F. Ryan, Volcanic episodicity and a non-steady-state rift valley along Northeast Pacific spreading centers: evidence from SeaMARC I, *J. Geophys. Res.*, *91*, 13925-13940, 1986.

Kleinrock, M. C., and R. N. Hey, Detailed tectonics near the tip of the Galapagos 95.5° W propagator: how the lithosphere tears and a spreading axis develops, *J. Geophys. Res.*, *94*, 13,801-13,838, 1989.

Klitgord, K. D., and J. Mammerickx, Northern East Pacific Rise: magnetic anomaly and bathymetric framework, *J. Geophys. Res.*, *87*, 6725-6750, 1982.

Kong, L. S. L., R. S. Detrick, P. J. Fox, L. A. Mayer, and W. B. F. Ryan, The morphology and tectonics of the MARK area from Sea Beam and Sea MARC I observations (Mid-Atlantic Ridge 23° N), *Mar. Geophys. Res.*, *10*, 59-90, 1988.

Krause, D. C., and H. W. Menard, Depth distribution and bathymetric classification of some seafloor profiles, *Mar. Geol.*, *3*, 169–193, 1965.

Lewis, B. T. R., Periodicities in volcanism and longitudinal magma flow on the East Pacific Rise at 23°N, *Geophys. Res. Lett.*, *6*, 753-756, 1979.

Lister, C. R. B., Qualitative models of spreading-center processes, including hydrothermal penetration, *Tectonophysics*, *37*, 203-218, 1977.

Longuet-Higgins, M. S., The statistical analysis of a random moving surface, *Philos. Trans. R. Soc. London, Ser. A*, *250*, 157–174, 1957.

Lord, R. D., The use of the Hankel transform in statistics, I, General theory and examples, *Biometrika*, *41*, 44–55, 1954.

Lonsdale, P., Structural geomorphology of a fast-spreading rise crest: The East Pacific Rise near 325'S, *Mar. Geophys. Res.*, *3*, 251-293, 1977.

Ludwig, W. J., and R. E. Houtz, *Isopach Map of the Sediments in the Pacific Ocean Basin and Marginal Sea Basins*, 1:13,999,369, American Association of Petroleum Geologists, Tulsa, Okla., 1979.

Macdonald, K. C., Mid-ocean ridges: Fine scale tectonic, volcanic and hydrothermal processes within the plate boundary zone, *Ann. Rev. Earth Planet. Sci.*, *10*, 155-190, 1982.

Macdonald, K. C., and T. M. Atwater, Evolution of rifted ocean ridges, *Earth Plan. Sci. Lett.*, *39*, 319-327, 1978.

Macdonald, K. C., and B. P. Luyendyk, Deep-tow studies of the structure of the Mid-Atlantic ridge near lat 37° N., *Geol. Soc. Am. Bull.*, *88*, 621–636, 1977.

Macdonald, K. C., and B. P. Luyendyk, Investigation of faulting and abyssal hill formation on the flanks of the East Pacific Rise (21°N) using ALVIN, *Mar. Geophys. Res.*, *7*, 515-535, 1985.

Macdonald, K. C., and P. J. Fox, The axial summit graben and cross-sectional shape of the East Pacific Rise as indicators of axial magma chambers and recent volcanic eruptions, *Earth Planet. Sci. Lett.*, *88*, 119-131, 1988.

Macdonald, K. C., J-C Sempere, and P. J. Fox, East Pacific Rise from Siqueiros to Orozco fracture zones: along-strike continuity of axial neovolcanic zone and structure and evolution of overlapping spreading centers, *J. Geophys. Res.*, *89*, 6049-6069, 1984.

Madsen, J. A., D. W. Forsyth, and R. S. Detrick, A new isostatic model for the East Pacific Rise crest, *J. Geophys. Res.*, *89*, 9997-10,015, 1984.

Madsen, J. A., P. J. Fox, and K. C. Macdonald, Morphotectonic fabric of the Orozco Transform Fault: Results from a Sea Beam investigation, *J. Geophys. Res.*, *91*, 3439-3454, 1986.

Madsen, J. A., D. J. Fornari, M. H. Edwards, D. G.. Gallo, M. R. Perfit, and A. N. Shor, Kinematic framework of the Cocos-Pacific plate boundary between 12° 50' N and 15° 10' N: Results from an extensive magnetic and SeaMARC II survey , submitted to *J. Geophys. Res*, 1990.

Malinverno A., Segmentation of topographic profiles of the sea floor based on a self-similar model, *IEEE J. Oceanic Eng.*, *14*, 348-359, 1989.

Mandelbrot, B. B., *The Fractal Geometry of Nature*, 468 pp., W. H. Freeman, New York, 1983.

Mandelbrot, B. B., Self-affine fractals and fractal dimension, *Phys. Scrip.*, *32*, 257–260, 1985.

Matérn, B., *Spatial Variation. Medd. SkogsforsknInst.*, *49*(5), 1–144, 1970.

Matsumoto, H., Characteristics of SeaMARC II phase data, submitted to *IEEE J. Ocean Eng.*,1990.

McDonald, M. F., and E. J. Katz, Quantitative method for describing the regional topography of the ocean floor, *J. Geophys. Res.*, *74*, 2597–2607, 1969.

McLachlan, N. W., *Bessel Functions for Engineers*, 239 pp., Oxford University Press, New York, 1955.

McNutt, M. K., Lithospheric flexure and thermal anomalies, *J. Geophys. Res.*, *89*, 11,180-11,194, 1984.

Menard, H. W., *Marine Geology of the Pacific*, McGraw-Hill, New York, 1964.

Menke, W., *Geophysical Data Analysis: Discrete Inverse Theory*, 260 pp., Academic, San Diego, Calif., 1984.

Minster, J. B., and T. H. Jordan, Present day plate motions, *J. Geophys. Res.*, *83*, 5331-5354, 1978.

Moran, P. A. P., A Gaussian Markovian process on a square lattice, *J. Appl. Probab.*, *10*, 54–62, 1973.

Needham, H. D., and J. Francheteau, Some characteristics of the rift valley in the Atlantic Ocean near 36°48'N, *Earth Planet. Sci. Lett*, *22*, 29-43, 1974.

Neidell, N. S., Spectral studies of marine geophysical profiles, *Geophysics*, *31*, 122–134, 1966.

Nikias, C. L., and M. R. Raghuveer, Bispectrum estimation: A digital signal processing framework, *Proc. IEEE*, *75*, 869-891, 1987.

Ouchi, T., A-B. K., Ibrahim, and G. V. Latham, Seismicity and structure in the Orozco Fracture Zone: Project ROSE phase II, *J. Geophys. Res.*, *87*, 8501-8507, 1982.

Papoulis, A., *Probability, Random Variables and Stochastic Processes*, 583 pp., Mcgraw-Hill, New York, 1965.

Parsons, B. and J. G. Sclater, An analysis of the variation of ocean floor bathymetry and heat flow with age, *J. Geophys. Res.*, *82*, 803-827, 1977.

Phipps-Morgan, J., E. M. Parmentier, and J. Lin., Mechanisms for the origin of mid-oceanic ridge axial topography: Implications for the thermal and mechanical structure of accreting plate boundaries, *J. Geophys. Res.*, *92*, 12,823-12,836, 1987.

Pockalny, R. A., P. J. Fox, and R. S. Detrick, A morphological comparison of abyssal hill topography using high-resolution multi-beam bathymetry data, submitted to *J. Geophys. Res.*, 1989.

Press, W. H., B. P. Flannery, S. A. Teukolsky, and W. T. Vetterling, *Numerical Recipes*, 818 pp., Cambridge, New York, 1986.

Priestly, M. B., *Spectral Analysis and Time Series*, 890 pp., Academic, San Diego, Calif., 1981.

Rea, D. K., Model for the formation of topographic features of the East Pacific Rise crest, *Geology*, *3*, 77-80, 1975.

Renard, V., and J. P. Allenou, SEA BEAM, multi-beam echosounding in "Jean Charcot", *Int. Hydrogr. Rev.*, *56*, 35–67, 1979.

Renard, V., R. Heikinian, J. Francheteau, R. D. Ballard, and H. Backer, Submersible observations at the axis of the ultra-fast-spreading East Pacific Rise (17° 30' to 21° 30' S), *Earth and Plan. Sci. Lett.*, *75*, 339-353, 1985.

Rona, P. A., R. N. Harbison, and S. A. Bush, Abyssal hills of the eastern central north Atlantic, *Mar. Geol.*, *16*, 275-292, 1974.

Schouten, H., and C. Denham, Deconvolution of faulted normal seafloor in the North Atlantic FAMOUS area (abstract), *Eos Trans. AGU*, *64*, 314, 1983.

Searle, R., GLORIA survey of the East Pacific Rise near 3.5° S: Tectonic and volcanic characteristics of a fast spreading mid-ocean rise, *Tectonophysics*, *101*, 319-344, 1984.

Sinton, J. M., D. S. Wilson, D. M. Christie, R. N. Hey, and J. R. Delaney, Petrological consequences of rift propagation on oceanic spreading ridges, *Earth. Planet. Sci. Lett.*, *62*, 193-207, 1983.

Smith, D. K., and T. H. Jordan, The size distribution of Pacific seamounts, *Geophys. Res. Let.*, *14*, 1119–1122, 1987.

Smith, D. K., and T. H. Jordan, Seamount statistics in the Pacific Ocean, *J. Geophys. Res.*, *93*, 2899–2917, 1988.

Stanton, T. K., Echo fluctuations from the rough seafloor: Predictions based on acoustically measured microrelief properties, *J. Accoust. Soc. Am.*, *78*, 715–721, 1985.

Tapponnier, P., and J. Francheteau, Necking of the lithosphere and mechanics of slowly accreting plate boundaries, *J. Geophys. Res.*, *83*, 3955-3970, 1978.

Tatarski, V. I., *Wave Propagation in a Turbulent Medium*, 285 pp., McGraw-Hill, New York, 1961.

Taylor, H. M., and S. Karlin, *An Introduction to Stochastic Modeling*, 399 pp., Academic, San Diego, Calif., 1984.

Toomey, D. R., S. C. Solomon, and G. M. Purdy, Microearthquakes beneath median valley of Mid-Atlantic Ridge near 23° N: Topography and tectonics, *J. Geophys. Res.*, *93*, 9093-9112, 1988.

von Kármán, T., Progress in the statistical theory of turbulence, *J. Mar. Res.*, *7*, 252–264, 1948.

Weissel J. K., and D. H. Hayes, The Australian-Antarctic discordance: New results and implications, *J. Geophys. Res.*, *79*, 2579-2587, 1974.

Whittle, P., On stationary processes in the plane, *Biometrika*, *41*, 434–449, 1954.

Yesyunin, R. Y., Description of bottom relief by means of the spatial correlation function, *Oceanology*, *15*, 719–721, 1975.

DOCUMENT LIBRARY

January 17, 1990

Distribution List for Technical Report Exchange

Attn: Stella Sanchez-Wade
Documents Section
Scripps Institution of Oceanography
Library, Mail Code C-075C
La Jolla, CA 92093

Hancock Library of Biology &
Oceanography
Alan Hancock Laboratory
University of Southern California
University Park
Los Angeles, CA 90089-0371

Gifts & Exchanges
Library
Bedford Institute of Oceanography
P.O. Box 1006
Dartmouth, NS, B2Y 4A2, CANADA

Office of the International
Ice Patrol
c/o Coast Guard R & D Center
Avery Point
Groton, CT 06340

NOAA/EDIS Miami Library Center
4301 Rickenbacker Causeway
Miami, FL 33149

Library
Skidaway Institute of Oceanography
P.O. Box 13687
Savannah, GA 31416

Institute of Geophysics
University of Hawaii
Library Room 252
2525 Correa Road
Honolulu, HI 96822

Marine Resources Information Center
Building E38-320
MIT
Cambridge, MA 02139

Library
Lamont-Doherty Geological
Observatory
Columbia University
Palisades, NY 10964

Library
Serials Department
Oregon State University
Corvallis, OR 97331

Pell Marine Science Library
University of Rhode Island
Narragansett Bay Campus
Narragansett, RI 02882

Working Collection
Texas A&M University
Dept. of Oceanography
College Station, TX 77843

Library
Virginia Institute of Marine Science
Gloucester Point, VA 23062

Fisheries-Oceanography Library
151 Oceanography Teaching Bldg.
University of Washington
Seattle, WA 98195

Library
R.S.M.A.S.
University of Miami
4600 Rickenbacker Causeway
Miami, FL 33149

Maury Oceanographic Library
Naval Oceanographic Office
Stennis Space Center
NSTL, MS 39522-5001

Marine Sciences Collection
Mayaguez Campus Library
University of Puerto Rico
Mayagues, Puerto Rico 00708

Library
Institute of Oceanographic Sciences
Deacon Laboratory
Wormley, Godalming
Surrey GU8 5UB
UNITED KINGDOM

The Librarian
CSIRO Marine Laboratories
G.P.O. Box 1538
Hobart, Tasmania
AUSTRALIA 7001

Library
Proudman Oceanographic Laboratory
Bidston Observatory
Birkenhead
Merseyside L43 7 RA
UNITED KINGDOM

50272-101

REPORT DOCUMENTATION PAGE	**1. REPORT NO.** WHOI-90-24	**2.**	**3. Recipient's Accession No.**

4. Title and Subtitle

Stochastic Modelling of Seafloor Morphology

5. Report Date

June 1990

6.

7. Author(s)

John Anson Goff

8. Performing Organization Rept. No.

WHOI-90-24

9. Performing Organization Name and Address

The Woods Hole Oceanographic Institution
Woods Hole, Massachusetts 02543

10. Project/Task/Work Unit No.

11. Contract(C) or Grant(G) No.

(C)

(G)

12. Sponsoring Organization Name and Address

The Office of Naval Research through the Massachusetts Institute of Technology

13. Type of Report & Period Covered

Ph.D. Thesis

14.

15. Supplementary Notes

This report should be cited as: John Anson Goff, 1990. Stochastic Modelling of Seafloor Morphology. Ph.D. Thesis, MIT/WHOI, WHOI 90-24.

16. Abstract (Limit: 200 words)

At scale lengths less than 100 km or so, statistical descriptions of seafloor morphology can be usefully employed to characterize processes which form and reshape abyssal hills, including ridge crest volcanism, off-axis tectonics and volcanism, mass wasting, sedimentation, and post-depositional transport. The objectives of this thesis are threefold: (1) to identify stochastic paramenterizations of small scale topography that are geologically useful, (2) to implement procedures for estimating these parameters from multibeam and side-scan sonar surveys that take into account the finite precision, resolution, and sampling of real data sets, and (3) to apply these techniques to the study of marine geological problems.

17. Document Analysis a. Descriptors

1. seafloor morphology
2. abyssal hills
3. stochastic modelling

b. Identifiers/Open-Ended Terms

c. COSATI Field/Group

18. Availability Statement Approved for publication; distribution unlimited.	**19. Security Class (This Report)** UNCLASSIFIED	**21. No. of Pages** 266
	20. Security Class (This Page)	**22. Price**

(See ANSI-Z39.18) *See Instructions on Reverse* OPTIONAL FORM 272 (4-77)
(Formerly NTIS-35)
Department of Commerce